

Document Version

Final published version

Citation (APA)

Xie, J. (2026). *Auxetic Cementitious Composites for Energy Harvesting*. [Dissertation (TU Delft), Delft University of Technology]. <https://doi.org/10.4233/uuid:95794c62-4555-4a3d-af03-e0b5c365a0fc>

Important note

To cite this publication, please use the final published version (if applicable).
Please check the document version above.

Copyright

In case the licence states "Dutch Copyright Act (Article 25fa)", this publication was made available Green Open Access via the TU Delft Institutional Repository pursuant to Dutch Copyright Act (Article 25fa, the Taverne amendment). This provision does not affect copyright ownership.
Unless copyright is transferred by contract or statute, it remains with the copyright holder.

Sharing and reuse

Other than for strictly personal use, it is not permitted to download, forward or distribute the text or part of it, without the consent of the author(s) and/or copyright holder(s), unless the work is under an open content license such as Creative Commons.

Takedown policy

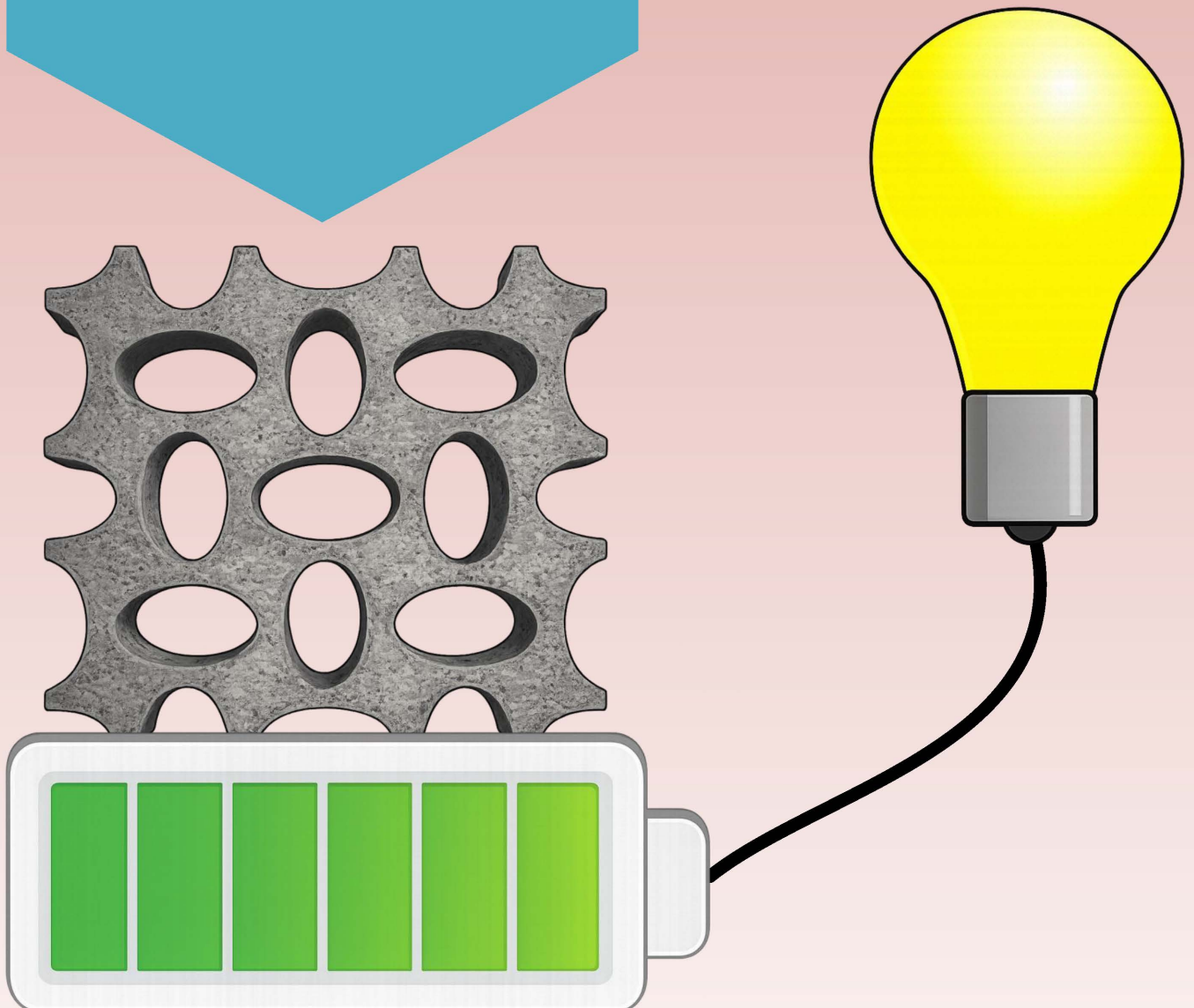
Please contact us and provide details if you believe this document breaches copyrights.
We will remove access to the work immediately and investigate your claim.

Auxetic Cementitious Composites

For Energy Harvesting

 TU Delft

$$D_j = d_{jkl} \cdot T_{kl}$$



Jinbao Xie 谢津宝

Propositions

Accompanying the dissertation

Auxetic Cementitious Composites for Energy Harvesting

by

Jinbao Xie

1. The ubiquity of cementitious materials makes cementitious energy harvesters a promising technology. [This proposition pertains to this dissertation]
2. Optimization in one performance metric often necessitates trade-offs that compromise other performance attributes. [This proposition pertains to this dissertation]
3. Guiding a numerical model with machine learning to perform optimization is more efficient than generating a dataset from model outputs and then training a separate machine learning model for optimization. [This proposition pertains to this dissertation]
4. Waiting with intention is not the same as waiting without direction — one empowers, the other drains.
5. The impact of results in exploratory experiment is strongly influenced by the number of trial-and-error iterations experienced during the experimental process.
6. Robust engineering modeling should be grounded in experimental investigation, as empirical observations are fundamental to the development of theoretical models and critical for their validation.
7. Reflective thinking during fragmented or leisure time is the most effective strategy for overcoming bottlenecks in research.
8. Although often considered undesirable, certain defects arranged in regular patterns may enhance the material's deformability and toughness.
9. The final turns hiding the finish line in marathons creates a mental barrier, making the last stretch feel harder despite being close to the goal.
10. The best way to reduce anxiety about a distant future is to focus on the present and embrace each step of the journey.

These propositions are regarded as opposable and defensible, and have been approved as such by the promoters Dr. B. Šavija and Prof.dr.ir. E. Schlangen.

**Auxetic Cementitious Composites
For Energy Harvesting**

**Auxetic Cementitious Composites
For Energy Harvesting**

Dissertation

for the purpose of obtaining the degree of doctor
at Delft University of Technology
by the authority of the Rector Magnificus, Prof.dr.ir. H. Bijl
chair of the Board for Doctorates
to be defended publicly on
Monday 2 March 2026 at 17:30

By

Jinbao XIE

This dissertation has been approved by the promotor.

Composition of the doctoral committee:

Rector Magnificus	chairperson
Dr. B. Šavija	Delft University of Technology, promotor
Prof.dr.ir. E. Schlangen	Delft University of Technology, promotor

Independent members:

Prof.dr. G. Ye	Delft University of Technology
Prof.dr.ir. L.J. Sluys	Delft University of Technology
Dr. G. Lavidas	Delft University of Technology
Prof.dr. Y. Xu	Chongqing University, China
Prof.dr. Y. Farnam	Drexel University, USA



Keywords: Auxetic cementitious cellular composites, Energy Harvesting, Additive manufacturing, Piezoelectric effect, Strain-hardening cementitious composites, Concrete damage plasticity model, Bayesian Optimization

Printed by: Ipskamp Printing, The Netherlands

Cover design: Jinbao Xie

Copyright © 2026 by Jinbao Xie

All rights reserved. This copy of the thesis has been supplied on the condition that anyone who consults it is understood to recognize that its copyright rests with its author and that no quotation from the thesis and no information derived from it may be published without the author's prior consent.

ISBN: 978-94-6384-914-2

An electronic copy of this dissertation is available at <http://repository.tudelft.nl/>

Live in the moment (活在当下)

CONTENTS

SUMMARY	V
SAMENVATTING	VII
CHAPTER 1 GENERAL INTRODUCTION	1
1.1 RESEARCH BACKGROUND	2
1.1.1 Architected cementitious cellular composites (ACCCs)	2
1.1.2 Considerations for ACCC energy harvester	2
1.2 RESEARCH OBJECTIVES AND SCOPE	3
1.2.1 RESEARCH OBJECTIVES	3
1.2.2 RESEARCH SCOPE	4
1.3 RESEARCH APPROACH	4
1.4 THESIS OUTLINE	5
REFERENCES	6
CHAPTER 2 LITERATURE REVIEW	9
2.1 INTRODUCTION	10
2.2 ENERGY HARVESTING USING PIEZOELECTRIC MATERIALS	10
2.3 ENERGY HARVESTING USING CEMENTITIOUS MATERIALS	12
2.4 AUXETIC CEMENTITIOUS COMPOSITES	15
2.5 FINAL REMARKS	20
REFERENCES	20
CHAPTER 3 ELLIPTICAL-SHAPED ACCC ENERGY HARVESTER—EXPERIMENTS	27
3.1 INTRODUCTION	28
3.2 MATERIALS AND METHODS	29
3.2.1 Specimen preparation	29
3.2.2 Experimental test	32
3.3 RESULTS AND DISCUSSION	33
3.4 CONCLUSIONS	38
REFERENCES	38

CHAPTER 4 BENCHMARK ENERGY HARVESTING MODEL FOR FIBER-REINFORCED CEMENTITIOUS COMPOSITES UTILIZING SURFACE-MOUNTED PIEZOELECTRIC MATERIALS	41
4.1 INTRODUCTION	42
4.2 THEORETICAL MODELING	42
4.2.1 Concrete damage plasticity (CDP) model	42
4.2.2 Interaction between ECC and piezoelectric polymer	44
4.2.3 Piezoelectric model for piezoelectric polymer	46
4.2.4 Flowchart of the energy harvesting model	49
4.3 Model validation	50
4.3.1 Experiment setup	50
4.3.2 Energy harvesting modelling	51
4.3.3 Results and discussion	56
4.4 CONCLUSIONS	61
REFERENCES.....	62
CHAPTER 5 ELLIPTICAL-SHAPED ACCC ENERGY HARVESTER—MODELLING...	65
5.1 INTRODUCTION	66
5.2 MECHANICAL MODEL	68
5.2.1 CDP model for preloading	68
5.2.2 Reconstruction of ACCCs	70
5.2.3 Second-elasticity model of ACCCs	71
5.2.4 Parametric modeling of PVDF film	72
5.2.5 Interaction between ACCCs and PVDF	72
5.3 ANALYTICAL FORMULAS FOR PIEZOELECTRIC MODEL	73
5.4 MODELLING RESULTS AND DISCUSSION	76
5.5 CONCLUSIONS	82
REFERENCES.....	83
CHAPTER 6 ENHANCED AUXETIC CEMENTITIOUS CELLULAR COMPOSITE (ACCC) ENERGY HARVESTER USING STRAIN-HARDENING CEMENTITIOUS COMPOSITES (SHCC)	85
6.1 INTRODUCTION	86
6.2 DESIGN THEORY	86
6.3 SAMPLE PREPARATION AND MIXTURE DESIGN	89
6.4 EXPERIMENTAL TEST	90
6.5 RESULTS AND DISCUSSION	92
6.5.1 Material properties	92

6.5.2 Compressive behavior of ACCCs	97
6.5.3 Energy harvesting capability of ACCCs	105
6.6 CONCLUSIONS	110
REFERENCES.....	111
CHAPTER 7 BAYESIAN-DRIVEN MODULATION OF RECOVERABLE STRAIN IN AUXETIC CEMENTITIOUS CELLULAR COMPOSITES FOR OPTIMAL ENERGY HARVESTERS	115
7.1 INTRODUCTION	116
7.2 MATERIALS AND METHODS	117
7.2.1 Materials and specimen preparation	117
7.2.2 Experiments	119
7.3 ENERGY HARVESTING MODELLING	122
7.3.1 Mechanical model	123
7.3.2 Energy harvesting model	128
7.4 Bayesian optimization (BO)	129
7.4.1 Theory	129
7.4.2 Bayesian Optimization setup	131
7.5 RESULTS AND DISCUSSION	141
7.5.1. Optimization results	141
7.5.2. Experimental validation	147
7.6 CONCLUSIONS	150
REFERENCES.....	151
CHAPTER 8 MULTI-CELL AUXETIC CEMENTITIOUS CELLULAR COMPOSITE (ACCC) PVDF-BASED ENERGY HARVESTER	153
8.1 INTRODUCTION	154
8.2 MATERIALS AND METHODS	155
8.2.1 Materials and specimen preparation	155
8.2.2 Experiments	157
8.3. RESULTS AND DISCUSSION	161
8.3.1 Mechanical behavior during pre-compression	161
8.3.2 Energy harvesting results	162
8.4. CONCLUSIONS	167
REFERENCES.....	168
CHAPTER 9 CONCLUSIONS AND RECOMMENDATIONS	171
9.1 RETROSPECTION	172
9.2 CONCLUSIONS	173

9.3 RECOMMENDATIONS	174
9.3.1 Other types of ACCC energy harvester	174
9.3.2 Enhanced hinge-joint of ACCC energy harvester	176
REFERENCES.....	176
Appendix A (Supplementary information to Chapter 5).....	179
ACKNOWLEDGEMENTS	185
LIST OF PUBLICATIONS.....	189
CURRICULUM VITAE.....	191

SUMMARY

Auxetic cementitious composites (ACCCs), composed of fiber-reinforced cementitious materials, exhibit notable deformability and structural resilience due to their auxetic characteristics. These properties make them excellent candidates for efficient energy harvesting, especially when integrated with surface-mounted piezoelectric elements. Moreover, ACCCs demonstrate reversible deformation under cyclic loading and maintain their quasi-elastic behavior over extended use, which underscores their promise for long-term energy harvesting applications. Despite growing interest in energy harvesting, most existing research has concentrated on auxetic materials derived from metals and polymers, while auxetic cementitious composites remain largely underexplored. Current investigations into ACCCs have predominantly focused on their mechanical properties, with limited emphasis on their potential for multifunctional applications such as energy harvesting. Given the abundance and low cost of cementitious materials, ACCCs offer a promising and sustainable avenue for the development of cost-effective energy harvesting systems. In this thesis, the feasibility of utilizing ACCCs for energy harvesting was systematically investigated.

First, a novel piezoelectric energy harvester (PEH) integrating ACCCs with surface-mounted polyvinylidene fluoride (PVDF) films is proposed to convert strain energy into usable electrical power. In this configuration, the ACCC–PVDF system is initially compressed to a prescribed displacement and subsequently subjected to cyclic loading, thereby enabling continuous voltage generation for energy harvesting. The influence of loading amplitude and frequency on the output voltage response of the harvester is further investigated.

Then, this study employs numerical modeling to quantitatively analyze the piezoelectric mechanisms governing the ACCC-based energy harvester. A general theoretical framework was first developed to evaluate the energy harvesting performance of fiber-reinforced cementitious materials with surface-mounted PVDF. Building on this computational framework, a specialized computational model was formulated to capture both the mechanical deformation and electrical response of the ACCC harvester. The mechanical behavior of ACCCs was represented using the concrete damage plasticity (CDP) model during the preloading stage, which was subsequently transitioned to an elastic model for cyclic loading. Analytical expressions describing the piezoelectric effect were then derived from the simulated mechanical responses to predict the PVDF output voltage. Modelling results showed good agreement with experimental data.

The final stage of this work focuses on optimizing the ACCC-based energy harvester. At the material level, a strain-hardening cementitious composite (SHCC) mixture with enhanced

softening behavior was developed to enhance fiber-bridging performance at ACCC joints, thereby enabling stable auxetic behavior across diverse geometries. This advancement permits systematic evaluation of geometric configurations to identify designs with superior energy harvesting performance. Nevertheless, the inherent brittleness of cementitious materials remains a critical challenge, as geometric modifications can induce splitting and compromise auxetic behavior. To overcome the limitations of labor-intensive experiments, the previously developed energy harvesting models were employed to generate simulation datasets; however, large-scale simulations proved computationally demanding. To address this issue, a machine learning–assisted framework integrating the energy harvesting model with Bayesian Optimization (BO) was implemented, enabling efficient identification of high-performance ACCC geometries for energy harvesting while using constraints to prevent splitting failure and non-auxetic behavior of ACCCs under compression. The optimal configuration derived from this framework was fabricated using additive manufacturing–assisted casting and experimentally validated, confirming its enhanced energy harvesting capability. Furthermore, the machine learning–driven design was extended by assembling the optimized single-cell ACCC into a 2×2 multi-cell configuration, demonstrating the scalability and practicality of the approach for real-world energy harvesting applications.

This PhD study proposed a strain-based ACCC energy harvester that leverages the recoverable deformation within the auxetic behavior range of ACCC structures. Combining experimental evaluation, numerical modeling, and machine learning, the research enhances the recoverable deformation capacity of ACCCs, thereby increasing the energy output of the harvester. The recoverable deformation of ACCCs is identified as the governing mechanism, as the harvested energy is determined by the mechanical energy generated during deformation and its subsequent conversion. Therefore, these findings also provide broader insights for future studies on other energy harvesting strategies employing auxetic cementitious composites as substrates.

SAMENVATTING

Auxetische cementgebonden composieten (ACCC's), bestaande uit vezelversterkte cementshoudende materialen, vertonen opmerkelijke vervormbaarheid en structurele veerkracht dankzij hun auxetische eigenschappen. Deze eigenschappen maken ze uitstekende kandidaten voor efficiënte energieopwekking, vooral wanneer ze worden gecombineerd met op het oppervlak gemonteerde piëzo-elektrische elementen. Bovendien vertonen ACCC's omkeerbare vervorming onder cyclische belasting en behouden ze hun quasi-elastisch gedrag bij langdurig gebruik, wat hun potentieel voor duurzame energieopwekking benadrukt. Ondanks de groeiende belangstelling voor energieopwekking, heeft het merendeel van het bestaande onderzoek zich geconcentreerd op auxetische materialen op basis van metalen en polymeren, terwijl auxetische cementgebonden composieten grotendeels onontgonnen blijven. Huidige studies naar ACCC's hebben zich voornamelijk gericht op hun mechanische eigenschappen, met beperkte aandacht voor multifunctionele toepassingen zoals energieopwekking. Gezien de overvloed en lage kosten van cementgebonden materialen, bieden ACCC's een veelbelovende en duurzame mogelijkheid voor de ontwikkeling van kosteneffectieve systemen voor energieopwekking. In dit proefschrift is de haalbaarheid van het gebruik van ACCC's voor energieopwekking systematisch onderzocht.

Allereerst wordt een nieuw piëzo-elektrisch energieopwekkingsysteem (PEH) voorgesteld, waarbij ACCC's worden geïntegreerd met op het oppervlak gemonteerde polyvinylideenfluoride (PVDF)-folies om vervormingsenergie om te zetten in bruikbare elektrische energie. In deze configuratie wordt het ACCC-PVDF-systeem eerst samengedrukt tot een voorgeschreven verplaatsing en vervolgens onderworpen aan cyclische belasting, waardoor continue spanningsgeneratie voor energieopwekking mogelijk wordt. Het effect van belastingsamplitude en frequentie op de uitgangsspanning van de harvester wordt verder onderzocht.

Vervolgens maakt deze studie gebruik van numerieke modellering om de piëzo-elektrische mechanismen van de ACCC-gebaseerde energieopwekker kwantitatief te analyseren. Eerst is een algemeen theoretisch kader ontwikkeld om de energieopwekkingsprestaties van vezelversterkte cementgebonden materialen met op het oppervlak gemonteerde PVDF te evalueren. Gebaseerd op dit theoretische kader is een gespecialiseerd computationeel model geformuleerd om zowel de mechanische vervorming als de elektrische respons van de ACCC-harvester te beschrijven. Het mechanische gedrag van ACCC's werd tijdens de voorbelastingfase weergegeven met het "concrete damage plasticity" (CDP)-model, dat vervolgens werd omgewerkt naar een elastisch model voor cyclische belasting. Analytische uitdrukkingen voor het piëzo-elektrische effect werden afgeleid uit de gesimuleerde

mechanische respons om de PVDF-uitgangsspanning te voorspellen. De modelleerresultaten vertoonden goede overeenstemming met experimentele gegevens.

Het laatste stadium van dit werk richt zich op het optimaliseren van de ACCC-gebaseerde energieopwekker. Op materiaalkundig niveau werd een “strain-hardening cementitious composite” (SHCC)-mengsel ontwikkeld met verbeterd softening-gedrag om de scheur overbruggende prestaties van de vezels bij ACCC-verbindingen te versterken, waardoor stabiel auxetisch gedrag over diverse geometrieën mogelijk werd. Deze vooruitgang maakt systematische evaluatie van geometrische configuraties mogelijk om ontwerpen met superieure energieopwekkingsprestaties te identificeren. Desondanks blijft de inherente brosheid van cementhoudende materialen een kritische uitdaging, aangezien geometrische aanpassingen scheurvorming kunnen veroorzaken en het auxetische gedrag kunnen aantasten. Om de beperkingen van arbeidsintensieve experimenten te overwinnen, werden de eerder ontwikkelde energieopwekkingsmodellen gebruikt om simulatiegegevens te genereren; echter bleken grootschalige simulaties computationeel veeleisend. Om dit probleem aan te pakken, werd een door machine learning ondersteund kader geïmplementeerd, dat het energieopwekkingsmodel integreert met Bayesian Optimization (BO), waardoor efficiënt de ACCC-geometrieën met hoge prestaties voor energieopwekking konden worden geïdentificeerd, met beperkingen om scheurvorming en verlies van auxetisch gedrag onder compressie te voorkomen. De optimale configuratie die uit dit kader werd afgeleid, werd vervaardigd met behulp van giettechnieken die ondersteund werden door 3D-printen. De configuratie werd experimenteel gevalideerd, waarmee de verbeterde energieopwekkingscapaciteit werd bevestigd. Verder werd het door machine learning gestuurde ontwerp uitgebreid door de geoptimaliseerde enkelvoudige ACCC-cel samen te stellen in een 2×2 multi-celconfiguratie, waarmee de schaalbaarheid en praktische toepasbaarheid voor energieopwekking in de praktijk werd aangetoond.

Deze promotieonderzoek stelt een op vervorming gebaseerde ACCC-energieopwekker voor, die gebruikmaakt van de terugwinbare vervorming binnen het auxetische gedragsbereik van ACCC-structuren. Door experimentele evaluatie, numerieke modellering en machinelearning te combineren, wordt de terugwinbare vervormingscapaciteit van ACCC's verbeterd, waardoor de energie-output van de harvester toeneemt. De terugwinbare vervorming van ACCC's wordt geïdentificeerd als het bepalende mechanisme, aangezien de opgewekte energie wordt bepaald door de mechanische energie die tijdens vervorming wordt gegenereerd en de daaropvolgende omzetting. Deze bevindingen bieden daarom ook bredere inzichten voor toekomstige studies naar andere energieopwekkingsstrategieën met auxetische cementgebonden composieten als substraat.

1

GENERAL INTRODUCTION

This chapter provides a general introduction to the research background. It then outlines the research goals and scope. Next, the approaches used to achieve the research objectives are briefly discussed. Finally, the chapter concludes with an outline of the thesis.

1.1 RESEARCH BACKGROUND

1.1.1 Architected cementitious cellular composites (ACCCs)

Auxetic materials, which exhibit negative Poisson's ratios, have emerged as a growing area of research interest. Conventional materials typically expand laterally when compressed, exhibiting a positive Poisson's ratio. In contrast, auxetic materials contract in the transverse direction under compression and expand laterally when stretched. This counterintuitive mechanical response stems from specialized internal architectures and often results in enhanced properties such as greater fracture resistance, improved energy dissipation, and superior impact absorption. In most cases, the auxetic effect in metamaterials is driven by localized buckling mechanisms [1-3].

Xu et al. [4] developed a cellular structure using a fiber-reinforced cementitious composite, incorporating periodic elliptical perforations as the base design. Under uniaxial compression, this structure exhibited a unique auxetic behavior, characterized by a negative Poisson's ratio. The auxetic behavior of ACCCs arises from the rotation of sections around hinge-like joints facilitated by fiber bridging, along with the inward folding of the hollow regions [4, 5]. After being pre-compressed to a specified displacement, the elliptical-shaped ACCCs displayed compliant behavior and a quasi-elastic response under cyclic loading. This remarkable deformation resilience allows for the effective conversion of mechanical energy into other forms, such as electricity.

However, the exploration of architected cementitious materials for energy harvesting has remained relatively underexplored. To the best of the author's knowledge, no studies had been reported in this area at the beginning of this PhD project in 2021. By the completion of this thesis in 2025, only one study [6] had investigated the use of architected cellular structures in cementitious materials for energy harvesting. Considering the widespread availability and low cost of cementitious materials, energy harvesters developed from ACCCs exhibit great potential for powering electronic devices within infrastructure, supporting the advancement of sustainable and smart infrastructure systems.

1.1.2 Considerations for ACCC energy harvester

Energy harvesting is the process of capturing ambient energy and converting it into usable electrical power to support self-powered devices. This approach is particularly suited for compact, portable, low-power, and remote electronics that require minimal or no maintenance. Common energy harvesting technologies include piezoelectric, thermoelectric, photovoltaic, triboelectric, and electromagnetic systems [7-12]. Among these, piezoelectric energy harvesters stand out due to their ability to generate a broad range of voltages and high power densities, independent of environmental conditions.

Recently, the integration of piezoelectric materials for harvesting energy from the mechanical deformation of cementitious materials has attracted considerable interest. This is largely due to the widespread availability and excellent mechanical properties of cement-based materials. Additionally, their relatively low cost makes them a promising energy source. Among these, fiber-reinforced cementitious composites—such as strain-hardening cementitious composites (SHCC)—are particularly notable for their tensile strain-hardening behavior and superior crack

control. These characteristics enable structures to exhibit enhanced deformability and ductility, which in turn increases the capacity of energy harvesting. Nevertheless, the deformability and recoverable deformation capacity of SHCC remain limited.

Recently, ACCCs fabricated from fiber-reinforced cementitious materials have demonstrated remarkable deformability and structural integrity due to their auxetic behavior. These properties make them highly promising for efficient energy harvesting using surface-mounted piezoelectric materials. Furthermore, ACCCs show recoverable deformation under cyclic loading and can consistently maintain this quasi-elastic behavior throughout 25000 loading cycles [4], further emphasizing their potential for energy harvesting applications. Therefore, this study will focus on a novel piezoelectric energy harvester (PEH) that incorporates ACCCs and surface-mounted piezoelectric materials, based on strain-induced piezoelectric mechanisms. The energy harvester will be systematically designed, fabricated, and tested to evaluate its electrical energy output. Figure 1-1 illustrates possible applications of ACCC energy harvesters in powering smart infrastructure systems. These harvesters could be integrated into speed bumps to collect energy generated by vehicle traffic. Additionally, they may be installed in coastal regions to harness kinetic energy from ocean wave activity.

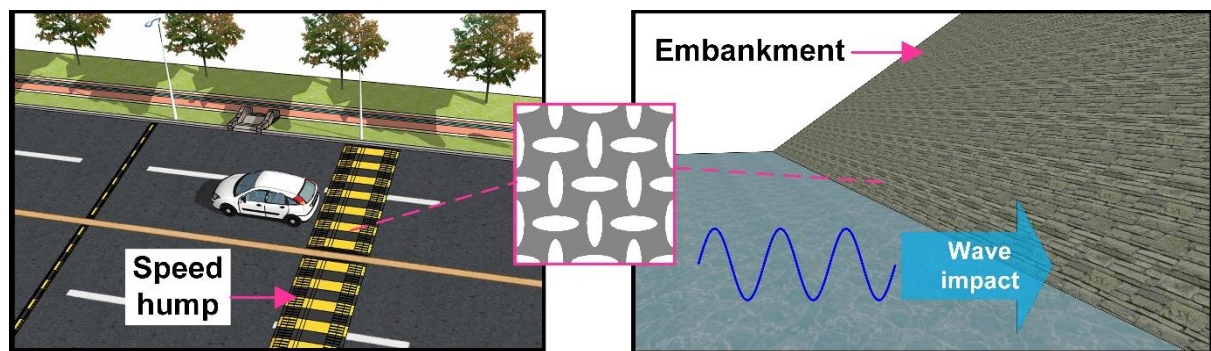


Figure 1-1 Potential applications of ACCC energy harvester.

1.2. RESEARCH OBJECTIVES AND SCOPE

1.2.1. RESEARCH OBJECTIVES

The primary objective of this research is to harness the recoverable deformation of ACCCs within the auxetic behavior range to develop an energy harvester integrated with piezoelectric materials. To accomplish this goal, the following research questions are explored:

- How can piezoelectric materials be integrated into ACCCs to effectively harness the recoverable strain for energy harvesting?
- How can the mechanical–electrical interaction of the ACCC energy harvester be simulated using a combination of mechanical model and piezoelectric model?

- How can the shape configurations of the ACCC energy harvester be optimized under specific constraints, such as maintaining auxetic behavior?

1.2.2. RESEARCH SCOPE

In this study, the ACCCs were fabricated through an additive manufacturing (AM)-assisted casting approach. The AM process involved the use of a 3D printer (Ultimaker S5) with Fused Deposition Modeling (FDM) to print ACCC-shaped templates using acrylonitrile butadiene styrene (ABS) plastic. These printed templates were subsequently used to produce silicone rubber molds, which acted as the casting formwork for the cementitious composites. A polymer fiber-reinforced cementitious material was used as the matrix to enable fiber-bridging effects, which contribute to the auxetic behavior of the ACCCs. A piezoelectric film, Polyvinylidene Difluoride (PVDF), was bonded around the ligament region of the central elliptical hole in the specimen using silicone rubber adhesive and left to cure for several hours until fully hardened. Through this configuration, the recoverable deformation strain energy of the ACCCs could be effectively transferred to the bonded PVDF film, thereby generating electrical energy.

1.3 RESEARCH APPROACH

To achieve the research objective, the following three steps are undertaken:

Step 1: Experimental investigation of the energy harvesting potential of ACCCs integrated with piezoelectric material.

- The ACCCs are initially pre-compressed to the strain range where auxetic behavior occurs and then subjected to cyclic loading. The recoverable strain exhibited by the ACCCs during these cycles generates significant mechanical energy, which is harnessed and converted into electrical energy through the integration of piezoelectric materials.
- In the energy harvesting tests, the output voltages of the ACCC-based harvester are evaluated under different loading amplitudes and loading frequencies.

Step 2: Numerical simulation of the mechanical-electrical interaction in the ACCC energy harvester.

- The energy harvesting model of ACCCs was developed, which comprises two phases: preloading and cyclic loading. The mechanical behavior of ACCCs during the preloading stage is simulated using the concrete damage plasticity model, which is then transitioned to a second-elasticity model for the cyclic loading stage. Based on the simulated mechanical responses, analytical formulas for the piezoelectric effect were developed to calculate the output voltage generated by the piezoelectric materials.

Step 3: Optimization of the ACCC energy harvester with machine learning (ML).

- The energy harvesting model is first validated against experimental results. It is then utilized to generate a dataset for machine learning applications. Finally, the optimized ACCC energy harvester is tested to demonstrate performance improvements.

1.4 THESIS OUTLINE

As seen in [Figure 1–2](#), this thesis is organized into five parts. The chapters are structured as follows:

Part I: Provides a general introduction and a review of the relevant literature.

Chapter 1 introduces the research background, outlines the research objectives, and provides an overview of the thesis structure.

Chapter 2 offers a literature review focusing on the unique characteristics and potential applications of ACCC energy harvester.

Part II: Deals with the experimental fabrication and testing of the ACCC energy harvester.

Chapter 3 presents an experimental study on the energy harvesting potential of ACCCs integrated with piezoelectric materials.

Part III: Proposes an energy harvesting model to simulate the mechanical–piezoelectric interaction within the ACCC energy harvester

Chapter 4 presents a benchmark energy harvesting model for fiber-reinforced cementitious composites utilizing surface-mounted piezoelectric materials.

Chapter 5 develops an energy harvesting model for the ACCC energy harvester incorporating surface-mounted piezoelectric materials.

Part IV: Optimization of the ACCC energy harvester with machine learning.

Chapter 6 integrates strain-hardening cementitious composites into the ACCC energy harvester to enhance its elastomer-like behavior.

Chapter 7 proposes a learning-driven framework that integrates the energy harvesting model with Bayesian Optimization (BO) to modulate hinge-like recoverable strain capacity of ACCCs for Optimal Energy Harvesters.

Chapter 8 performs cyclic testing on the optimized ACCC energy harvester with multiple cells.

Part V: Presents the thesis conclusions and indicates outlook for future research.

Chapter 9 summarizes the key findings of this thesis and offers recommendations for future investigations.

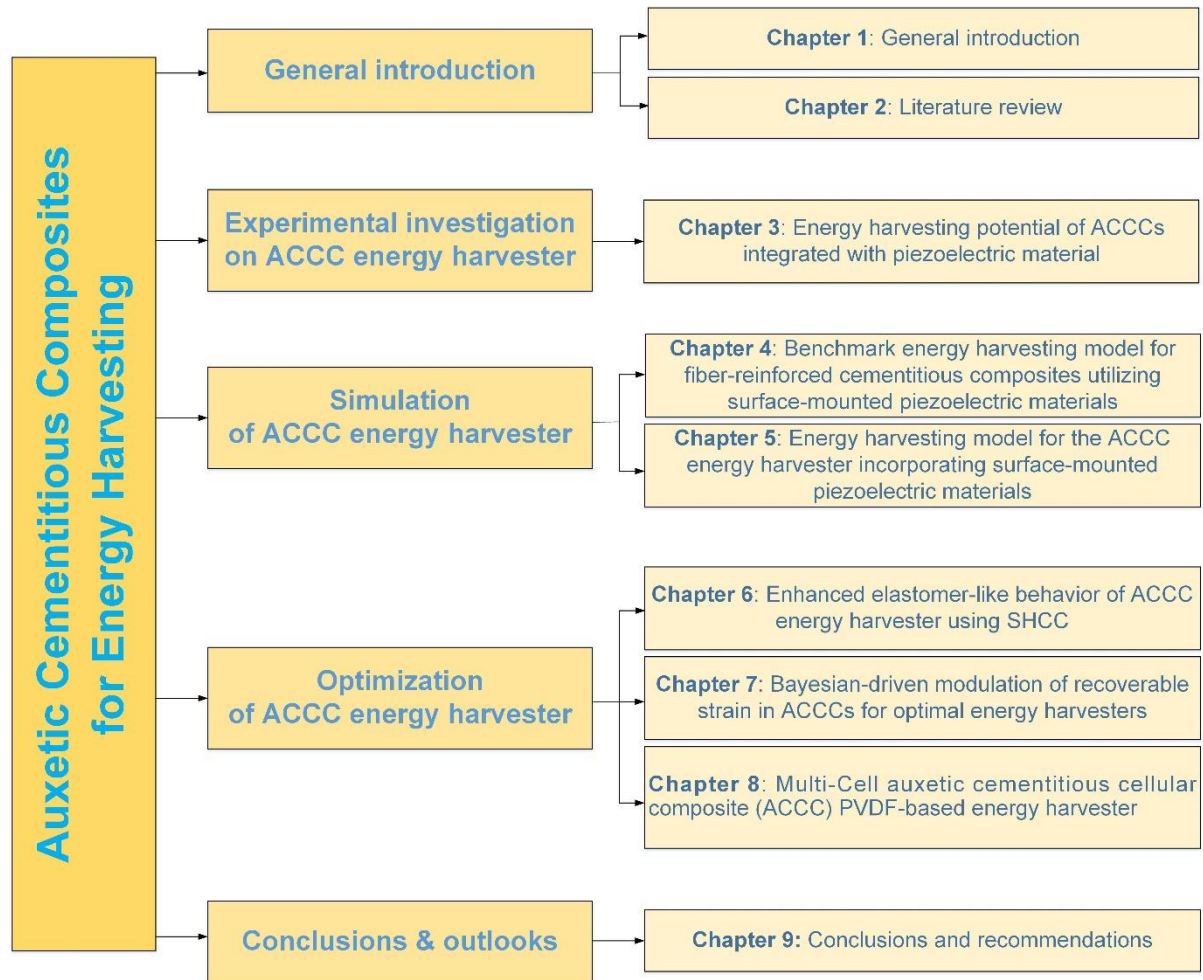


Figure 1-2 Thesis outline

REFERENCES

- [1] X. Ren, R. Das, P. Tran, T.D. Ngo, Y.M. Xie, Auxetic metamaterials and structures: a review, *Smart Materials and Structures*, 27 (2018) 023001. [10.1088/1361-665X/aaa61c](https://doi.org/10.1088/1361-665X/aaa61c).
- [2] K.E. Evans, Auxetic polymers: a new range of materials, *Endeavour*, 15 (1991) 170-174. [https://doi.org/10.1016/0160-9327\(91\)90123-S](https://doi.org/10.1016/0160-9327(91)90123-S).
- [3] W. Jiang, X. Ren, S.L. Wang, X.G. Zhang, X.Y. Zhang, C. Luo, Y.M. Xie, F. Scarpa, A. Alderson, K.E. Evans, Manufacturing, characteristics and applications of auxetic foams: A state-of-the-art review, *Composites Part B: Engineering*, 235 (2022) 109733. <https://doi.org/10.1016/j.compositesb.2022.109733>.
- [4] Y. Xu, H. Zhang, E. Schlangen, M. Luković, B. Šavija, Cementitious cellular composites with auxetic behavior, *Cement and Concrete Composites*, 111 (2020) 103624. <https://doi.org/10.1016/j.cemconcomp.2020.103624>.
- [5] Y. Xu, E. Schlangen, M. Luković, B. Šavija, Tunable mechanical behavior of auxetic cementitious cellular composites (CCCs): Experiments and simulations, *Construction and Building Materials*, 266 (2021) 121388. <https://doi.org/10.1016/j.conbuildmat.2020.121388>.
- [6] K. Barri, Q. Zhang, J. Kline, W. Lu, J. Luo, Z. Sun, B.E. Taylor, S.G. Sachs, L. Khazanovich, Z.L. Wang, A.H. Alavi, Multifunctional Nanogenerator-Integrated Metamaterial Concrete Systems for

Smart Civil Infrastructure, *Advanced Materials*, 35 (2023) 2211027.

<https://doi.org/10.1002/adma.202211027>.

[7] T. Fan, G. Zou, L. Yang, Nano piezoelectric/piezomagnetic energy harvester with surface effect based on thickness shear mode, *Composites Part B: Engineering*, 74 (2015) 166-170.

<https://doi.org/10.1016/j.compositesb.2015.01.012>.

[8] U. Yaqoob, A.S.M.I. Uddin, G.-S. Chung, Synthesis of poly(vinylidene fluoride-trifluoroethylene)-0.65Pb(Mg_{1/3}Nb_{2/3})O₃-0.35PbTiO₃-reduced graphene oxide-composite sheet and its application to flexible energy harvesting, *Composites Part B: Engineering*, 136 (2018) 92-100. <https://doi.org/10.1016/j.compositesb.2017.09.011>.

[9] E. Ghafari, F. Severgnini, S. Ghahari, Y. Feng, E.J. Lee, C. Zhang, X. Jiang, N. Lu, Thermoelectric Nanocomposite for Energy Harvesting, *Multifunctional Nanocomposites for Energy and Environmental Applications*, (2018) 173-202.

<https://doi.org/10.1002/9783527342501.ch8>.

[10] N. Lu, I. Ferguson, III-nitrides for energy production: photovoltaic and thermoelectric applications, *Semiconductor Science and Technology*, 28 (2013) 074023. 10.1088/0268-1242/28/7/074023.

[11] G. Zhu, Z.-H. Lin, Q. Jing, P. Bai, C. Pan, Y. Yang, Y. Zhou, Z.L. Wang, Toward Large-Scale Energy Harvesting by a Nanoparticle-Enhanced Triboelectric Nanogenerator, *Nano Letters*, 13 (2013) 847-853. 10.1021/nl4001053.

[12] S.P. Beeby, R.N. Torah, M.J. Tudor, P. Glynn-Jones, T. O'Donnell, C.R. Saha, S. Roy, A micro electromagnetic generator for vibration energy harvesting, *Journal of Micromechanics and Microengineering*, 17 (2007) 1257-1265. 10.1088/0960-1317/17/7/007.

2

LITERATURE REVIEW

The recoverable deformation of ACCCs during the auxetic behavior range provides abundant mechanical energy, which can be transferred into electrical energy using surface-mounted piezoelectric patches. Accordingly, this chapter presents a comprehensive literature review on piezoelectric energy harvesting, energy harvesting utilizing cementitious materials, and auxetic cementitious materials. It begins with a brief introduction to the piezoelectric effect, followed by an overview of recent advancements in energy harvesting applications using two widely adopted piezoelectric materials: lead zirconate titanate (PZT) and polyvinylidene fluoride (PVDF). Subsequently, the chapter reviews studies on energy harvesting from cementitious materials, including piezoelectric and triboelectric mechanisms. Finally, it presents an overview of the mechanical properties and multifunctional investigations of auxetic cementitious composites, with particular emphasis on their energy harvesting potential.

2.1 Introduction

Energy harvesting is a process by which the ambient energy is captured and converted into usable electrical energy for self-powered devices, such as small-sized, portable, low-power, and remote electronics that do not require replacement or maintenance. The most common energy harvesting materials and devices include piezoelectrics [1, 2], thermoelectrics [3], photovoltaics [4], triboelectrics [5], electromagnetics [6], etc. Among them, piezoelectric energy harvesters are especially effective given that they produce a wide range of voltage and power density regardless of weather conditions. Furthermore, they are easy for installation and processing with a low price. Recently, use of energy-harvesting systems in civil structures has aroused great interest, as it could potentially power infrastructures (e.g., buildings, railways, highways, bridges) with energy self-sufficiency.

Civil structures are commonly exposed to a variety of reciprocating dynamic loads, including those generated by railways, vehicles, pedestrians, waves, rain, and wind. As most of these structures are constructed from cementitious materials, their mechanical deformation under such loading conditions presents a substantial source of mechanical energy. This energy can be effectively harvested and converted into significant electrical output through suitable piezoelectric mechanisms. Consequently, this self-powered approach, which leverages widely available ambient energy, holds great potential for advancing the development of sustainable and intelligent infrastructure systems. However, the inherent brittleness and limited deformability of cementitious materials present significant challenges, limiting their widespread adoption in practical engineering applications.

ACCCs made from fiber-reinforced cementitious materials typically demonstrate high deformability and robust structural integrity, attributed to their auxetic behavior. These features make them particularly suitable for efficient energy harvesting when paired with surface-mounted piezoelectric materials. Additionally, ACCCs exhibit recoverable deformation under cyclic loading and reliably sustain this quasi-elastic performance through 25,000 loading cycles [7], highlighting their strong potential for energy harvesting applications. However, most existing energy harvesting research has focused on auxetic materials derived from polymers and metals, and the exploration of auxetic cementitious materials for this purpose remains largely unexplored.

2.2 ENERGY HARVESTING USING PIEZOELECTRIC MATERIALS

Piezoelectric transformation occurs when mechanical action (stress and strain) is applied to a polarized piezoelectric material; then, opposite bound charges occur on the surfaces of both ends of the material that are connected to electrodes, as shown in [Figure 2-1](#) [8]. When the two electrodes are connected to an electrical power management circuit, the output voltage can be stored as electrical energy for electric power supply. In the past few decades, PZT has been the most widely used piezoelectric ceramic material in many designs of energy harvesters for civil infrastructure and buildings. Many researchers have used PZT piezoceramic disks embedded into pavements to collect the electrical energy from vibration induced by moving vehicles on public roadways [9-12], thereby creating so-called piezoelectric energy harvester (PEH) ([Figure 2-2](#)). These PZT-based piezoelectric energy harvesters have also been further optimized

for a power-intensive design, so as to better collect road energy by efficiently utilizing the vehicle load [13]. However, the intrinsic brittleness of the piezoceramic material (PZT) limits its application on curved surfaces and high strain conditions as in the case of civil infrastructure and buildings.

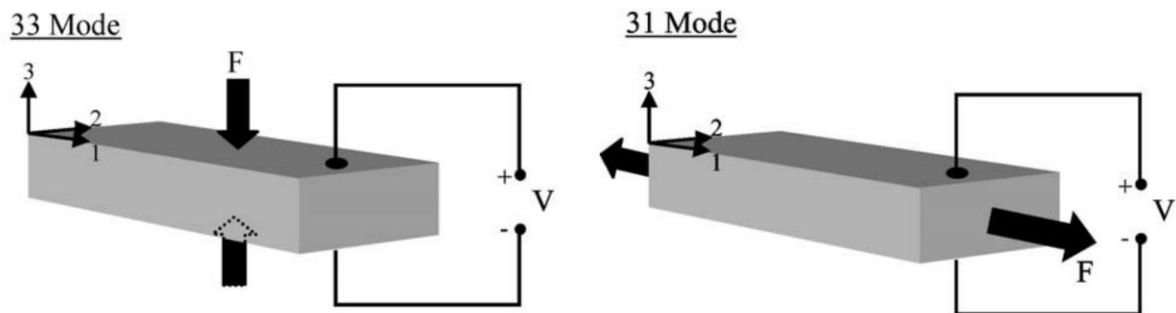


Figure 2-1 Schematic representation of 33 mode and 31 mode for piezoelectric materials (adapted from [8])

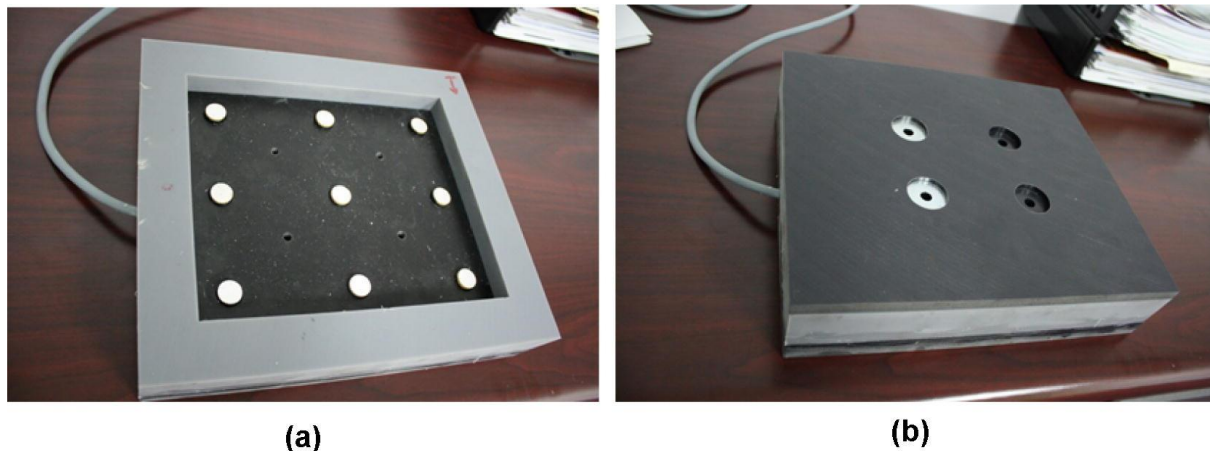


Figure 2-2 PEH without (a) and with cover (b) for harvest pavement deformation energy. (adapted from [9])

PVDF is the most popular commercial flexible piezoelectric polymer because it can be easily fabricated as a thin film with large compliance, high ductility, and excellent piezoelectric performance [14]. Considerable research has been dedicated to extracting vibration energy from PVDF transducers using piezoelectric cantilever beam configurations, such as unimorph (a substrate beam with a bonded piezoelectric layer) and bimorph (a substrate beam with two symmetric piezoelectric layers bonded to both sides) devices [15, 16]. A major barrier correlated with vibration-based piezoelectric energy harvesters in civil engineering is that these devices tend to exhibit weak power output since excited frequencies from environmental vibrations are usually away from the resonant frequency of those harvesters. Nevertheless, due to their flexural behavior, PVDF strain-based energy harvesters have the potential to generate high voltage. Moreover, thin PVDF films can be flexibly installed in many locations of infrastructures to collect abundant strain energy under a wide range of dynamic loads (e.g., passing vehicles [14], human movements [17-20], rain and wind [21], sound pressure [22]), which can be converted into electrical energy. Multiple PVDF films can also be arranged to enhance energy harvesting. Jung et al. [14] developed a PVDF energy harvester for roadways,

rivaling piezoelectric ceramic-based systems. The device, comprising six pre-curved bimorph units aligned vertically, generated 200 mW across a 40 k Ω load resistor in modeled roadway testing in the laboratory.

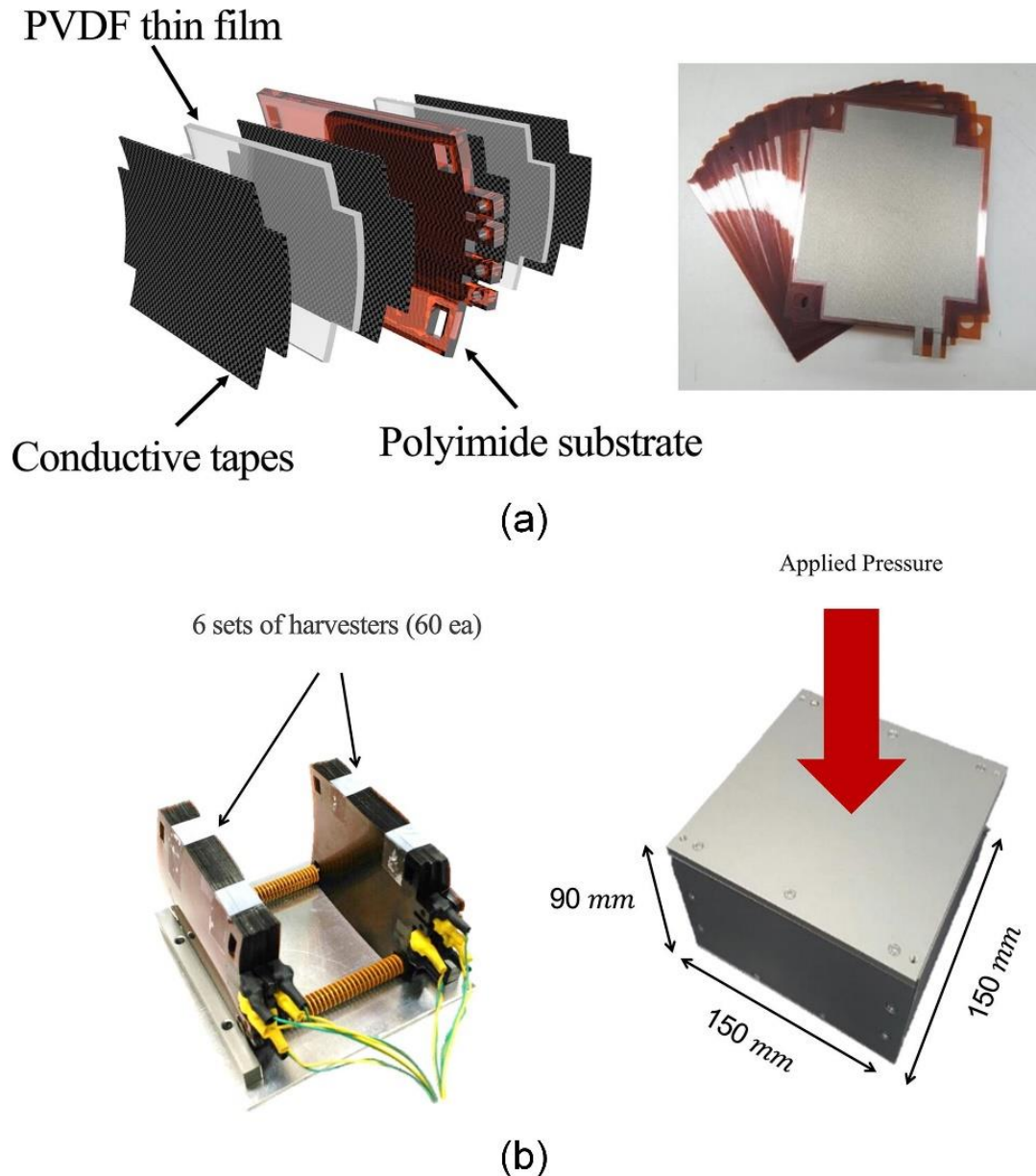


Figure 2-3 Single energy harvester device utilizing a PVDF thin film. (a) Schematic and photograph of the bimorph structured energy harvester. (b) the internal and external structure of the assembled energy harvester module. (adapted from [14])

2.3. ENERGY HARVESTING USING CEMENTITIOUS MATERIALS

Recently, the use of piezoelectric materials for energy harvesting from the mechanical deformation of cementitious materials has gained significant attention due to the widespread availability, exceptional performance, and comparatively low cost of cementitious materials, making them a highly attractive source of energy. As shown in Figure 2-4, Cahill et al. [23]

utilized PZT and PVDF to collect mechanical energy from trains passing over a reinforced concrete (RC) bridge at different speeds. The train-induced energy is sufficient to power small wireless sensors used for structural health monitoring (SHM). For cement-based materials, fiber-reinforced cementitious composites—such as strain-hardening cementitious composites—are well recognized for their tensile strain-hardening behavior and superior crack control performance [24-31]. By using fiber-reinforced cementitious materials, a structure can have large deformability and high ductility, which improves the energy harvesting efficiency of using flexible PVDF. As shown in Figure 2-5, Su et al. [32] studied the energy harvesting potential of flexible SHCC incorporating surface-mounted PVDF subjected to four-point bending tests. The maximum cumulative output voltage was reported to reach 17218 mV under a loading rate of 2.0 mm/s. This was attributed to the high strain capacity of SHCC, which allows significant straining of the surface mounted PVDF film. Therefore, cementitious composites with high deformation capacity could potentially allow highly efficient energy harvesting with surface mounted PVDF. The addition of short fibers has transformed the properties of cementitious materials, which also facilitates the creation of cementitious materials with complex internal structures, known as architected cement-based materials (ACMs) [33-39]. These ACMs demonstrate significant potential due to their superior deformation capacity, which notably enhances energy harvesting capabilities.

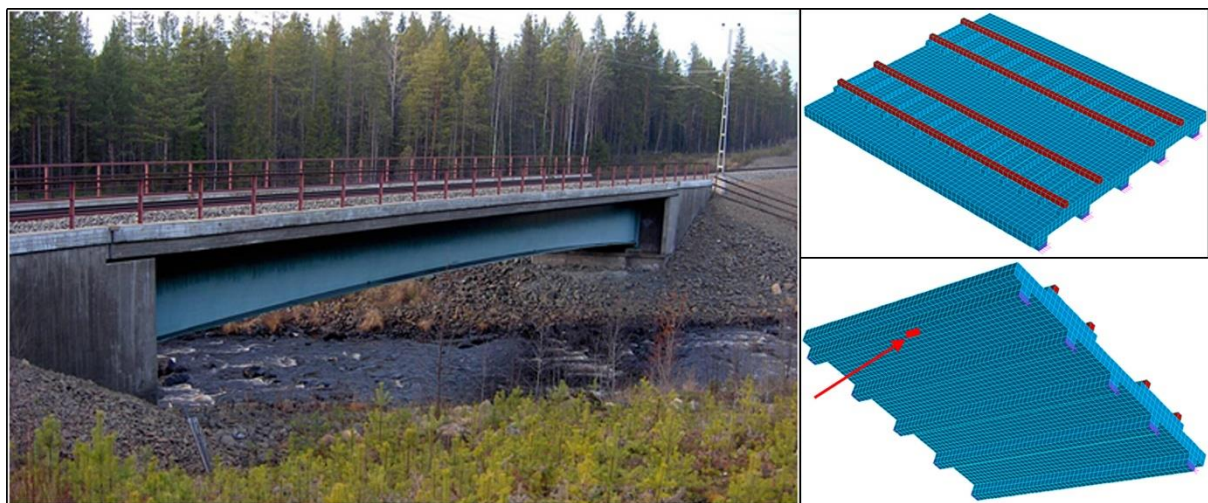


Figure 2-4 Energy harvesting from train-Induced response in bridges: in situ experiments and modelling. (adapted from [23]).

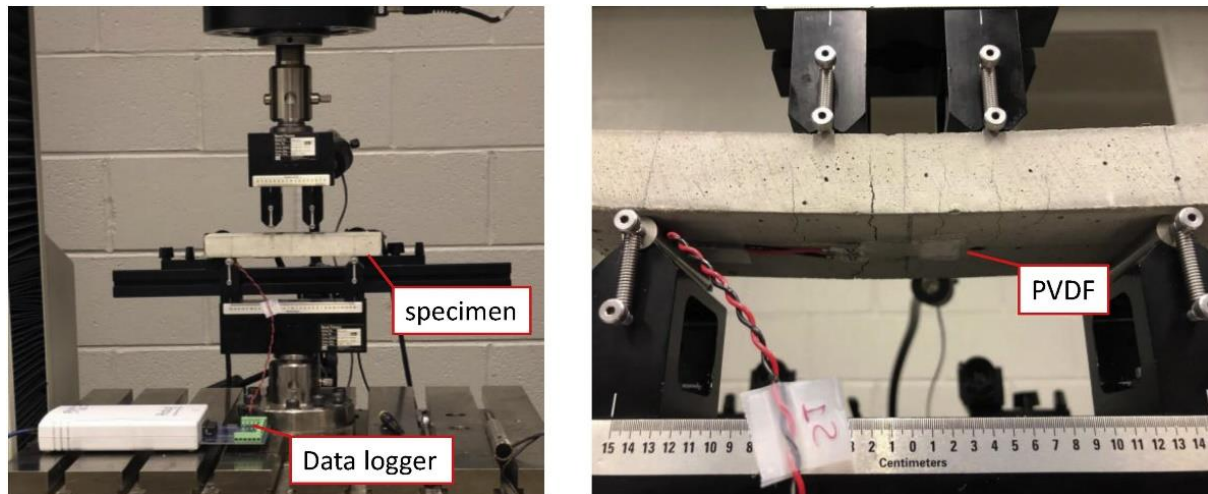


Figure 2-5 Energy harvesting performance of ECC under bending tests (adapted from [32])

Recently, carbon-based conductive fillers have been integrated into cementitious composites to enable energy harvesting through triboelectric mechanisms. Kuntharin et al. [40] demonstrated the harvesting of mechanical energy from human footsteps using a triboelectric nanogenerator (TENG) constructed from cementitious materials enhanced with highly conductive Super P carbon black nanoparticles. Ra et al. [41] utilized cementitious materials with carbon fiber fillers to fabricate triboelectric nanogenerators for contact electrification driven energy harvesting and storage. As shown in Figure 2-6, Dong et al. [42, 43] incorporated carbon-based conductive fillers (such as graphene, recycled carbon fiber (rCF)) into cementitious composites as cement-based triboelectric nanogenerators (CBTENGs) for energy harvesting in building and civil infrastructure systems. However, the inherent brittleness and limited deformability of cementitious materials remain significant limitations, restricting their broader implementation in practical energy harvesting applications. Additionally, the incorporation of conductive fillers may compromise the mechanical performance of cementitious materials, potentially preventing ACCCs from exhibiting the desired negative Poisson's ratio behavior.

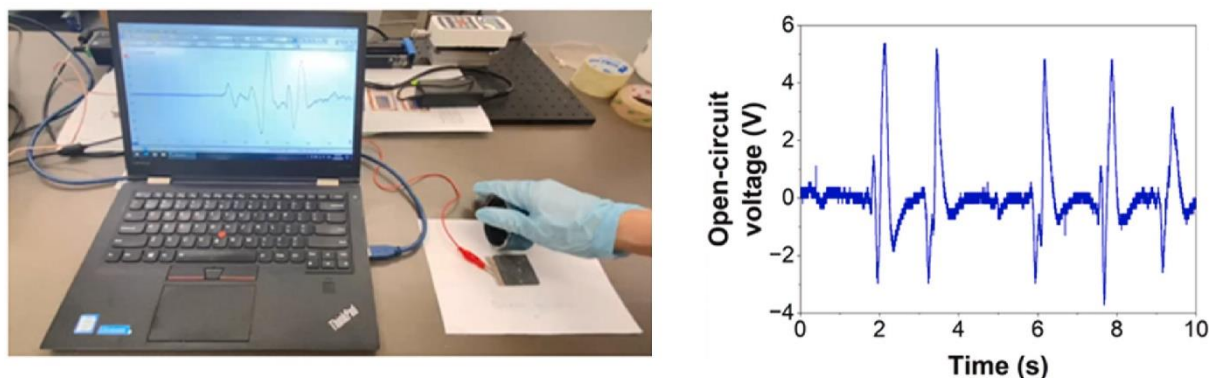


Figure 2-6 Laboratory-scale test of the interaction between a CBTENG and a PTFE-covered wheel (adapted from [43])

2.4 AUXETIC CEMENTITIOUS COMPOSITES

Auxetic materials, which exhibit negative Poisson's ratios, have emerged as a growing area of research interest. Conventional materials typically expand laterally when compressed, exhibiting a positive Poisson's ratio. In contrast, auxetic materials contract in the transverse direction under compression and expand laterally when stretched. This counterintuitive mechanical response stems from specialized internal architectures and often results in enhanced properties such as greater fracture resistance, improved energy dissipation, and superior impact absorption. In most cases, the auxetic effect in metamaterials is driven by localized buckling mechanisms [44-46]. Xu et al. [7] developed a cellular structure using a fiber-reinforced cementitious composite, incorporating periodic elliptical perforations as the base design, as shown in Figure 2-7. Under uniaxial compression, this structure exhibited a unique auxetic behavior, characterized by a negative Poisson's ratio. The auxetic behavior of ACCCs arises from the rotation of sections around hinge-like joints facilitated by fiber bridging, along with the inward folding of the hollow regions [7, 47]. After being pre-compressed to a specified displacement, the elliptical-shaped ACCCs displayed compliant behavior and a quasi-elastic response under cyclic loading. This remarkable deformation resilience allows for the effective conversion of mechanical energy into other forms, such as electricity.

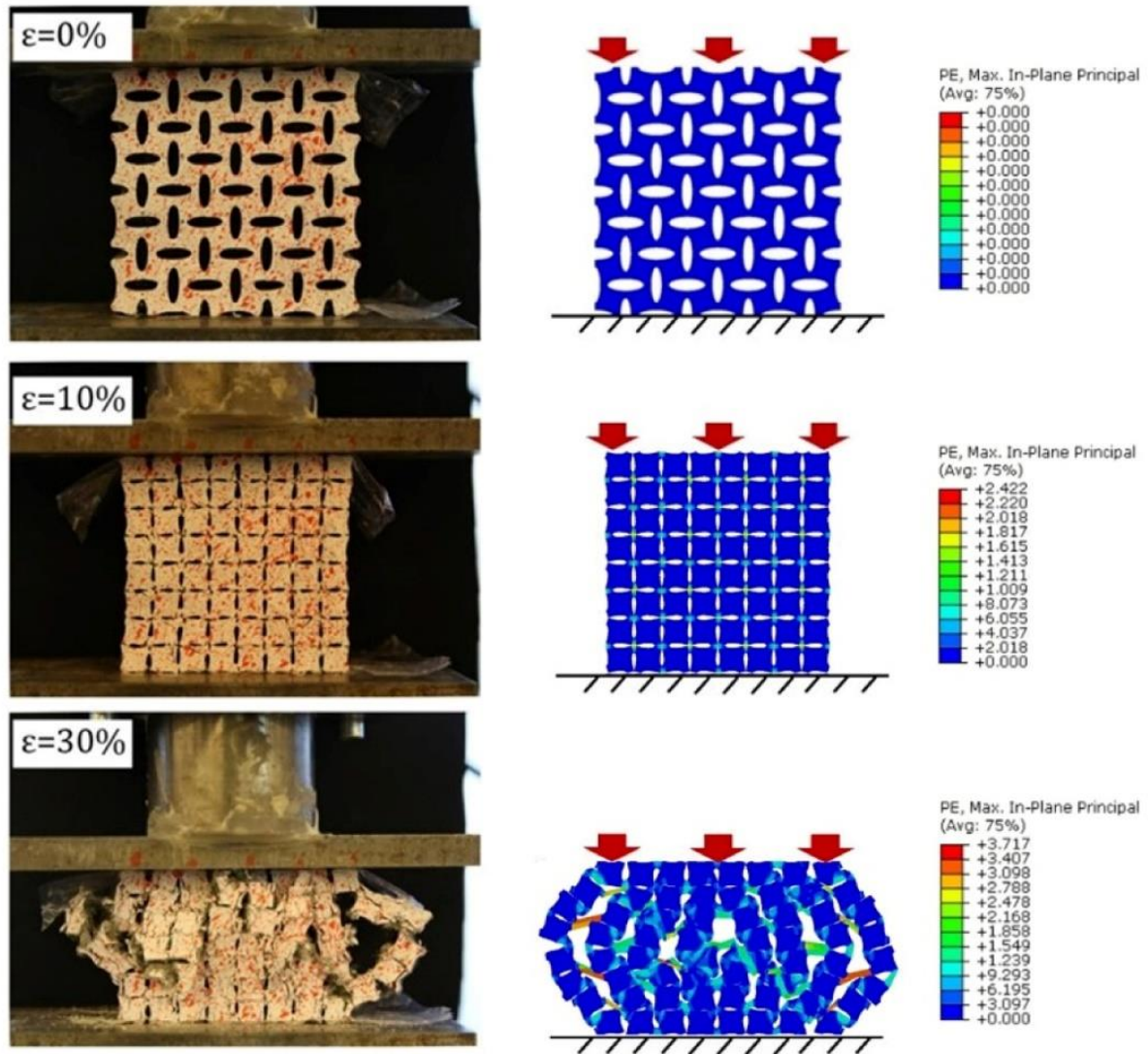


Figure 2-7 Deformation behavior of ACCCs (adapted from [47])

Xu et al. [48] developed a 3D auxetic cementitious-polymeric composite structure (3D-ACPC) comprising a 3D printed polymeric shell and cementitious mortar. This composite exhibits compressive strain-hardening behavior, ensuring a high capacity for energy absorption. Chen et al. [49] fabricated 2D re-entrant, cross-chiral, and buckling-induced auxetic structures using engineered cementitious composites (ECC) and investigated their mechanical response through uniaxial compressive and flexural testing, as shown in Figure 2-8. Xu et al. [50, 51] created auxetic cementitious composites by embedding 3D printed polymeric auxetic reinforcement structures within cementitious mortar. These composites demonstrated notable compressive ductility, high recoverable deformability, and superior energy dissipation capability through the reciprocal integration of auxetic structures and cementitious mortar. Nguyen-Van et al. [52] utilized the Primitive minimal surface, one type of the triply periodic minimal surface (TPMS) structure, to reinforce cement-based beams. This configuration demonstrated significant resilience in bearing loads during impact testing. Chen et al. [53] conducted an experimental investigation into the static and dynamic compressive behavior of various structures, including

3D octet, re-entrant honeycomb, and triangular lattice, reinforced with ultra-high performance concrete (UHPC), as well as steel fiber-reinforced UHPC.

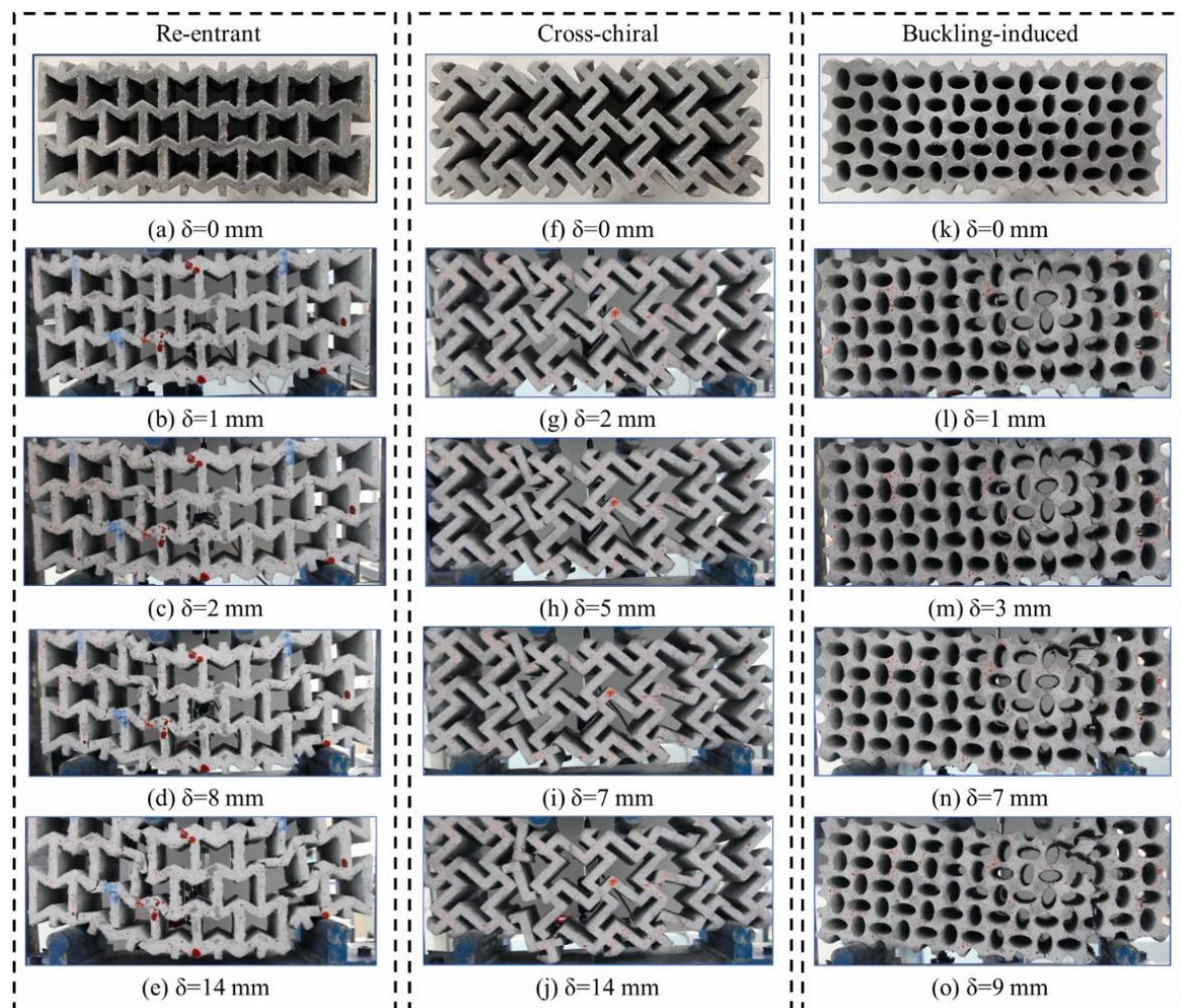


Figure 2-8 Fracture patterns of flexural ECC specimens at different deflections (δ represents mid-span deflection). (adapted from [49])

Typically, ACCCs exhibit two distinct stages with two peak stress points under uniaxial compression, marked by the strain at which self-contact occurs within the central hole between the top and bottom ends (i.e., the self-contact point). ACCCs begin to display a higher magnitude of negative Poisson's ratio (high auxetic behavior) after the first peak stress. Upon reaching the self-contact point, the magnitude of the negative Poisson's ratio starts to decrease until it reaches zero and then becomes a positive Poisson's ratio. The range from the first peak stress point to the self-contact point represents a compressive strain range characterized by high auxetic behavior. Within this range, ACCCs demonstrate significant deformation capacity and a certain level of recoverable elastic deformation—a pseudo-elastic characteristic not typically found in traditional cementitious materials. The remarkable recoverable deformation behavior of ACCCs, akin to elastomers, broadens the potential applications of elastomer-like cementitious materials. They can be employed to create advanced multifunctional cementitious composites, incorporating features such as mechanical tunability, energy harvesting, and

sensing capabilities. Barri et al. [54] integrated concrete mixture with graphite powder and auxetic polymer structures, resulting in a concrete material system that exhibits unprecedented mechanical and electrical tunability due to snap-through buckling behavior. As shown in Figure 2-8, Valverde-Burneo [55] has developed a multifunctional cementitious material with an addition of recycled carbon fibers. This material exhibits both conductive and auxetic properties, making it a promising candidate for self-sensing concrete applications.

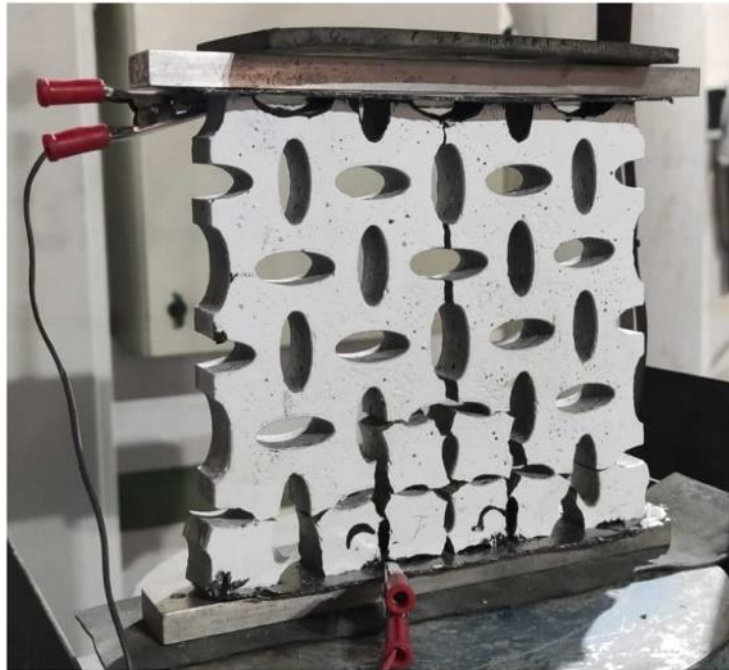


Figure 2-9 Electronic conduction test of ACCC incorporating carbon fiber (adapted from [55])

Recently, machine learning has been increasingly applied to predict the mechanical properties of ACCCs, offering a promising approach for further optimization and tailoring performance for specific engineering scenarios. Ohno et al. [56] proposed a novel framework for the simulation and reinforcement learning-driven design of truss-type ACMs, enabling the efficient identification of high-performance configurations. Lyngdoh et al. [57] integrated finite element model (FEM) with machine learning (ML) to predict Poisson's ratios in cementitious cellular composites. Their focus was on evaluating a negative Poisson's ratio by strategically positioning elliptical voids, without considering plasticity or post-crack behavior.

ACCCs, fabricated from fiber-reinforced cementitious materials, exhibit high deformability and superior structural integrity, primarily attributed to their auxetic behavior. These characteristics render ACCCs particularly promising for efficient energy harvesting when integrated with surface-mounted piezoelectric elements. Moreover, ACCCs display recoverable deformation under cyclic loading while maintaining stable quasi-elastic behavior. Xu et al. [7] reported that ACCCs achieved a reversible deformation of 2.5%, substantially exceeding that of conventional cementitious materials and sustained over 25,000 loading cycles, further highlighting their potential for energy harvesting applications. Despite these advantages, current research on vibration-based energy harvesting has predominantly focused on auxetic materials derived from metals and polymers [15, 58-65]. For instance, Bolat et al. [58]

conducted both experimental and numerical investigations to evaluate the electrical power output of auxetic aluminum beams with piezoelectric elements (PZT) attached to the auxetic region, as illustrated in Figure 2-10. Similarly, Chowdhury et al. [15] proposed optimal design configurations for a bimorph piezoelectric energy harvester utilizing an auxetic brass substrate beam with symmetrically bonded piezoelectric layers, demonstrating enhanced power output compared to conventional systems. As shown in Figure 2-11, Zhou et al. [60] employed 3D printing to fabricate an auxetic structure onto a polymer film-based piezoelectric nanogenerator (PENG), enabling the conversion of bending deformation into in-plane stretching. This transformation activates the 3-1-direction piezoelectric effect. By leveraging the anticlastic behavior of the auxetic design, the previously underutilized bending deformation of the film is effectively harnessed for energy harvesting. As a result, the bending-induced output voltage of the PENG was enhanced by a factor of 8.3. In contrast, the application of auxetic cementitious materials for energy harvesting remains largely unexplored. Given the abundance and low cost of cementitious materials, ACCCs offer significant potential for sustainable and cost-effective energy harvesting solutions.

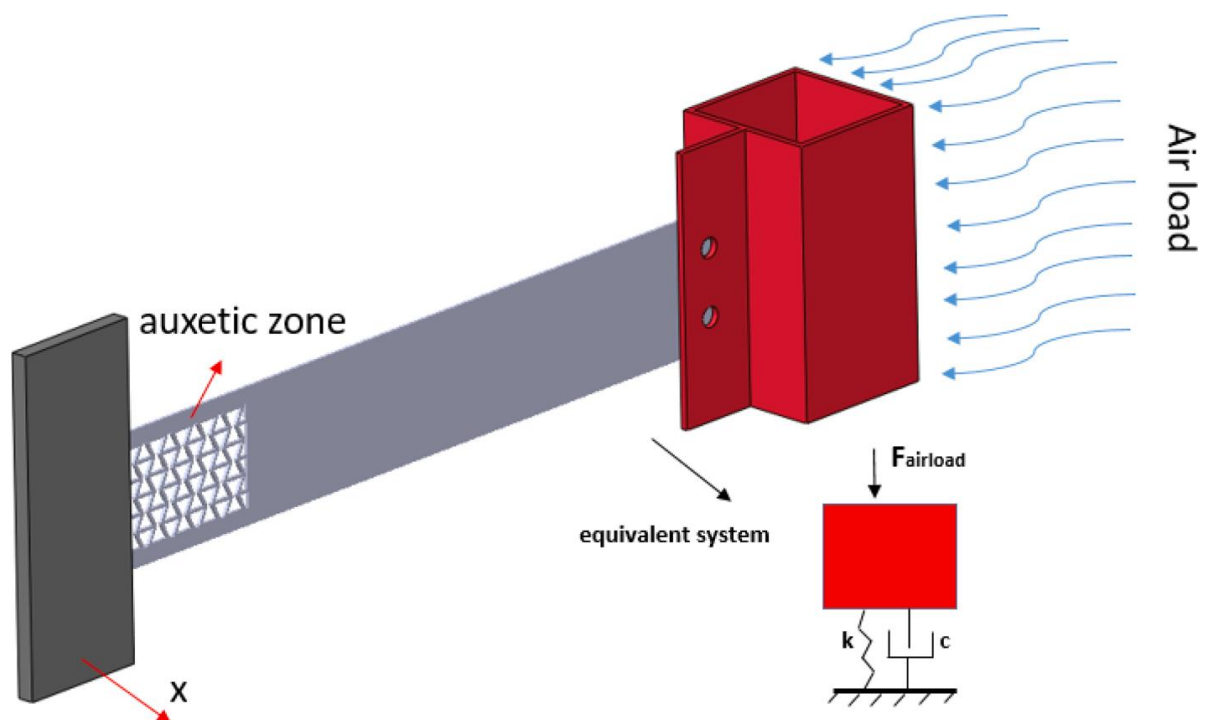


Figure 2-10 Vibrational response of auxetic aluminum beams with PZT integrated into the auxetic region. (adapted from [58])

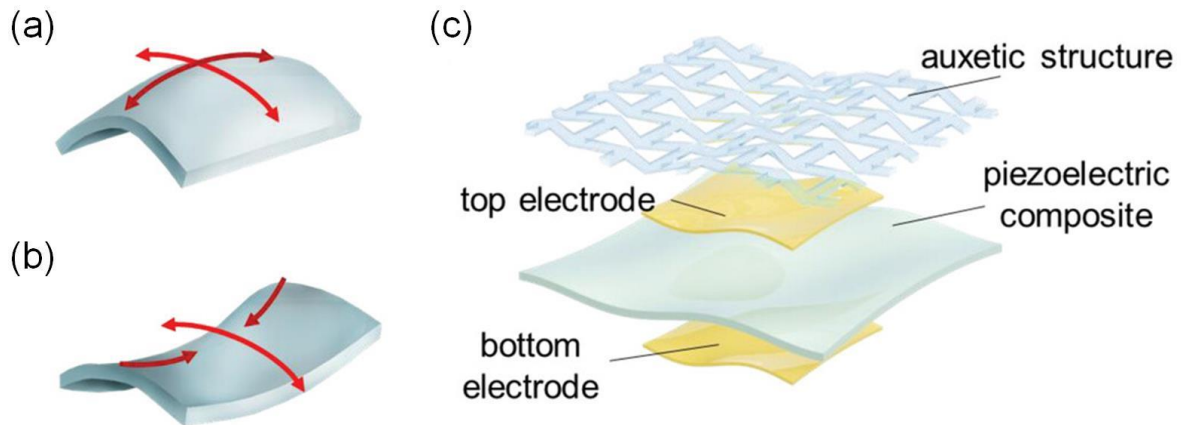


Figure 2-11 The structure of the auxetic-piezoelectric nanogenerator. (adapted from [60])

2.5 FINAL REMARKS

The utilization of piezoelectric materials for energy harvesting from the mechanical deformation of cementitious materials has recently obtained considerable attention, owing to the widespread availability, excellent performance, and relatively low cost of these materials. Such attributes render cementitious materials a promising candidate for sustainable energy harvesting applications. However, the intrinsic brittleness and limited deformability of conventional cementitious materials pose significant challenges, thereby constraining their broader practical implementation in energy harvesting systems. The introduction of fiber reinforcement into cementitious composites has been demonstrated to improve ductility, thereby enhancing the deformation capacity and mechanical energy that can be harvested. Moreover, the development of architected cement-based materials enables the fabrication of complex cementitious structures, further augmenting deformability and mechanical energy absorption. These improvements, when combined with the piezoelectric effect, contribute to enhanced energy harvesting capabilities. Among ACMs, ACCCs exhibit greater deformation under compressive loads and recoverable deformation under cyclic loading, highlighting their strong potential for energy harvesting applications. However, most existing research on energy harvesting has focused on auxetic materials made from metals and polymers, leaving the use of auxetic cementitious materials largely unexplored. Current research on ACCCs is primarily focused on their mechanical behavior, with limited attention given to multifunctional applications such as energy harvesting. Considering the widespread availability and low cost of cementitious materials, ACCCs present a promising pathway for developing sustainable and cost-effective energy harvesting systems. The subsequent chapters will address these research gaps and challenges.

REFERENCES

- [1] T. Fan, G. Zou, L. Yang, Nano piezoelectric/piezomagnetic energy harvester with surface effect based on thickness shear mode, *Composites Part B: Engineering*, 74 (2015) 166-170. <https://doi.org/10.1016/j.compositesb.2015.01.012>.

- [2] U. Yaqoob, A.S.M.I. Uddin, G.-S. Chung, Synthesis of poly(vinylidene fluoride-trifluoroethylene)-0.65Pb(Mg₁/3Nb₂/3)O₃-0.35PbTiO₃-reduced graphene oxide-composite sheet and its application to flexible energy harvesting, *Composites Part B: Engineering*, 136 (2018) 92-100. <https://doi.org/10.1016/j.compositesb.2017.09.011>.
- [3] E. Ghafari, F. Severgnini, S. Ghahari, Y. Feng, E.J. Lee, C. Zhang, X. Jiang, N. Lu, Thermoelectric Nanocomposite for Energy Harvesting, *Multifunctional Nanocomposites for Energy and Environmental Applications*, (2018) 173-202. <https://doi.org/10.1002/9783527342501.ch8>.
- [4] N. Lu, I. Ferguson, III-nitrides for energy production: photovoltaic and thermoelectric applications, *Semiconductor Science and Technology*, 28 (2013) 074023. 10.1088/0268-1242/28/7/074023.
- [5] G. Zhu, Z.-H. Lin, Q. Jing, P. Bai, C. Pan, Y. Yang, Y. Zhou, Z.L. Wang, Toward Large-Scale Energy Harvesting by a Nanoparticle-Enhanced Triboelectric Nanogenerator, *Nano Letters*, 13 (2013) 847-853. 10.1021/nl4001053.
- [6] S.P. Beeby, R.N. Torah, M.J. Tudor, P. Glynne-Jones, T. O'Donnell, C.R. Saha, S. Roy, A micro electromagnetic generator for vibration energy harvesting, *Journal of Micromechanics and Microengineering*, 17 (2007) 1257-1265. 10.1088/0960-1317/17/7/007.
- [7] Y. Xu, H. Zhang, E. Schlangen, M. Luković, B. Šavija, Cementitious cellular composites with auxetic behavior, *Cement and Concrete Composites*, 111 (2020) 103624. <https://doi.org/10.1016/j.cemconcomp.2020.103624>.
- [8] S. Roundy, P.K. Wright, J. Rabaey, A study of low level vibrations as a power source for wireless sensor nodes, *Computer Communications*, 26 (2003) 1131-1144. [https://doi.org/10.1016/S0140-3664\(02\)00248-7](https://doi.org/10.1016/S0140-3664(02)00248-7).
- [9] H. Xiong, L. Wang, Piezoelectric energy harvester for public roadway: On-site installation and evaluation, *Applied Energy*, 174 (2016) 101-107. <https://doi.org/10.1016/j.apenergy.2016.04.031>.
- [10] H. Zhao, J. Yu, J. Ling, Finite element analysis of Cymbal piezoelectric transducers for harvesting energy from asphalt pavement, *Journal of the Ceramic Society of Japan*, 118 (2010) 909-915. 10.2109/jcersj2.118.909.
- [11] C. Wang, S. Wang, Z. Gao, X. Wang, Applicability evaluation of embedded piezoelectric energy harvester applied in pavement structures, *Applied Energy*, 251 (2019) 113383. <https://doi.org/10.1016/j.apenergy.2019.113383>.
- [12] K. Huang, H. Zhang, J. Jiang, Y. Zhang, Y. Zhou, L. Sun, Y. Zhang, The optimal design of a piezoelectric energy harvester for smart pavements, *International Journal of Mechanical Sciences*, 232 (2022) 107609. <https://doi.org/10.1016/j.ijmecsci.2022.107609>.
- [13] Y. Cao, J. Li, A. Sha, Z. Liu, F. Zhang, X. Li, A power-intensive piezoelectric energy harvester with efficient load utilization for road energy collection: Design, testing, and application, *Journal of Cleaner Production*, 369 (2022) 133287. <https://doi.org/10.1016/j.jclepro.2022.133287>.
- [14] I. Jung, Y.-H. Shin, S. Kim, J.-y. Choi, C.-Y. Kang, Flexible piezoelectric polymer-based energy harvesting system for roadway applications, *Applied Energy*, 197 (2017) 222-229. <https://doi.org/10.1016/j.apenergy.2017.04.020>.
- [15] A. Roy Chowdhury, N. Saurabh, R. Kiran, S. Patel, Effect of porous auxetic structures on low-frequency piezoelectric energy harvesting systems: a finite element study, *Applied Physics A*, 128 (2021) 62. 10.1007/s00339-021-05199-w.
- [16] L. Wang, L. Zhao, Z. Jiang, G. Luo, P. Yang, X. Han, X. Li, R. Maeda, High accuracy comsol simulation method of bimorph cantilever for piezoelectric vibration energy harvesting, *AIP Advances*, 9 (2019) 095067. 10.1063/1.5119328.
- [17] M. Kashfi, P. Fakhri, B. Amini, N. Yavari, B. Rashidi, L. Kong, R. Bagherzadeh, A novel approach to determining piezoelectric properties of nanogenerators based on PVDF nanofibers using iterative finite element simulation for walking energy harvesting, *Journal of Industrial Textiles*, 51 (2020) 531S-553S. <https://doi.org/10.1177/1528083720926493>.

- [18] L. Mateu, F. Moll, Optimum Piezoelectric Bending Beam Structures for Energy Harvesting using Shoe Inserts, *Journal of Intelligent Material Systems and Structures*, 16 (2005) 835-845. <https://doi.org/10.1177/1045389X05055280>.
- [19] L. Mateu, F. Moll, Appropriate charge control of the storage capacitor in a piezoelectric energy harvesting device for discontinuous load operation, *Sensors and Actuators A: Physical*, 132 (2006) 302-310. <https://doi.org/10.1016/j.sna.2006.06.061>.
- [20] L. Moro, D. Benasciutti, Harvested power and sensitivity analysis of vibrating shoe-mounted piezoelectric cantilevers, *Smart Materials and Structures*, 19 (2010) 115011. 10.1088/0964-1726/19/11/115011.
- [21] D. Vatansever, R.L. Hadimani, T. Shah, E. Siores, An investigation of energy harvesting from renewable sources with PVDF and PZT, *Smart Materials and Structures*, 20 (2011) 055019. 10.1088/0964-1726/20/5/055019.
- [22] Y. Wang, X. Zhu, T. Zhang, S. Bano, H. Pan, L. Qi, Z. Zhang, Y. Yuan, A renewable low-frequency acoustic energy harvesting noise barrier for high-speed railways using a Helmholtz resonator and a PVDF film, *Applied Energy*, 230 (2018) 52-61. <https://doi.org/10.1016/j.apenergy.2018.08.080>.
- [23] P. Cahill, N. Nuallain Nora Aine, N. Jackson, A. Mathewson, R. Karoumi, V. Pakrashi, Energy Harvesting from Train-Induced Response in Bridges, *Journal of Bridge Engineering*, 19 (2014) 04014034. [https://doi.org/10.1061/\(ASCE\)BE.1943-5592.0000608](https://doi.org/10.1061/(ASCE)BE.1943-5592.0000608).
- [24] B. Zhu, J. Pan, M. Zhang, C.K.Y. Leung, Predicting the strain-hardening behavior of polyethylene fibre reinforced engineered cementitious composites accounting for fibre-matrix interaction, *Cement and Concrete Composites*, 134 (2022) 104770. <https://doi.org/10.1016/j.cemconcomp.2022.104770>.
- [25] V.C. Li, On Engineered Cementitious Composites (ECC) A Review of the Material and Its Applications, *Journal of Advanced Concrete Technology*, 1 (2003) 215-230. 10.3151/jact.1.215.
- [26] J.-X. Zhu, K.-F. Weng, B.-T. Huang, L.-Y. Xu, J.-G. Dai, Ultra-High-Strength Engineered Cementitious Composites (UHS-ECC) panel reinforced with FRP bar/grid: Development and flexural performance, *Engineering Structures*, 302 (2024) 117193. <https://doi.org/10.1016/j.engstruct.2023.117193>.
- [27] J.-C. Lao, R.-Y. Ma, L.-Y. Xu, Y. Li, Y.-N. Shen, J. Yao, Y.-S. Wang, T.-Y. Xie, B.-T. Huang, Fly ash-dominated High-Strength Engineered/Strain-Hardening Geopolymer Composites (HS-EGC/SHGC): Influence of alkalinity and environmental assessment, *Journal of Cleaner Production*, 447 (2024) 141182. <https://doi.org/10.1016/j.jclepro.2024.141182>.
- [28] Q.-H. Li, A.-M. Luo, B.-T. Huang, G.-Z. Wang, S.-L. Xu, Bond behavior between steel bar and strain-hardening fiber-reinforced cementitious composites under fatigue loading, *Engineering Structures*, 314 (2024) 118354. <https://doi.org/10.1016/j.engstruct.2024.118354>.
- [29] V.C. Li, Tailoring ECC for Special Attributes: A Review, *International Journal of Concrete Structures and Materials*, 6 (2012) 135-144. 10.1007/s40069-012-0018-8.
- [30] E.-H. Yang, V.C. Li, Tailoring engineered cementitious composites for impact resistance, *Cement and Concrete Research*, 42 (2012) 1066-1071. <https://doi.org/10.1016/j.cemconres.2012.04.006>.
- [31] W. Zhou, Y. Xu, Z. Meng, J. Xie, Y. Zhou, E. Schlangen, B. Šavija, Filament stitching: An architected printing strategy to mitigate anisotropy in 3D-Printed engineered cementitious composites (ECC), *Cement and Concrete Composites*, 160 (2025) 106044. <https://doi.org/10.1016/j.cemconcomp.2025.106044>.
- [32] Y.-F. Su, R.R. Kotian, N. Lu, Energy harvesting potential of bendable concrete using polymer based piezoelectric generator, *Composites Part B: Engineering*, 153 (2018) 124-129. <https://doi.org/10.1016/j.compositesb.2018.07.018>.
- [33] V. Nguyen-Van, J. Liu, S. Li, G. Zhang, H. Nguyen-Xuan, P. Tran, Modelling of 3D-printed bio-inspired Bouligand cementitious structures reinforced with steel fibres, *Engineering Structures*, 274 (2023) 115123. <https://doi.org/10.1016/j.engstruct.2022.115123>.

- [34] J. Liu, S. Li, K. Fox, P. Tran, 3D concrete printing of bioinspired Bouligand structure: A study on impact resistance, *Additive Manufacturing*, 50 (2022) 102544. <https://doi.org/10.1016/j.addma.2021.102544>.
- [35] G. Du, Y. Sun, Y. Qian, Flexural performance of nature-inspired 3D-printed strain-hardening cementitious composites (3DP-SHCC) with Bouligand structures, *Cement and Concrete Composites*, 149 (2024) 105494. <https://doi.org/10.1016/j.cemconcomp.2024.105494>.
- [36] W. Zhou, W. McGee, H.S. Gökçe, V.C. Li, A bio-inspired solution to alleviate anisotropy of 3D printed engineered cementitious composites (3DP-ECC): Knitting/tilting filaments, *Automation in Construction*, 155 (2023) 105051. <https://doi.org/10.1016/j.autcon.2023.105051>.
- [37] M. Moini, J. Olek, J.P. Youngblood, B. Magee, P.D. Zavattieri, Additive Manufacturing and Performance of Architected Cement-Based Materials, *Advanced Materials*, 30 (2018) 1802123. <https://doi.org/10.1002/adma.201802123>.
- [38] S.M. Sajadi, C.S. Tiwary, A.H. Rahmati, S.L. Eichmann, C.J. Thaemlitz, D. Salpekar, A.B. Puthirath, P.J. Boul, M.M. Rahman, A. Meiyazhagan, P.M. Ajayan, Deformation resilient cement structures using 3D-printed molds, *iScience*, 24 (2021) 102174. <https://doi.org/10.1016/j.isci.2021.102174>.
- [39] Z. Wan, Y. Xu, S. He, Y. Chen, J. Xie, B. Šavija, Direct ink writing of vascularized self-healing cementitious composites, *Cement and Concrete Composites*, 144 (2023) 105295. <https://doi.org/10.1016/j.cemconcomp.2023.105295>.
- [40] S. Kuntharin, V. Harnchana, J. Sintusiri, P. Thongbai, A. Klamchuen, K. Sinthiptharakoon, V. Amornkitbamrung, P. Chindapasirt, Smart triboelectric floor based on calcium silicate-carbon composite for energy harvesting and motion sensing applications, *Sensors and Actuators A: Physical*, 358 (2023) 114423. <https://doi.org/10.1016/j.sna.2023.114423>.
- [41] Y. Ra, I. You, M. Kim, S. Jang, S. Cho, D. Kam, S.-J. Lee, D. Choi, Toward smart net zero energy structures: Development of cement-based structural energy material for contact electrification driven energy harvesting and storage, *Nano Energy*, 89 (2021) 106389. <https://doi.org/10.1016/j.nanoen.2021.106389>.
- [42] W. Dong, S. Gao, S. Peng, L. Shi, S.P. Shah, W. Li, Graphene reinforced cement-based triboelectric nanogenerator for efficient energy harvesting in civil infrastructure, *Nano Energy*, 131 (2024) 110380. <https://doi.org/10.1016/j.nanoen.2024.110380>.
- [43] W. Dong, C. Zhao, S. Peng, C. Wu, T. Kim, K. Wang, W. Li, Recycled carbon fibre/cement-based triboelectric nanogenerators toward energy-efficient and smart civil infrastructure, *Composites Part B: Engineering*, 303 (2025) 112603. <https://doi.org/10.1016/j.compositesb.2025.112603>.
- [44] X. Ren, R. Das, P. Tran, T.D. Ngo, Y.M. Xie, Auxetic metamaterials and structures: a review, *Smart Materials and Structures*, 27 (2018) 023001. 10.1088/1361-665X/aaa61c.
- [45] K.E. Evans, Auxetic polymers: a new range of materials, *Endeavour*, 15 (1991) 170-174. [https://doi.org/10.1016/0160-9327\(91\)90123-S](https://doi.org/10.1016/0160-9327(91)90123-S).
- [46] W. Jiang, X. Ren, S.L. Wang, X.G. Zhang, X.Y. Zhang, C. Luo, Y.M. Xie, F. Scarpa, A. Alderson, K.E. Evans, Manufacturing, characteristics and applications of auxetic foams: A state-of-the-art review, *Composites Part B: Engineering*, 235 (2022) 109733. <https://doi.org/10.1016/j.compositesb.2022.109733>.
- [47] Y. Xu, E. Schlangen, M. Luković, B. Šavija, Tunable mechanical behavior of auxetic cementitious cellular composites (CCCs): Experiments and simulations, *Construction and Building Materials*, 266 (2021) 121388. <https://doi.org/10.1016/j.conbuildmat.2020.121388>.
- [48] Y. Xu, B. Šavija, 3D auxetic cementitious-polymeric composite structure with compressive strain-hardening behavior, *Engineering Structures*, 294 (2023) 116734. <https://doi.org/10.1016/j.engstruct.2023.116734>.
- [49] M. Chen, S. Fang, G. Wang, Y. Xuan, D. Gao, M. Zhang, Compressive and flexural behavior of engineered cementitious composites based auxetic structures: An experimental and numerical

- study, *Journal of Building Engineering*, 86 (2024) 108999. <https://doi.org/10.1016/j.jobe.2024.108999>.
- [50] Y. Xu, Z. Meng, R.J.M. Bol, B. Šavija, Spring-like behavior of cementitious composite enabled by auxetic hyperelastic frame, *International Journal of Mechanical Sciences*, 275 (2024) 109364. <https://doi.org/10.1016/j.ijmecsci.2024.109364>.
- [51] Y. Xu, B. Šavija, Auxetic cementitious composites (ACCs) with excellent compressive ductility: Experiments and modeling, *Materials & Design*, 237 (2024) 112572. <https://doi.org/10.1016/j.matdes.2023.112572>.
- [52] V. Nguyen-Van, J. Liu, C. Peng, G. Zhang, H. Nguyen-Xuan, P. Tran, Dynamic responses of bioinspired plastic-reinforced cementitious beams, *Cement and Concrete Composites*, 133 (2022) 104682. <https://doi.org/10.1016/j.cemconcomp.2022.104682>.
- [53] M. Chen, Z. Chen, Y. Xuan, T. Zhang, M. Zhang, Static and dynamic compressive behavior of 3D printed auxetic lattice reinforced ultra-high performance concrete, *Cement and Concrete Composites*, 139 (2023) 105046. <https://doi.org/10.1016/j.cemconcomp.2023.105046>.
- [54] K. Barri, Q. Zhang, J. Kline, W. Lu, J. Luo, Z. Sun, B.E. Taylor, S.G. Sachs, L. Khazanovich, Z.L. Wang, A.H. Alavi, Multifunctional Nanogenerator-Integrated Metamaterial Concrete Systems for Smart Civil Infrastructure, *Advanced Materials*, 35 (2023) 2211027. <https://doi.org/10.1002/adma.202211027>.
- [55] D. Valverde-Burneo, N. García-Troncoso, I. Segura, M. García-Laborda, Multifunctional cementitious composite: Conductive and auxetic behavior, *Case Studies in Construction Materials*, 20 (2024) e03358. <https://doi.org/10.1016/j.cscm.2024.e03358>.
- [56] M. Ohno, M. Pierre, K. Imagawa, T. Ishida, Simulation and learning-driven design for architected cement-based materials, *Journal of Building Engineering*, 65 (2023) 105768. <https://doi.org/10.1016/j.jobe.2022.105768>.
- [57] G.A. Lyngdoh, N.-K. Kelter, S. Doner, N.M.A. Krishnan, S. Das, Elucidating the auxetic behavior of cementitious cellular composites using finite element analysis and interpretable machine learning, *Materials & Design*, 213 (2022) 110341. <https://doi.org/10.1016/j.matdes.2021.110341>.
- [58] F.Ç. Bolat, A. Sugeç, A. Özdemir, Design, numerical analysis and experiments of different types auxetic beams for vibration based energy harvester, *Mechanical Systems and Signal Processing*, 210 (2024) 111170. <https://doi.org/10.1016/j.ymssp.2024.111170>.
- [59] K. Chen, Q. Gao, S. Fang, D. Zou, Z. Yang, W.-H. Liao, An auxetic nonlinear piezoelectric energy harvester for enhancing efficiency and bandwidth, *Applied Energy*, 298 (2021) 117274. <https://doi.org/10.1016/j.apenergy.2021.117274>.
- [60] X. Zhou, K. Parida, J. Chen, J. Xiong, Z. Zhou, F. Jiang, Y. Xin, S. Magdassi, P.S. Lee, 3D Printed Auxetic Structure-Assisted Piezoelectric Energy Harvesting and Sensing, *Advanced Energy Materials*, 13 (2023) 2301159. <https://doi.org/10.1002/aenm.202301159>.
- [61] H. Zhang, S. Chen, M. Karimi, B. Li, S. Saydam, M. Hassan, Numerical and experimental investigation of an auxetic piezoelectric energy harvester with frequency self-tuning capability, *Smart Materials and Structures*, 33 (2024) 055022. 10.1088/1361-665X/ad3bfe.
- [62] A. Pandey, J. Adhikari, D. Singh, V. Narain, R. Kumar, Smart structural framework for energy harvesting using auxetic metamaterial-embedded flex-tensional piezoelectric bridges, *International Journal of Mechanics and Materials in Design*, (2025) 10.1007/s10999-025-09794-0.
- [63] Q. Gao, Y. Lu, Y. Shi, W.H. Liao, G. Yin, J. Li, F. Xiao, R. Qiu, Enhancing the Output Performance of Energy Harvesters Using Hierarchical Auxetic Structure and Optimization Techniques, *IEEE Transactions on Industrial Electronics*, 71 (2024) 11641-11649. 10.1109/TIE.2023.3331108.
- [64] P. Eghbali, D. Younesian, A. Moayedizadeh, M. Ranjbar, Study in circular auxetic structures for efficiency enhancement in piezoelectric vibration energy harvesting, *Scientific Reports*, 10 (2020) 16338. 10.1038/s41598-020-73425-1.

- [65] Q. Gao, W. Li, Y. Shi, W.-H. Liao, G. Yin, J. Li, C. Wang, R. Qiu, A rotating auxetic energy harvester for vehicle wheels, *Engineering Structures*, 288 (2023) 116190.
<https://doi.org/10.1016/j.engstruct.2023.116190>.

3

ELLIPTICAL-SHAPED ACCC ENERGY HARVESTER

—EXPERIMENTS

Auxetic cementitious cellular composites exhibit extraordinary mechanical properties, such as high deformability, high energy absorption, and high indentation resistance. When subjected to cyclic loading, the architected ACCCs show compliant behavior, and a quasi-elastic response which is highly resistant to fatigue. This flexible behavior of ACCCs presents a large deformation with much strain energy, which can be converted into electrical energy via surface-mounted piezoelectric films. In this chapter, a novel piezoelectric energy harvester design consisting of ACCCs and surface-mounted PVDF was proposed to convert strain-based energy to useable electrical energy. The ACCC-PVDF energy harvesting system was first compressed to a certain displacement and then subjected to cyclic loading to consistently generate voltage for energy harvesting.

3.1 INTRODUCTION

Energy harvesting is a process by which the ambient energy is captured and converted into usable electrical energy for self-powered devices, such as small-sized, portable, low-power, and remote electronics that do not require replacement or maintenance. The most common energy harvesting materials and devices include piezoelectrics [1, 2], thermoelectrics [3], photovoltaics [4], triboelectrics [5], electromagnetics [6], etc. Among them, piezoelectric energy harvesters are especially effective given that they produce a wide range of voltage and power density regardless of weather conditions.

Due to their auxetic behavior, auxetic cementitious cellular composites possess exceptional mechanical properties, including high deformability, excellent energy absorption, and strong resistance to indentation [7, 8]. When compressed within the auxetic behavior range and subjected to cyclic loading, these architected materials demonstrate a compliant response characterized by recoverable deformation. This response, referred to as a second elastic behavior, occurs after the initial elastic phase and exhibits secondary quasi-elastic characteristics. The flexible nature of ACCCs allows for large deformations and significant strain energy storage, making them highly suitable for strain-driven piezoelectric energy harvesting in infrastructure applications.

In this chapter, a novel piezoelectric energy harvester with ACCCs and surface-mounted PVDF films based on strain-induced piezoelectric mechanisms (Figure 3-1) has been designed, fabricated, and experimentally tested. The ACCC-PVDF energy harvesting system was first compressed to a predetermined displacement and then subjected to cyclic loading for generating voltage. The output voltage of the energy harvester under different loading amplitudes and frequencies are further investigated. Presumably, the proposed ACCC-PVDF energy harvesting system can be deployed in coastal areas to harvest kinetic energy from ocean waves. Furthermore, it can also be efficiently employed to absorb impact energy in speed bumps on vehicle roads or bike lane pavements. The energy harvested from these applications can be used to power electronics in infrastructure, contributing to the development of various smart infrastructure systems.

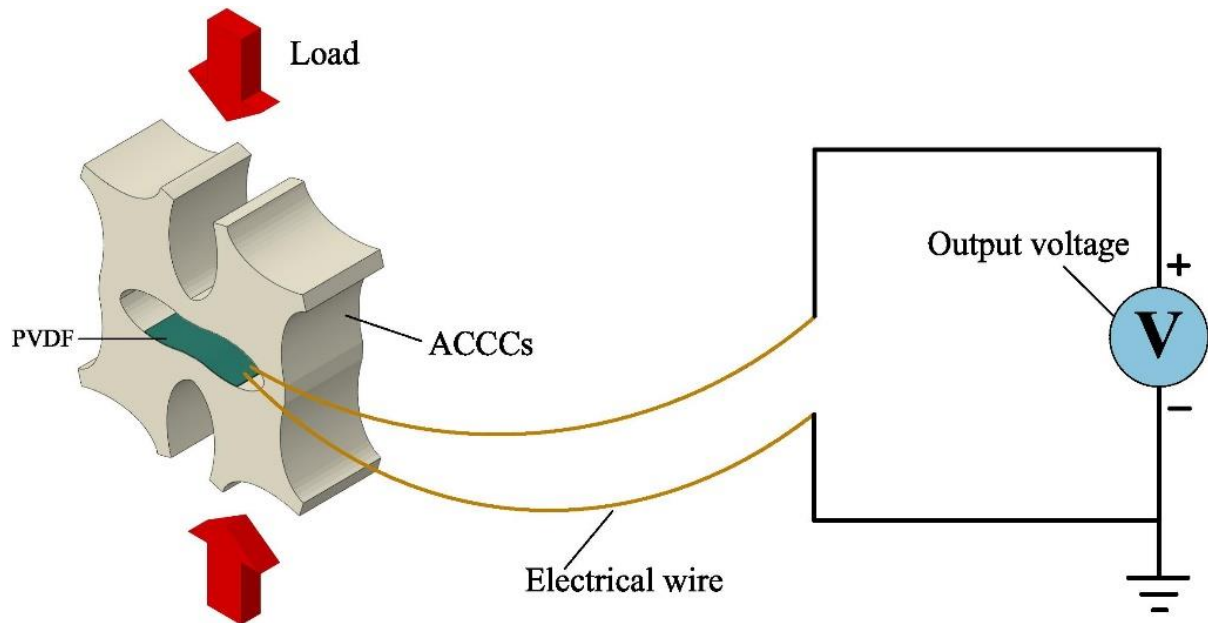


Figure 3-1 Schematic of the energy harvesting design of ACCCs

3.2 MATERIALS AND METHODS

3.2.1 Specimen preparation

A unit cell of the ACCCs was chosen for energy harvesting experiments. The design parameters of the unit cell are shown in Figure 3-2. The specimens were created using the so-called “indirect printing” process reported in [7, 8], as follows:

- First, the designed unit cell is 3D printed with a FDM 3D printer Ultimaker 2+, and ABS is used as printing material.
- Then, the printed unit cell is glued in a card box. Subsequently, a two-component silicone rubber (Poly-Sil PS 8510) is mixed (1:1 by mass) and poured in the box.
- After storing in room temperature for two hours, the silicone rubbers solidifies. Then the hardened silicone rubber was detached from the box such that a silicone mold was obtained.
- Cementitious mixture was casted in the silicone rubber mold. After curing under room temperature for two days, the specimen was demolded from the silicone mold and stored in the curing chamber (20°C, 96%RH) until the age of 28 days.
- Two hours before testing, the specimens were taken out of the curing chamber. One PVDF film is glued by silicone rubber (same as the Poly-Sil PS8510) on the central elliptical hole of each specimen and left for hardening for two hours. As shown in Figure 3-3, the LDT0-028K PVDF film has an area of 24.81 mm x 13.21 mm ($l_p \times w_p$) with a thickness of 0.2 mm (h_p) (including the protective layer against surface oxidation of the silver ink electrode area [9-11]). Herein, the piezoelectric layer in the PVDF film has a thickness of 28 μm (t_p).

The mortar mixture of ACCCs contained CEM I 42.5 N, fly ash, sand with a grain size ranging from 125 to 250 μm , water, polycarboxylate superplasticizer, viscosity modifying agent (VMA), and fiber. Table 3-1 provides the mixture compositions of ACCCs, which was tailored based on a previously used ACCC mix [7, 8]. For the ACCCs, a fine-grained fiber reinforced mortar was employed as the constituent material. The Polyvinyl Alcohol (PVA) fiber produced by Changzhou TianYi Engineering Fiber was used as the reinforcement at a volume fraction of 2%. The physical and mechanical properties of the PVA fiber are presented in Table 3-2. To improve the fiber distribution, VMA in the form of methylcellulose powder from Shanghai Ying Jia Industrial Development Co. Ltd. was utilized. To achieve the desired workability, MasterGlenium 51, a polycarboxylate-based superplasticizer manufactured by BASF (Germany), was utilized. To ensure thorough casting of the cement materials within the small mold, a higher water-to-binder ratio of 0.46 was chosen to facilitate good fluidity.

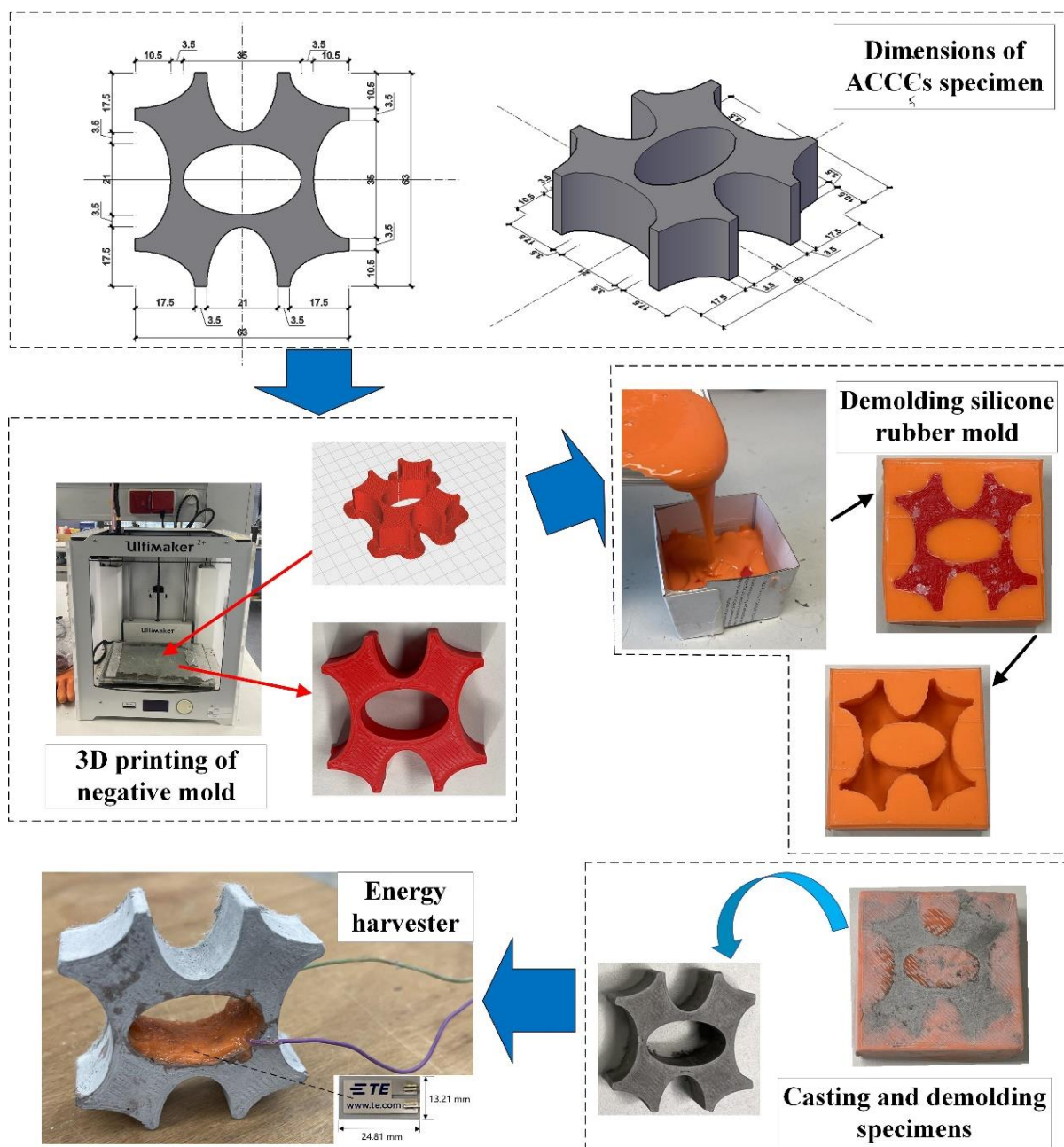


Figure 3-2 Specimen preparation

The dry ingredients including CEM I 42.5, fly ash, sand and VMA were mixed for four minutes using a Hobart machine. Water and superplasticizer were then added into the dry mixture, followed by an additional 2 minutes of mixing. Afterwards, the fibers were incorporated into the mortar slowly and mixed for additional 2 minutes. To ensure an even distribution of fibers within the matrix, high-speed rotation was further employed to mix the fibers for another 5 minutes. Afterwards, the mixed fresh paste was cast into the silicone molds. Each specimen was filled into the mold in two layers, and each layer underwent 20 seconds of vibration to ensure thorough consolidation. Finally, they were covered with plastic films to prevent evaporation. Following a three-day curing period at room temperature, the specimens were removed from the molds and subsequently placed in a curing chamber (20°C, 96%RH) until the age of 28 days.

Table 3-1 Mix ratios of ACCCs (kg/m³)

Cement	Fly ash	Sand (125 μ m to 250 μ m)	Water	Superplasticizer (Glenium 51)	VMA	PVA Fiber
453	535	370	450	1.58	0.29	25.6

Table 3-2 Material properties of PVA fiber

Diameter (μ m)	Length (mm)	Tensile strength (GPa)	Young's modulus (GPa)	Density (g/cm ³)
15	6	1.6	34	1.28

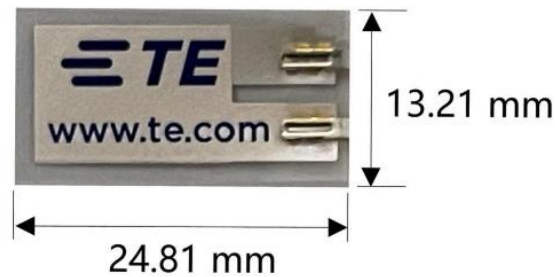


Figure 3-3 Geometric measurement for LDT0-028 K PVDF film.

3.2.2 Experimental test

Figure 3-4 illustrates the energy harvesting test setup and loading scheme for the ACCC energy harvester. The cyclic tests were performed using an MTS fatigue machine with a 10 kN capacity. The Direct Current (DC) output voltage of the harvester was measured using a Keysight 34461A digital multimeter (DMM). Due to the high internal impedance of LDT0 PVDF (approximately 11.2 M Ω based on pure capacitance estimation [11]), the multimeter's input impedance was set to a mode over 10 G Ω to ensure accurate open-circuit voltage measurements. The PVDF was connected to the multimeter using two wires, and a plastic film was placed between the loading plate and the specimen to minimize friction. To address minor horizontal movement caused by uneven deformation or asymmetrical cracking in the cementitious materials during cyclic loading, tape was used to stabilize the bottom loading plate. As shown in Figure 3-5, the P1a-shaped specimen was initially compressed by displacement loading, starting at zero and increasing to U (5.0 mm), reducing the specimen's height to 58 mm. This was followed by cyclic displacement loading in the form of a sinusoidal wave with a constant amplitude ($A = 1$ mm) and frequency ($f = 1$ Hz). Each test was performed with three replicates. To investigate the effects of loading amplitude and loading frequency, the amplitudes of 1.0 mm and 2.0 mm, the frequencies of 0.3 Hz, 1.0 Hz and 2.0 Hz were considered in energy harvesting experiments.

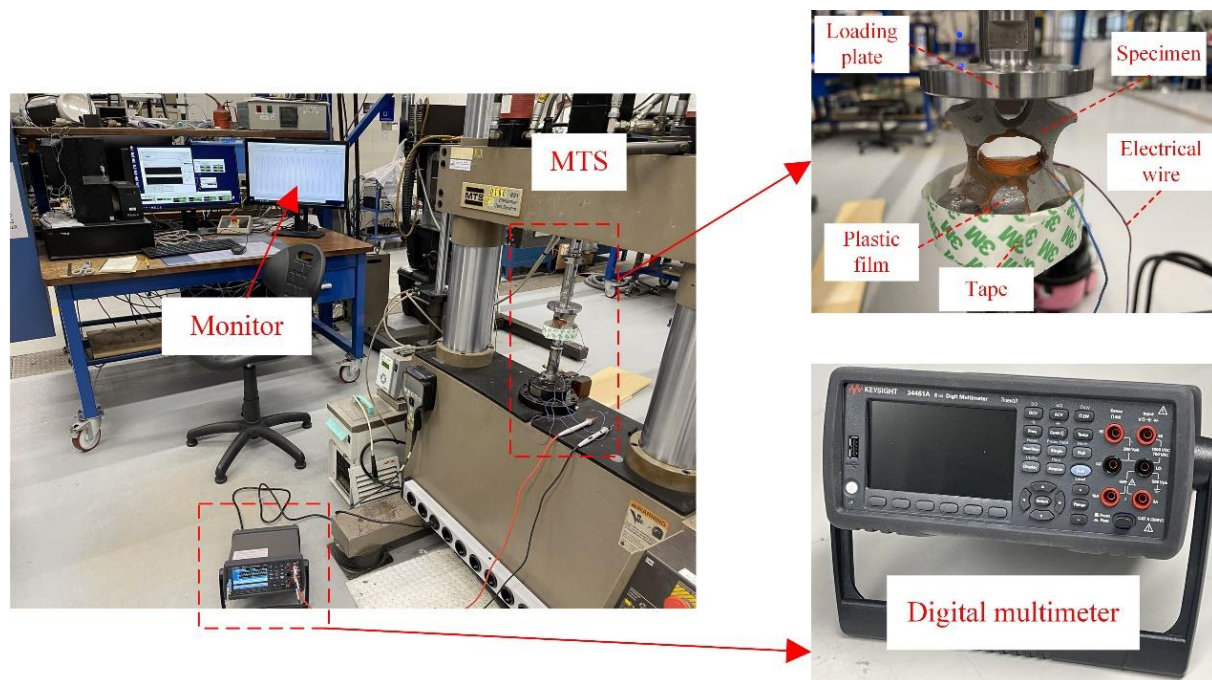


Figure 3-4 Experimental setup for energy harvesting test

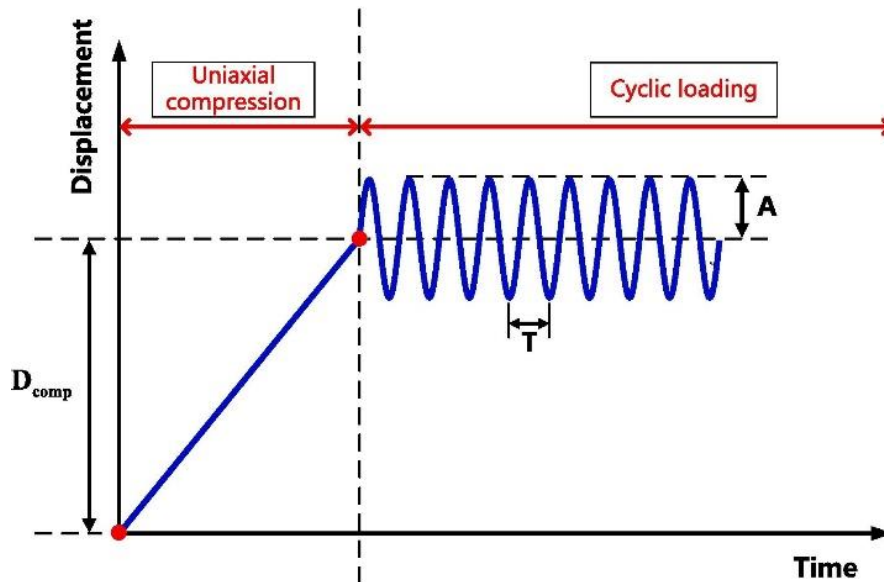


Figure 3-5 Loading scheme for energy harvesting test

3.3 RESULTS AND DISCUSSION

Figure 3-6 and Table 3-3 present the results of energy harvesting experiments for the ACCC-PVDF system under various loading frequencies and amplitudes over a 10-second period. During each loading cycle, the output voltage increases as the compressive displacement grows. When the maximum displacement is applied, the output voltage reaches its peak. Conversely, as the loading plate moves away from the ACCCs, the output voltage decreases to zero. Additionally, Figure 3-6 highlights the influence of loading frequency and amplitude on the output voltage of the ACCC-PVDF system. At a constant loading amplitude, the output voltage rises with increasing loading frequency. Similarly, increasing the loading amplitude from 1.0 mm to 2.0 mm results in higher output voltages. Notably, the effect of loading amplitude on the output voltage is more pronounced than that of loading frequency. For instance, at a loading amplitude of 1.0 mm, the maximum output voltages were 4.7 V, 5.2 V, and 5.6 V for loading frequencies of 0.3 Hz, 1.0 Hz, and 2.0 Hz, respectively. At a higher loading amplitude of 2.0 mm, the corresponding maximum output voltages increased to 10.5 V, 11.5 V, and 11.8 V, respectively.

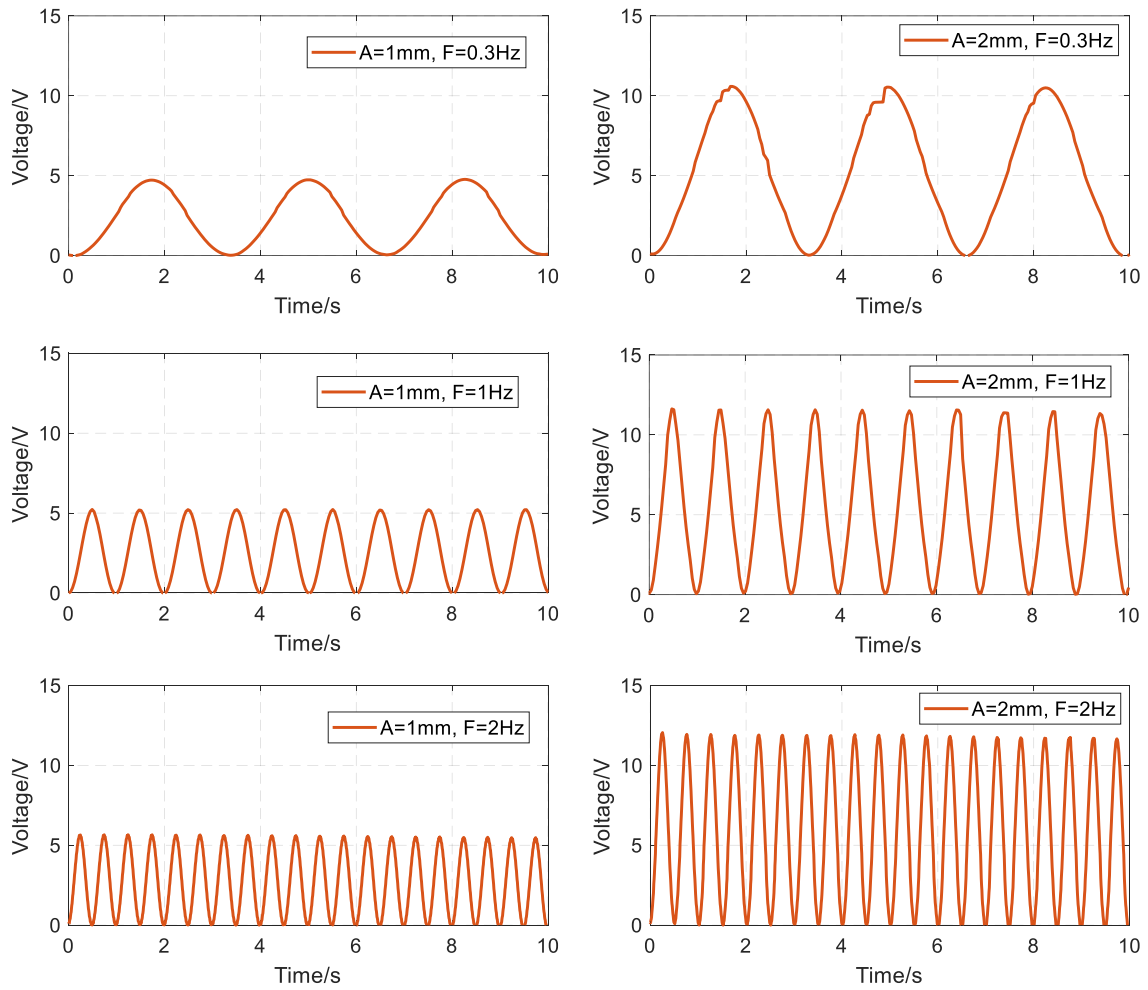


Figure 3-6 Energy harvesting test results of the ACCC-PVDF system

Table 3-3 Output voltage under different amplitudes and frequencies

	F=0.3Hz	F=1Hz	F=2Hz
A=1mm	4.7V	5.2V	5.6V
A=2mm	10.5V	11.5V	11.8V

Figure 3-7, Figure 3-8, and Table 3-4 display the dynamic stress-strain curves obtained during energy harvesting tests under various loading frequencies and amplitudes over a 10-second duration. Within each loading cycle, the stress increases with growing compressive strain and reaches its peak at the maximum compressive strain. As the loading plate moves away from the ACCCs, the stress gradually decreases to zero. Figure 3-7 and Figure 3-8 also demonstrate the effects of loading frequency and amplitude on the dynamic stress-strain curves of the ACCC-PVDF system. At a constant loading amplitude, the stress tends to decrease approximately as the loading frequency increases. Similarly, an increase in the loading

amplitude from 1.0 mm to 2.0 mm results in a reduction in stress. Notably, the effect of loading amplitude on stress is more significant than that of loading frequency. For example, at a loading amplitude of 1.0 mm, the maximum stresses observed were 0.0096 MPa, 0.0092 MPa, and 0.0092 MPa for loading frequencies of 0.3 Hz, 1.0 Hz, and 2.0 Hz, respectively. When the loading amplitude increased to 2.0 mm, the corresponding maximum stresses decreased to 0.0067 MPa, 0.0059 MPa, and 0.0049 MPa, respectively. Since the stress generated by the energy harvester during the cyclic test is very low compared with the stiffness of the testing machine in the compression cyclic setup, the machine-recorded displacement accurately reflects the actual applied loading displacement.

Table 3-4 Peak stresses under different amplitudes and frequencies

	F=0.3Hz	F=1Hz	F=2Hz
A=1mm	0.0096MPa	0.0092MPa	0.0092MPa
A=2mm	0.0067MPa	0.0059MPa	0.0049MPa

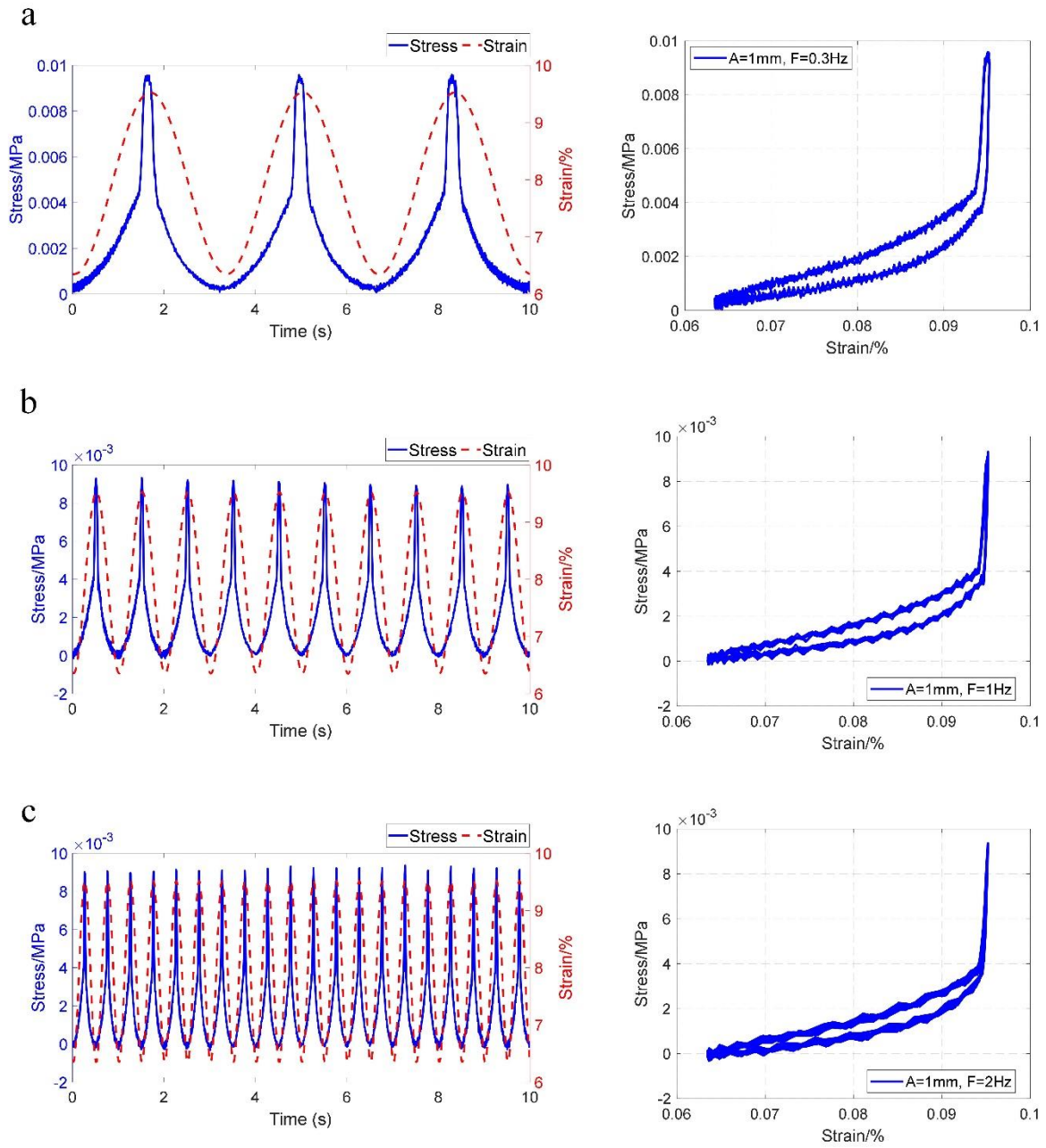


Figure 3-7 Dynamic stress-strain curves during energy harvesting tests under a loading amplitude of 1.0 mm with different loading frequencies.

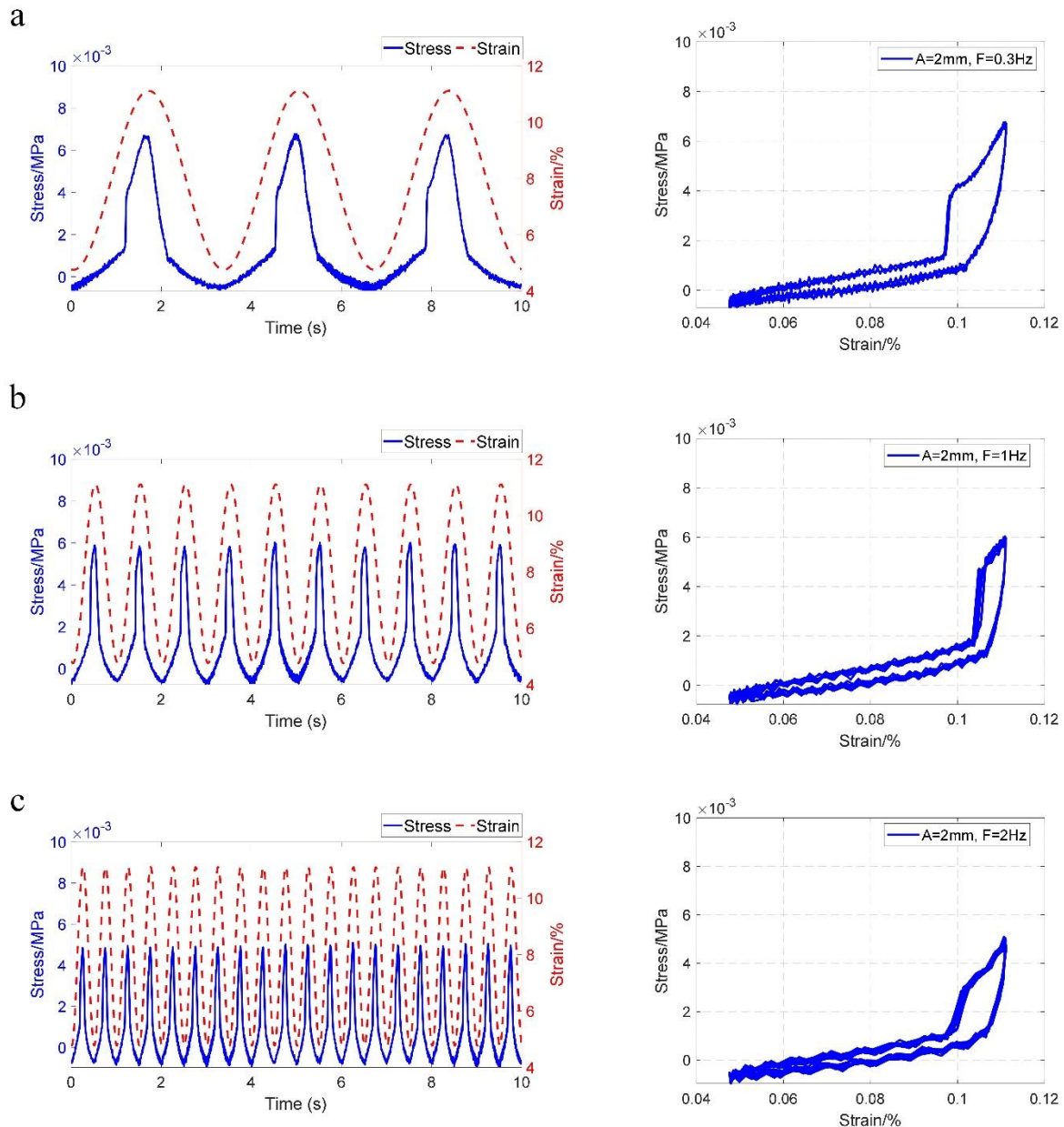


Figure 3-8 Dynamic stress-strain curves during energy harvesting tests under a loading amplitude of 2.0 mm with different loading frequencies.

Under cyclic loading, the dynamic strain at the joint of the ACCCs is transferred to the PVDF film through the bonding material. Therefore, the integrity of the bonding interface plays a critical role in effective strain transfer. In the absence of debonding, an increase in loading frequency—corresponding to greater acceleration and inertial force—typically leads to a higher dynamic strain transferred to the PVDF, resulting in increased voltage output. However, at higher frequencies, partial debonding of the bonding layer may occur due to increased dynamic shear forces, thereby reducing the efficiency of strain transfer to the piezoelectric film. Consequently, although the voltage output still exhibits a certain degree of increase with frequency, the increase is not proportional and becomes progressively limited.

3.4 CONCLUSIONS

Leveraging the compliant behavior and high deformability of ACCCs, this chapter presents a novel piezoelectric energy harvester integrating ACCCs with surface-mounted PVDF film. The harvester, based on strain-induced piezoelectric mechanisms, has been designed, fabricated, and experimentally tested for energy harvesting applications. The main conclusions are as follows:

- The energy harvesting experiments reveal that the ACCC-PVDF system produces a sinusoidal output voltage, reaching a peak of several volts during each cycle of cyclic loading. At a loading frequency of 2 Hz and a loading amplitude of 2.0 mm, the system achieves a maximum output voltage of 11.8 V, demonstrating significant potential for supplying self-power electronics in infrastructure applications.
- The energy harvesting experiments revealed that the output voltage of the ACCC-PVDF system increases with the loading amplitude and loading frequency. Notably, the effect of loading amplitude on the output voltage is more pronounced than that of loading frequency.
- The ACCC-PVDF energy harvester exhibits a pseudo-elastic stress-strain behavior during dynamic cyclic loading for energy harvesting. The results indicate that the peak stress of the harvester generally decreases with both loading amplitude and loading frequency. However, the influence of loading amplitude on peak stress is significantly greater than that of loading frequency.

In this chapter, the potential of the ACCC-PVDF energy harvester to generate output voltages has been demonstrated during energy harvesting experiments. However, the underlying mechanical and electrical mechanisms behind these observations require further investigation. Numerical modeling offers a valuable tool to analyze and theoretically predict the energy harvesting potential of cementitious materials in complex scenarios. Moreover, a model-based approach enables the exploration of how mechanical and electrical parameters influence energy harvesting, facilitating performance assessment and optimization for future applications. This will be further discussed in chapters 4 and 5.

REFERENCES

- [1] T. Fan, G. Zou, L. Yang, Nano piezoelectric/piezomagnetic energy harvester with surface effect based on thickness shear mode, *Composites Part B: Engineering*, 74 (2015) 166-170. <https://doi.org/10.1016/j.compositesb.2015.01.012>.
- [2] U. Yaqoob, A.S.M.I. Uddin, G.-S. Chung, Synthesis of poly(vinylidene fluoride-trifluoroethylene)-0.65Pb(Mg_{1/3}Nb_{2/3})O₃-0.35PbTiO₃-reduced graphene oxide-composite sheet and its application to flexible energy harvesting, *Composites Part B: Engineering*, 136 (2018) 92-100. <https://doi.org/10.1016/j.compositesb.2017.09.011>.
- [3] E. Ghafari, F. Severgnini, S. Ghahari, Y. Feng, E.J. Lee, C. Zhang, X. Jiang, N. Lu, Thermoelectric Nanocomposite for Energy Harvesting, *Multifunctional Nanocomposites for Energy and Environmental Applications*, (2018) 173-202. <https://doi.org/10.1002/9783527342501.ch8>.

- [4] N. Lu, I. Ferguson, III-nitrides for energy production: photovoltaic and thermoelectric applications, *Semiconductor Science and Technology*, 28 (2013) 074023. 10.1088/0268-1242/28/7/074023.
- [5] G. Zhu, Z.-H. Lin, Q. Jing, P. Bai, C. Pan, Y. Yang, Y. Zhou, Z.L. Wang, Toward Large-Scale Energy Harvesting by a Nanoparticle-Enhanced Triboelectric Nanogenerator, *Nano Letters*, 13 (2013) 847-853. 10.1021/nl4001053.
- [6] S.P. Beeby, R.N. Torah, M.J. Tudor, P. Glynn-Jones, T. O'Donnell, C.R. Saha, S. Roy, A micro electromagnetic generator for vibration energy harvesting, *Journal of Micromechanics and Microengineering*, 17 (2007) 1257-1265. 10.1088/0960-1317/17/7/007.
- [7] Y. Xu, E. Schlangen, M. Luković, B. Šavija, Tunable mechanical behavior of auxetic cementitious cellular composites (CCCs): Experiments and simulations, *Construction and Building Materials*, 266 (2021) 121388. <https://doi.org/10.1016/j.conbuildmat.2020.121388>.
- [8] Y. Xu, H. Zhang, E. Schlangen, M. Luković, B. Šavija, Cementitious cellular composites with auxetic behavior, *Cement and Concrete Composites*, 111 (2020) 103624. <https://doi.org/10.1016/j.cemconcomp.2020.103624>.
- [9] J.W. Sohn, J. Jeon, S.B. Choi, An Investigation on Dynamic Signals of MFC and PVDF Sensors: Experimental Work, *ADVANCES IN MECHANICAL ENGINEERING*, (2013) <https://doi.org/10.1155/2013/420345>.
- [10] Y.-F. Su, R.R. Kotian, N. Lu, Energy harvesting potential of bendable concrete using polymer based piezoelectric generator, *Composites Part B: Engineering*, 153 (2018) 124-129. <https://doi.org/10.1016/j.compositesb.2018.07.018>.
- [11] H.-H. Huang, K.-S. Chen, Design, analysis, and experimental studies of a novel PVDF-based piezoelectric energy harvester with beating mechanisms, *Sensors and Actuators A: Physical*, 238 (2016) 317-328. <https://doi.org/10.1016/j.sna.2015.11.036>.

4

BENCHMARK ENERGY HARVESTING MODEL FOR FIBER-REINFORCED CEMENTITIOUS COMPOSITES UTILIZING SURFACE-MOUNTED PIEZOELECTRIC MATERIALS

In the auxetic cementitious cellular composites energy harvester (developed in Chapter 3), elastic strain energy mainly concentrated around the hinge-like joints is then converted into electrical energy via surface-mounted piezoelectric films. This conversion process involves a complex electromechanical interaction between the ACCCs and the bonded PVDF film. To understand these piezoelectric mechanisms, a general theoretical model was developed to evaluate the energy harvesting performance of fiber-reinforced cementitious materials incorporating surface-mounted PVDF. In the mechanical part, concrete damage plasticity (CDP) model based on the explicit dynamic analysis was utilized to simulate the dynamic flexural behavior of fiber-reinforced cementitious beam under four-point bending. The mechanism of force transfer through the bond layer between the PVDF film and the beam was simulated by a surface-surface sliding friction model. Then, the electromechanical behavior of the piezoelectric film was simulated by a piezoelectric finite element model. The theoretical model was validated against experimentally measured mechanical and electrical data reported in the literature.

4.1. INTRODUCTION

In Chapter 3, a novel piezoelectric energy harvester with ACCCs and surface-mounted PVDF film based on strain-induced piezoelectric mechanisms has been designed, fabricated, and experimentally tested. The energy harvester was first compressed to a predetermined displacement and then subjected to cyclic loading for generating voltage. Herein, the energy harvesting mechanism converts mechanical energy into electrical energy through the piezoelectric effect. This mechanical energy originates from the recoverable strain energy of ACCCs within the auxetic deformation range and is transferred to the PVDF via the bonding material. The PVDF then utilizes this transferred strain to generate output voltage. The recoverable strain primarily arises from the hinge-like joints with rough and cracked surfaces, which transmit strain to the surface-mounted PVDF through complex interactions. Therefore, understanding the interaction mechanisms between the cracked, rough cementitious surface and the PVDF is essential. However, no known piezoelectric model for energy harvesting was associated with fiber-reinforced cementitious material with surface-mounted piezoelectric films.

This chapter presents a theoretical model for evaluating the energy harvesting performance of fiber-reinforced cementitious materials incorporating surface-mounted PVDF. In the mechanical part, CDP model based on the explicit dynamic analysis was utilized to simulate the dynamic flexural behavior of fiber-reinforced cementitious beam under different dynamic loading rates. The mechanism of force transfer through the bond layer between the PVDF film and fiber-reinforced cementitious beam was simulated by a surface-surface sliding friction model wherein the PVDF film was simplified as shell element to reduce computational cost. Then, the electromechanical behavior of the piezoelectric film was simulated by a piezoelectric finite element model. A simplified model was also given for a quick calculation. The theoretical model was verified with the experimentally measured mechanical and electrical results from the literature.

4.2. THEORETICAL MODELING

4.2.1. Concrete damage plasticity model

The CDP model [1-3] was adopted for simulating the nonlinear behavior of fiber-reinforced cementitious material due to plasticity and damage, which is:

$$\sigma = (1-d)E_0(\varepsilon - \varepsilon^{pl}) \quad (1)$$

where σ is the stress; ε , ε^{pl} are the total strain and plastic strain, respectively. E_0 represents the initial Young's modulus of fiber-reinforced cementitious material. d represents the damage factor used for quantifying stiffness degradation, in a range of 0 to 1. And it requires that the d increases monotonically with strain. Here, as fiber reinforced cementitious material was used, the stress doesn't decrease monotonically with strain when the material is loaded in tension. Hence, stiffness degradation was not considered.

The following yield criterion in the CDP model is used to describe the initiation of plastic strain.

$$F = \frac{1}{1-\alpha} \left(\bar{q} - 3\alpha\bar{p} + \beta(\varepsilon^{pl}) \left\langle \bar{\sigma}_{\max} \right\rangle - \gamma \left\langle -\bar{\sigma}_{\max} \right\rangle \right) - \bar{\sigma}_c(\varepsilon_c^{pl}) \quad (2)$$

where

$$\alpha = \frac{(\sigma_{b0}/\sigma_{c0})-1}{2(\sigma_{b0}/\sigma_{c0})-1} \quad (3)$$

$$\beta = \frac{\bar{\sigma}_c(\varepsilon_c^{pl})}{\sigma_t(\varepsilon_t^{pl})-1}(1-\alpha)-(1+\alpha) \quad (4)$$

$$\gamma = \frac{3(1-K_c)}{2K_c-1} \quad (5)$$

where \bar{p} represents the effective hydrostatic pressure. \bar{q} represents the von Mises equivalent effective stress. The subscripts 't' and 'c' represent tension and compression, respectively. $\bar{\sigma}_{\max}$ refers to the maximum principal effective stress. σ_{b0}/σ_{c0} refers to the ratio of initial equibiaxial and initial uniaxial compressive yield stress, which takes a default value of 1.16 in ABAQUS. K_c describes the ratio of second stress invariants on tensile and compressive meridians for a given invariant \bar{p} , which takes a default value of 1.16 in ABAQUS.

Assuming non-associated potential plastic flow in the CDP model, the flow potential G based on the Drucker-Prager hyperbolic function takes the form

$$G = \sqrt{(\varepsilon_{ec}\sigma_{t0}\tan\psi)^2 + \bar{q}^2} - \bar{p}\tan\psi \quad (6)$$

where ψ is the dilation angle. σ_{t0} is the uniaxial tensile stress at failure. ε_{ec} is the eccentricity that defines the rate at which the function approaches the asymptote, which generally takes a value of 0.1 in ABAQUS.

According to Zhou et al. [4], the constitutive relationship of a typical fiber reinforced cementitious material (ECC) can be simplified as shown in Figure 4-1. Herein, its compressive model (Figure 4-1(a)) can be represented as

$$\sigma_c = \begin{cases} E_0\varepsilon & 0 < \varepsilon \leq \varepsilon_{0.4} \\ E_0\varepsilon(1-\alpha) & \varepsilon_{0.4} < \varepsilon \leq \varepsilon_0 \\ m(\varepsilon - \varepsilon_0) + f'_{cr} & \varepsilon_0 < \varepsilon \leq \varepsilon_l \\ n(\varepsilon - \varepsilon_0) + \sigma_l & \varepsilon_l < \varepsilon \leq \varepsilon_{\max} \end{cases} \quad (7)$$

where ε_0 refers to the strain at the peak load. $\varepsilon_{0.4}$ refers to the strain at 40% of the peak load. f'_{cr} represents the stress at the peak load. m, n determine the slope of the bilinear curve, which can be calibrated by experiments. σ_l, ε_l represent the stress and strain at the inflection point, respectively. α refers to the reduction factor for elastic modulus, which is calculated as follows

$$\alpha = a \frac{E_0\varepsilon}{f'_{cr}} - b \quad (8)$$

where a and b can be obtained according to the slope of the equivalent hardening line. As indicated in Figure 4-1(b), the tensile behavior of ECC can be represented by a trilinear curve, which can be described by Eq. (9) [5]. Herein, the second part of the curve ($\varepsilon_{t0} < \varepsilon \leq \varepsilon_{tp}$) is employed to model the tension stiffening characteristics of ECC. $\sigma_{t0}, \sigma_{tp}, \varepsilon_{t0}, \varepsilon_{tp}$ can be used to modify the tension stiffening behavior of ECC according to the experimental tensile data.

$$\sigma_t = \begin{cases} E_0 \varepsilon & 0 < \varepsilon \leq \varepsilon_{t0} \\ \sigma_{t0} + (\sigma_{tp} - \sigma_{t0}) \left(\frac{\varepsilon - \varepsilon_{t0}}{\varepsilon_{tp} - \varepsilon_{t0}} \right) & \varepsilon_{t0} < \varepsilon \leq \varepsilon_{tp} \\ \sigma_{tp} \left(1 - \frac{\varepsilon - \varepsilon_{tp}}{\varepsilon_{tu} - \varepsilon_{tp}} \right) & \varepsilon_{tp} < \varepsilon \leq \varepsilon_{tu} \\ 0 & 0 \end{cases} \quad (9)$$

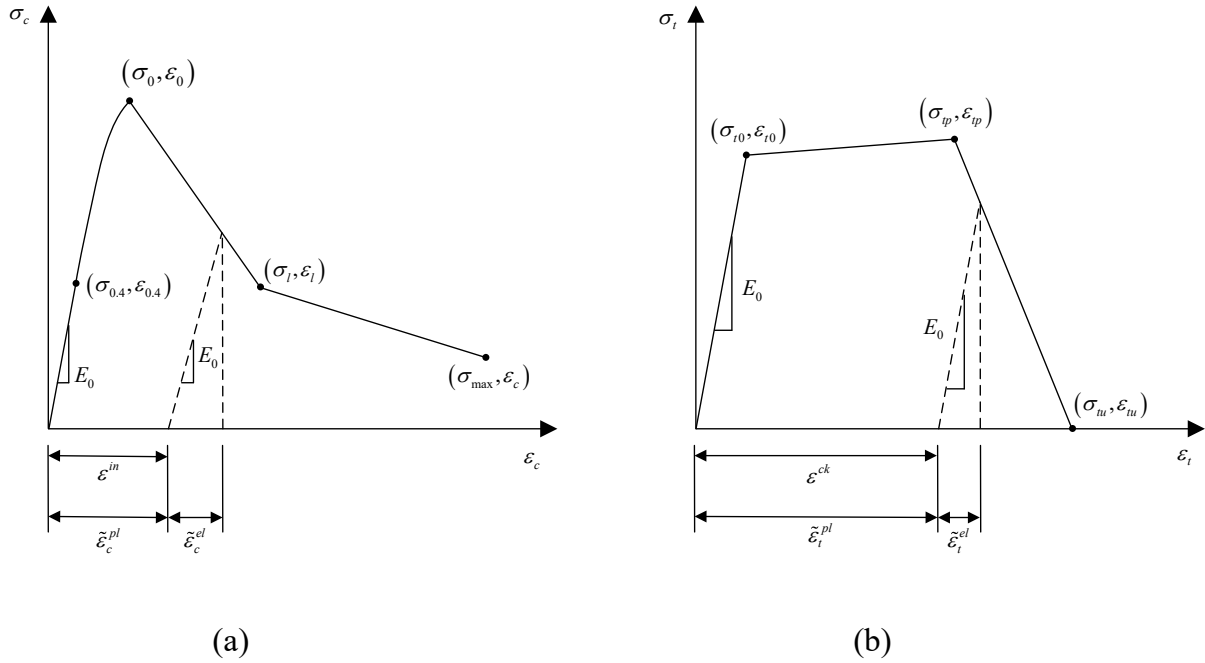


Figure 4-1 Constitutive relations of the CDP model for ECC: (a) Compression; (b) Tension.

4.2.2. Interaction between ECC and piezoelectric polymer

In general, piezoelectric patches or polymers wrapped with a protective cover are surface bonded to the host structure by adhesives. Previous studies have indicated that a surface-mounted piezoelectric patch is not perfectly bonded with the host structure during its deformation process (including patch debonding, patch breakage/scratch, and patch detaching [6, 7]), which has significant impacts on the output voltage [8]. Figure 4-2 presents the mechanism for the interaction between the host structure and the piezoelectric polymer. Herein, ‘1’ represents the axial direction, ‘3’ represents the vertical direction. As indicated in Figure 4-2(a), there is a bond layer between the host structure and the piezoelectric polymer, which limits the separation of the two in the normal direction. In the tangential direction, the relative movement of the two is limited by corresponding adhesive friction (τ) that occurs at the interface between the host structure and the bond layer, as well as the interface between the bond layer and the piezoelectric polymer. However, it should be noted that the bond layer deforms unevenly due to the shear lag effect [9, 10], which results in relative slip between the

host structure and the piezoelectric polymer, as shown in Figure 4-2(b). Herein, u_p is the deformed position of the interface between the bond layer and the host structure. u_b is the deformed position of the interface between the bond layer and the piezoelectric polymer. Generally, if debonding occurs on these interfaces during the deformation process (especially in the bending case), u_p will reduce to u_p' , u_b will reduce to u_b' , as shown in Figure 4-2(c). These effects inevitably cause a difference in deformation between the piezoelectric polymer and the associated host structure surface.

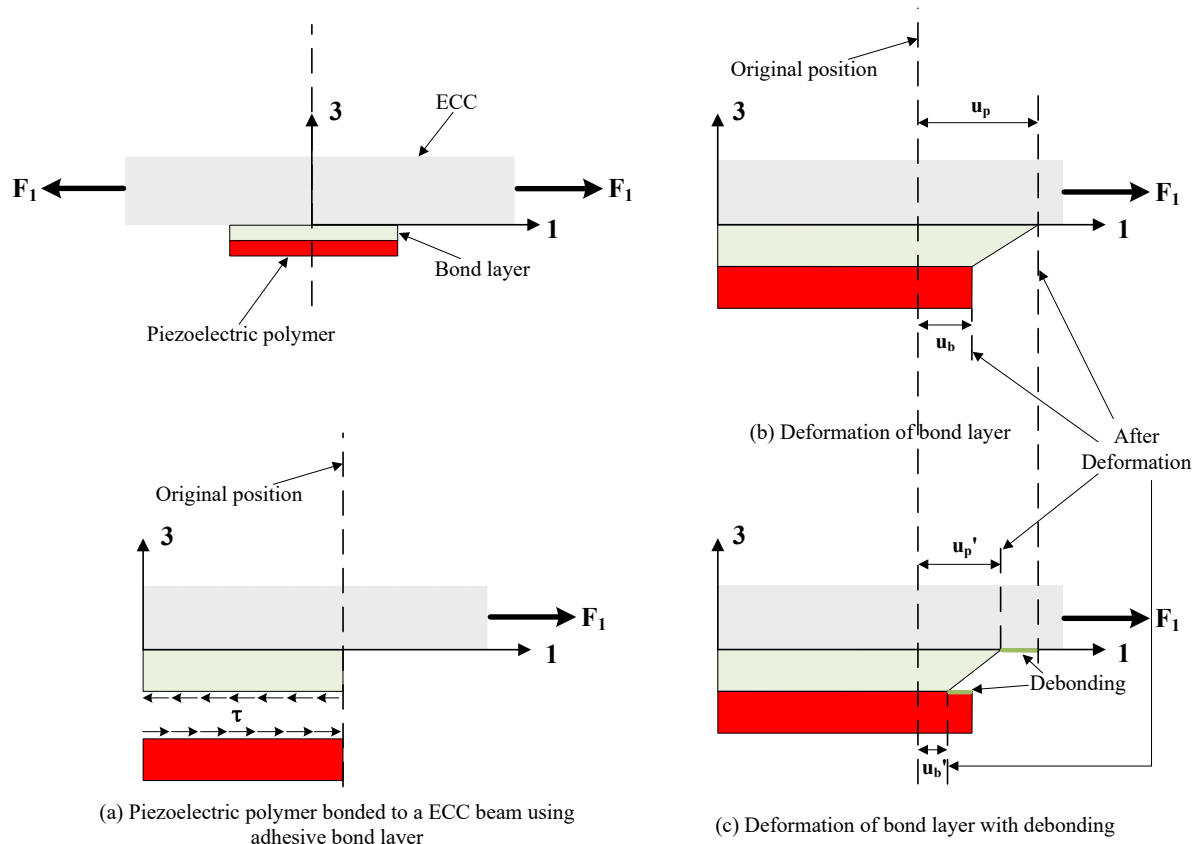


Figure 4-2 Interaction between the host structure and the piezoelectric polymer using adhesive bond layer

Compared to the host structure, the adhesive layer has a negligible mass and stiffness, and is thus omitted from the mechanical simulation [10]. Then, for the force transmission of the adhesive layer, the piezoelectric polymer and the host structure are exposed to the adhesive friction from the bond layer, which can be simplified by a surface-surface friction model. To be specific, the bottom surface of the host structure is the master surface, and the top surface of the piezoelectric polymer is the slave surface. A sliding friction model with a friction coefficient is considered for the two surfaces in the tangential direction. In the normal direction, the slave surface is not allowed to detach from the master surface, and there is also no overclosure between the two surfaces, which means the slave surface can not penetrate the master surface. In this way, the strain difference between the piezoelectric polymer and the associated host structure surface induced by the bonding condition can be reflected in the model.

4.2.3. Piezoelectric model for piezoelectric polymer

4.2.3.1. FE model for a piezoelectric element

The constitutive equations for the mechanical–electric field coupling effect in a piezoelectric material can be formulated as [11]:

$$\begin{aligned} S_{ij} &= s_{ijkl}^E \cdot T_{kl} + d_{kij} \cdot E_k \\ D_j &= d_{jkl} \cdot T_{kl} + e_{jk}^T \cdot E_k \end{aligned} \quad (10)$$

where D_j is the electric displacement. E_k is the electric field. S_{ij} is the mechanical strain. T_{kl} is the mechanical stress. d_{kij} and d_{jkl} refer to the piezoelectric strain coefficients. s_{ijkl}^E represents the mechanical compliance measured at constant electric field. e_{jk}^T refers to the dielectric permittivity measured at constant stress. The superscripts ‘ E ’ and ‘ T ’ represent that this quantity is measured at constant electric field and constant mechanical stress, respectively. For d_{kij} and d_{jkl} , the first subscript indicates the direction of the electric field, and the second and third subscripts together indicate the direction of the associated mechanical stress.

The tensor form of Eq. (10) can be written as:

$$\begin{bmatrix} \mathbf{S} \\ \mathbf{D} \end{bmatrix} = \begin{bmatrix} \mathbf{s}^E & -\mathbf{d}^t \\ \mathbf{d} & \mathbf{e}^T \end{bmatrix} \begin{bmatrix} \mathbf{T} \\ \mathbf{E}_{el} \end{bmatrix} \quad (11)$$

where \mathbf{S} is the strain tensor. \mathbf{D} is the electrical displacement vector. \mathbf{T} is the stress tensor. \mathbf{E}_{el} is the electrical field vector. The superscripts ‘ E ’ and ‘ T ’ represent that this quantity is measured at constant electric field and constant mechanical stress respectively. \mathbf{s}^E is the compliance tensor measured at constant electric field. \mathbf{e}^T is the dielectric permittivity tensor measured at constant stress. \mathbf{d} is piezoelectric strain tensor. The superscript ‘ t ’ represents the transpose matrix of this quantity. \mathbf{d}^t is the transpose matrix of \mathbf{d} .

Similarly, Eq. (10) can be applied to a PVDF film under identical stress conditions. However, in scenarios involving uneven stress, such as in the bending case discussed in this Chapter, the PVDF film must be subdivided into numerous small rectangular elements. Each rectangular element can then utilize Eq. (10) as its constitutive equation. A piezoelectric element has both the mechanical degrees of freedom (the displacement vector $\boldsymbol{\delta}$) and the electrical degrees of freedom (the electric potential array $\boldsymbol{\phi}$), which can be used to calculate \mathbf{S} and \mathbf{E}_{el} :

$$\begin{bmatrix} \mathbf{S} \\ \mathbf{E}_{el} \end{bmatrix} = \begin{bmatrix} \mathbf{B}_u & 0 \\ 0 & \mathbf{B}_\phi \end{bmatrix} \begin{bmatrix} \boldsymbol{\delta} \\ \boldsymbol{\phi} \end{bmatrix} \quad (12)$$

$$\mathbf{B}_u = \nabla N_u \quad (13)$$

$$\mathbf{B}_\phi = \nabla N_\phi \quad (14)$$

where N_u, N_ϕ are shape functions in terms of displacement and electric potential, respectively.

\mathbf{B}_u is the strain-displacement matrix containing the derivatives of N_u ; \mathbf{B}_ϕ is the electrical field-electric potential matrix containing the derivatives of N_ϕ .

Based on Hamilton’s principle, the governing FE dynamic equations for a piezoelectric finite element can be derived as

$$\begin{bmatrix} \mathbf{m}_{uu} & 0 \\ 0 & 0 \end{bmatrix} \begin{Bmatrix} \hat{\mathbf{u}} \\ \hat{\phi} \end{Bmatrix}_e + \begin{bmatrix} \mathbf{c}_{uu} & 0 \\ 0 & 0 \end{bmatrix} \begin{Bmatrix} \dot{\hat{\mathbf{u}}} \\ \dot{\hat{\phi}} \end{Bmatrix}_e + \begin{bmatrix} \mathbf{k}_{uu} & \mathbf{k}_{u\phi} \\ \mathbf{k}_{u\phi}^t & \mathbf{k}_{\phi\phi} \end{bmatrix} \begin{Bmatrix} \hat{\mathbf{u}} \\ \hat{\phi} \end{Bmatrix}_e = \begin{Bmatrix} \mathbf{f}^{ext} \\ q^{ext} \end{Bmatrix}_e \quad (15)$$

where the subscript ‘ e ’ indicates element quantities. $\hat{\mathbf{u}}, \dot{\hat{\mathbf{u}}}, \ddot{\hat{\mathbf{u}}}$ represent vectors of nodal displacement, velocity, and acceleration, respectively. $\hat{\phi}, \dot{\hat{\phi}}, \ddot{\hat{\phi}}$ represent the electric potential, the first derivative of the electric potential, and the second derivative of the electric potential, respectively. \mathbf{f}^{ext} is the external force. q^{ext} is the external point charge.

Mechanical stiffness matrix of an element e (dV represents the differential volume) is given as:

$$\mathbf{k}_{uu} = \iiint \mathbf{B}_u^t \mathbf{c}^E \mathbf{B}_u dV \quad (16)$$

Mass matrix of an element e is:

$$\mathbf{m}_{uu} = \iiint \rho N_u^t N_u dV \quad (17)$$

Mechanical damping matrix of an element e is:

$$\mathbf{c}_{uu} = \alpha \iiint \rho N_u^t N_u dV + \beta \iiint \mathbf{B}_u^t \mathbf{c}^E \mathbf{B}_u dV \quad (18)$$

Dielectric stiffness matrix of an element e is given as:

$$\mathbf{k}_{\phi\phi} = \iiint \mathbf{B}_\phi^t \boldsymbol{\varepsilon}^S \mathbf{B}_\phi dV \quad (19)$$

Piezoelectric coupling matrix of an element e is:

$$\mathbf{k}_{u\phi} = \iiint \mathbf{B}_u^t \mathbf{e}^t \mathbf{B}_\phi dV \quad (20)$$

The global governing equation for all piezoelectric elements can be assembled as:

$$\mathbf{M}_{uu} \ddot{\mathbf{u}} + \mathbf{D}_{uu} \dot{\mathbf{u}} + \mathbf{K}_{uu} \mathbf{u} + \mathbf{K}_{u\phi} \boldsymbol{\phi} = \mathbf{F} \quad (21)$$

$$\mathbf{K}_{u\phi}^t \mathbf{u} + \mathbf{K}_{\phi\phi} \boldsymbol{\phi} = \mathbf{Q} \quad (22)$$

where $\ddot{\mathbf{u}}, \dot{\mathbf{u}}, \mathbf{u}, \boldsymbol{\phi}$ are the global degrees of freedom at nodes. $\mathbf{M}_{uu}, \mathbf{D}_{uu}, \mathbf{K}_{uu}, \mathbf{K}_{u\phi}, \mathbf{K}_{\phi\phi}, \mathbf{F}, \mathbf{Q}$ are the globally assembled quantities for the mechanical mass matrix, the mechanical damping matrix, the mechanical stiffness matrix, the piezoelectric coupling matrix, the dielectric stiffness matrix, the external force, and the external point charge, respectively.

4.2.3.2. Simplified model

In general, complex interactions exist between the ECC specimen and the piezoelectric polymer with complex boundary conditions, making it difficult to model. Therefore, a simplified method needs to be developed for calculating the output voltage. The electrodes of a piezoelectric film are only installed in the plane perpendicular to the direction 3 (Figure 4-3), thus $D_1 = D_2 = 0$. When the piezoelectric film is used as a sensor to measure the mechanical strain for the output voltage, no external electric field is applied. Hence, the electric displacement D_3 in Eq. (10) can be simply obtained as

$$D_3 = d_{31}\sigma_1 + d_{32}\sigma_2 + d_{33}\sigma_3 \quad (23)$$

For the PVDF film, d_{32} is 10 times smaller than d_{31} or d_{33} , which can be discarded in Eq. (23) for calculating D_3 generated in the direction 3 [12]. Combined with geometric parameters of the piezoelectric film, Eq. (23) can be rewritten in Eq. (24) as the superposition of the two charge generation modes: mode 31 and mode 33 [13, 14].

$$q_3 = d_{31} F_1 l_p / t_p + d_{33} F_3 \quad (24)$$

where q_3 is the generated charge in the direction 3. F_1 is the axial force (i.e., in the direction 1) applied in the PVDF film. F_3 is the longitudinal force (i.e., in the direction 3) applied in the PVDF film. l_p , w_p , t_p are the length, width and thickness of the piezoelectric film, respectively.

As indicated in Figure 4-3, when an axial force is applied on the piezoelectric film along the direction 1, the voltage occurs in the two electrodes (i.e., the direction 3), which is generally called d_{31} -coupling mode (mode 31) for voltage generation. Similarly, d_{33} -coupling mode (mode 33) indicates that the voltage generated in the direction 3 is from the force applied in the direction 3.

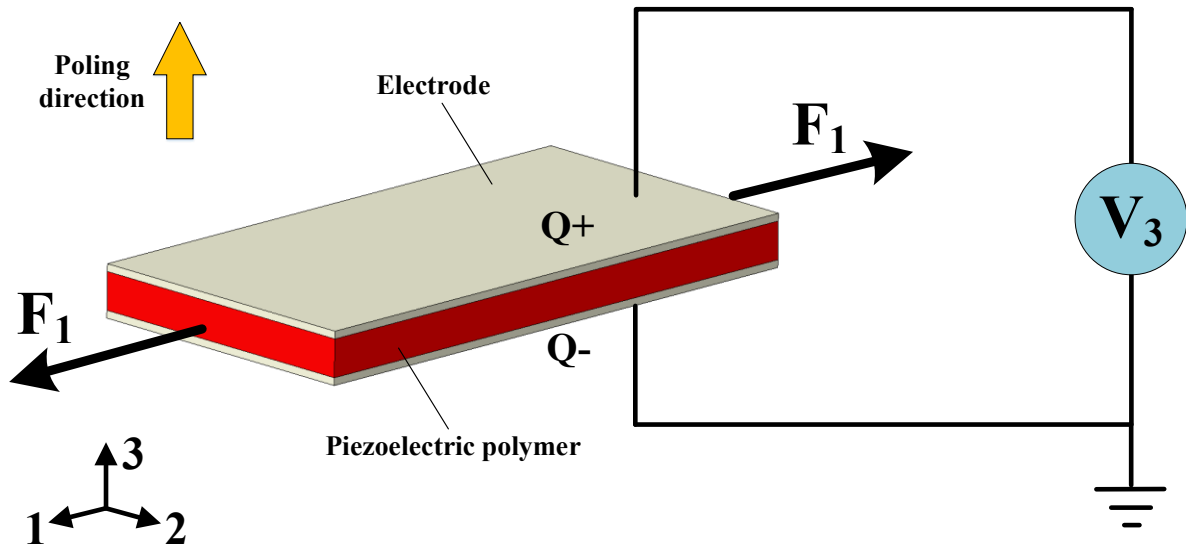


Figure 4-3 Schematic representation of a piezoelectric film with a d_{31} -coupling mode

Generally, a PVDF film has a very small thickness (micrometer range), and thus the ratio of l_p/t_p is on the order of 1000. Assuming the same mechanical energy input ($F_1 = F_3$), the charge generated in mode 31 is about 700 times greater than that in mode 33 (see Eq. (24)) [12]. For simplicity, the charge generated can be calculated with a d_{31} -coupling mode based on the axial strain of the piezoelectric film.

$$q_3 = d_{31}F_1l_p/t_p \quad (25)$$

As illustrated in Figure 4-3, the top and bottom surfaces of a piezoelectric film are electrodes with a vertical poling direction (i.e., direction 3). The electrode makes the corresponding surface of the piezoelectric film become an equipotential surface, which indicates that all nodes in the surface have the same electric potential. For the entire piezoelectric film, the FE-based piezoelectric model can be simplified to calculate its average strain. The average strain of the piezoelectric film can be calculated as [15]:

$$\varepsilon_{ave} = \frac{1}{V_{tol}} \sum_{j=1}^{N_{el}} \left[\frac{1}{N_{no}} \sum_{i=1}^{N_{no}} \varepsilon_i^j \right] \Delta V_j \quad (26)$$

where ε_i^j is the strain at node i belonging to the volume of element j located on a subvolume

of the piezoelectric film. N_{no} is the number of nodes which belong to the related element volume. ΔV_j is the volume of element j located on a subvolume of the piezoelectric film. N_{el} is the number of elements which belongs to the piezoelectric film. V_{tol} is the total volume of the piezoelectric film.

The voltage generated in d_{31} -coupling mode can be calculated by the piezoelectric strain constant d_{31} as indicated in Eqs. (27)-(28) [16]. Herein, the capacitance C_p of the piezoelectric film can be obtained as:

$$C_p = \frac{e_{33} l_p w_p}{t_p} \quad (27)$$

Where e_{33} is the 3rd-directional dielectric constant of the piezoelectric film.

Then, based on Eq. (25), the voltage generated can be determined as follows

$$V_p = \frac{d_{31} E_p l_p w_p}{C_p} \varepsilon_{ave} \quad (28)$$

where E_p is the Young's modulus of the piezoelectric film.

4.2.4. Flowchart of the energy harvesting model

The output voltage is used as an indicator of the harvesting energy from fiber reinforced cementitious materials. Figure 4-4 shows the schematical representation and flowchart of an energy harvesting model for evaluating the output voltage of PVA-ECC with surface-mounted PVDF, which includes the CDP model for mechanical analysis, the interaction between PVA-ECC specimen and PVDF, and the piezoelectric model of PVDF (including FEM and a simplified formula) for calculating the output voltage.

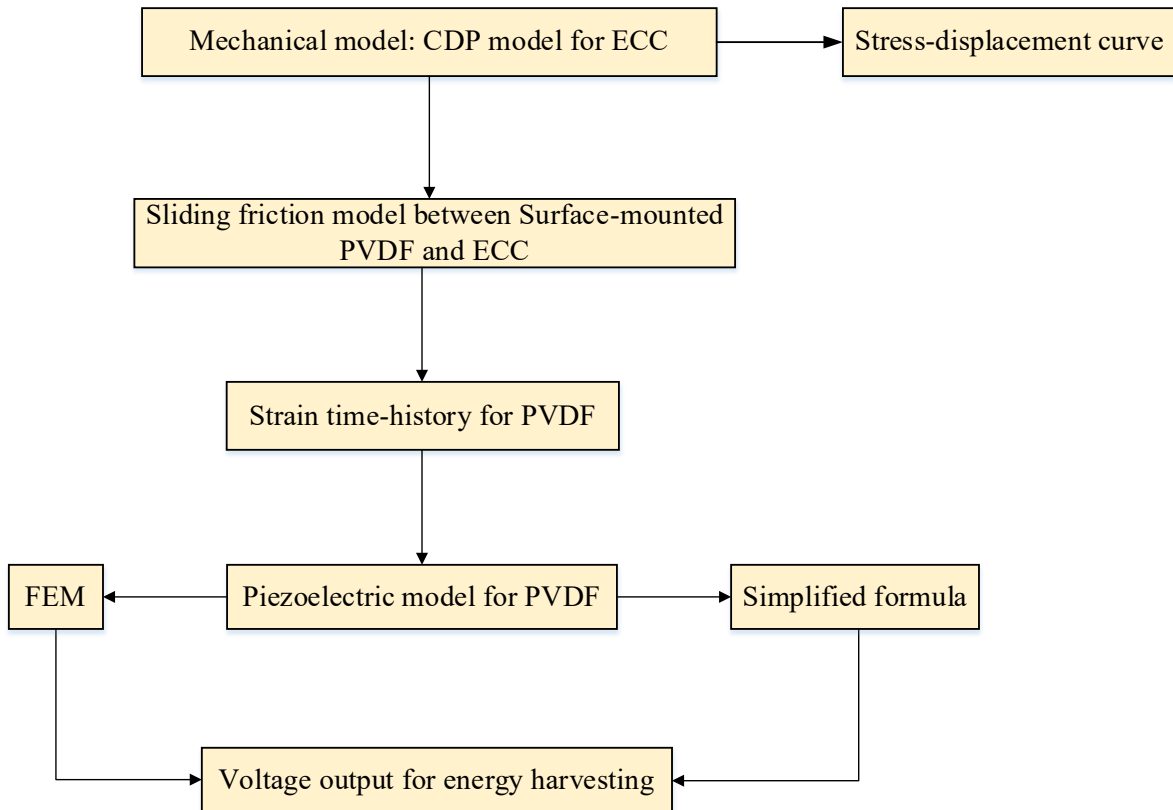


Figure 4-4 Flowchart of the energy harvesting model of ECC using surface-mounted PVDF

4.3. Model validation

4.3.1. Experiment setup

The energy harvesting model of fiber-reinforced cementitious materials with surface-mounted PVDF was further validated by using an energy harvesting results from the literature [17]. In the experiment, a four-point bending test was implemented to study the dynamic flexural behavior of ECC, as indicated in Figure 4-5. The ECC specimen has a load span of 50 mm (one third of the support span 150 mm). A PVDF film was externally bonded to the underside surface of the ECC specimen at the mid-span. Lead attachment of the PVDF film was accomplished using riveted lugs connected with 28 AWG wire. The PVDF film has an area of 73 mm x 16 mm with a thickness of 40 μm . As indicated by the manufacturer, the PVDF film is generally laminated to a 0.125 mm polyester substrate as a protective layer. This protective layer made of thin polyurethane can prevent surface oxidation of the silver ink electrode area [17, 18]. Thus, the total thickness of the PVDF film in the mechanical model is taken as 0.165 mm. Displacement control was adopted for the ECC specimen with three different loading rates of 0.5, 1.0, 2.0 mm/s. During the flexural test, a voltage data logger with the terminal board was used to simultaneously record the output voltage from the PVDF film per millisecond.

Table 4-1 gives the mixture proportions of ECC by relative weight in terms of cement. Herein Type I Ordinary Portland cement, class C fly ash, silica sand with the maximum particle size of 0.2 mm were used for ECC. PVA fiber has a diameter of 39 μm and a length of 8 mm. The complete mix design is given in Table 4-2.

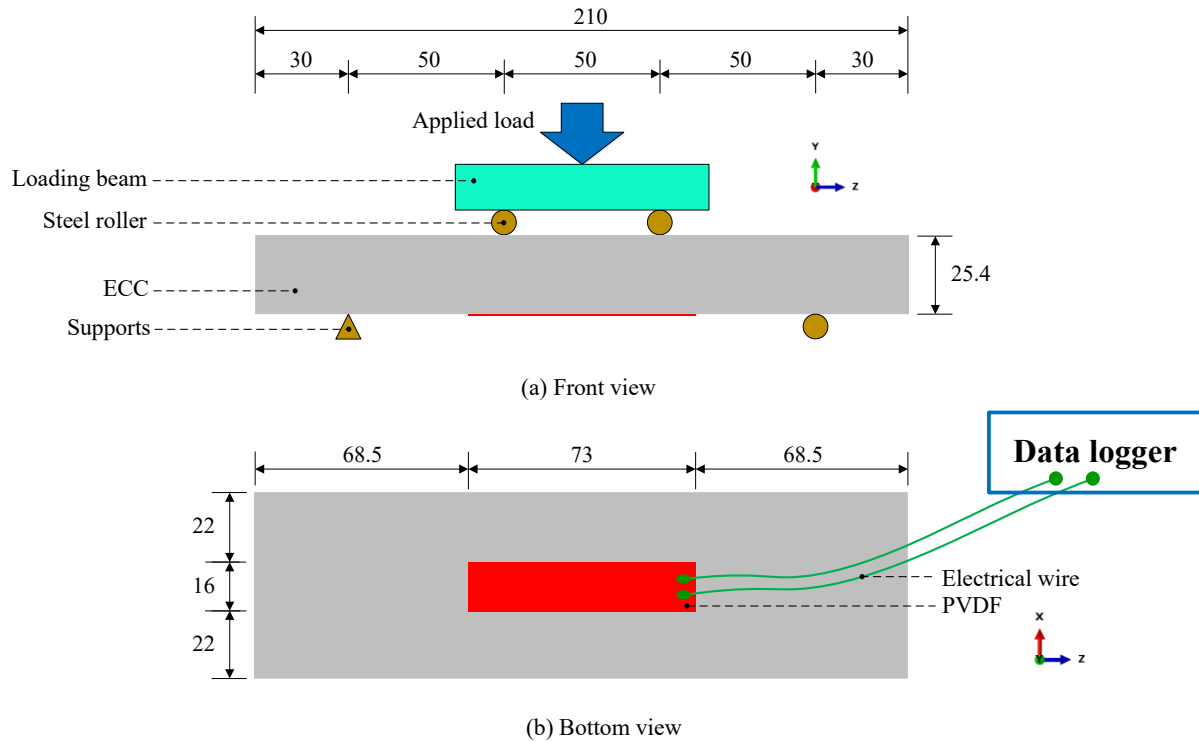


Figure 4-5 Experiment setup for 4-point bending test used for model validation (unit: mm)

4.3.2. Energy harvesting modelling

As shown in Figure 4-6(a), the ECC specimen has a size of 210 mm x 60 mm x 25.4 mm based on the actual geometry of the experimental setup. Dynamic velocity was applied on the top surfaces of the two steel bars located on the top surface of the specimen. Simply supported boundary conditions were adopted for the two steel bars located on the bottom surface of the specimen. To ensure continuous force transmission, tied constraints were used in the interactions between steel bar and ECC. The ECC specimen and steel bars are all meshed by C3D8R (the eight-node linear hexahedral solid element with reduced integration) in Abaqus. The CDP model parameters for ECC [5, 17, 19] are listed in Table 4-3. ρ_{ECC} refers to the density of ECC. ν_{ECC} refers to Poisson's ratio of ECC. For small strains, however, the material of the PVDF film is considered mechanically isotropic [16]. The elastic modulus, Poisson's ratio of steel are 198.0 GPa and 0.3, respectively. The steel density is taken as 7900 kg/m³.

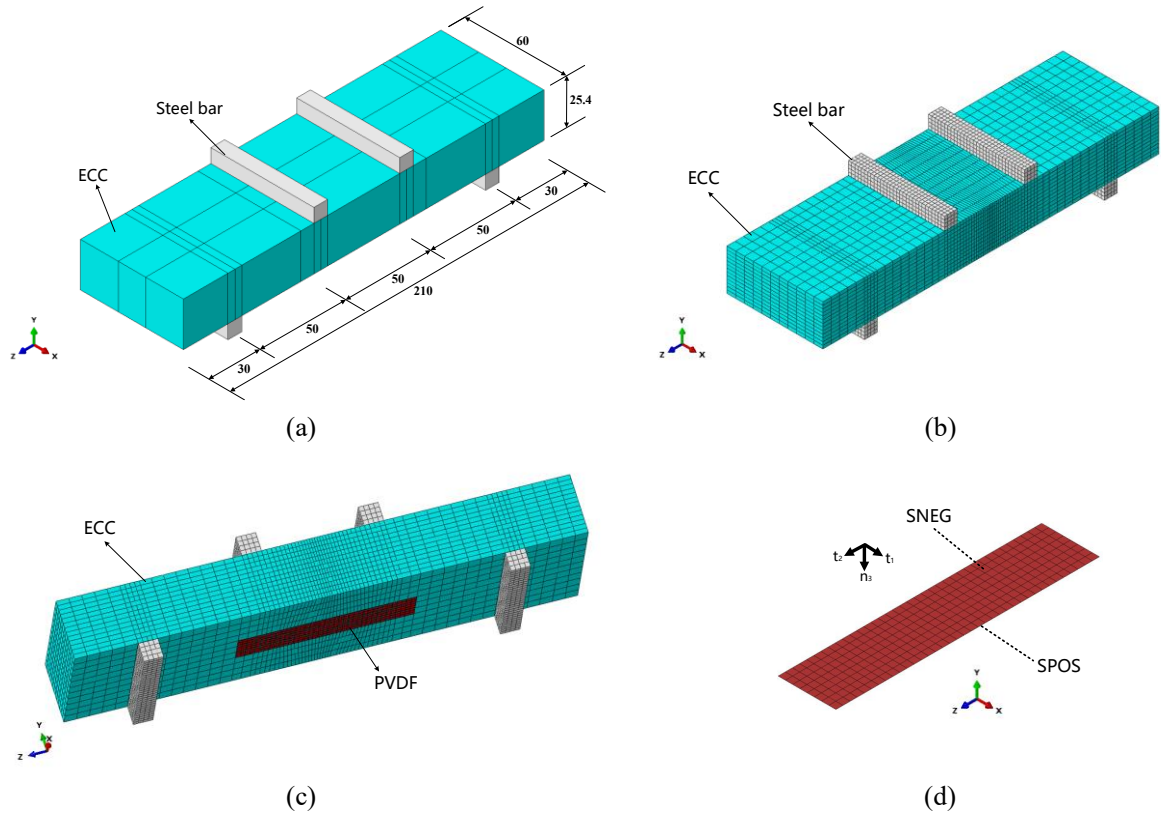


Figure 4-6 Mechanical model of bendable PVA-ECC with surface-mounted PVDF, (a) model configuration (unit: mm), (b) model meshing, (c) location of the PVDF film attached, (d) shell element for PVDF film.

Table 4-1 Mixture proportions (by relative weight in terms of cement) [17].

Type	Cement	Fly ash	Silica sand	water	Superplasticizer	PVA Fiber (by volume)
PVA-ECC	1.0	1.2	0.8	0.5	0.008	2.0%

Table 4-2 Material properties of PVA fiber [17].

Type	Diameter (μm)	Length (mm)	Tensile Strength (MPa)	Elastic Modulus (GPa)	Specific Gravity
RECS-15	39	8	1600	41	1.3

Table 4-3 CDP model parameters for PVA-ECC.

ρ_{ECC} (kg/m^3)	E_0 (GPa)	ν_{ECC}	$\sigma_{b0} / \sigma_{c0}$	K_c	ψ	\mathcal{E}_{ec}	Viscosity Parameter
1870	28	0.2	1.16	0.667	35	0.1	0.001

The stress-strain relationship of the ECC under compression and tension in CDP model were taken based on its experimental results of uniaxial compression and tension tests from the literature [4, 5, 20]. In Figure 4-7 and Table 4-5, Case 1 corresponds to a loading rate of 0.5 mm/s, Case 2 to 1.0 mm/s, and Case 3 to 2.0 mm/s. As known, the 4-point bending test of ECC is mainly governed by the tensile behavior of the material model. Thus, the compressive behavior parameters are taken based on the experimental values for all cases. The tensile

behavior parameters are obtained by several iterations to get a best fitting of the experimental stress–displacement curve using the numerical model. The energy harvesting model specifically targets the pre-peak stress-displacement curve, excluding the portion after the peak stress where failure occurs, as this segment is crucial for practical engineering applications. This is because that the damage generally occurs after the peak point of the flexural stress (i.e., the softening range) [21, 22], leading to subsequent failure and rendering energy harvesting unsustainable. For the material parameters of CDP model in ECC, compressive behavior parameters are listed in Table 4-4, and tensile behavior parameters in Table 4-5. During a tensile test, it is calculated by subtracting the elastic strain corresponding to the undamaged material from the total strain. In plain concrete, cracking usually occurs after the first inflection point, indicating the completion of the elastic phase and the transition into the softening phase accompanied by damage. The damping effect has not been considered since the loading rates are low. Mesh size dependence analysis has been performed to determine the optimized mesh, which ensures the accuracy and reliability of the model while reducing computational cost. Due to complex links of constraints and interactions in the model, double-precision analysis for Abaqus/Explicit was adopted to ensure the desired accuracy of the solution.

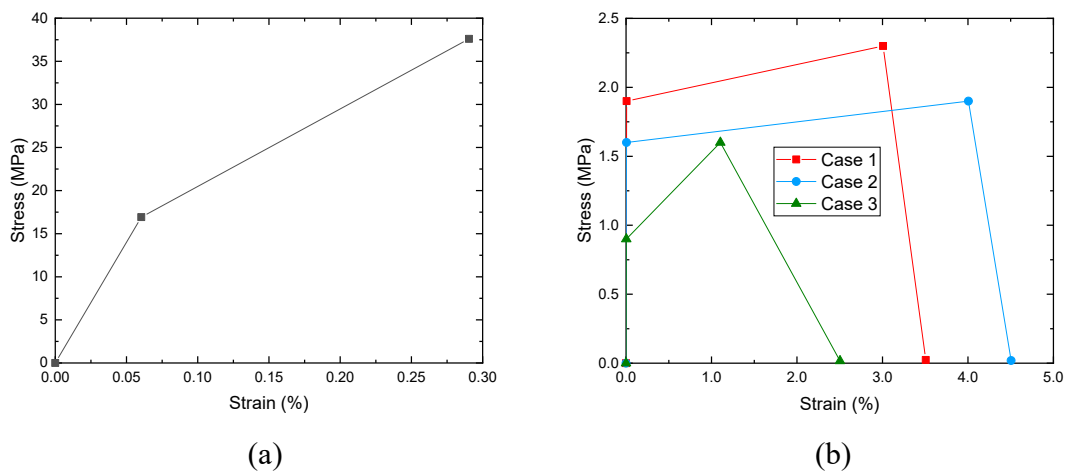


Figure 4-7 Stress-strain relationship of the ECC, (a) under uniaxial compression, (b) under uniaxial tension.

Table 4-4 Compressive behavior parameters

Yield stress (MPa)	Inelastic strain (%)
16.92	0
37.6	0.23

Table 4-5 Tensile behavior parameters

Case 1		Case 2		Case 3	
Yield stress (MPa)	Cracking strain (%)	Yield stress (MPa)	Cracking strain (%)	Yield stress (MPa)	Cracking strain (%)
1.9	0	1.6	0	0.9	0
2.3	3.0	1.9	4.0	1.6	1.1
0.023	3.5	0.019	4.5	0.016	2.5

Generally, the thickness of a PVDF film is a range of 20-40 μm , which is much thinner than its length and width. If the PVDF film is modeled by solid elements with a very small size to consider its thickness, it enforces the entire simulation to run using a very small integration time increment, which inevitably results in very fine meshes and correspondingly prohibitive analysis time. Instead, the PVDF film can be simulated by using shell elements due to its small thickness and linear-elastic deformation (see [Figure 4-6\(d\)](#)). The shell element in Abaqus adopted the local coordinate system with two tangential directions of t_1, t_2 (corresponding to positive x, z direction in the global coordinate system) and the normal direction of n_3 (corresponding to negative y direction in the global coordinate system). SNEG refers to the face of the PVDF film that is in contact with the ECC specimen. SPOS refers to the other side of the PVDF film that is not in contact with the ECC specimen. The strain in these two faces was included to calculate the average strain of the PVDF film since the shell element has several integration points along the thickness. Surface interaction was used between PVDF and the bottom surface of the ECC specimen. Hard contact was adopted to minimize the overclosure of PVDF and the bottom surface of the ECC specimen. Moreover, no separation relationship was used to prevent the two surfaces from separating in the normal direction after contact. In the tangential direction, sliding friction with a friction coefficient was adopted for simulating the relative slip behavior of the ECC specimen and the PVDF film. The value of the tangential sliding friction coefficient was influenced by factors such as the contact materials (specifically, PVDF film and ECC), their bonding conditions and contact pressure under different loading rates. The tangential sliding friction coefficient in the energy harvesting model was determined by comparison with experiment results regarding the output voltage. In the simulation, the sliding friction coefficients between the PVDF film and the specimen under loading rates of 0.5 mm/s, 1.0 mm/s and 2.0 mm/s are 0.005, 0.0063, 0.065, respectively.

[Figure 4-8\(a\)](#) gives the configuration of a PVDF film with a length of l_p , a width of w_p and a height of h_p . The piezoelectric film is bonded to the bottom surface of the ECC specimen in the pure moment segment. Thus, the small bending behavior of the piezoelectric film is mainly controlled by the axial strain in the length direction (the direction 1), especially when the deflection at the mid-point is not so much. The average axial strain of the PVDF film obtained from the mechanical model was imposed on one end of the film by an average axial displacement loading, which can be obtained by the product of the length and the axial strain of the film ([Eq. \(29\)](#)). The other end of the film is fixed.

$$u_{ave}(t) = l_p \varepsilon_{ave}(t) \quad (29)$$

An 8-node linear piezoelectric brick element C3D8E in ABAQUS was adopted to simulate the piezoelectric effect of the PVDF film induced by the bending ECC. The element has both the mechanical degrees of freedom (displacements) and electrical degrees of freedom (electric potential), which can be calculated simultaneously. As shown in [Figure 4-8\(b\)](#), the 3-axis (i.e., the thickness direction) was set as the poling direction in the finite element (FE) model for piezoelectric simulation. The bottom surface of the PVDF film was set as the ground electrode (i.e., zero potential). The top surface of the PVDF film was set as an equipotential surface, which indicates that all nodes in this surface have the same electric potential of V_{top} . Herein, constraint equations were used to ensure that all nodes in a surface have the same electric potential. An implicit dynamic analysis was utilized to calculate the real-time voltage output generated from the PVDF film due to the piezoelectric effects. In experiments in literature [\[17\]](#), the Voltage data logger (ADC-20) was used to record open circuit voltage. Correspondingly,

the piezoelectric model was utilized for calculating the open circuit voltage. In the piezoelectric FE model, the PVDF film has an area of 73 mm x 16 mm ($l_p \times w_p$) with a thickness of 40 μm (h_p). Herein, only the thickness of 40 μm can generate an electrical potential. The PVDF film was assigned with typical piezoelectric and mechanical properties of PVDF obtained from the literature [17, 18, 23, 24], as outlined in Table 4-6. Wherein ρ_e is the density of PVDF. g_{31} , g_{33} are the piezoelectric voltage constants of PVDF. f_{eu} is the yield strength of PVDF. k_{31} is the electromechanical coupling factor of PVDF. P_e is the pyroelectric coefficient. ν_p is the Poisson's ratio. For small strains, however, the material of the PVDF film is considered mechanically isotropic [16].

Table 4-6 Piezoelectric and mechanical properties of PVDF

Material properties	Value	Units	Material properties	Value	Units
ρ_e	1780	kg/m ³	E_e	2	GPa
ν_p	0.34	-	f_{eu}	45–55	MPa
d_{31}	23	pC/N	d_{32}	1.476	pC/N
d_{33}	-33.8	pC/N	d_{15}	20	pC/N
e_{33}	$1.15e^{-10}$	F/m	g_{31}	$216 e^{-3}$	m ² /C
g_{33}	$-330e^{-3}$	m ² /C	k_{31}	12%	-
P_e	30	C/m ² · K			

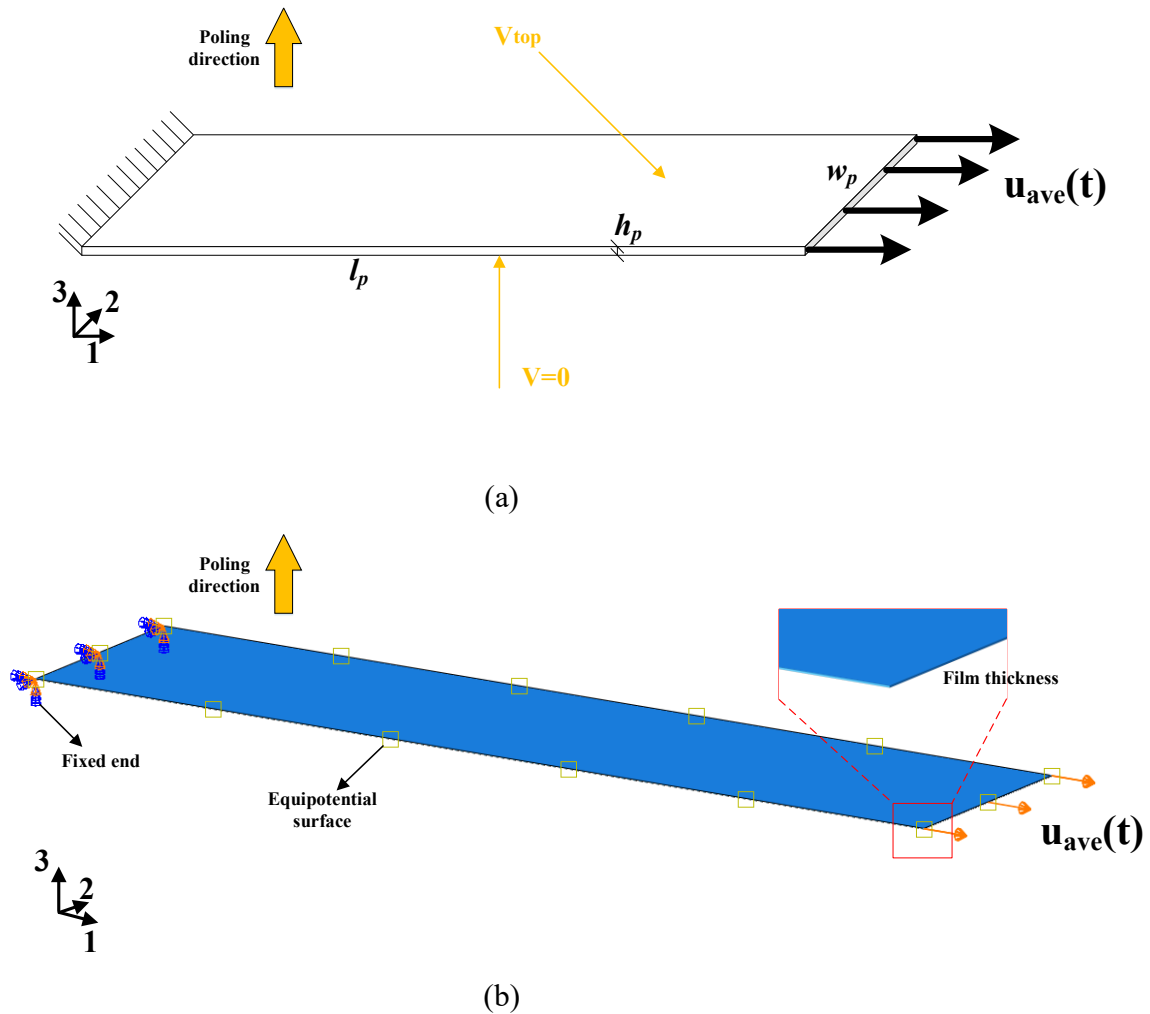
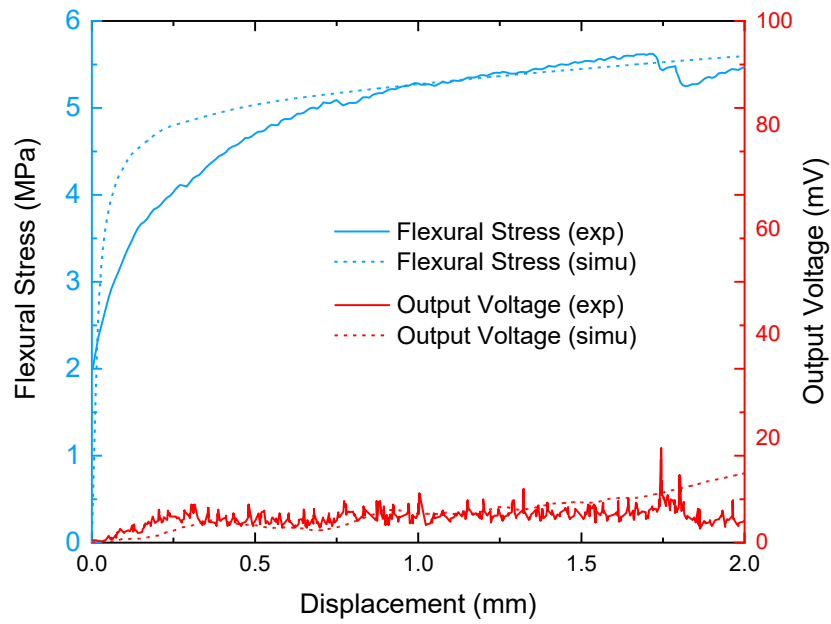


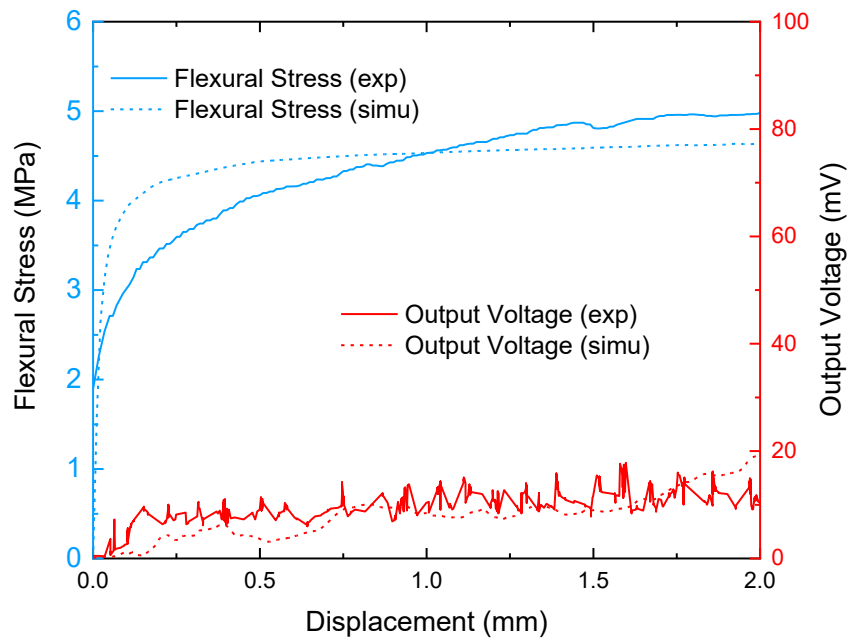
Figure 4-8 Piezoelectric model for the PVDF film, (a) the PVDF film applied by the average axial displacement, (b) FEM model based on piezoelectric elements.

4.3.3. Results and discussion

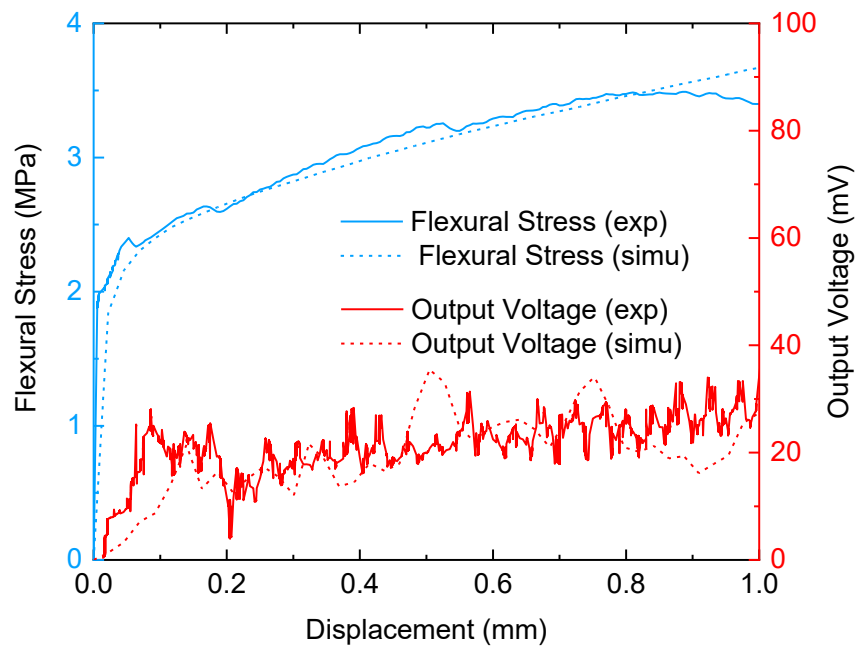
As shown in Figure 4-9, the simulated results from the simplified method are in good agreement with experimental data [17]. The flexural stress–displacement curve refers to the left y-axis, and the output voltage–displacement curve refers to the right y-axis. Herein, the midpoint displacement of the bottom surface of the specimen was considered. It is found that, under different loading rates, the flexural stress increases quickly with the increase of the midpoint displacement in the initial stage. Correspondingly, the output voltage also shows a rapid increase with the increase of the displacement during the initial stage. This is because that the specimen is initially loaded in the elastic and rapid strain-hardening range, which provides a rapid strain increment to generate a higher voltage increment. Then, when it enters the later plastic stage with a slow strain-hardening, the stress shows a relatively slow increase with the displacement increase. Accordingly, the output voltage slowly increases with the displacement increase during the later plastic stage.



(a) 0.5mm/s loading rate



(b) 1.0mm/s loading rate



(c) 2.0mm/s loading rate

Figure 4-9 Comparisons of the flexural stress and output voltage versus mid-point displacement between experimental data [17] and simulated results under different loading rates.

As seen in Figure 4-9, it is found that the output voltage increases as the loading rate increases. The simulated and experimental results for average output voltages at loading rates of 0.5 mm/s, 1.0 mm/s, and 2.0 mm/s are close. The simulated values are around 5.69 mV, 8.05 mV, and 19.58 mV, respectively, while the experimental values are 6.01 mV, 10.59 mV, and 21.24 mV. This agreement between the simulated voltage and experimented data indicates that the developed model is able to calculate the effects of dynamic loading rates on the flexural stress and corresponding output voltage. The slight discrepancies observed at the initial loading stage are likely due to surface irregularities and microcracks that formed on the bottom surface of the experimental specimens, leading to a faster initial voltage response. In contrast, the numerical model assumes a smooth, crack-free surface and no crack formation within the elastic stage, resulting in a more gradual increase in simulated voltage at the onset of loading. As indicated in Eq. (28), the output voltage generated by the PVDF film is linearly associated with the axial strain applied on the film. According to the manufacturer, more than 10 mV can be generated by the PVDF per micro strain [17]. In the model, the axial strain of the PVDF film is extracted under different loading rates, as shown in Figure 4-10. Wherein the displacement also indicates the mid-point displacement as in Figure 4-9 for different loading rates. ε_{ave} refers to the axial average strain of the PVDF film. It can be found that the axial average strain of the PVDF film exhibits a comparable relationship to the output voltage concerning mid-point displacement. Similar to the output voltage, the axial strain of the film was higher under 2.0 mm/s loading rate and decreases with the decrease of the loading rate.

The axial strain of the film under 1.0 mm/s loading rate is relatively close to that under 0.5 mm/s loading rate since the low loading rates of 0.5 mm/s and 1.0 mm/s are close to quasi-static loading. As indicated in this model, the axial strain of the film is significantly influenced by the sliding friction coefficient between the film and the specimen. Accordingly, the sliding friction coefficient under 1.0 mm/s loading rate is 0.0063, which is slightly larger than 0.005 under 0.5 mm/s loading rate. The sliding friction coefficient under 2.0 mm/s loading rate is 0.065, which is ten times higher than that under 1.0 mm/s loading rate or 0.05 mm/s loading rate. This friction-induced voltage mechanism in this model reveals that a higher loading rate causes more frictional contact between the PVDF film and the ECC specimen due to inertia forces arising from dynamic effects, which results in a higher axial strain of the film to generate more output voltage.

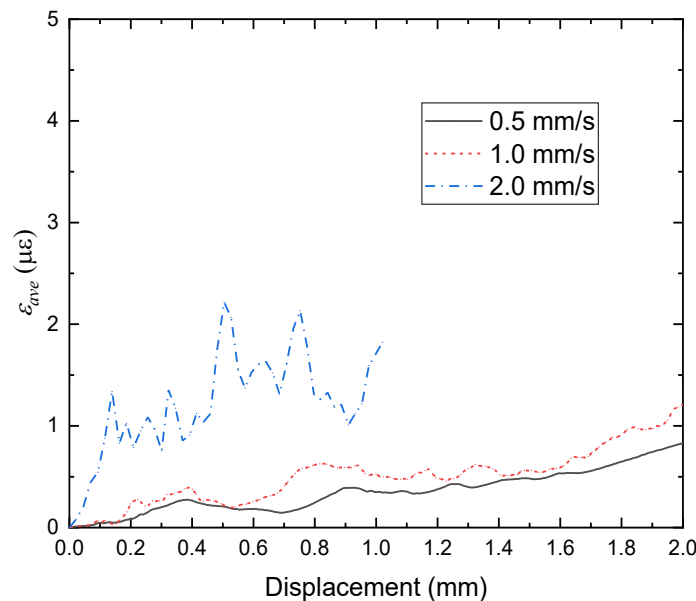


Figure 4-10 Comparisons of the axial average strain versus mid-point displacement under different loading rates.

In the FEM-based piezoelectric model, the axial strain of the film is applied to the film as the time-history loading. In the FEM, the dielectric constants and the mechanical properties of the PVDF film are considered to be isotropic. Damping was not considered since loading rates were low. Dielectric loss was not considered due to the very short loading time and constant loading rates without frequency [25]. Compared to the simplified method, the FEM considers the inertia force due to mass, and d_{32} , d_{33} during the dynamic analysis. Figure 4-11 gives a comparison of the simulated voltage results between FEM and simplified method under different loading rates.

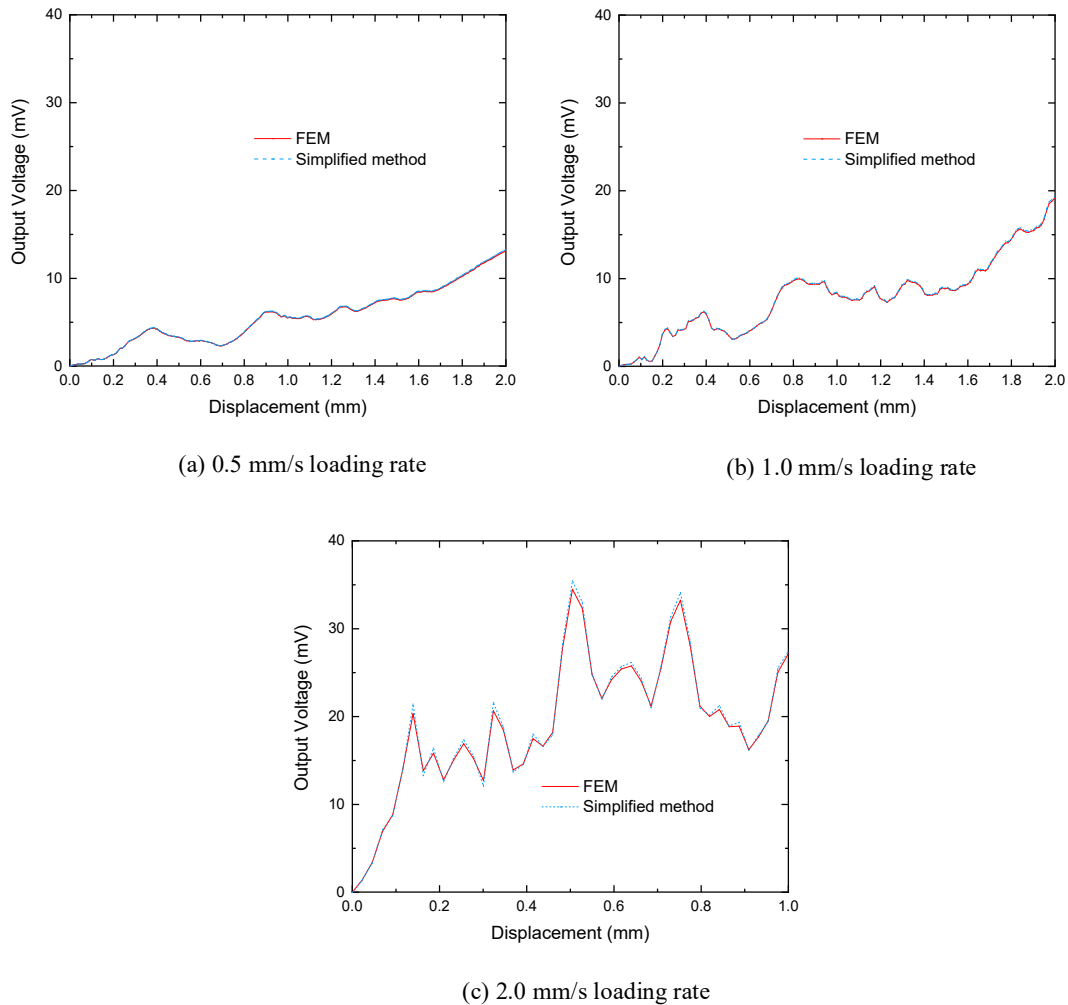


Figure 4-11 Comparisons of the output voltage versus mid-point displacement between FEM and simplified method under different loading rates.

As shown in Figure 4-11, there is a good agreement between the FEM and simplified method. Nonetheless, there remains a very small difference between the two results when the loading rate increases from 0.5 mm/s to 2.0 mm/s. This is because the FEM considers the mass of the PVDF film to consider inertial force, and the kinetic energy also increases with the increase of loading rate, both of which are not considered by the simplified method. The small difference reveals that the PVDF film mass is very small, which has a minor influence on its output voltage in the FEM. The output voltage is mainly from the strain energy of the film during its mechanical deformation. Although damping effects on the piezoelectric simulation are not considered since loading rates were low, the FE model is able to consider it, while the simplified method is not. Figure 4-12 also gives voltage distributions of the PVDF film in FEM under different loading rates of 0.5 mm/s, 1.0 mm/s, 2.0 mm/s, when the corresponding mid-point displacements reach 2.0 mm, 2.0 mm, 1.0 mm, respectively. The unit in the legend of Figure 4-12 is volt. As the ground electrode, the electric potential on the bottom surface was 0 volt. It can be found that the voltages distribute along the film thickness direction with an electric field strength. The electric potential on the top surface increases as the loading rate increases. They are 13.20 mV, 19.10 mV, 28.77mV under different loading rates of 0.5 mm/s, 1.0 mm/s, 2.0

mm/s, respectively, when corresponding ECC specimens reach near their peak stresses.

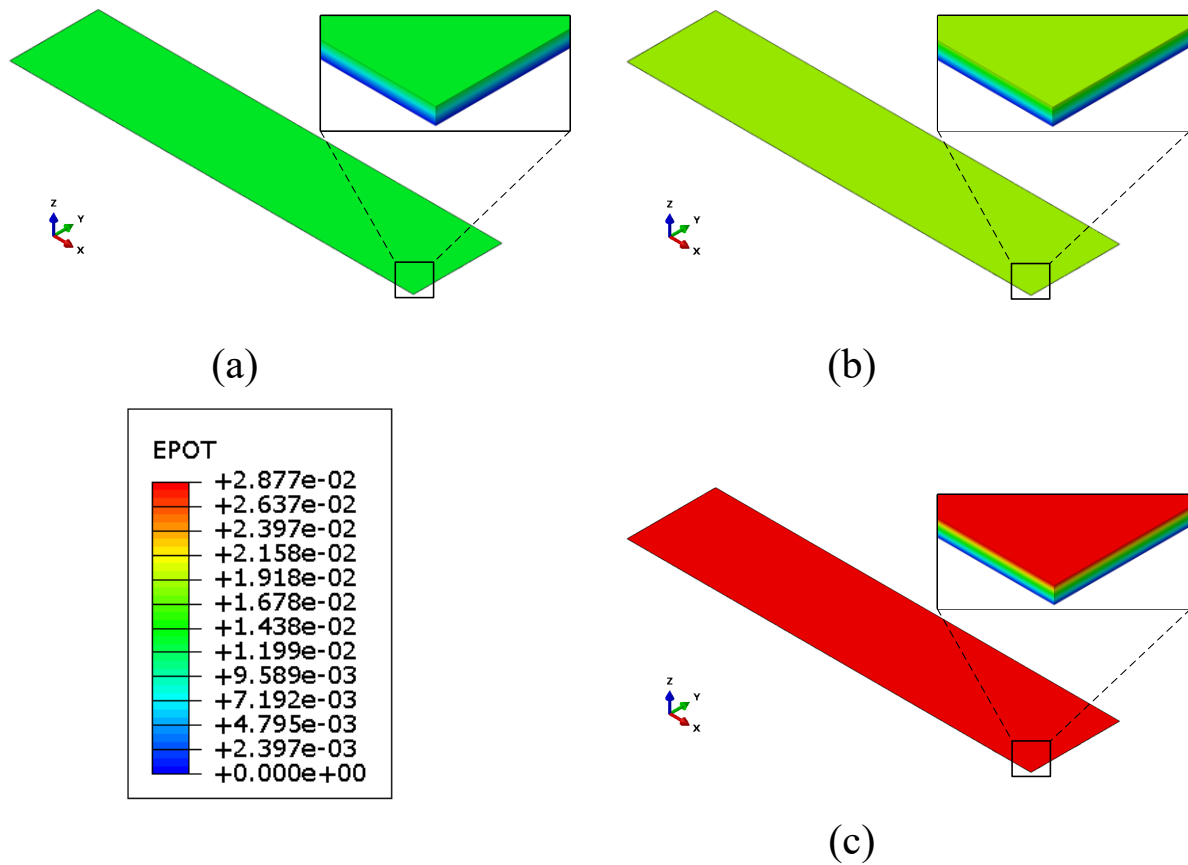


Figure 4-12 Voltage distribution of the PVDF film under 0.5 mm/s loading rate (a), 1.0 mm/s loading rate (b), and 2.0 mm/s loading rate (c).

4.4. CONCLUSIONS

In this chapter, a theoretical energy harvesting model has been developed for calculating the output voltage of fiber-reinforced cementitious materials incorporating surface-mounted piezoelectric films. Several important conclusions can be drawn as follows

- In the mechanical model, the dynamic flexural behavior of ECC was simulated by the CDP model. The surface-mounted PVDF film was simplified as a shell element to reduce computation cost while keep calculation accuracy. The force transfer between ECC and PVDF due to the bond layer was simulated by a sliding friction model. The good agreement between simulation results and experimental data in literature proves the accuracy and reliability of the proposed model.
- In the piezoelectric simulation, both FEM and simplified formulas were used to calculate the output voltage from the PVDF film, and the two results correspond to each other. Compared to simplified formulas, FEM can be used in complex stress states with consideration of mass, damping, and material heterogeneity for mechanical and piezoelectric parameters.
- In the PVDF-ECC energy harvesting system, the output voltage generated increases with the increase of the dynamic loading rate. This is because a greater dynamic loading

rate enhances the interaction between the PVDF and the ECC specimen, which results in a higher friction coefficient between the two. Thus, a higher axial strain is transferred to the PVDF film to generate a higher output voltage.

This newly proposed model considers a series of energy harvesting parameters, including dynamic loading rates, PVA-ECC mechanical properties, interaction between PVA-ECC and PVDF, geometry and material properties of PVDF. The theoretical model developed in this study can be of great use in the design for harvesting energy from fiber-reinforced cementitious materials incorporating surface-mounted piezoelectric films. This theoretical model can be also considered as a benchmark model to simulate the energy harvesting process of ACCCs in the following chapters.

REFERENCES

- [1] R. Faria, J. Oliver, M. Cervera, A strain-based plastic viscous-damage model for massive concrete structures, *International Journal of Solids and Structures*, 35 (1998) 1533-1558. [https://doi.org/10.1016/S0020-7683\(97\)00119-4](https://doi.org/10.1016/S0020-7683(97)00119-4).
- [2] J.Y. Wu, J. Li, R. Faria, An energy release rate-based plastic-damage model for concrete, *International Journal of Solids and Structures*, 43 (2006) 583-612. <https://doi.org/10.1016/j.ijsolstr.2005.05.038>.
- [3] D.-C. Feng, X.-D. Ren, J. Li, Softened Damage-Plasticity Model for Analysis of Cracked Reinforced Concrete Structures, *Journal of Structural Engineering*, 144 (2018) 04018044. [https://doi.org/10.1061/\(ASCE\)ST.1943-541X.0002015](https://doi.org/10.1061/(ASCE)ST.1943-541X.0002015).
- [4] J. Zhou, J. Pan, C.K.Y. Leung, Mechanical Behavior of Fiber-Reinforced Engineered Cementitious Composites in Uniaxial Compression, *Journal of Materials in Civil Engineering*, 27 (2015) 04014111. 10.1061/(ASCE)MT.1943-5533.0001034.
- [5] D. Meng, T. Huang, Y.X. Zhang, C.K. Lee, Mechanical behavior of a polyvinyl alcohol fibre reinforced engineered cementitious composite (PVA-ECC) using local ingredients, *Construction and Building Materials*, 141 (2017) 259-270. <https://doi.org/10.1016/j.conbuildmat.2017.02.158>.
- [6] T. Jothi Saravanan, S. Singh Chauhan, Study on pre-damage diagnosis and analysis of adhesively bonded smart PZT sensors using EMI technique, *Measurement*, 188 (2022) 110411. <https://doi.org/10.1016/j.measurement.2021.110411>.
- [7] B.-P. Nguyen, Q.H. Tran, T.-T. Nguyen, A.M.S. Pradhan, T.-C. Huynh, Understanding Impedance Response Characteristics of a Piezoelectric-Based Smart Interface Subjected to Functional Degradations, *Complexity*, 2021 (2021) 5728679. 10.1155/2021/5728679.
- [8] W. Yan, W.Q. Chen, Structural Health Monitoring Using High-Frequency Electromechanical Impedance Signatures, *Advances in Civil Engineering*, 2010 (2010) 429148. <https://doi.org/10.1155/2010/429148>.
- [9] S. Bhalla, C.K. Soh, Electromechanical Impedance Modeling for Adhesively Bonded Piezo-Transducers, *Journal of Intelligent Material Systems and Structures*, 15 (2004) 955-972. 10.1177/1045389X04046309.
- [10] Y.Y. Lim, K.Z. Kwong, W.Y.H. Liew, R.V. Padilla, C.K. Soh, Parametric study and modeling of PZT based wave propagation technique related to practical issues in monitoring of concrete curing, *Construction and Building Materials*, 176 (2018) 519-530. <https://doi.org/10.1016/j.conbuildmat.2018.05.074>.

- [11] IEEE Standard on Piezoelectricity, in: ANSI/IEEE Standard 176-1987, Institute of Electrical and Electronics Engineers Inc., 1988.
- [12] L. Mateu, F. Moll, Optimum Piezoelectric Bending Beam Structures for Energy Harvesting using Shoe Inserts, *Journal of Intelligent Material Systems and Structures*, 16 (2005) 835-845. <https://doi.org/10.1177/1045389X05055280>.
- [13] H.J. Jung, H. Jabbar, Y. Song, T.H. Sung, Hybrid-type (d33 and d31) impact-based piezoelectric hydroelectric energy harvester for watt-level electrical devices, *Sensors and Actuators A: Physical*, 245 (2016) 40-48. <https://doi.org/10.1016/j.sna.2016.04.013>.
- [14] S.R. Anton, H.A. Sodano, A review of power harvesting using piezoelectric materials (2003–2006), *Smart Materials and Structures*, 16 (2007) R1-R21. 10.1088/0964-1726/16/3/r01.
- [15] R. Lerch, Simulation of piezoelectric devices by two- and three-dimensional finite elements, *IEEE Transactions on Ultrasonics, Ferroelectrics, and Frequency Control*, 37 (1990) 233-247. 10.1109/58.55314.
- [16] J. Sirohi, I. Chopra, Fundamental Understanding of Piezoelectric Strain Sensors, *Journal of Intelligent Material Systems and Structures*, 11 (2000) 246-257. 10.1106/8BFB-GC8P-XQ47-YCQ0.
- [17] Y.-F. Su, R.R. Kotian, N. Lu, Energy harvesting potential of bendable concrete using polymer based piezoelectric generator, *Composites Part B: Engineering*, 153 (2018) 124-129. <https://doi.org/10.1016/j.compositesb.2018.07.018>.
- [18] J.W. Sohn, J. Jeon, S.B. Choi, An Investigation on Dynamic Signals of MFC and PVDF Sensors: Experimental Work, *ADVANCES IN MECHANICAL ENGINEERING*, (2013) <https://doi.org/10.1155/2013/420345>.
- [19] Y. Xu, E. Schlangen, M. Luković, B. Šavija, Tunable mechanical behavior of auxetic cementitious cellular composites (CCCs): Experiments and simulations, *Construction and Building Materials*, 266 (2021) 121388. <https://doi.org/10.1016/j.conbuildmat.2020.121388>.
- [20] G.A. Arce, H. Noorvand, M.M. Hassan, T. Rupnow, N. Dhakal, Feasibility of low fiber content PVA-ECC for jointless pavement application, *Construction and Building Materials*, 268 (2021) 121131. <https://doi.org/10.1016/j.conbuildmat.2020.121131>.
- [21] J. Lubliner, J. Oliver, S. Oller, E. Oñate, A plastic-damage model for concrete, *International Journal of Solids and Structures*, 25 (1989) 299-326. [https://doi.org/10.1016/0020-7683\(89\)90050-4](https://doi.org/10.1016/0020-7683(89)90050-4).
- [22] J. Wang, A.P. Jivkov, Q.M. Li, D.L. Engelberg, Experimental and numerical investigation of mortar and ITZ parameters in meso-scale models of concrete, *Theoretical and Applied Fracture Mechanics*, 109 (2020) 102722. <https://doi.org/10.1016/j.tafmec.2020.102722>.
- [23] M. Derakhshani, N. Momenzadeh, T.A. Berfield, Analytical and experimental study of a clamped-clamped, bistable buckled beam low-frequency PVDF vibration energy harvester, *Journal of Sound and Vibration*, 497 (2021) 115937. <https://doi.org/10.1016/j.jsv.2021.115937>.
- [24] A. Roy Chowdhury, N. Saurabh, R. Kiran, S. Patel, Effect of porous auxetic structures on low-frequency piezoelectric energy harvesting systems: a finite element study, *Applied Physics A*, 128 (2021) 62. 10.1007/s00339-021-05199-w.
- [25] P. Li, W. Jiang, R. Lu, D. Yuan, J. Shan, J. Xiao, Design and durability of PZT/PVDF composites based on pavement perception, *Construction and Building Materials*, 323 (2022) 126621. <https://doi.org/10.1016/j.conbuildmat.2022.126621>.

5

ELLIPTICAL-SHAPED ACCC ENERGY HARVESTER

—MODELLING

The auxetic cementitious cellular composites energy harvester demonstrated its ability to generate electrical energy during energy harvesting experiments. However, this process involves a complex electromechanical interaction between the ACCCs and the surface-mounted PVDF. After pre-compression, ACCCs exhibit elastomer-like behavior, showing recoverable deformation during cyclic loading. The hinge-like strain in the ligament of ACCCs can be transferred to the bonded PVDF, producing a voltage output for energy harvesting. This hinge-like strain is influenced by the geometry of the pre-compressed ACCCs, which includes elastic-plastic deformation and the pre-compression damage evolution of fiber-reinforced cementitious materials. The deformed ACCCs after pre-compression further display second elasticity behavior due to fiber bridging. In this chapter, an energy harvesting model was developed to simulate the energy harvesting process of the ACCC energy harvester, incorporating both the mechanical and electrical aspects. This model extends the general computational framework established in Chapter 4 for cementitious materials with surface-mounted PVDF by integrating the specific mechanical deformation behavior of ACCCs and the corresponding electrical response of the PVDF film. Model validation was carried out using experimental results previously presented in Chapter 3, demonstrating good agreement between the simulated and measured outputs.

5.1 INTRODUCTION

In Chapter 3, a novel piezoelectric energy harvester with ACCCs and surface-mounted PVDF film based on strain-induced piezoelectric mechanisms has been designed, fabricated, and experimentally tested. The ACCC-PVDF energy harvesting system was first compressed to a predetermined displacement and then subjected to cyclic loading for generating voltage. The output voltages of the energy harvester under different loading amplitudes and frequencies were further investigated. This chapter develops a numerical model to simulate the energy harvesting process of the ACCC energy harvester, providing insights into the mechanical and electrical mechanisms behind experimental observations. It also provides a numerical prediction of the energy harvesting potential of cementitious materials with complex geometries. Additionally, the model can capture the effects of mechanical and electrical parameters on energy harvesting, enabling optimization of the design for future applications. The model builds upon the general framework introduced in Chapter 4 for cementitious materials with surface-mounted PVDF. It is further refined by incorporating the distinct mechanical deformation characteristics of ACCCs and the resulting electrical response of the PVDF film.

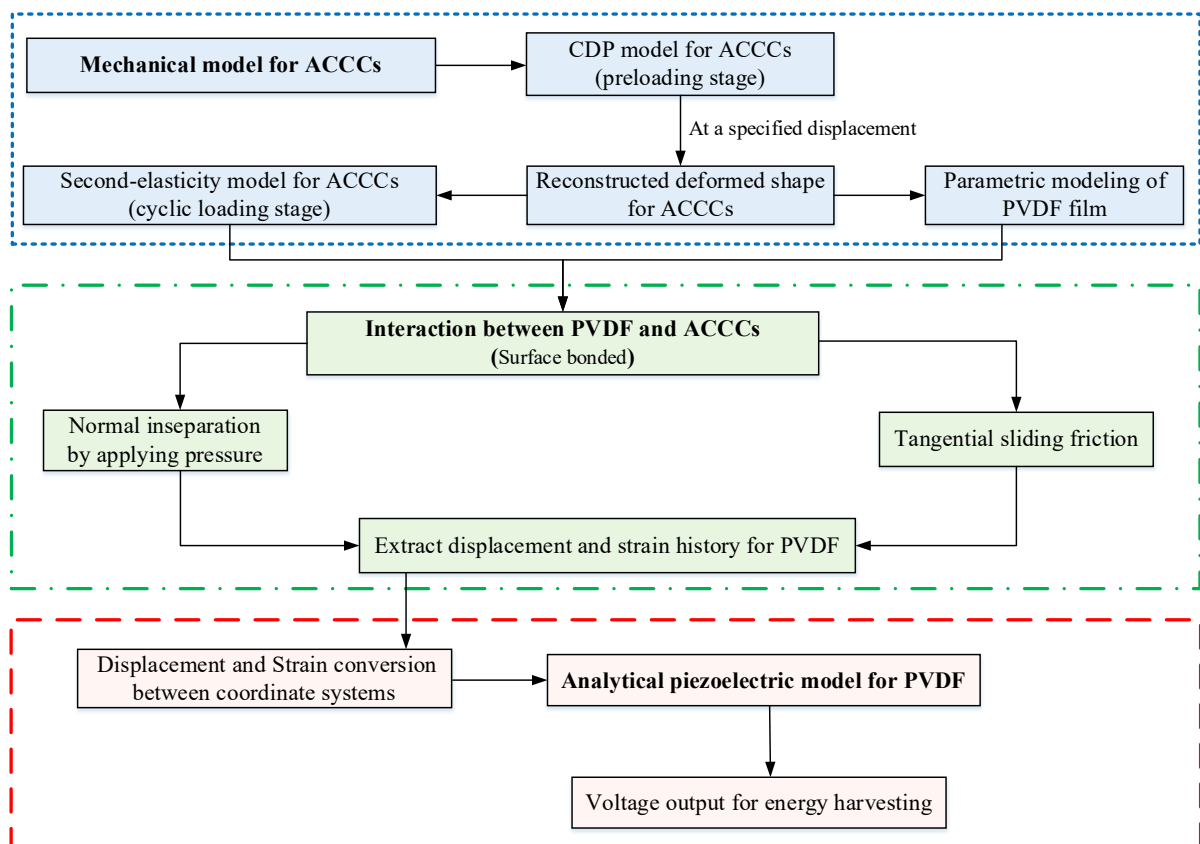


Figure 5-1 Flowchart of the energy harvesting model for ACCC-PVDF system. The blue box consists of the steps for the mechanical modeling. The green box consists of the steps to consider the interaction between PVDF and ACCCs. The red box consists of the steps to conduct the piezoelectric modeling.

Figure 5-1 gives a flowchart of the energy harvesting model for the ACCC-PVDF system. The mechanical model of ACCCs consists of two parts, preloading and cyclic loading. During the preloading phase, CDP model was used to quantify the mechanical behavior of ACCCs. Due to its limitations, the CDP model was unable to simulate the second-elasticity behavior of the ACCCs during cyclic loading. Instead, the second-elasticity model was used to characterize the elastic behavior. To enable the conversion between the CDP and second-elasticity models, the deformed shape of the ACCCs at a specific loading displacement calculated by the CDP model was reconstructed as the initial geometry for the second-elasticity model. Afterwards, the interaction between PVDF and ACCCs was considered for the strain transfer, as shown in the green box of Figure 5-1. Then, the mechanical response of the PVDF film was extracted to calculate the output voltage, based on the analytical piezoelectric model of PVDF film (the red box of the Figure 5-1).

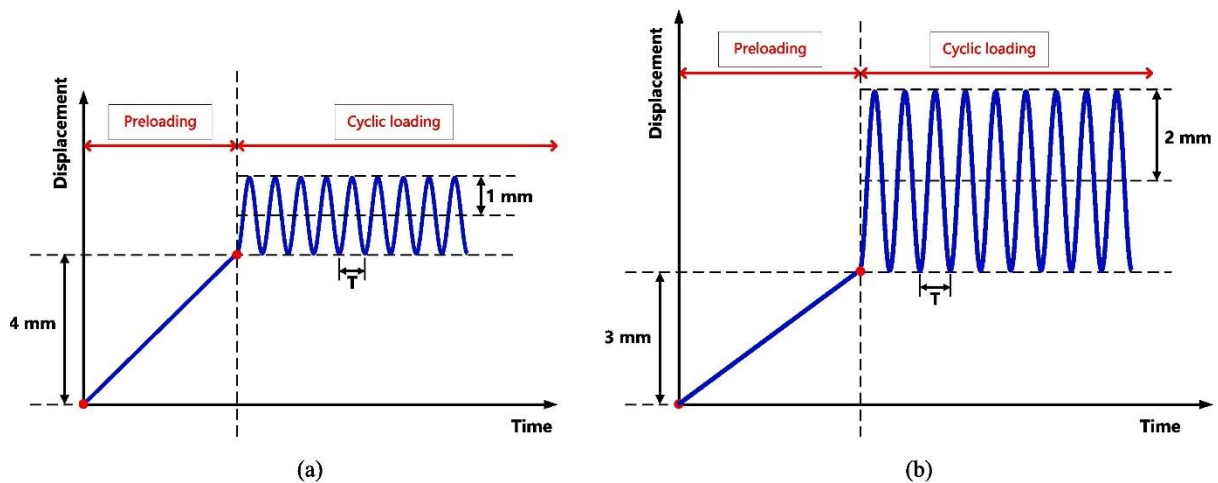


Figure 5-2 Loading plans for energy harvesting models, (a) amplitude 1.0 mm, (b) amplitude 2.0 mm.

Compared with the experimental loading plan in Chapter 3, corresponding loading plans for energy harvesting with different amplitudes have been adopted in models, as shown in Figure 5-2. In the energy harvesting experiments, the specimens were first pre-compressed during the uniaxial compression test until the displacement reaches 5.0 mm. For convenience, the deformed geometry of the specimen at the displacement of 4.0 mm was reconstructed as the initial shape for cyclic loading, since the range from the displacement of 4.0 mm to 5.0 mm belongs to the second-elasticity range. Furthermore, during the cyclic loading test with a 1.0 mm amplitude, the specimen becomes stress-free at a displacement of 4.0 mm because of the loading plate detaching from the specimen. Correspondingly, the reconstructed model has no initial stress before cyclic loading. Similarly, for the cyclic loading test with an amplitude of 2.0 mm, the deformed geometry of the specimen at the displacement of 3.0 mm was chosen as the initial shape for cyclic loading. While the first cycle is somewhat influenced by the boundary conditions, the stable voltage magnitudes of energy harvesting results from the second cycle onwards were extracted for analysis with zero volt as a benchmark.

5.2 MECHANICAL MODEL

5.2.1 CDP model for preloading

The elastic-plastic behavior of cementitious composites reinforced by PVA fibers can be simulated by CDP model. The theory of using CDP model for simulating the mechanical behavior of ACCCs has been presented in previous research [1]. As seen in Figure 5-3a, b, during the preloading stage, the mechanical behavior of ACCCs is modeled based on CDP model from zero to a certain loading displacement. The deformed specimen with plastic strain distribution at the displacement of 4.0 mm was displayed in Figure 5-3b when the loading amplitude is 1.0 mm.

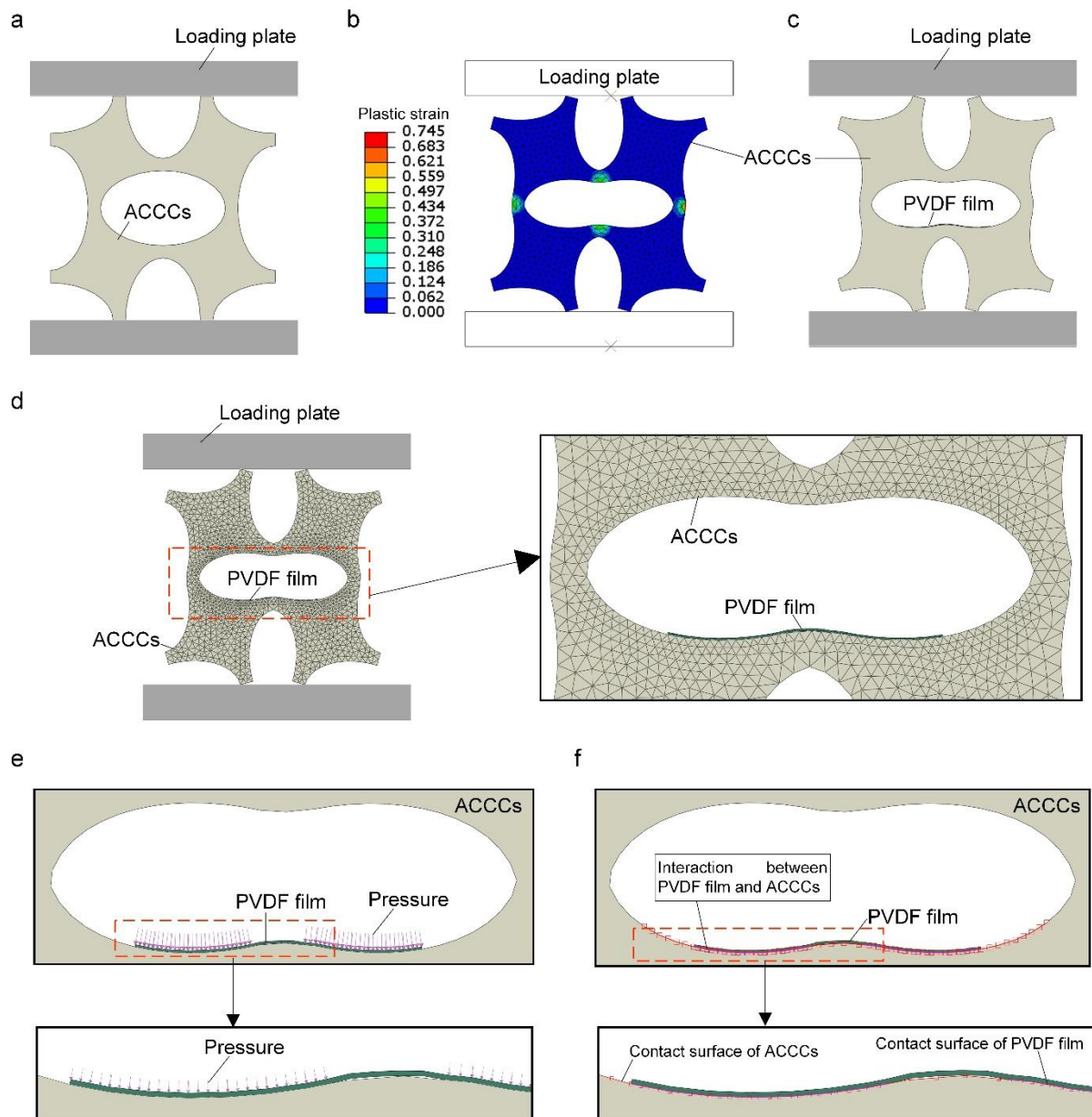


Figure 5-3 Modelling of energy harvesting with ACCCs and surface-mounted PVDF, (a) initial shape before preloading, (b) deformed shape at the displacement of 4.0 mm, (c) reconstructed shape for cyclic loading, (d) finite meshing and PVDF film configuration for cyclic loading, (e) normal pressure applied on PVDF film for

simulating normal inseparability, (f) interaction between PVDF film and ACCCs.

The CDP model parameters for the ACCCs are listed in Table 5-1. There, ρ refers to the density of the ACCCs. E_0 is the initial elastic modulus of the ACCCs. ν is the Poisson's ratio of the ACCCs. $\sigma_{b0} / \sigma_{c0}$ is the ratio between the initial yield stress in equi-biaxial compression and uniaxial compression. K_c represents the ratio of the second stress invariants on the tensile and compressive meridians. ψ refers to the dilation angle. ε_{ec} is the flow potential eccentricity. For the material parameters of CDP model, tensile behavior parameters and compressive behavior parameters for the ACCCs are listed in Table 5-2, Table 5-3, respectively. The CDP model parameters for the ACCCs under tension and compression have been calibrated by using experimental results of uniaxial tension and compression tests by Xu et al. [1, 2]. The loading plate is made of steel with the elastic modulus of 198.0 GPa, the Poisson's ratio of 0.3 and the density of 7900 kg/m³.

The CDP model of ACCCs under quasi-compression was simulated using the ABAQUS/explicit module. The meshing of the ACCC specimen was achieved using CPS3, a 3-node linear plane stress triangular element without hourglass effect. An analysis of mesh size dependence was conducted to ascertain the optimal mesh configuration. A quasi-static displacement was imposed on the top plate in the direction of compression. The bottom plate remained fixed. In our previous compression experiments for ACCCs [1], plastic films were employed to minimize friction between the ACCC specimen and the loading plates. Consequently, a low friction coefficient of 0.105 was adopted to simulate the slight friction between the specimen and the loading plates. To minimize the overclosure between the specimen and the loading plates, a hard contact approach was implemented.

Table 5-1 CDP model parameters for ACCCs.

ρ (kg/m ³)	E_0 (MPa)	ν	$\sigma_{b0} / \sigma_{c0}$	K_c	ψ	ε_{ec}	Viscosity Parameter
1870	3997	0.2	1.16	0.667	35	0.1	0.001

Table 5-2 Tensile behavior parameters for ACCCs

Yield Stress (MPa)	Cracking Strain (%)
2.358	0
1.283	0.0519
1.671	0.180
1.477	0.265
1.235	0.505
0.959	0.669
0.641	0.962
0.334	1.551
0.193	1.995

Table 5-3 Compressive behavior parameters for ACCCs

Yield Stress (MPa)	Inelastic Strain (%)
8.376	0

12.273	0.0158
12.027	0.0367
10.984	0.0765
10.586	0.0889
10.060	0.1264
9.948	0.1557
10.720	0.2030
11.333	0.2312

5.2.2 Reconstruction of ACCCs

As displayed in [Figure 5-3b](#), the deformed shape of ACCCs at a certain loading displacement will be reconstructed by topological information as the initial geometry for the cyclic loading. As shown in [Figure 5-4](#), a new algorithm called node-order-track algorithm was developed to conduct topological reconstruction of geometric shapes at a specific time of loading process. The algorithm reconstructs the geometric shape based on topological information (i.e., node order recorded) and node coordinates at the current moment. The current node coordinates are obtained by adding the corresponding displacements to the original coordinates. The node-order-track algorithm is used to extract the deformed geometric profile of ACCCs at a certain loading displacement by Python-based programming in ABAQUS. As displayed in [Figure 5-3c](#), when the displacement reached 4.0 mm, the deformed shape at this moment was reconstructed as the initial shape for cyclic loading with the loading amplitude of 1.0 mm. Similarly, the deformed shape at the displacement of 3.0 mm was reconstructed as the initial shape for cyclic loading with the loading amplitude of 2.0 mm. The geometric entity enclosed by the extracted profile is then generated and meshed with the same element type but different element distribution or topology information (see [Figure 5-3d](#)).

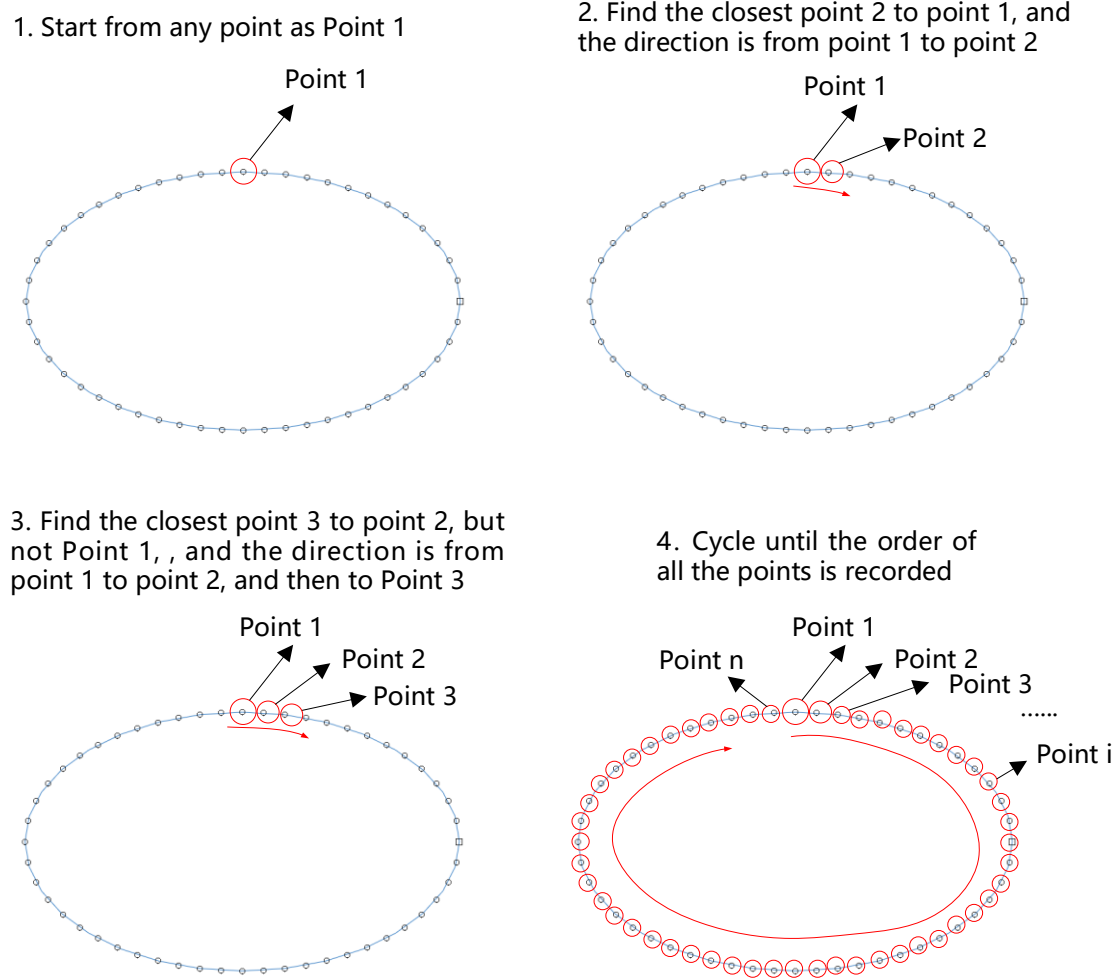


Figure 5-4 Topological reconstruction of geometric shapes based on node-order-track algorithm

5.2.3 Second-elasticity model of ACCCs

The second-elasticity phenomenon of ACCCs can be observed from the stress-strain curve in previous studies [2-4]. The range of second-elasticity in ACCCs was utilized for energy harvesting via cyclic loading. Here, the ACCCs will be considered as a second-elasticity model with an equivalent structural elastic modulus of the whole unit cell during the cyclic loading stage, as elucidated in Figure 5-3d. To this end, the reconstructed geometric shape of ACCCs at a certain loading displacement (i.e., the end of preloading stage) is used as the initial shape for second-elasticity model during cyclic loading. For the material properties, the elastic modulus of the base material of the ACCCs in the second-elasticity model was taken as 1825 MPa by fitting previous experimental data [2-4] of stress-strain curve during the strain range of cyclic loading. The Poisson's ratio of the base material is 0.2. During cyclic loading simulation, a sinusoidal displacement consistent with the loading scheme employed in cyclic tests was applied to the top plate, while the bottom plate remained fixed. The interaction between the specimen and the loading plates was maintained as established in the compression model.

5.2.4 Parametric modeling of PVDF film

The energy harvesting is only considered in the second-elasticity phase. Thus, the modeling of the PVDF film for energy harvesting is only considered in the second-elasticity stage, as illustrated in the blue box of [Figure 5-1](#). The PVDF film undergoes a small strain with a large displacement due to its flexural behavior. Therefore, the size of the curved PVDF film attached on the central elliptical hole of ACCC specimen remains consistent with its original size. As the PVDF film is an elastic material, its output voltage is governed by the extent of strain variation, which remains independent of its strain history. This strain variation is determined by how the film deviates from its original curvature during deformation. Thus, the initial curvature of the PVDF film will affect the output voltage. The parametric modeling of the PVDF film was based on the reconstructed shape of the ACCCs (see Section A.1 in [Appendix A](#)). The internal profile of the deformed ACCCs in [Figure 5-3c](#) was chosen and translated inward by a thickness of PVDF film (0.2 mm) to obtain the whole PVDF film, which can be tailored according to the length of PVDF film and the bonded position of PVDF film. Then, the flat middle part of the PVDF film was modified to a transition arc by smoothing with the δ_p of 0.025 (the shape parameter defined in Section A.1 in [Appendix A](#)). The PVDF film configuration via parametric construction above can be seen in [Figure 5-3d](#). In the mechanical model, the PVDF film is considered isotropic due to small strain.

5.2.5 Interaction between ACCCs and PVDF

In FEM, the general method considering normal inseparability of contact elements mainly constrains their relative normal displacement by penalty function. This is efficient when the contact surface is close to the plane wherein contact elements do not have significant relative movement differences along their normal direction. However, this method is limited when the surface has a greater curvature, which was presented in Section A.2 in [Appendix A](#). To ensure that the PVDF film maintains normal contact with the ACCCs, a new modeling approach was developed that considers the consistent normal inseparability of contact elements along the curved surface. By applying a certain pressure in the normal direction of contact elements, the PVDF film and ACCCs will not be separated in the normal direction, as illustrated in [Figure 5-3e](#). Simultaneously, the PVDF film is able to maintain a certain level of sliding along the curved surface of the ACCCs. The application of pressure to various positions (i.e., contact elements) can also be utilized to consider different de-bonding conditions. Furthermore, within the elastic range of the ACCC-PVDF system, the applied pressure does not result in a change in the amplitude of strain. Consider the bonding condition during cyclic loading, the pressure of 0.35 MPa was applied to prevent the separation of PVDF film and ACCCs. As seen in [Figure 5-3e](#), the transition arc in the middle of the PVDF film was not applied pressure due to the presence of cracks in the middle region of the ACCCs. The tangential sliding friction coefficient in the energy harvesting model was calibrated by comparison with experiment results regarding the output voltage. [Figure 5-3f](#) displayed the contact surface of the ACCCs and contact surface of PVDF film for considering their mechanical interaction. The mesh in the region where the interaction occurs is refined to ensure the computational accuracy, as indicated in [Figure 5-3d](#). The interaction between the PVDF film and ACCCs was simulated using the surface-to-surface interaction in ABAQUS. To ensure result accuracy, the ABAQUS/explicit module with double-precision analysis was employed.

5.3 ANALYTICAL FORMULAS FOR PIEZOELECTRIC MODEL

The mechanical response of the bonded PVDF film can be obtained from the mechanical model of the ACCC-PVDF system presented above. On this basis, analytical formulas for the piezoelectric model have been developed for calculating the output voltage due to piezoelectric effects of the PVDF film, as seen in the red box of Figure 5-1. The PVDF film used in the study has a curved shape, which makes it challenging to apply piezoelectric formulas. To overcome this challenge, the film needs to be divided into straight rectangular segments, which allows for easier application of the piezoelectric formulas. This is schematically illustrated in Figure 5-5. Herein, each rectangular segment consists of two triangular elements (the element type for meshing) with four nodes. As shown in Figure 5-5, four nodes of each rectangular segment have time-dependent displacements as $u_1^i, u_2^i, u_3^i, u_4^i$ at time t_i and $u_1^{i+1}, u_2^{i+1}, u_3^{i+1}, u_4^{i+1}$ at time t_{i+1} . In Figure 5-5, the piezoelectric strain coefficient d_{31} relates the generated electric charge in the thickness direction to the applied stress along the length direction (piezoelectric mode 31). The piezoelectric strain coefficient d_{33} relates the generated electric charge in the thickness direction to the applied stress along the thickness direction (piezoelectric mode 33). For most rectangular segments, their local coordinate systems are different from the global coordinate system and change over time. The directions of the local coordinate system of each rectangular segment can be calculated by the displacements of the four nodes for later coordinates conversion. The PVDF film was meshed by triangular elements, and thus each rectangular segment is comprised of two triangular elements. The centroid strain of the rectangular segment is an average value of the four node strains of the two triangular elements, as indicated in Figure 5-6. Then, the centroid strain of each rectangular segment in the global coordinate system should be converted to the strain in its local coordinate system, as shown in Figure 5-6.

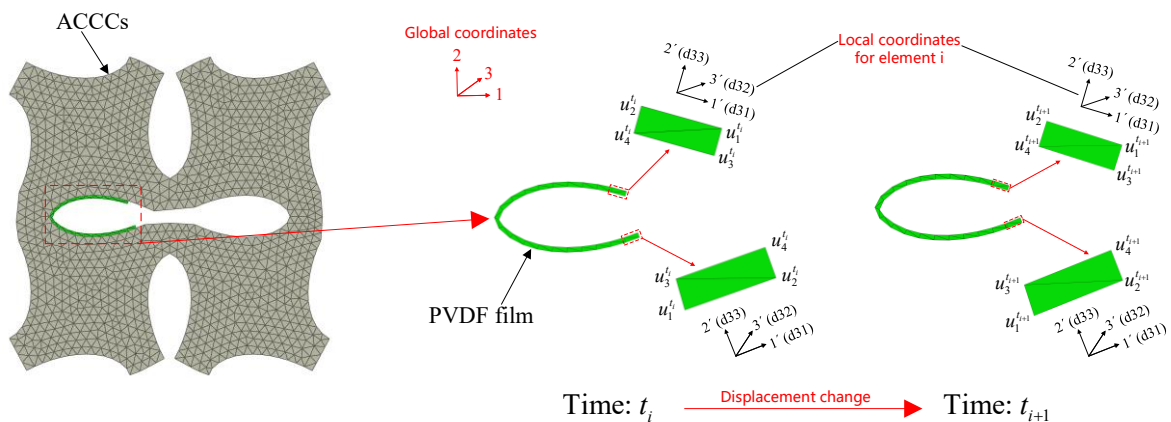


Figure 5-5 Subdivided piezoelectric film for analytical calculation

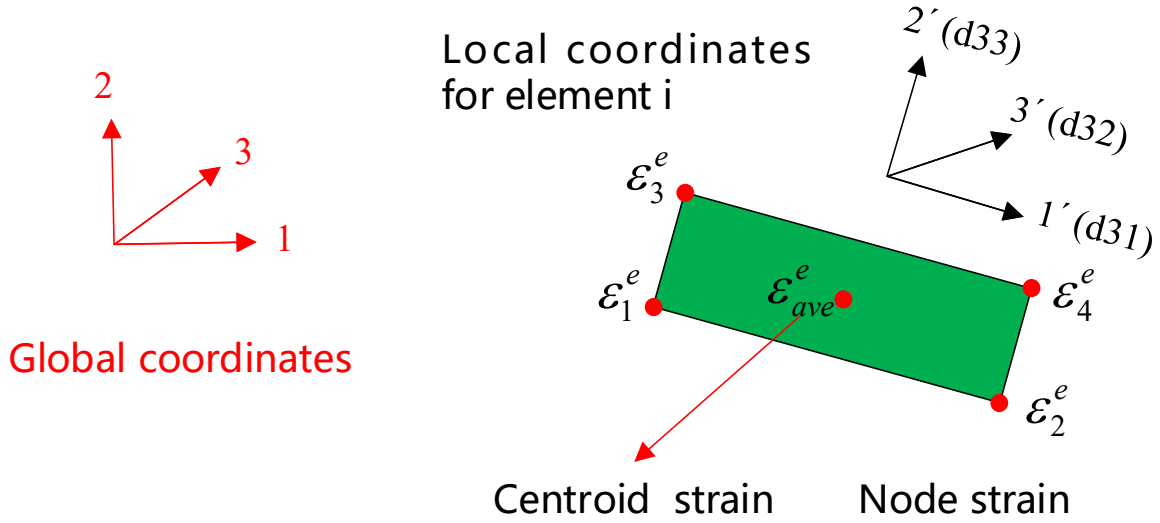


Figure 5-6 The centroid strain of each rectangular block by an averaging method

The strain ϵ'_m in the local coordinate system can be obtained via the strain ϵ_m in the global coordinate system. Detailed derivation of formulas can be found in Section A.3 in [Appendix A](#).

$$\begin{aligned} \begin{bmatrix} \epsilon'_{11} & \epsilon'_{12} \\ \epsilon'_{21} & \epsilon'_{22} \end{bmatrix} &= \begin{bmatrix} \cos \theta & \sin \theta \\ -\sin \theta & \cos \theta \end{bmatrix} \begin{bmatrix} \epsilon_{11} & \epsilon_{12} \\ \epsilon_{21} & \epsilon_{22} \end{bmatrix} \begin{bmatrix} \cos \theta & -\sin \theta \\ \sin \theta & \cos \theta \end{bmatrix} \\ &= \begin{bmatrix} \epsilon_{11} \cos^2 \theta + \epsilon_{22} \sin^2 \theta & \cos \theta \sin \theta (\epsilon_{11} - \epsilon_{22}) \\ \cos \theta \sin \theta (\epsilon_{11} - \epsilon_{22}) & \epsilon_{11} \sin^2 \theta + \epsilon_{22} \cos^2 \theta \end{bmatrix} \end{aligned} \quad (30)$$

where superscript \cdot indicates variables in the local coordinate system. θ is the angle between the two coordinate systems.

Then the mechanical responses of the PVDF film need to be inputted into the piezoelectric model for calculating the output voltage. In general, the constitutive equations for the mechanical–electric field coupling effect in a piezoelectric material can be formulated as

$$\begin{aligned} S_{ij} &= s_{ijkl}^E \cdot T_{kl} + d_{kij} \cdot E_k \\ D_j &= d_{jkl} \cdot T_{kl} + e_{jk}^T \cdot E_k \end{aligned} \quad (31)$$

where S_{ij} refers to the strain. s_{ijkl}^E is the mechanical compliance measured at constant electric field (superscript E). T_{kl} refers to the stress. E_k refers to the electric field. D_j refers to the electric displacement. e_{jk}^T is the dielectric permittivity measured at constant stress (superscript T). d_{kij} , d_{jkl} are the piezoelectric strain coefficients wherein the first subscript represents the direction of the electric field, and the second and third subscripts together represent the stress direction.

For rectangular segment i , the piezoelectric film's electrodes are located exclusively in the plane that is perpendicular to the thickness direction, thus $D_1^i = D_2^i = 0$. When the piezoelectric film is used as a sensor to measure the mechanical strain for the output voltage,

no external electric field is applied. Hence, the electric displacement D_3^i due to the stresses $\sigma_1^{i'}$, $\sigma_2^{i'}$, $\sigma_3^{i'}$ in three directions of local coordinate system can be simply obtained as

$$D_3^i = d_{31}\sigma_1^{i'} + d_{33}\sigma_2^{i'} + d_{32}\sigma_3^{i'} \quad (32)$$

The ACCCs are loaded in the plane stress state, thus the out-of-plane stress is

$$\sigma_3^{i'} = 0 \quad (33)$$

Afterwards, the generated charge on the piezoelectric film can be obtained as the superposition of the two charge generation modes: mode 31 and mode 33, as indicated in Eq. (34).

$$q_3^i = l_i w_i (d_{31}\sigma_1^{i'} + d_{33}\sigma_2^{i'}) \quad (34)$$

where l_i , w_i are the length and width of each rectangular segment, respectively. l_p , w_p , t_p are the length, width, and thickness of the PVDF film. The piezoelectric film is divided into n rectangular segments of equal size along both its length and width dimensions (i.e., $l_p = nl_i$, $w_p = nw_i$). The directions of length, width, and thickness of the PVDF film correspond to direction 1, direction 3, and direction 2 in the local coordinate system, respectively.

The constitution in the plane stress state can be described as

$$\begin{Bmatrix} \sigma_1^{i'} \\ \sigma_2^{i'} \\ \tau_{12}^{i'} \end{Bmatrix} = \frac{E_p}{(1-\nu_p^2)} \begin{bmatrix} 1 & \nu_p & 0 \\ \nu_p & 1 & 0 \\ 0 & 0 & \frac{(1-\nu_p)}{2} \end{bmatrix} \begin{Bmatrix} \varepsilon_1^{i'} \\ \varepsilon_2^{i'} \\ \gamma_{12}^{i'} \end{Bmatrix} \quad (35)$$

where E_p , ν_p refer to the elastic modulus and Poisson's ratio of the PVDF film, respectively.

$\tau_{12}^{i'}$ is in-plane shear stress in local coordinate system. $\varepsilon_1^{i'}$, $\varepsilon_2^{i'}$ are the in-plane strains in the two directions of local coordinate system. $\gamma_{12}^{i'}$ is in-plane shear strain in local coordinate system.

Thus, with the combination of Eq. (34), Eq. (35) can be formulated as

$$q_3^i = l_i w_i \left(d_{31} \frac{E_p}{(1-\nu_p^2)} (\varepsilon_1^{i'} + \nu_p \varepsilon_2^{i'}) + d_{33} \frac{E_p}{(1-\nu_p^2)} (\nu_p \varepsilon_1^{i'} + \varepsilon_2^{i'}) \right) \quad (36)$$

The capacitance C_i of each rectangular segment can be calculated as

$$C_i = \frac{e_{33} l_i w_i}{t_p} \quad (37)$$

where t_p is the thickness of the piezoelectric layer in the PVDF film. e_{33} refers to the dielectric constant in the direction 2 of the PVDF film. Correspondingly, the capacitance C_p of the PVDF film can be represented as

$$C_p = \frac{e_{33} l_p w_p}{t_p} = n^2 C_i \quad (38)$$

The charges q_p on the electrodes of the PVDF film can be obtained by summing up the charges for each segment using Eq. (39).

$$q_p = \sum_{i=1}^n q_i = \frac{V_p C_p}{n} \quad (39)$$

where V_p is the total voltage of the PVDF film, which consistent across all segments. Therefore, V_p can be expressed as the sum of two voltage components due to mode 31 and mode 33, respectively.

$$V_p = V_{p,1} + V_{p,2} \quad (40)$$

$$V_{p,1} = \frac{l_p w_p d_{31}}{C_p} \frac{E_p}{n(1-\nu_p^2)} \sum_{i=1}^n (\varepsilon_1^{i'} + \nu_p \varepsilon_2^{i'}) = \frac{l_p w_p d_{31}}{C_p} \frac{1}{n} \sum_{i=1}^n \sigma_1' = \frac{l_p w_p d_{31}}{C_p} \bar{\sigma}_1' \quad (41)$$

$$V_{p,2} = \frac{l_p w_p d_{33}}{C_p} \frac{E_p}{n(1-\nu_p^2)} \sum_{i=1}^n (\nu_p \varepsilon_1^{i'} + \varepsilon_2^{i'}) = \frac{l_p w_p d_{33}}{C_p} \frac{1}{n} \sum_{i=1}^n \sigma_2' = \frac{l_p w_p d_{33}}{C_p} \bar{\sigma}_2' \quad (42)$$

wherein $\bar{\sigma}_1'$ is defined as the equivalent d_{31} -directional stress for the PVDF film. $\bar{\sigma}_2'$ is the equivalent d_{33} -directional stress for the PVDF film. $V_{p,1}$ is defined as the cumulative voltage induced by $\bar{\sigma}_1'$. $V_{p,2}$ is the cumulative voltage induced by $\bar{\sigma}_2'$.

Therefore, the mechanical responses calculated in the local coordinate system were inputted into the analytical formulas of the piezoelectric model to obtain the output voltage. It is noteworthy that the analytical formulas for piezoelectric model can calculate the voltage components and corresponding stress components under two charge generation modes of d_{31} and d_{33} . Table 5-4 gives the piezoelectric properties and mechanical properties of the PVDF film used in the piezoelectric model. Wherein ρ_p refers to the density of the PVDF film. f_{eu} is the yield strength of the PVDF film. k_{31} is the electromechanical coupling factor of the PVDF film.

Table 5-4 Piezoelectric properties and mechanical properties of PVDF

Material properties	Value	Units	Material properties	Value	Units
ρ_p	1780	kg/m ³	E_p	2	GPa
ν_p	0.34	-	f_{eu}	45–55	Mpa
d_{31}	23	pC/N	d_{32}	1.476	pC/N
d_{33}	-33.8	pC/N	d_{15}	20	pC/N
e_{33}	1.15e ⁻¹⁰	F/m	k_{31}	12%	-

5.4 MODELLING RESULTS AND DISCUSSION

As displayed in Figure 5-7, the simulated results based on the energy harvesting model of the ACCC-PVDF system presented a great agreement with the experimental measurements, confirming the validity of our model. Figure 5-7 also shows that the energy harvesting model can account for the effects of loading amplitude and loading frequency on the output voltage. It can be found that, as the loading amplitude increases, the harvested voltage increases accordingly. In comparison, the effects of loading amplitude on the output voltage are more significant than those of loading frequency. The reason is that the ACCCs-PVDF system exhibits increased strain energy and greater flexural deformation in response to a higher loading amplitude. In addition, the increased flexural deformation of the ACCC-PVDF system results in a more curved contact surface between the two. This curved surface significantly impedes the sliding of the PVDF film, leading to an increase in frictional forces, as explained in Section A.2 in Appendix A. Correspondingly, the models subjected to a larger loading amplitude

exhibit higher friction coefficients, as demonstrated in [Table 5-5](#).

Table 5-5 Friction coefficients under different loading amplitudes and loading frequencies

Loading amplitude	1.0 mm			2.0 mm		
Loading frequency	0.3 Hz	1.0 Hz	2.0 Hz	0.3 Hz	1.0 Hz	2.0 Hz
Friction coefficients	0.028	0.032	0.035	0.08	0.085	0.09

As demonstrated by the experimental results in Chapter 3, the output voltage increases with loading frequency when subjected to the same loading amplitude. When the PVDF film is firmly bonded to the surface of the ACCCs, the dynamic principal stress induced during cyclic loading develops along its tangential direction (i.e., the direction of its length). This stress increases with loading frequency due to inertial effects. The tangential stress is primarily influenced by the frictional force between the PVDF film and the ACCCs surface. This relationship is captured in the calibrated energy harvesting model, which incorporates varying friction coefficients along the tangential direction, as shown in [Table 5-5](#). The model demonstrates that, at a constant loading amplitude, higher loading frequencies correspond to increased friction coefficients, leading to greater output voltage in the simulated results.

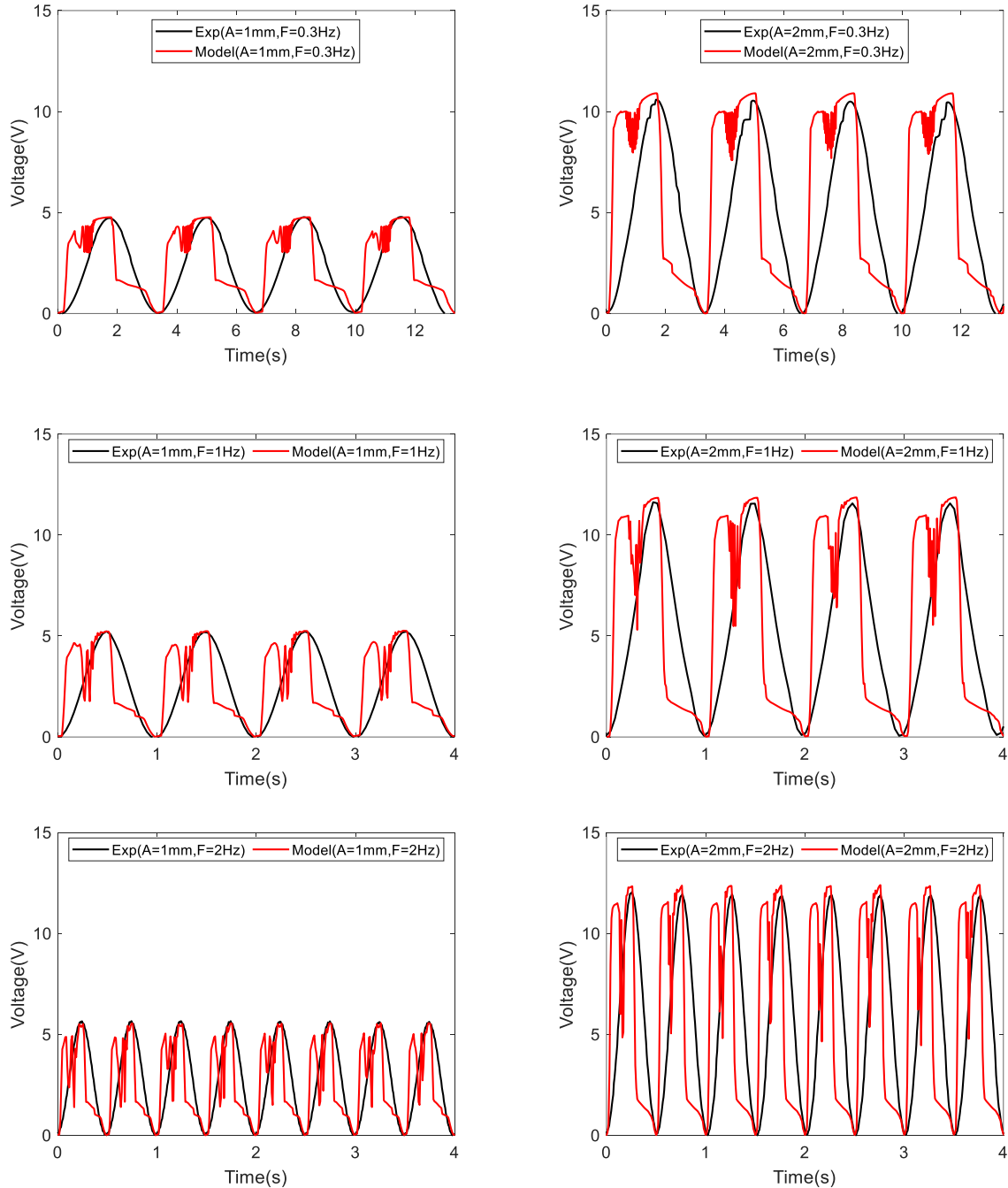


Figure 5-7 Comparisons of the output voltage between simulated results and experimental data under different loading frequencies and different loading amplitudes.

The energy harvesting model allows for the calculation of voltage components induced by the two charge generation modes of d_{31} and d_{33} , as well as their corresponding stresses under varying loading amplitudes and frequencies. Figure 5-8 and Figure 5-9 display these results. The total voltage of the PVDF film ($V(\text{total})$) in Figure 5-8 and Figure 5-9 is the algebraic sum of the voltage components generated by d_{31} and d_{33} . $\sigma_1(d_{31})$ represents the equivalent d_{31} -directional stress $\bar{\sigma}'_1$ (i.e., the equivalent tangential stress) for the PVDF film; $\sigma_2(d_{33})$

represents the equivalent d_{33} -directional stress $\bar{\sigma}'_2$ (i.e., the equivalent normal stress) for the PVDF film. The equivalent d_{31} -directional stress $\bar{\sigma}'_1$ is significantly larger than the d_{33} -directional stress $\bar{\sigma}'_2$ during per cycle for energy harvesting. Correspondingly, the output voltage $V_{p,1}$ generated by d_{31} -coupling mode (V1(d31) in Figure 5-8 and Figure 5-9) is greater than the output voltage $V_{p,2}$ generated by d_{33} -coupling mode (V2(d32) in Figure 5-8 and Figure 5-9). This is because the flexural behavior of the PVDF film enables it to utilize the d_{31} -coupling mode, which results in a strong voltage generation.

The results presented in Figure 5-8 and Figure 5-9 also illustrate the effects of loading amplitude and loading frequency on the output voltage regarding the stress components and corresponding voltage components. It can be found that the magnitude of $\bar{\sigma}'_1, \bar{\sigma}'_2$ under the loading amplitude of 2.0 mm are greater than those under the loading amplitude of 1.0 mm. Correspondingly, $V_{p,1}, V_{p,2}$ become greater when the loading amplitude increases from 1.0 mm to 2.0 mm. Under a constant loading amplitude, the magnitude of $\bar{\sigma}'_1$ demonstrates a significant increase as the loading frequency is elevated from 0.3 Hz to 2.0 Hz. In contrast, the magnitude of $\bar{\sigma}'_2$ exhibits only a marginal rise over the same frequency range. These trends are further reflected in the behavior of $V_{p,1}$ and $V_{p,2}$: $V_{p,1}$ increases notably with loading frequency, while $V_{p,2}$ shows a slight incremental response to the frequency increase under consistent loading amplitude conditions.

It should be noted that the model suppresses normal separation between the bonded PVDF and ACCCs by applying a certain pressure in the normal direction of the contact elements. However, this pressure is not sufficient to completely restrict the relative normal displacement between the two components. As a result, the principal stress directions within individual elements of the PVDF film do not consistently align with their tangential directions. This misalignment contributes to the oscillations observed in the simulation outcomes. Additionally, the central region of the PVDF is positioned above the crack and lacks direct contact with the ACCCs, which also contributes to the vibrations in the model results.

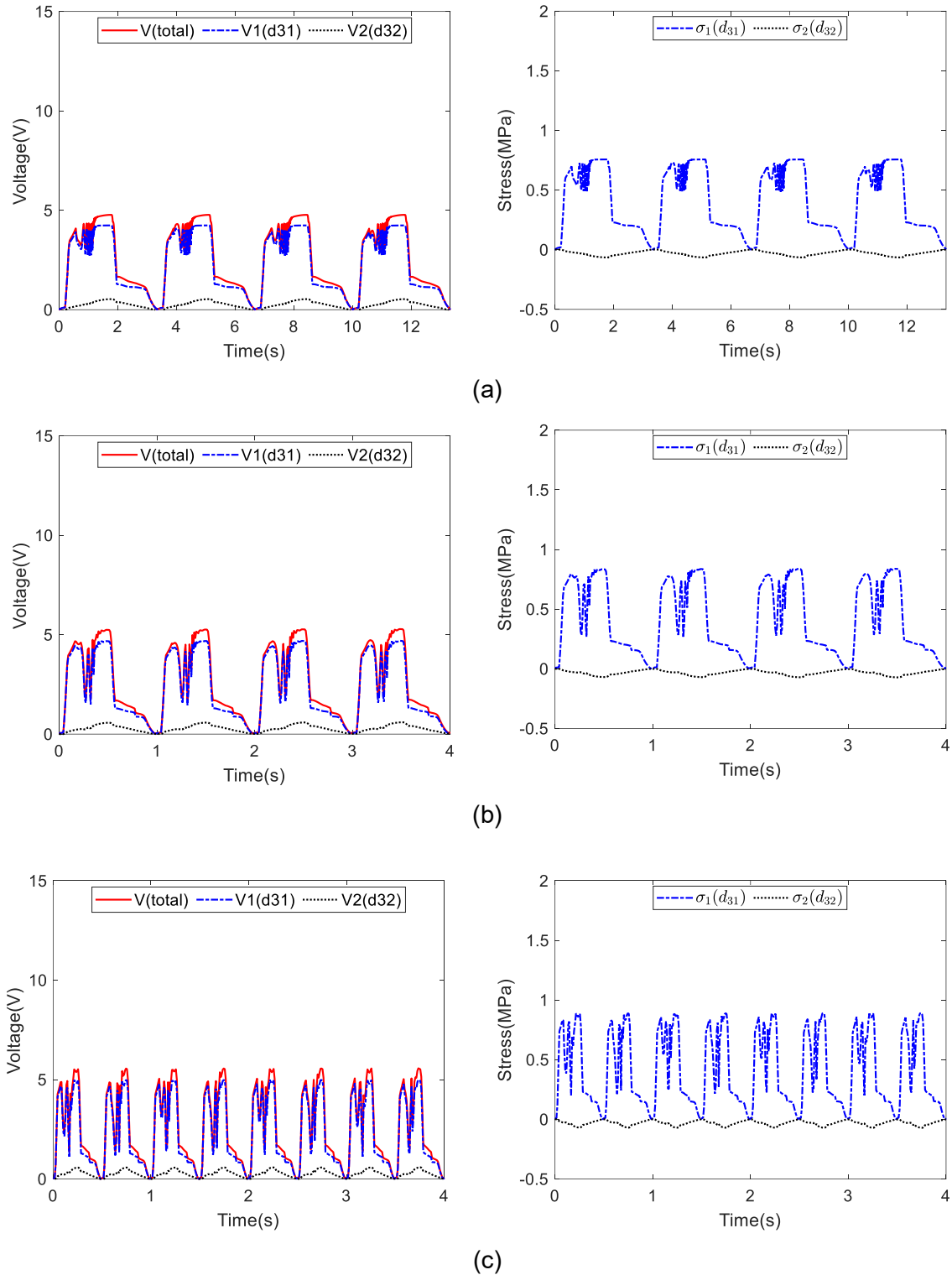


Figure 5-8 Voltage components and stress components generated by d_{31} and d_{33} under different frequencies with the loading amplitude of 1.0 mm, (a) $A = 1.0$ mm, $f = 0.3$ Hz, (b) $A = 1.0$ mm, $f = 1.0$ Hz, (c) $A = 1.0$ mm, $f = 2.0$ Hz.

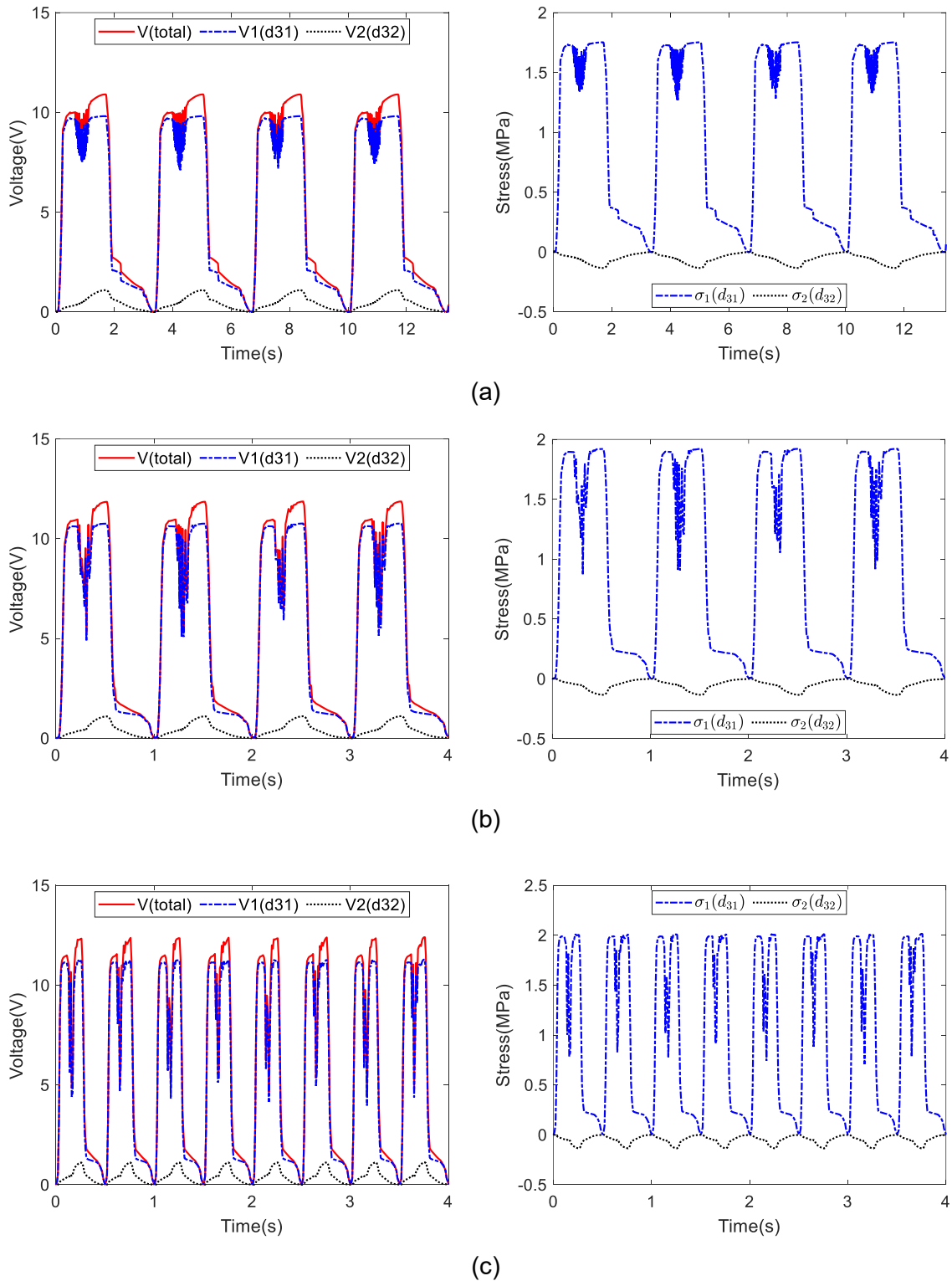


Figure 5-9 Voltage components and stress components generated by d_{31} and d_{33} under different frequencies with the loading amplitude of 2.0 mm, (a) $A = 2.0$ mm, $f = 0.3$ Hz, (b) $A = 2.0$ mm, $f = 1.0$ Hz, (c) $A = 2.0$ mm, $f = 2.0$ Hz.

5.5 CONCLUSIONS

Building on the experimental results of the ACCC energy harvester, this chapter develops a numerical model to simulate its energy harvesting process. The model accounts for both the mechanical deformation of ACCCs and the corresponding electrical output of the surface-mounted PVDF film. The main conclusions are as follows:

- The energy harvesting experiments revealed that the output voltage of the ACCCs-PVDF system increases with both loading amplitude and loading frequency. The energy harvesting model can account for the effects of loading amplitude and frequency on the output voltage. Specifically, higher loading frequencies increase friction between the PVDF film and ACCCs, enhancing strain transfer and thereby increasing voltage output. Greater loading amplitudes induce larger flexural deformation of the PVDF and increase interfacial friction, also contributing to higher output voltage.
- In terms of the ACCC-PVDF system, the model results reveal its energy harvesting mechanisms with mechanical energy conversion based on two charge generation modes of d_{31} and d_{33} . The equivalent d_{31} -directional stress (i.e., the equivalent tangential stress) of the PVDF film is greater than its equivalent d_{33} -directional stress (i.e., the equivalent normal stress) during each cycle for energy harvesting. Correspondingly, the output voltage by d_{31} -coupling mode is higher than that by d_{33} -coupling mode per cycle for energy harvesting, which reflects strong energy output by d_{31} -coupling mode due to the flexural behavior of the PVDF film. As the loading amplitude increases, the magnitude of the stress components $\bar{\sigma}'_1$ and $\bar{\sigma}'_2$, as well as the corresponding voltage components $V_{p,1}$ and $V_{p,2}$, all increase. However, while the magnitude of $\bar{\sigma}'_1$ and $V_{p,1}$ increase with increasing loading frequency, the magnitude of $\bar{\sigma}'_2$ and $V_{p,2}$ presents a marginal increase with increasing loading frequency under consistent loading amplitude conditions.
- The energy harvesting model can reveal electromechanical mechanisms of the ACCC-PVDF system, considering various energy harvesting parameters such as the mechanical behavior of the ACCCs, the interaction between PVDF and ACCCs, and the analytical piezoelectric model of the PVDF film. The results of this model show good agreement with the experimentally measured output voltages, which can provide valuable insights for the design and optimization of architected cementitious composites that incorporate flexible piezoelectric polymers for energy harvesting applications.

The energy harvesting model systematically simulates the electromechanical interaction between ACCCs and PVDF in the ACCC energy harvester. Specially, the CDP model effectively captures the deformation behavior of cementitious materials under compression. The second elasticity model simulates recoverable elastic deformation during cyclic loading. The piezoelectric model calculates the voltage generated by the recoverable strain in the hinge-like ligament. Additionally, the energy harvesting model can be utilized to generate numerous simulation cases by incorporating various geometric variations of the ACCC shape, providing a dataset for machine learning-based optimization design. This will be further discussed in chapter 7.

REFERENCES

- [1] Y. Xu, E. Schlangen, M. Luković, B. Šavija, Tunable mechanical behavior of auxetic cementitious cellular composites (CCCs): Experiments and simulations, *Construction and Building Materials*, 266 (2021) 121388. <https://doi.org/10.1016/j.conbuildmat.2020.121388>.
- [2] Y. Xu, H. Zhang, E. Schlangen, M. Luković, B. Šavija, Cementitious cellular composites with auxetic behavior, *Cement and Concrete Composites*, 111 (2020) 103624. <https://doi.org/10.1016/j.cemconcomp.2020.103624>.
- [3] Y. Xu, *Architected Cementitious Cellular Materials Towards Auxetic Behavior*, Ph.D. thesis, Delft University of Technology, Delft, The Netherlands, 2021.
- [4] J. Xie, Y. Xu, Z. Wan, A. Ghaderiaram, E. Schlangen, B. Šavija, Auxetic cementitious cellular composite (ACCC) PVDF-based energy harvester, *Energy and Buildings*, 298 (2023) 113582. <https://doi.org/10.1016/j.enbuild.2023.113582>.

6

ENHANCED AUXETIC CEMENTITIOUS CELLULAR COMPOSITE (ACCC) ENERGY HARVESTER USING STRAIN-HARDENING CEMENTITIOUS COMPOSITES (SHCC)

As observed in the energy harvesting experiments in Chapter 3, the auxetic behavior of ACCCs results from the section rotation to accommodate compressive deformation into the hollow space. This was induced by fiber-bridging within the hinge-type joint, which further contributes to recoverable deformation for energy harvesting under cyclic compressive loading. While recoverable deformation was successfully attained, the ACCC energy harvester described in Chapter 3 exhibited a low stress level under cyclic test due to the limited fiber-bridging capacity of the material mixture. This restricts the effectiveness of ACCCs in sustaining recoverable deformation under higher loading conditions. This chapter aimed to enhance the load-bearing capacity and compressive deformation resilience of ACCC energy harvester within their auxetic range by incorporating strain-hardening cementitious composites (SHCC). The multiple cracks formed in the SHCC contribute to the distribution and accommodation of large deformation. This mechanism helps to limit the widening of the primary crack and ensures sustained fiber bridging performance during the stage of auxetic deformation.

Part of this chapter have been published as Xie, Jinbao, et al. " Enhanced elastomer-like auxetic cementitious materials through strain-hardening cementitious composites (SHCC) with extended softening properties", Cement and Concrete Composites, 161 (2025): 106069.

6.1 INTRODUCTION

The high deformation capacity of ACCCs originates from sectional rotation, which enables the structure to accommodate compressive deformation within its hollow space. This mechanism is facilitated by fiber-bridging at the hinge-type joints, contributing to the recoverability of deformation under cyclic compressive loading. As a result, substantial mechanical energy becomes available for conversion into electrical energy. The hinge-like joints accommodate rotational movement through the formation of triangular cracks, with fiber-bridging at the crack tips. This fiber-bridging not only supports the rotation but also contributes to its reversibility. In [Chapter 3](#), recoverable deformation was achieved using a fiber-reinforced cementitious mixture; however, the mixture led primarily to a single dominant crack. Due to its limited fiber-bridging capacity, the single widened crack in the joints is more prone to damage, particularly considering the heterogeneity of cementitious materials [1-4]. As a result, the ACCC energy harvester developed using this material exhibited a low stress level under cyclic testing. This shortcoming restricts the effectiveness of ACCCs in sustaining recoverable deformation under higher loading conditions such as vehicle loads, making it challenging for engineering applications. Additionally, the limited fiber-bridging capacity of the mixture hinders the formation of stable hinge joints in larger ligaments. This reduces the flexibility to explore various geometric configurations of ACCCs, thereby limiting the potential to tailor their mechanical and energy harvesting properties.

This chapter aimed to improve the load-bearing capacity and recoverable deformation elasticity of ACCC energy harvester during the stage of auxetic deformation by using SHCC as the base material. Elliptical-shaped ACCCs were designed and fabricated using two types of SHCC—one with short softening tail and one with long softening tail—through additive manufacturing-assisted casting. The ACCC specimens underwent uniaxial compression tests combined with DIC to evaluate their compressive behavior, Poisson's ratio variation, deformation pattern, and local joint analysis. Following initial compression into the high auxetic behavior range, cyclic tests assessed their energy harvesting capabilities. Results were compared with a reference mixture of fiber-reinforced cementitious materials with strain softening.

6.2 DESIGN THEORY

[Figure 6-1](#) gives a schematic illustration of the auxetic mechanism of ACCCs under uniaxial compression. Due to the chirality of each cell section in the studied structure, the joints are locally misaligned. The symmetric structure does not experience shear force at the joints in the middle. When a uniaxial compressive load is applied, these joints undergo a bending moment (indicated in green box) similar to a four-point bending condition ([Figure 6-1a](#)). This creates tensile stresses (indicated by red arrows) at the two ends of the minor axis and compressive stresses (indicated by blue arrows) at the two ends of the major axis ([Figure 6-1a](#)). Since cementitious materials are much weaker in tension than in compression, cracks form on the tension side. As shown in [Figure 6-1b](#), cementitious matrix without fiber or with insufficient fiber bridging will quickly develop cracks throughout the joint, causing the sections to separate. The auxetic behavior of ACCCs is achieved through section rotation by angle θ around the joints ([Figure 6-1a](#)) and inward folding at the hollow spaces. The behavior of the cracked

specimen depends on the fiber-bridging ability of the cementitious materials. Fiber is added to the cementitious matrix to limit crack development. As illustrated in [Figure 6-1c](#), the primary crack develops into a triangular shape under bending. When the crack opens on the tensile side of the joint, the fiber bridging within the crack restricts its growth, preserving the integrity of the compression side of the joint. As a result, the significant deformation in the joints accommodates most of the externally applied compressive strain, thereby reducing the amount of compression in the vertical ligaments and leading to a collective rotational motion and a corresponding decrease in compressive stress. These cracked joints function as hinges, facilitating section rotation and inward folding for auxetic behavior. In [Figure 6-1c](#), primarily only one crack forms in the joints of ACCCs during section rotation, and its poor fiber-bridging capacity results in limited rotational stiffness. When considering high load-capacity scenarios (i.e., vehicle load), this makes it difficult to apply in engineering applications. Low rotational stiffness from poor fiber-bridging and a single widened crack is highly vulnerable to damage, especially due to material heterogeneity.

An SHCC mixture might enable ACCCs to develop multiple cracks in the joints. Instead of one primary crack, these multiple cracks could share and collectively sustain large deformations. This would further reduce the opening of the primary crack and maintain effective fiber bridging during the later stages of high auxetic behavior. Typically, SHCC achieves large ductility through the formation of multiple small cracks, each sustaining limited strain. However, when the primary crack forms, it typically fails quickly with shortened softening tail. The significant rotation of ACCCs tends to produce one primary crack in the joints in the later stages, requiring this crack to sustain large deformations through effective fiber bridging. Extending the softening phase after the primary crack forms is expected to maintain effective fiber bridging and support the large deformations required for the auxetic behavior.

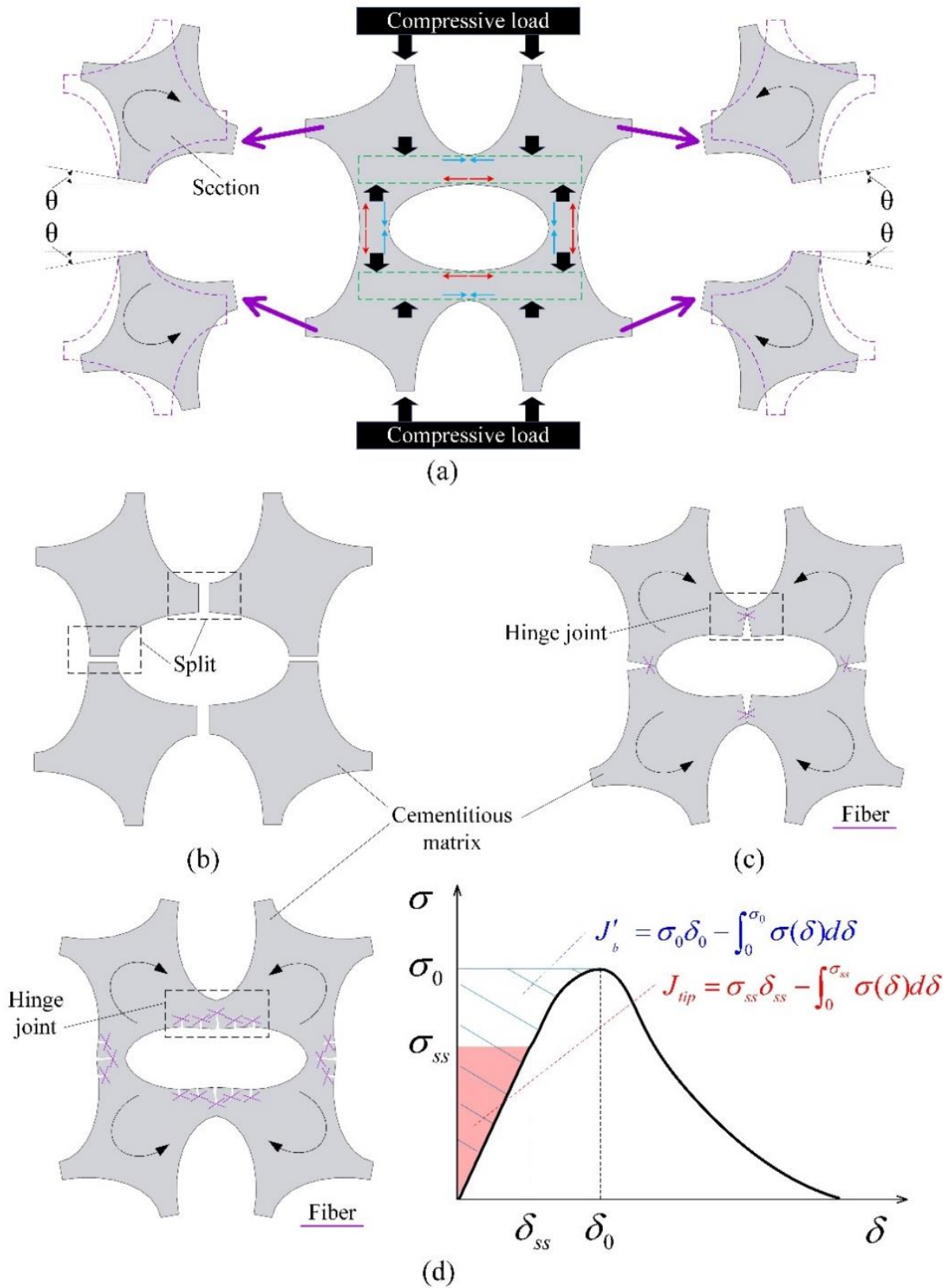


Figure 6-1 Auxetic behavior of ACCCs under compression, (a) section rotation, (b) ACCCs without fiber, (c) ACCCs with fiber-bridging in a single crack, (d) ACCCs with fiber-bridging in multiple cracks, and typical σ - δ relationship for fiber bridging in SHCC.

The pseudo strain-hardening (PSH) behavior of in SHCC [5-9] was achieved by an energy-based criterion for flat crack propagation (Figure 6-1d), which illustrates the relationship between fiber bridging stress (σ) and crack opening (δ). Specially, the crack-tip toughness J_{tip} of the matrix material should be lower than the maximum available complementary energy J'_b . The J_{tip} signifies the energy required to fracture the matrix material at the crack tip. The J'_b represents the maximum complementary energy, accounting for the upper limit of fiber bridging, which occurs when the peak stress and crack opening reach their maximum values σ_0 and δ_0 . In Figure 6-1d, J_{tip} and J'_b are represented by the shaded area and the hatched area, respectively.

6.3 SAMPLE PREPARATION AND MIXTURE DESIGN

The geometry of ACCC specimens for different mixtures was kept consistent, based on the P1-shaped unit cell introduced in Chapter 3. A fine-grained fiber-reinforced mortar was used as the constituent material for ACCCs, with different mixture proportions shown in Table 6-1. Based on the design theory outlined in Section 6.1, three mixtures were designed to achieve the target uniaxial tensile stress-strain curves shown in Figure 6-2. Mixture SS (reference), used in Chapter 3, shows strain softening behavior after reaching peak stress. This mixture has also been similarly used in previous studies [10-12] to facilitate the auxetic behavior of ACCCs. Mixture SHCC-SS is a typical SHCC that demonstrates significant strain hardening due to the development of numerous microcracks, followed by a short softening tail after crack localization occurs in the main crack [13-21]. The SHCC-LS mixture is specifically engineered to improve ductility by exhibiting moderate strain hardening and multiple cracking at the onset, followed by a long softening tail. This extended softening tail enhances fiber bridging within the primary crack after crack localization. The ingredients included CEM I 42.5 N, fly ash, sand (with a grain size between 125 and 250 μm), water, a polycarboxylate superplasticizer, VMA, and PVA fiber. Methylcellulose powder from Shanghai Ying Jia Industrial Development Co. Ltd. was used as a VMA to improve fiber distribution. To attain the desired workability, MasterGlenium 51, a polycarboxylate-based superplasticizer from BASF (Germany), was utilized. For the reference mixture (SS), 2% volume fraction of PVA fiber from Changzhou TianYi Engineering Fiber was used. The two SHCC mixtures were reinforced with 2% volume fraction of RECS15 PVA fiber from Kuraray GmbH. Fiber specifications are given in Table 6-2.

Table 6-1 Mixtures used in this study (by weight).

Label	C	FA	S/(C + FA)	W/(C + FA)	SP/(C + FA)	VMA/(C + FA)	PVA(Reference) (by volume)	PVA(RECS15) (by volume)
SS	1.0	1.2	0.37	0.46	0.0016	0.0003	2%	-
SHCC-LS	1.0	1.2	0.37	0.46	0.0016	0.0003	-	2%
SHCC-SS	1.0	2.2	0.26	0.32	0.0083	0.0003	-	2%

Table 6-2 Material properties of PVA fibers.

Fiber type	Diameter (μm)	Length (mm)	Tensile strength (GPa)	Young's modulus (GPa)	Density (g/cm^3)	Ultimate strain
PVA(Reference)	15	6	1.6	34	1.28	6.8%
PVA(RECS15)	40	8	1.6	41	1.3	6.0%

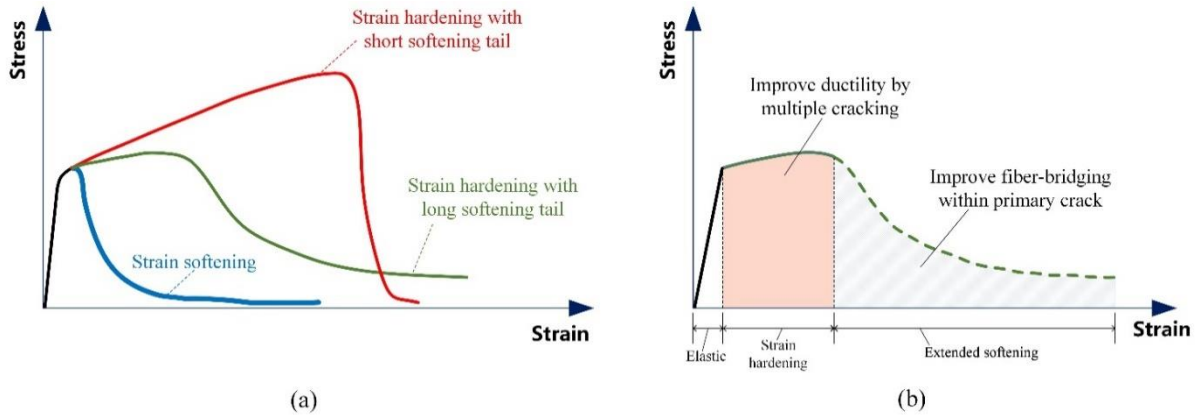


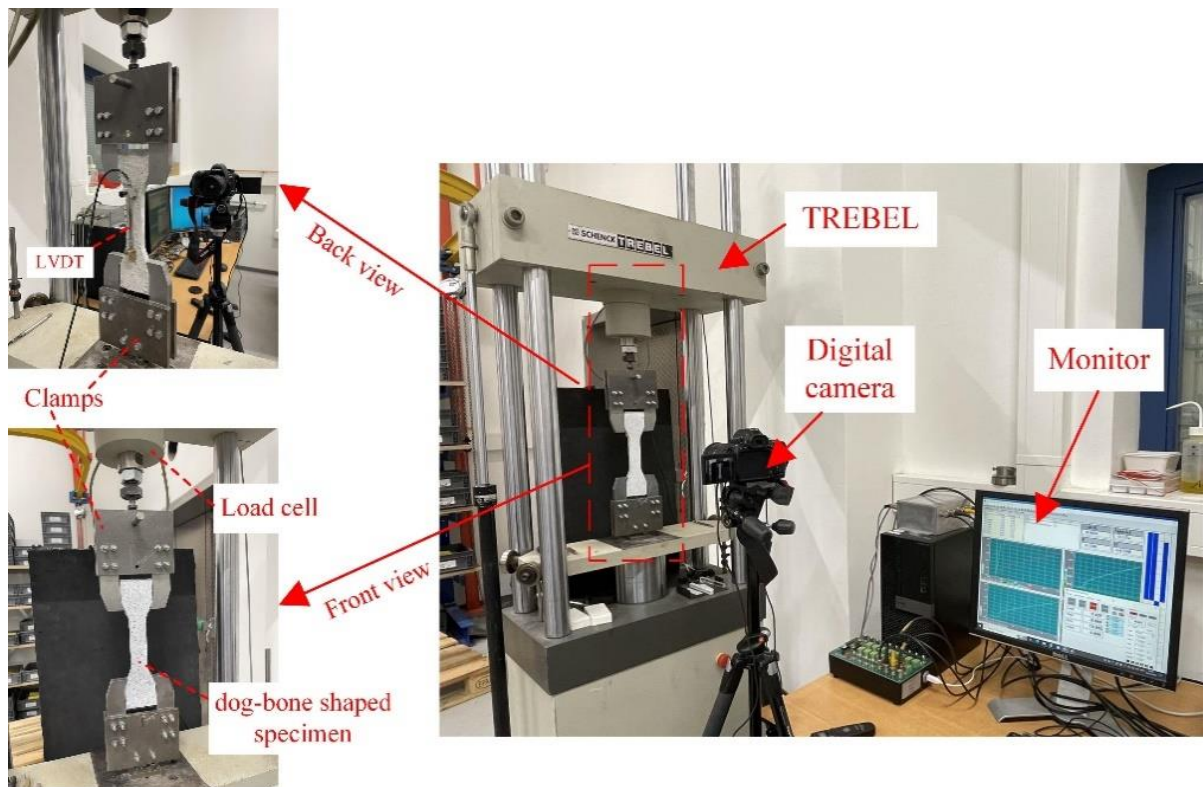
Figure 6-2 Uniaxial tensile behavior, (a) three mixtures, (b) SHCC mixture with extended softening.

The mixing procedure used was as follows: first, the dry ingredients—CEM I 42.5, fly ash, sand, and VMA—were mixed using a Hobart mixer for four minutes. Then, water and superplasticizer were added to the dry ingredients, followed by an additional two minutes of mixing. Next, fibers were gradually incorporated into the mortar and mixed for an additional two minutes, followed by high-speed mixing for five minutes to achieve uniform fiber dispersion throughout the matrix. The resulting fresh paste was poured into silicone molds, with each mold being filled in two layers. Each layer was vibrated for 20 seconds to ensure thorough consolidation. Plastic films were applied to cover the molds to prevent evaporation. After three days of curing at room temperature, the specimens were demolded and transferred to a curing chamber set at 20°C and 96% relative humidity, where they remained until reaching 28 days of age.

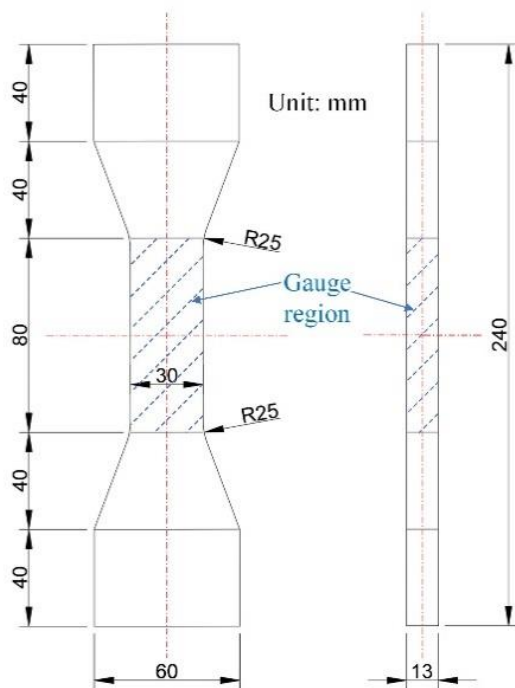
6.4 EXPERIMENTAL TEST

As shown in Figure 6-3a, uniaxial tensile tests using dog bone specimens, as recommended by the Japan Society of Civil Engineers [22], were conducted to evaluate the tensile behavior of the three mixtures after 28 days of curing. The dimensions of dog bone specimens are illustrated in Figure 6-3b, and they were cast using the mold depicted in Figure 6-3c. These tests utilized a TREBEL machine under displacement control with a constant loading rate of 0.005 mm/s. The displacement in the gauge region, with a testing volume of $13 \times 80 \times 30 \text{ mm}^3$ (indicated by the blue dashed lines in Figure 6-3b), was measured by the linear variable differential transducers (LVDT) positioned on the backside of the specimen. The deformation of the gauge region was also monitored across their entire area using DIC (digital image correlation). DIC involves capturing images with cameras to track and record the surface movement of a deforming solid. The gauge region for DIC measurements was first painted white and then sprayed with a black speckle pattern. During loading, images for DIC were captured every 5

seconds by using a digital camera. The DIC results were subsequently processed using GOM Correlate software. A minimum of three dog bone specimens were tested for each mixture to ensure reliable results.



(a)



(b)



(c)

Figure 6-3 (a) Setup for uniaxial tensile test using dog bone specimen, (b) dimensions of dog bone specimen, (c) mold for dog bone specimen.

As shown in Figure 6-4, uniaxial compression tests were performed on ACCC specimen using a UNITRONIC machine under displacement control at a rate of 0.01 mm/s. Deformation was monitored across the entire specimen area using DIC. The displacement of the specimens was measured using LVDTs. Similarly, the specimens used for DIC measurements were painted white and sprayed with a black speckle pattern. Images were captured every 10 seconds and processed using GOM Correlate software. The compressive stress-strain curve was obtained by calculating stress as the compressive force divided by the initial cross-sectional area ($63 \text{ mm} \times 20 \text{ mm}$) and strain as the applied displacement divided by the initial length (63 mm). Plastic films were used to reduce friction between the specimens and loading plates, facilitating the section rotation to achieve auxetic behavior.

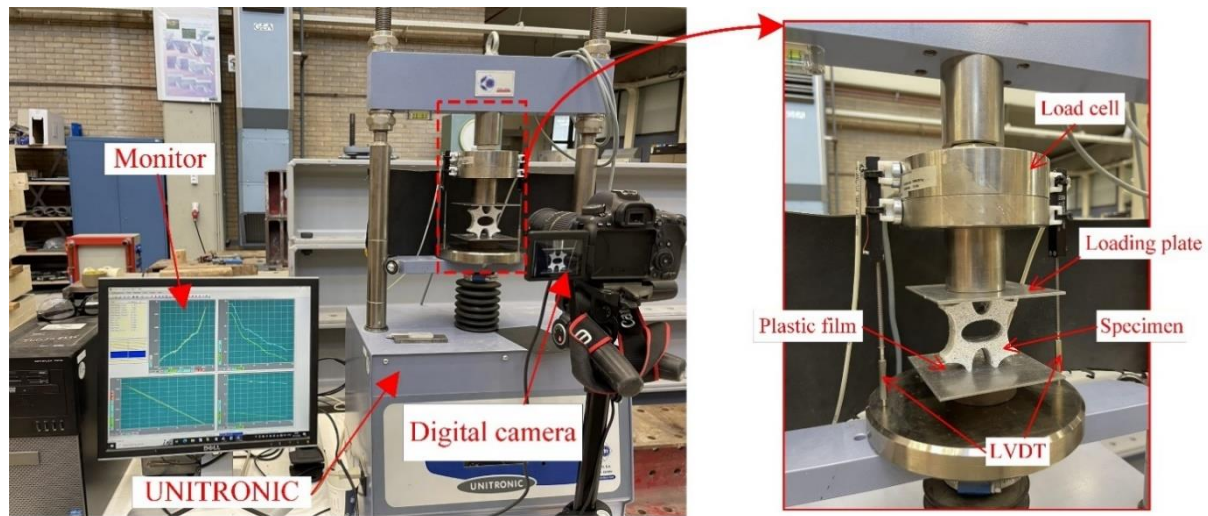


Figure 6-4 Experimental setup for uniaxial compression testing of ACCCs

The energy harvesting test setup and loading scheme for the ACCC energy harvester follows the same configuration as described in Chapter 3. Cyclic tests were conducted using an MTS fatigue testing machine with a capacity of 10 kN. The DC output voltage from the harvester was recorded using a Keysight 34461A digital multimeter. Given the high internal impedance of the LDT0 PVDF sensor [23], the multimeter's input impedance was set to a mode over $10 \text{ G}\Omega$ to ensure accurate open-circuit voltage measurements. The PVDF was wired to the multimeter using two connecting leads, and a plastic film was placed between the loading plate and the specimen to reduce friction. The ACCC specimen was first subjected to displacement loading, beginning at zero and increasing to a maximum displacement of 5.0 mm (U). This initial loading was followed by cyclic displacement applied in a sinusoidal waveform, with a fixed amplitude of 1 mm (A) and a frequency of 1 Hz (f). Each test was performed with three replicates.

6.5 RESULTS AND DISCUSSION

6.5.1 Material properties

Figures 6-5a, 6-5b, and 6-5c show the results of the uniaxial tensile tests for the mixtures SS, SHCC-LS, and SHCC-SS, respectively. Figure 6-5d presents the average values of the uniaxial tensile test results for each mixture. The target strain range is selected with a very small interval as the reference strain coordinate for averaging. The experimentally obtained stress curves are then interpolated based on these reference strain coordinates. Finally, the interpolated values at each reference strain coordinate are averaged. To ensure the accuracy of the interpolation results, the spacing of the reference strain coordinates is set significantly smaller than the intervals between the experimental data points. In Figure 6-5d, the highest strain point during the strain-hardening process was selected at the strain where the stress exhibits a significant decrease, marking the onset of softening. The starting and ending points of strain-hardening are marked in Figure 6-5d, with the strain-hardening starting points represented by circles within subsets and the ending points shown as solid circles. In this context, the blue color represents SS, the green color indicates SHCC-LS, and the red color signifies SHCC-SS. Table 6-3 gives detailed tensile properties of the three mixtures. Both SHCC-LS and SHCC-SS displayed tensile strain-hardening behavior, characterized by the emergence of multiple cracks. SHCC-LS demonstrated a moderate tensile strain capacity with strain-hardening behavior observed up to 2.030% strain, while SHCC-SS exhibited significant strain-hardening behavior extending up to 5.389% strain due to additional fiber-bridging cracks, as shown in Figures 6-5, 6-6 and Table 6-3. Compared to SS, the SHCC mixtures exhibit lower initial cracking strength under tensile loading but higher overall tensile strength, as shown in Figures 6-5, 6-6 and Table 6-3.

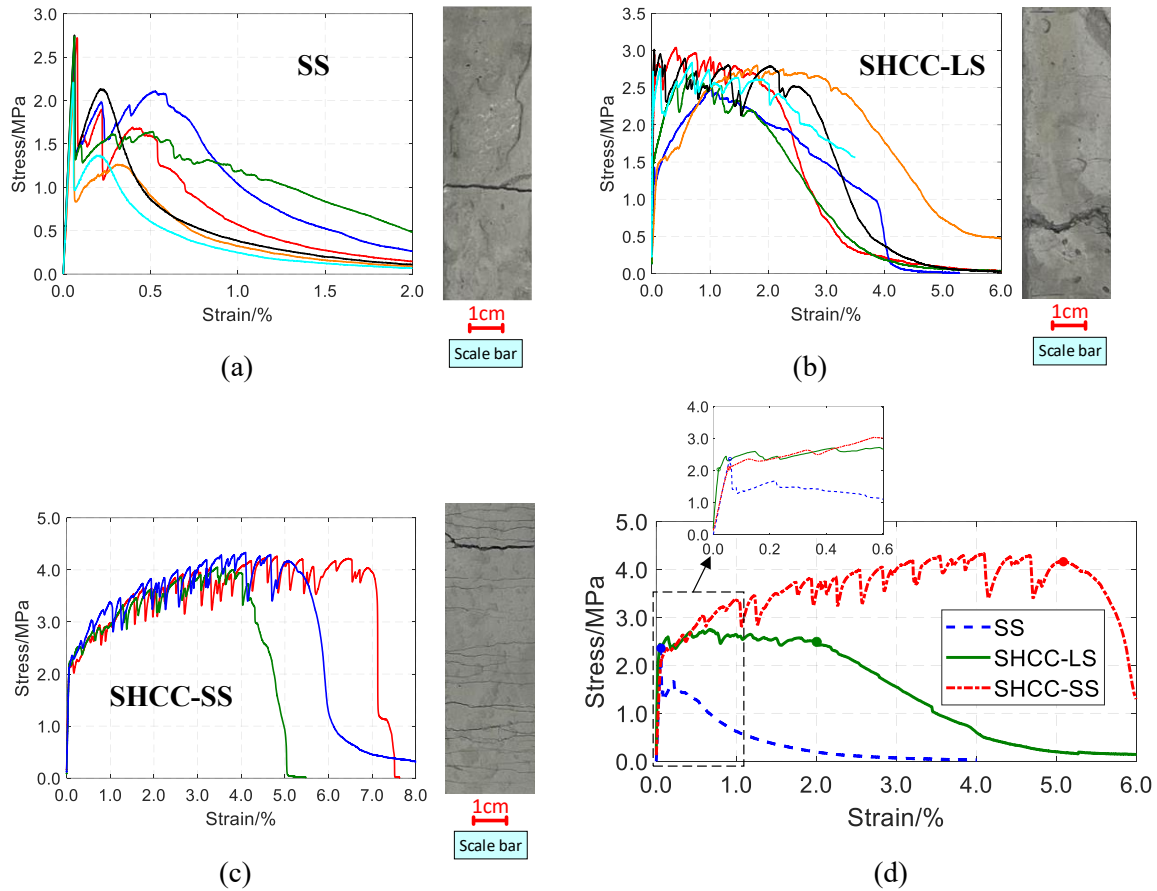


Figure 6-5 Uniaxial tensile tests results, (a) SS, (b) SHCC-LS, (c) SHCC-SS, (d) the average values of the three mixtures.

Figure 6-7 displays the major strain distribution of gauge region in the mixtures with SHCC based on DIC analysis. During uniaxial tension, SHCC-LS developed a significant crack at around 2% strain. As the tension increased, this crack gradually widened to dissipate energy, assisted by a few smaller cracks that also contributed to energy dissipation. In contrast, SHCC-SS showed more fine cracks to dissipate energy during tension, achieving a higher tensile strain capacity. It should be noted that SHCC-LS forms many small cracks at the localization of its main crack, which is due to fiber pull-out in this region. Figures 6-5, 6-6 and Table 6-3 also reveal that SHCC-LS has the highest strain softening range of 3.137% among the three mixtures. In contrast, SHCC-SS exhibits the lowest strain softening range of 1.157%, despite having the highest tensile strain capacity. Notably, SS shows a strain softening range of 1.934% even though it lacks strain-hardening behavior, which explains why ACCCs using this mixture still achieves auxetic behavior with low load-bearing capacity in previous study [24]. As in Section 6.1, ACCCs exhibit auxetic behavior when subjected to large deformations and tend to develop primary cracks with fiber bridging during the later stages of high auxetic behavior. Consequently, the single crack bridging capacity was evaluated for the three mixtures. As illustrated in Figure 6-7, SHCC-SS generates more cracks compared to SHCC-LS to achieve a greater tensile strain capacity. However, on average, the fiber bridging within each crack in SHCC-SS sustains a lower tensile strain than that in SHCC-LS.

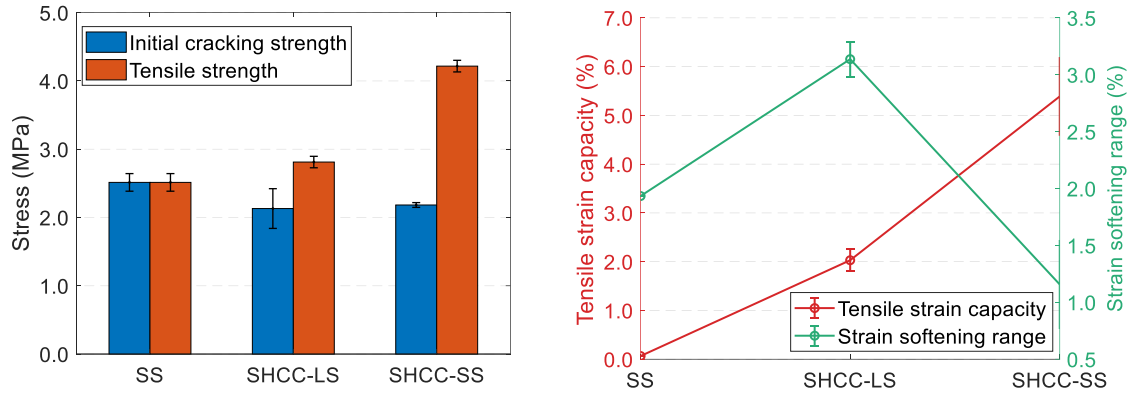


Figure 6-6 Comparison of tensile properties of different mixtures (error bars indicate standard deviation).

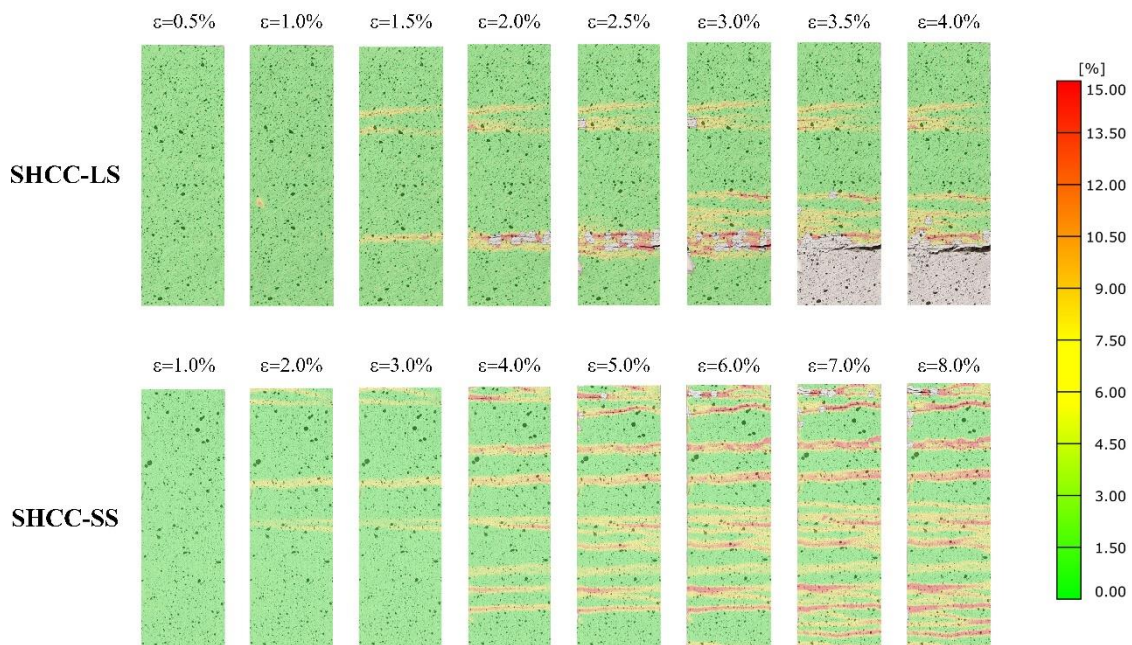


Figure 6-7 Major strain distribution during uniaxial tensile tests

ACCCs exhibit auxetic behavior through section rotation, which depends on the widening of crack openings on the tension side at the joint, while the compression side needs the material to have sufficient compressive strength to prevent failure. At the joint where ACCCs contact the loading plate, compressive forces are primarily transferred, and section rotation reduces the compressed contact area, resulting in increased compressive stress. Additionally, after self-contact of ACCCs, the structure predominantly shifts to compression to maintain its integrity, requiring the material to provide adequate compressive strength to ensure stability. The compressive behavior of the fiber-reinforced cementitious matrix was examined through uniaxial compression tests, following the test setup from our previous study [10]. These tests were conducted using the UNITRONIC machine under deformation control at a displacement rate of 0.01 mm/s. To measure displacement, two LVDTs were attached to opposite sides of each specimen. Six cubic specimens (20 mm \times 20 mm \times 20 mm) were tested in uniaxial compression for each mixture. The peak compressive stress from the stress-strain curve was used to determine the compressive capacity (i.e., compressive strength) of each mixture. [Figure](#)

6-9 and Table 6-3 compare the compressive strength of the three mixtures. SHCC-LS and SHCC-SS show higher compressive strength than SS. Generally, when cubic specimens are subjected to compressive failure, they present diagonal cracks caused by the combination of tensile stress and compressive stress. Once cracks appear, the fiber bridging capability in SHCC mixtures prevents them from further propagation. The external energy applied during compression is distributed through the formation of multiple new cracks, preserving overall structural integrity and enhancing compressive strength.

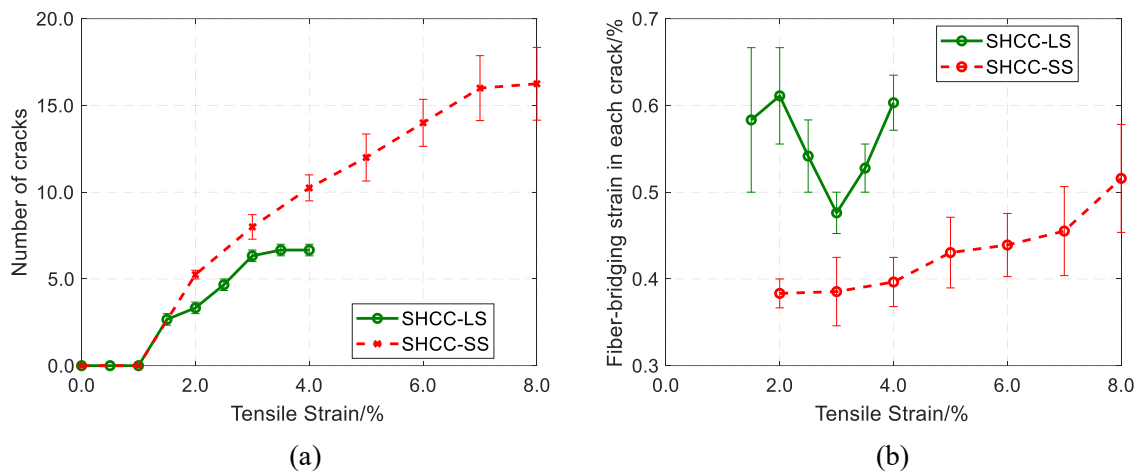


Figure 6-8 Tensile properties of the two SHCC mixtures, (a) tensile strain versus number of cracks, (b) tensile strain versus tensile strain sustained by fiber-bridging within each crack (normalized by the gauge length). (Error bars in all plots indicate standard deviation.)

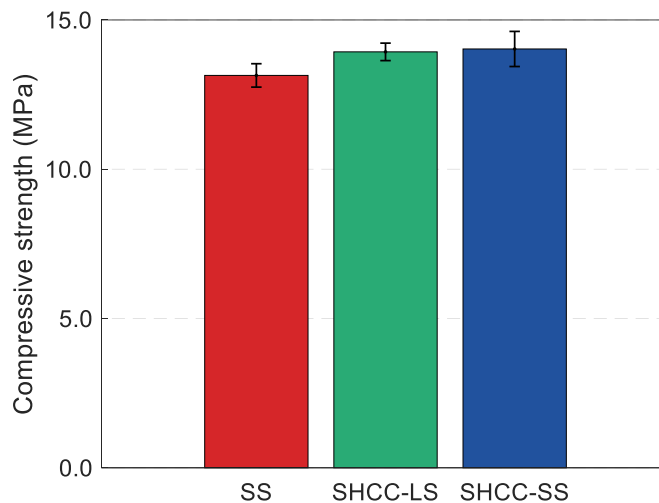


Figure 6-9 Compressive strength of different mixtures (error bars indicate standard deviation).

Table 6-3 Tensile and compressive properties of different mixtures.

Mixture	Tensile properties				Compressive properties
	Initial cracking strength (MPa)	Tensile strength (MPa)	Tensile strain capacity (%)	Strain softening range (%)	Compressive strength (MPa)
SS	2.514±0.129	2.514±0.129	0.066±0.003	1.934±0.003	13.142±0.392
SHCC-LS	2.131±0.291	2.812±0.084	2.030±0.226	3.137±0.154	13.931±0.293
SHCC-SS	2.183±0.035	4.217±0.085	5.389±0.807	1.157±0.391	14.028±0.588

6.5.2 Compressive behavior of ACCCs

(1) Compressive stress-strain curve

Figure 6-10 compares the stress-strain curves of ACCCs made from the three mixtures under uniaxial compression. The average stress-strain curves of ACCC under uniaxial compression in Figure 6-10d were obtained using the same averaging method as in Figure 6-10d. Figure 6-11 illustrates their deformation patterns under uniaxial compression. The mechanical response of ACCCs made from the three mixtures shows two distinct stages during uniaxial compression, determined by the threshold strain when contact occurs between the top and bottom ends of the central elliptical-shaped hole (i.e., self-contact within the central elliptical-shaped hole). In Stage I, the initial peak stress of ACCCs made from SHCC mixtures is approximately 0.4 MPa, which is higher than the 0.26 MPa observed in the reference, as seen in Figure 6-12. Regarding the range of high auxetic behavior in Stage I, ACCCs made from SHCC mixtures exhibit higher stress compared to the reference. ACCCs made from SHCC-LS exhibit slightly lower stress than SHCC-SS before 6.6% strain, but slightly higher stress beyond this point. The threshold strains for ACCCs using mixtures of SS, SHCC-LS, and SHCC-SS are 18.67%, 19.95%, and 19.37%, respectively. The reference has the smallest threshold strain, indicating the earliest self-contact or the shortest range of high auxetic behavior due to the largest crack in the joints. Conversely, ACCCs using SHCC mixtures have greater crack resistance capability, delaying the occurrence of self-contact in ACCCs and extending the range of high auxetic behavior. When compared to the SHCC-SS mixture, ACCCs made from SHCC-LS exhibit a higher threshold strain and a more delayed self-contact, indicating a longer range of high auxetic behavior. In Stage II, ACCCs made from SHCC-SS exhibit a rapid stress increase after self-contact and reach a higher stress level than the other two mixtures. Due to the delayed self-contact, ACCCs made from SHCC-LS show a slower stress increase in Stage II but eventually reach a higher second peak stress than the reference. The second peak stresses of ACCCs made from SHCC-LS and SHCC-SS are 6.00 MPa and 6.42 MPa, respectively, both exceeding the reference's peak stress of 5.03 MPa (see Figure 6-12 and Table 6-4). This indicates that ACCCs using SHCC exhibit enhanced crack resistance and better maintain structural integrity compared to the reference.

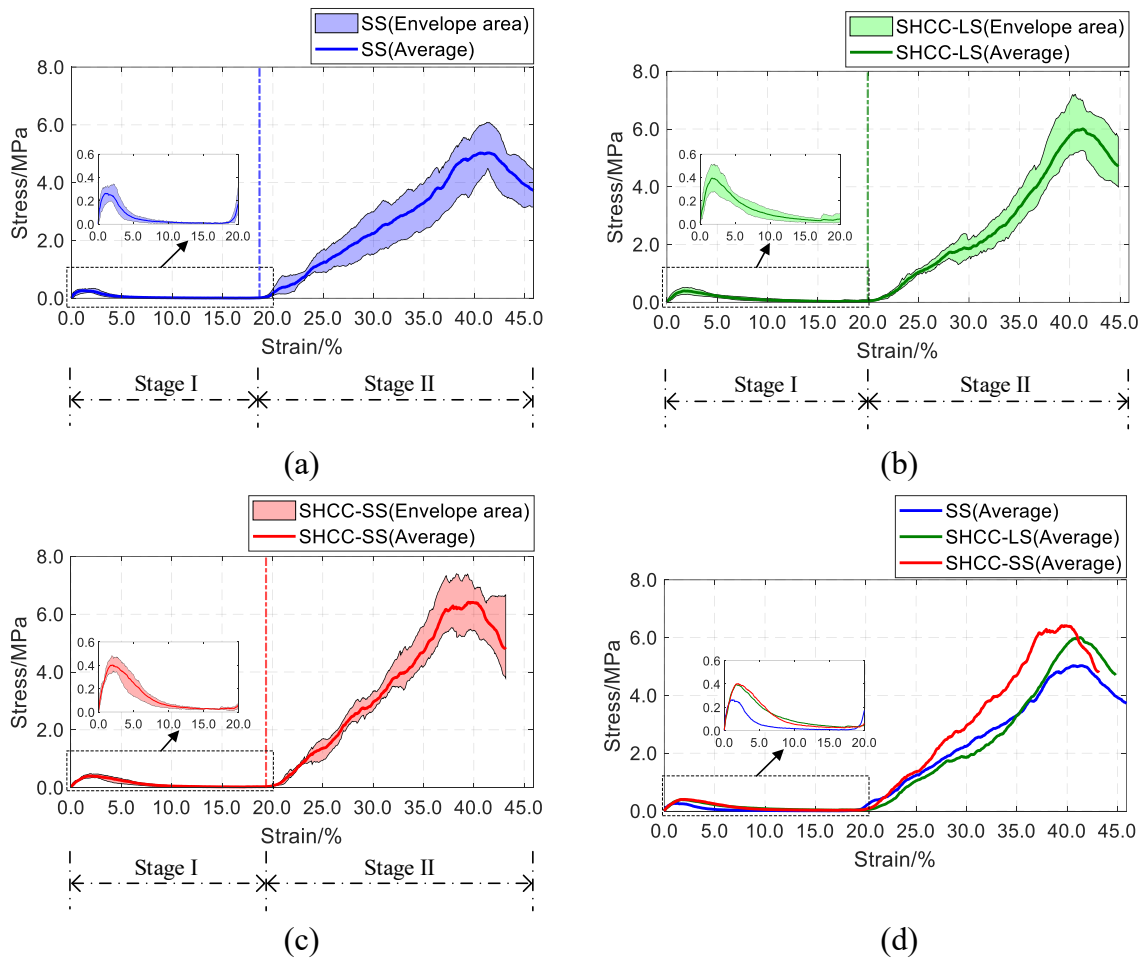


Figure 6-10 Stress-strain curve of ACCCs under uniaxial compression, (a) ACCCs using SS, (b) ACCCs using SHCC-LS, (c) ACCCs using SHCC-SS, (d) comparison of the three mixtures.

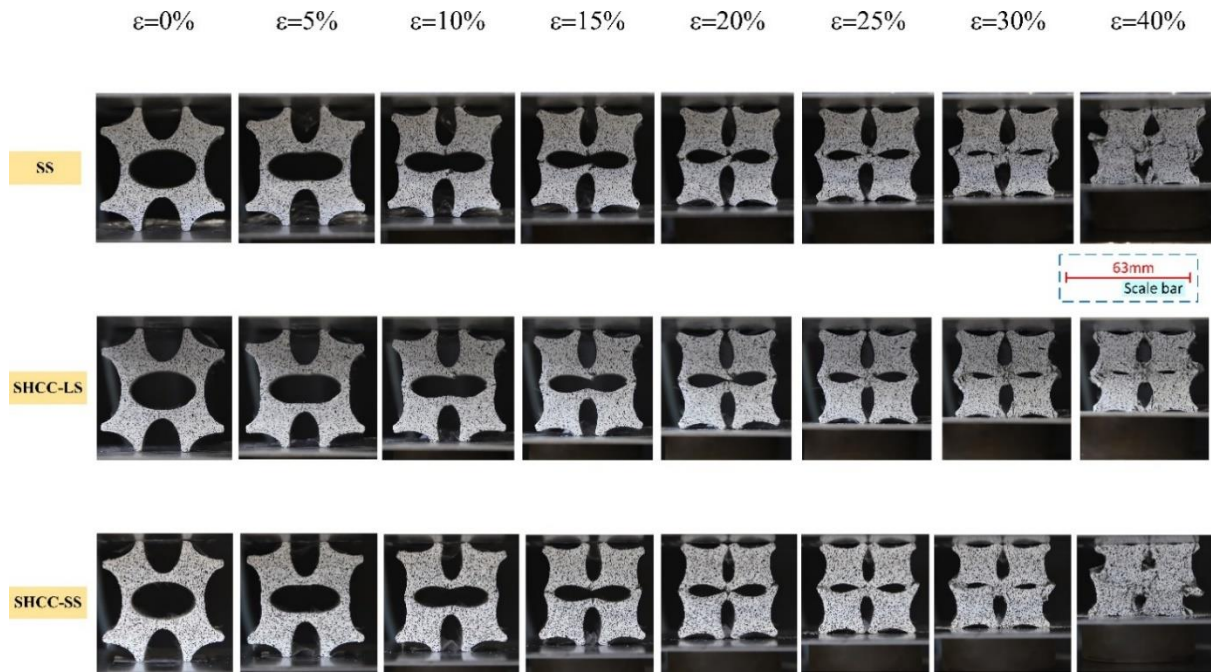


Figure 6-11 Deformation of elliptical ACCCs under uniaxial compression for the three mixtures.

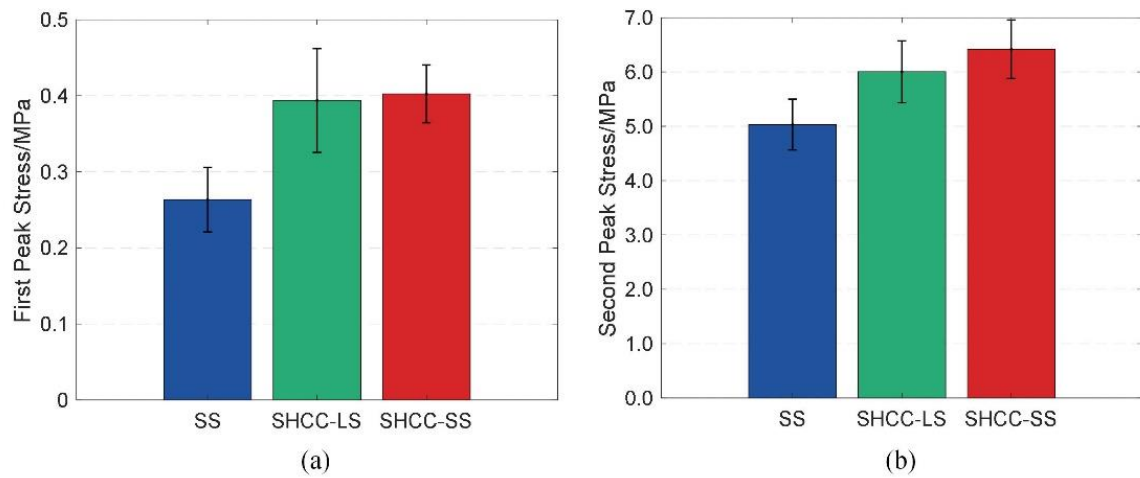


Figure 6-12 Comparison of (a) the first peak stress, (b) the second peak stress in ACCC specimens. (Error bars in all plots indicate standard deviation.)

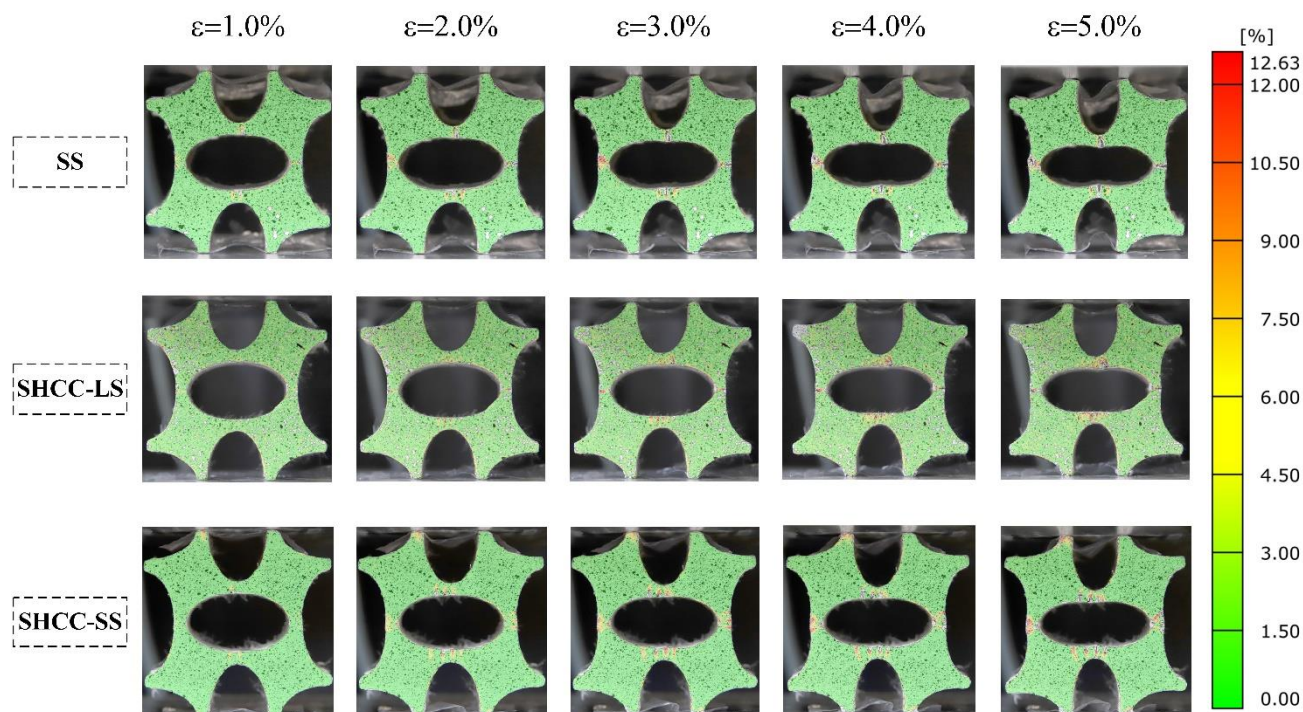
Table 6-4 Comparison of the first peak stress and the second peak stress in ACCC specimens.

Mixture	First peak stress	Second peak stress
SS	0.263±0.043	5.031±0.469
SHCC-LS	0.394±0.068	6.004±0.568
SHCC-SS	0.402±0.038	6.417±0.539

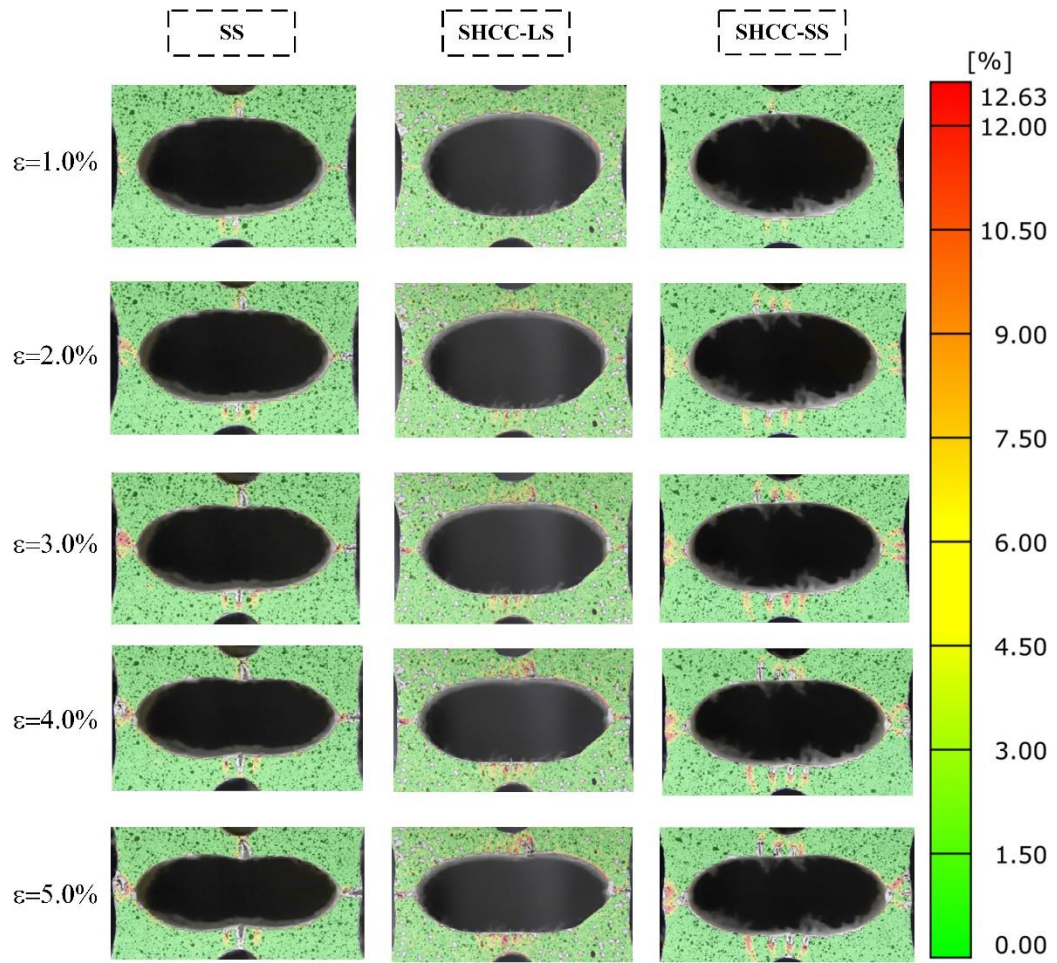
(2) Cracking behavior in the hinge joints

The auxetic behavior of ACCCs is a result of section rotation and inward folding at the post-

cracking hinge joint. The cracking behaviors of the hinge joint in the three mixtures were further analyzed, focusing on the number of cracks, the maximum crack mouth opening, and local strain. The maximum crack mouth opening represents the largest crack mouth opening among all cracks in the region, including the largest crack mouth opening formed by the merging of multiple cracks in the later stages of compression. The local strain in the joints is quantified as the ratio of the maximum crack mouth opening to the minor axis length. Using DIC analysis, the maximum crack mouth opening and the number of cracks in the joints were measured at each 5% increment of compressive strain. As shown in Figure 6-13, the number of cracks indicated by high major strain increased rapidly during this initial phase. Hence, the number of cracks was measured at every 1% increment of compressive strain up to 5%. The auxetic behavior of ACCCs is triggered by the rotation of sections around the four joints, each functioning as a hinge joint with a certain rotation stiffness. Considering symmetric deformation under uniaxial compression, the average values of these parameters for the top and bottom joints were calculated and are presented in Figure 6-14. The number of cracks in the joints increases with rising compressive strain for all three mixtures. ACCCs made from SS have significantly fewer cracks compared to those made from SHCC mixtures. Before nearly 1% strain, ACCCs made from SHCC-SS exhibit slightly more cracks than those made from SHCC-LS due to its greater strain hardening by multiple cracking. Afterwards, ACCCs made from SHCC-LS tend to develop more cracks in the joints than those made from SHCC-SS due to fiber pull-out behavior in localized regions. The maximum crack mouth opening in the joints also increases with compressive strain for all three mixtures. ACCCs made from SS have a notably larger maximum crack mouth opening compared to the SHCC mixtures. For ACCCs made from SHCC-LS, the maximum crack mouth opening is slightly lower than those made from SHCC-SS before 5% strain and becomes significantly lower after 5%.



(a) The entire structure



(b) Crack pattern at the joints.

Figure 6-13 Major strain distribution through DIC analysis.

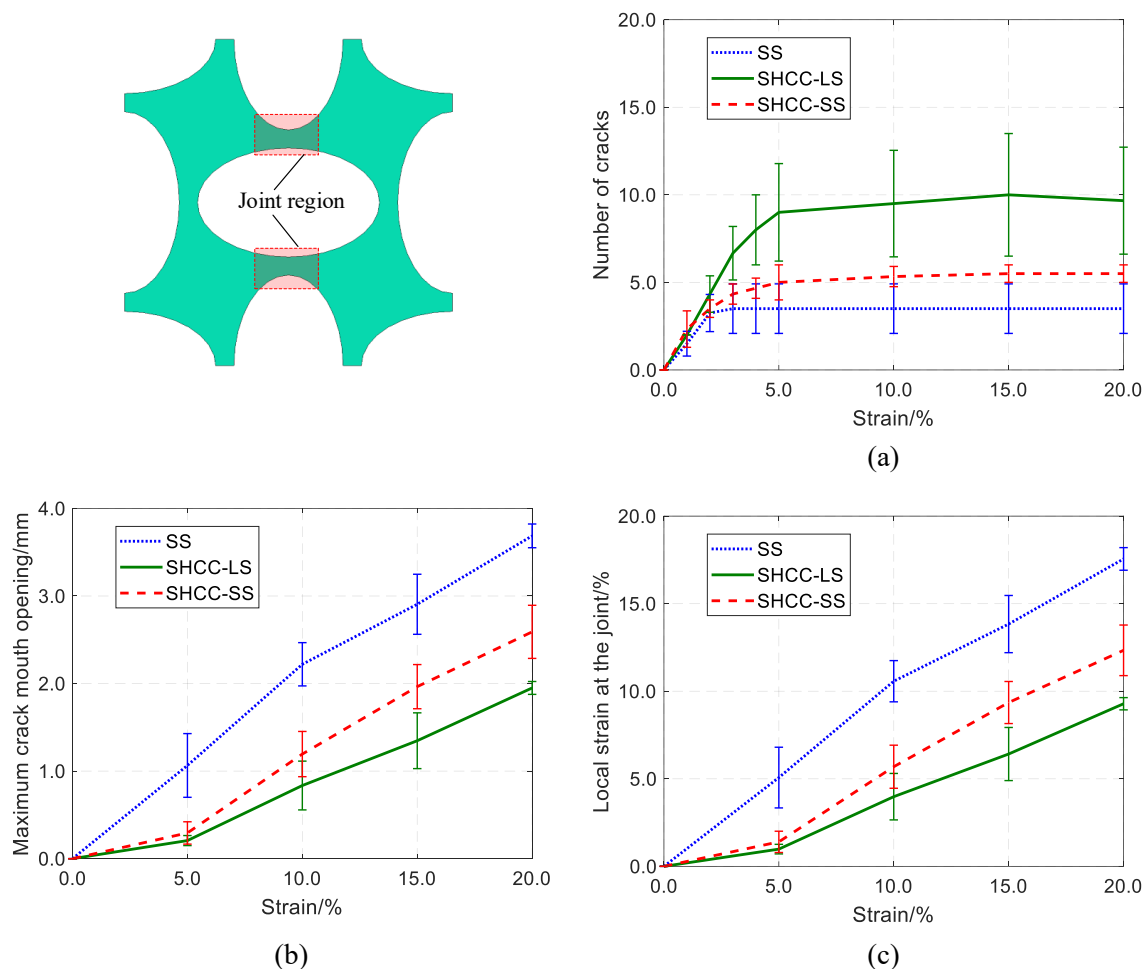


Figure 6-14 Number of cracks (a), maximum crack mouth opening (b), local strain (c) in the joints of ACCCs with the three mixtures (top and bottom joints). (Error bars in all plots indicate standard deviation.)

Figure 6-15 shows the average values of number of cracks, maximum crack mouth opening, and local strain from the left and right joints. Similarly, for all three mixtures, these parameters from the left and right joints follow the same trend as those from the top and bottom joints. Compared to the top and bottom joints, the left and right joints present fewer cracks for rotation. Because the load transfer direction in the left and right joints aligns with the structure's uniaxial compression, the transferred compressive force reduces the edge tensile stress from bending in these joints. This results in a smaller tensile region and fewer cracks. In contrast, the tensile forces at the top and bottom joints increase the edge tensile stress from bending, expanding the tensile region and leading to more cracks. Hence, the tensile stress at the top and bottom joints in SS quickly reaches yield stress and transitions into the plastic stage. Therefore, there is a significant decrease in load capacity, followed by the initiation and growth of cracks. Conversely, cracks in the left and right joints develop more slowly than those in the top and bottom joints. In SS, tensile stress is mainly managed by a single crack, which accommodates structural rotation and results in a significantly larger maximum crack mouth opening and local strain at the top and bottom joints compared to the left and right joints. In SHCC-based ACCCs, multiple cracks form to distribute the deformation required for structural rotation. This results in similar maximum crack mouth openings and local strain between the top and the bottom

joints, as well as the left and the right joints.

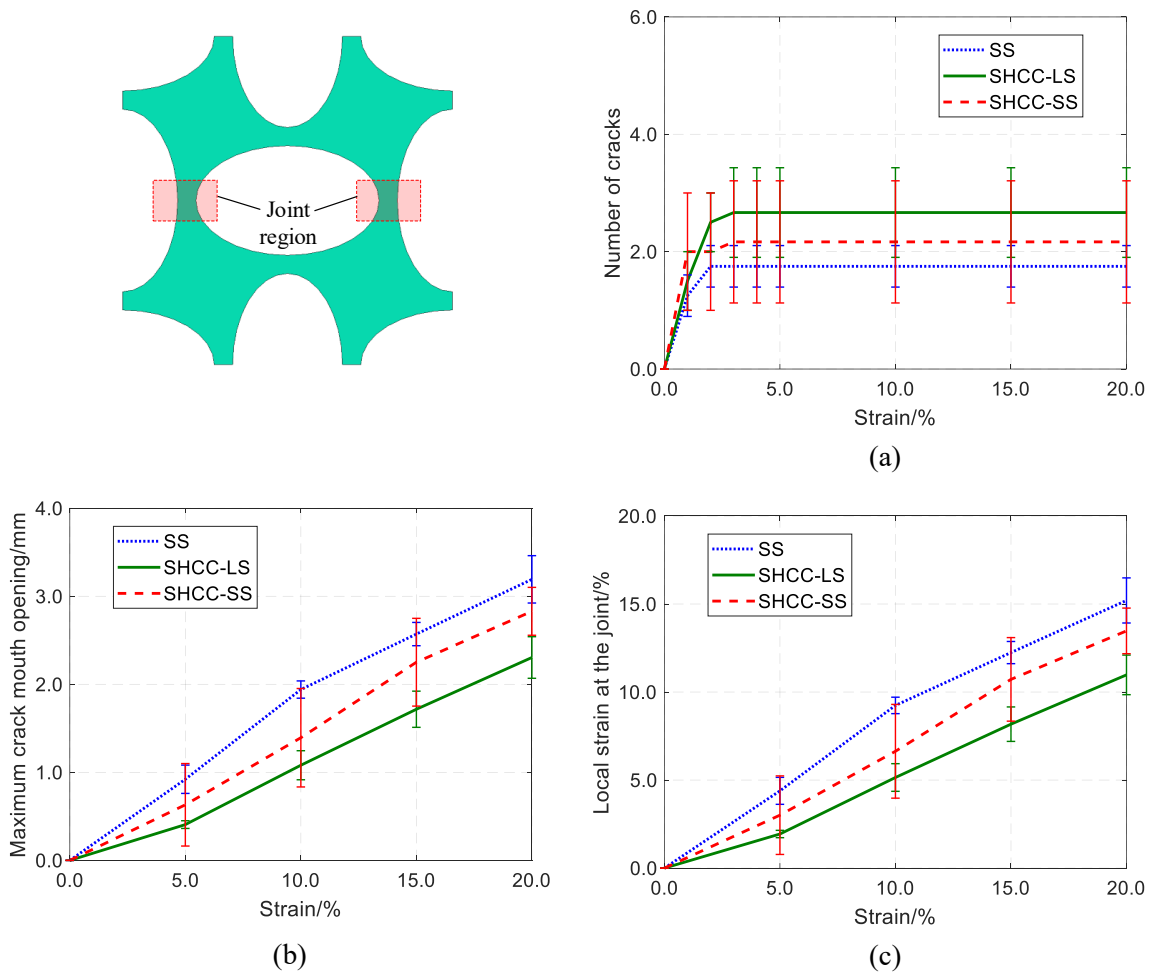


Figure 6-15 Number of cracks (a), maximum crack mouth opening (b), local strain (c) in the joints of ACCCs with the three mixtures (left and right joints). (Error bars in all plots indicate standard deviation.)

$$\nu = -\frac{\varepsilon_x}{\varepsilon_y} \quad (43)$$

Based on the DIC analysis, the Poisson's ratio of ACCCs during compression was calculated using the ratio of lateral strain to compressive strain, as described in Eq. (43). Herein, ε_x represents the ratio of the maximum projected length ($l_{x,\max}$ in Figure 6-16a) in the lateral direction (i.e., x -direction) to the initial length in the lateral direction, and ε_y denotes the compressive strain (i.e., y -direction).

As shown in Figure 6-1, the auxetic behavior in ACCCs under compression originates from the rotational movement of sections, enabled by fiber bridging at the joints of adjacent holes within the cementitious unit cell. Figure 6-16 shows the variation in lateral strain, rotation angle, and Poisson's ratio among ACCC specimens across three different mixtures. The strain range

from 15% to 20% is close to self-contact. Therefore, results for an additional 17.5% strain are included. The rotation angle in [Figure 6-16\(c\)](#) was measured using DIC. In the GOM Correlate software, DIC can determine the angle between two lines—one being the target line and the other serving as the reference axis (i.e., the x-axis or y-axis). As shown in [Figure 6-16\(a\)](#), the angle θ per frame in DIC is calculated by averaging the angles of each edge at the four end joints (marked as red edges) relative to the y-axis before self-contact occurs. The calculated angle variation during compression is then defined as the rotation angle. As shown in [Figure 6-16](#), from 0% to 15% strain, as compressive strain increases, all specimens initially exhibit a growing absolute magnitude of a negative Poisson's ratio, characterized by increased lateral contraction during compression due to more pronounced section rotation. Between 15% and 20% strain, the absolute value of Poisson's ratio continues to increase for ACCCs with SHCC-SS, whereas for the reference and ACCCs with SHCC-LS, it begins to decrease. This may be because ACCCs with SHCC-SS have the lowest absolute Poisson's ratio among the three, allowing them to continue increasing within this strain range through section rotation. Moreover, this strain range is very close to self-contact. The hinge joint crack is not perfectly centered due to the heterogeneity of the cementitious material, which could lead to the specimen reaching self-contact earlier or causing contact between the end joints (indicated by red edges in [Figure 6-16\(a\)](#)) and the loading plate. These contacts shift the load-bearing mechanism from fiber-bridging in the joints to primarily compression. With its higher compressive strength compared to SHCC-LS and the reference, SHCC-SS more effectively mitigates contact-induced damage. As a result, the section continues to rotate toward the center, further increasing lateral shrinkage strain in the x-direction and reducing the decline in the absolute value of Poisson's ratio. However, beyond 20% strain, as self-contact intensifies, the absolute magnitude of the negative Poisson's ratio decreases and begins to transition towards a positive Poisson's ratio. This happens because lateral contraction diminishes when section rotation halts and eventually transitions to lateral expansion under continued compression. The reference shows the shortest duration of a negative Poisson's ratio, with the absolute value of the negative Poisson's ratio rapidly decreasing after self-contact due to its poor crack-resistance capacity and less post-cracking fiber-bridging capacity. Nevertheless, ACCCs with SHCC demonstrate enhanced crack resistance and post-cracking fiber-bridging ability, resulting in a prolonged negative Poisson's ratio that lasts up to 40%. This accounts for their increased load-bearing capacity observed in the compressive stress-strain curve ([Figure 6-10](#)) and the maintained structural integrity ([Figure 6-11](#)). Still, the larger cracks in the reference cause more inward section rotation and greater contraction, leading to a higher absolute value of the negative Poisson's ratio before self-contact. It should be noted that ACCCs with SHCC-LS demonstrate greater lateral contraction, increased section rotation, and a higher absolute magnitude of negative Poisson's ratio before self-contact compared to ACCCs with SHCC-SS. As shown in [Figures 6-14](#) and [6-15](#), within the high auxetic behavior range, ACCCs with SHCC-LS exhibit a smaller maximum crack mouth opening in the joint and a greater number of cracks. This indicates that ACCCs with SHCC-LS can accommodate greater deformation by forming more small cracks in the joint, enabling lateral contraction and section rotation while preserving effective fiber bridging and rotational stiffness.

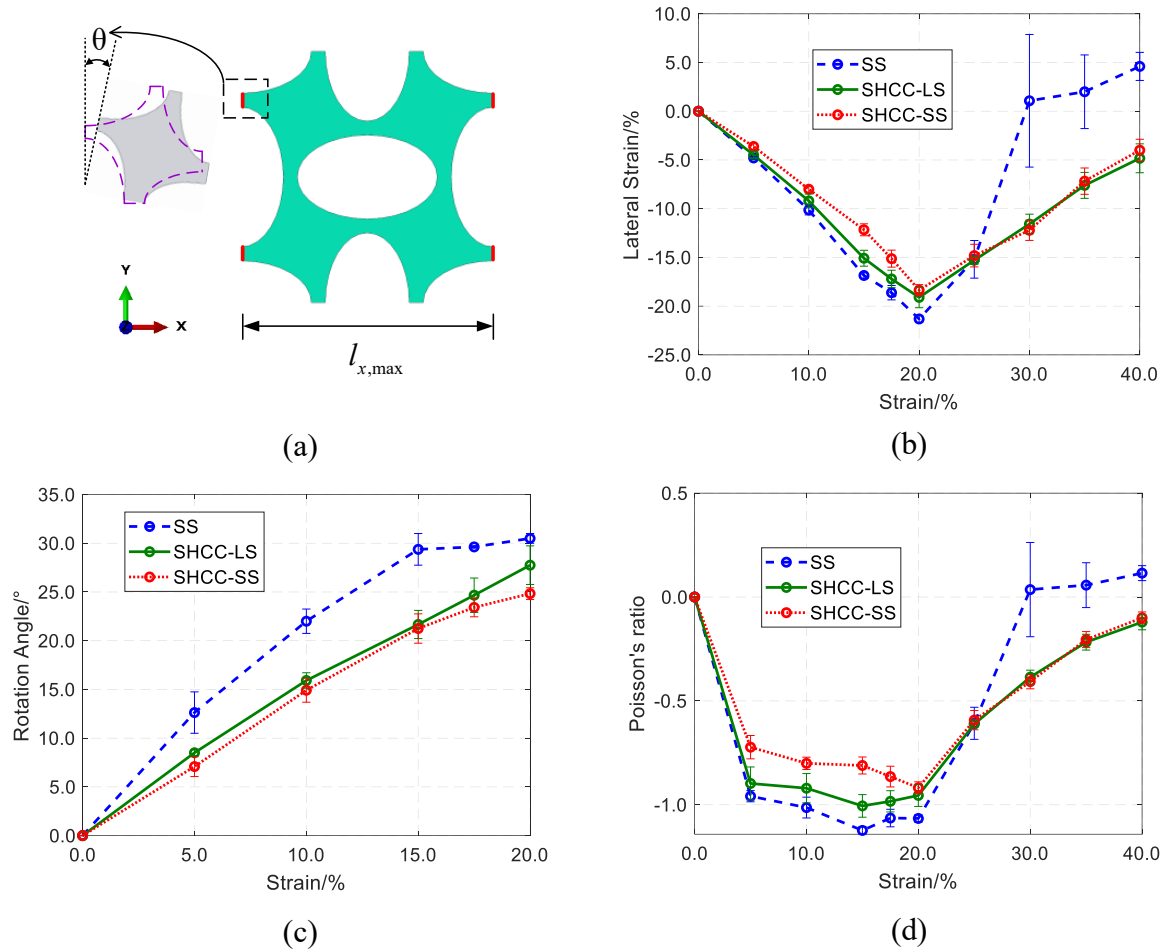


Figure 6-16 Schematic diagram of calculations in ACCCs, (b) Lateral strain variation, (c) Rotation angle variation, (d) Poisson's ratio variation. (Error bars in all plots indicate standard deviation.)

6.5.3 Energy harvesting capability of ACCCs

Figure 6-17 shows the dynamic stress of the energy harvesters for all three mixtures per cycle during cyclic loading. Three replicates of each mixture were tested in the energy harvesting experiments. Figure 6-18 illustrates the peak-to-peak voltage of the ACCC-PVDF energy harvester for the three mixtures over 10 cycles during energy harvesting experiments. Figure 6-19 and Table 6-5 shows the average voltage, dynamic stress, and recoverable deformation elasticity of the energy harvesters for all three mixtures during cyclic loading. The average values were computed over ten loading cycles. The modulus of elasticity for recoverable deformation was calculated by dividing the dynamic peak stress by the corresponding strain range.

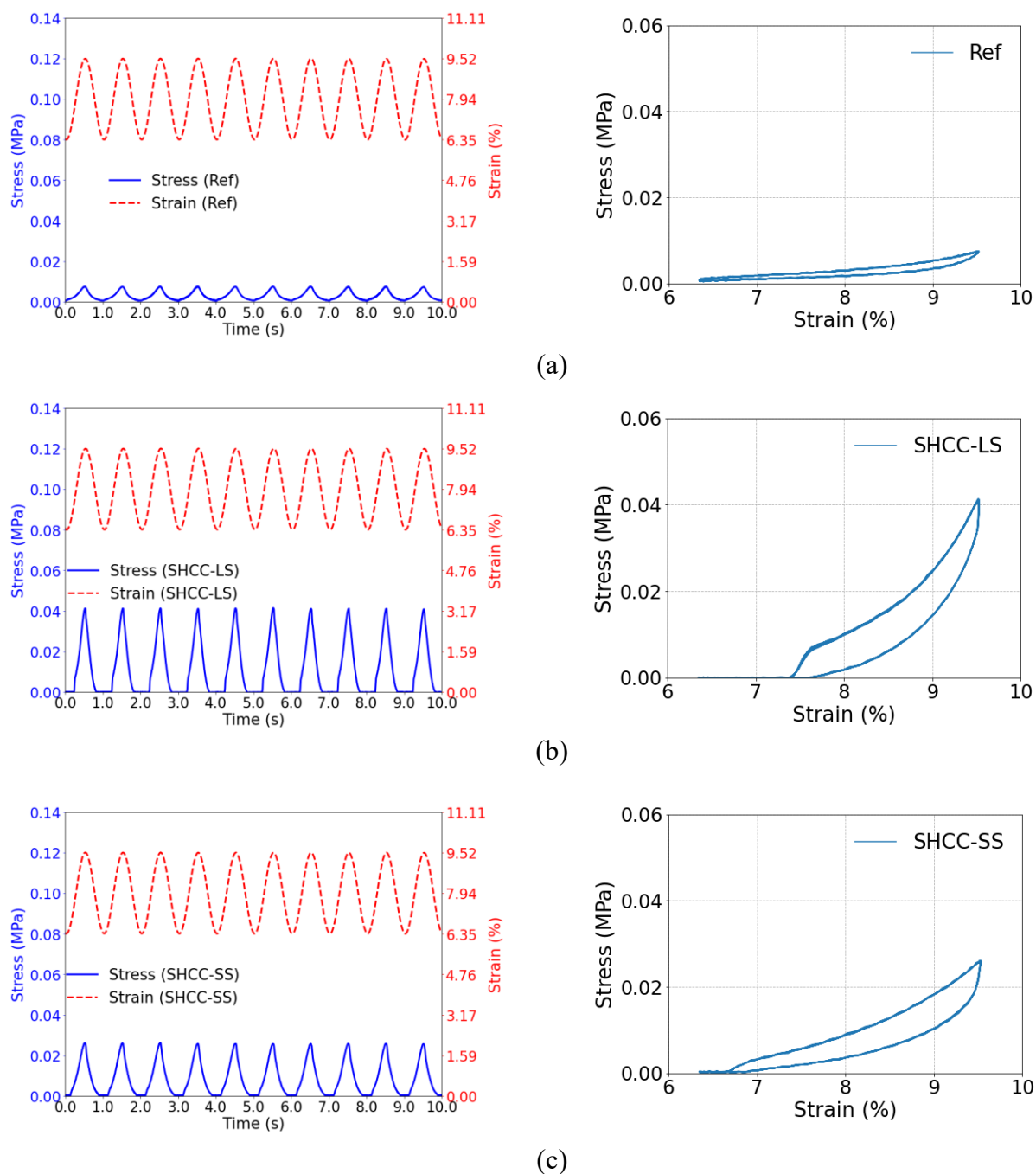
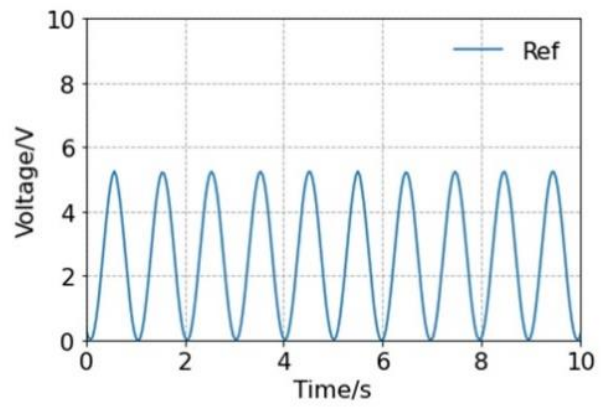
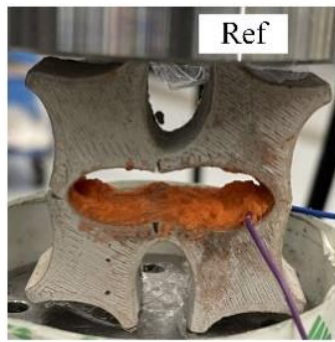


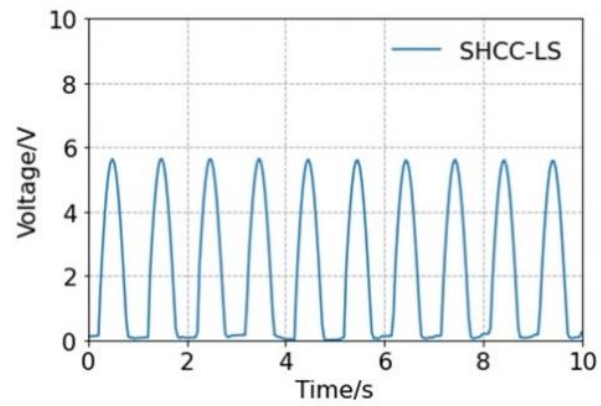
Figure 6-17 Stress-strain curve of ACCC-PVDF energy harvesters under cyclic loading.

In each cycle of sinusoidal displacement loading, the dynamic stress of the ACCC energy harvester for all three mixtures exhibits a sinusoidal pattern, as shown in Figure 6-17. Similarly, the generated voltage also follows a sinusoidal trend in response to the applied displacement variations. As the compressive displacement increases, both the dynamic stress and the voltage rise accordingly, reaching their respective peaks when the displacement reaches its maximum. Subsequently, as the loading plate gradually retracts from the ACCC specimen, both the dynamic stress and the voltage declines to nearly negligible levels. As shown in Figure 6-19 and Table 6-5, the reference exhibits a lower dynamic peak stress of 0.0084 ± 0.0007 MPa

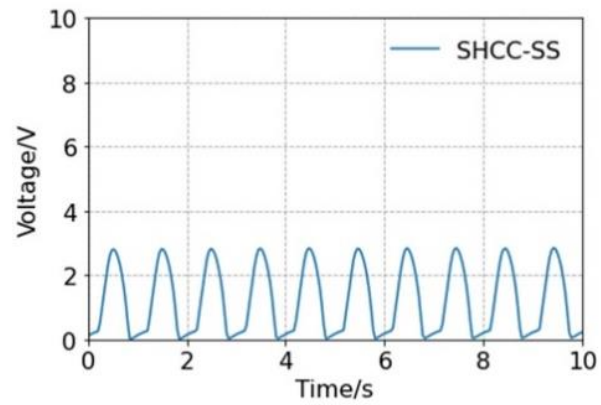
compared to the ACCC energy harvester made from SHCC mixtures. The ACCC energy harvester using the SHCC-LS mixture has a dynamic stress of 0.0322 ± 0.0042 MPa, which is higher than the 0.0283 ± 0.0022 MPa observed in the harvester with the SHCC-SS mixture. Similarly, the reference exhibits a dynamic modulus of elasticity for recoverable deformation of 0.2652 ± 0.0211 MPa, as shown in [Figure 6-19](#) and [Table 6-5](#). Compared to the reference, ACCCs made from SHCC-LS and SHCC-SS achieve dynamic elastic moduli of 1.01469 ± 0.1321 MPa and 0.8901 ± 0.0685 MPa, respectively, which are 3.8 and 3.4 times higher. Notably, the ACCC energy harvesters with the SHCC-LS mixture exhibit a greater modulus of elasticity for recoverable deformation than those with the SHCC-SS mixture. As seen in [Figure 6-19](#) and [Table 6-5](#), the energy harvester made from SHCC-LS shows the highest voltage, reaching nearly 5.20 ± 0.25 V, compared to the other two. However, the energy harvester made from the SHCC-SS mixture presents a lower voltage of 2.49 ± 0.31 V. This is lower than the 5.04 ± 0.56 V measured for the reference specimen.



(a)



(b)



(c)

Figure 6-18 Output voltage of ACCC-PVDF energy harvesters using different mixtures

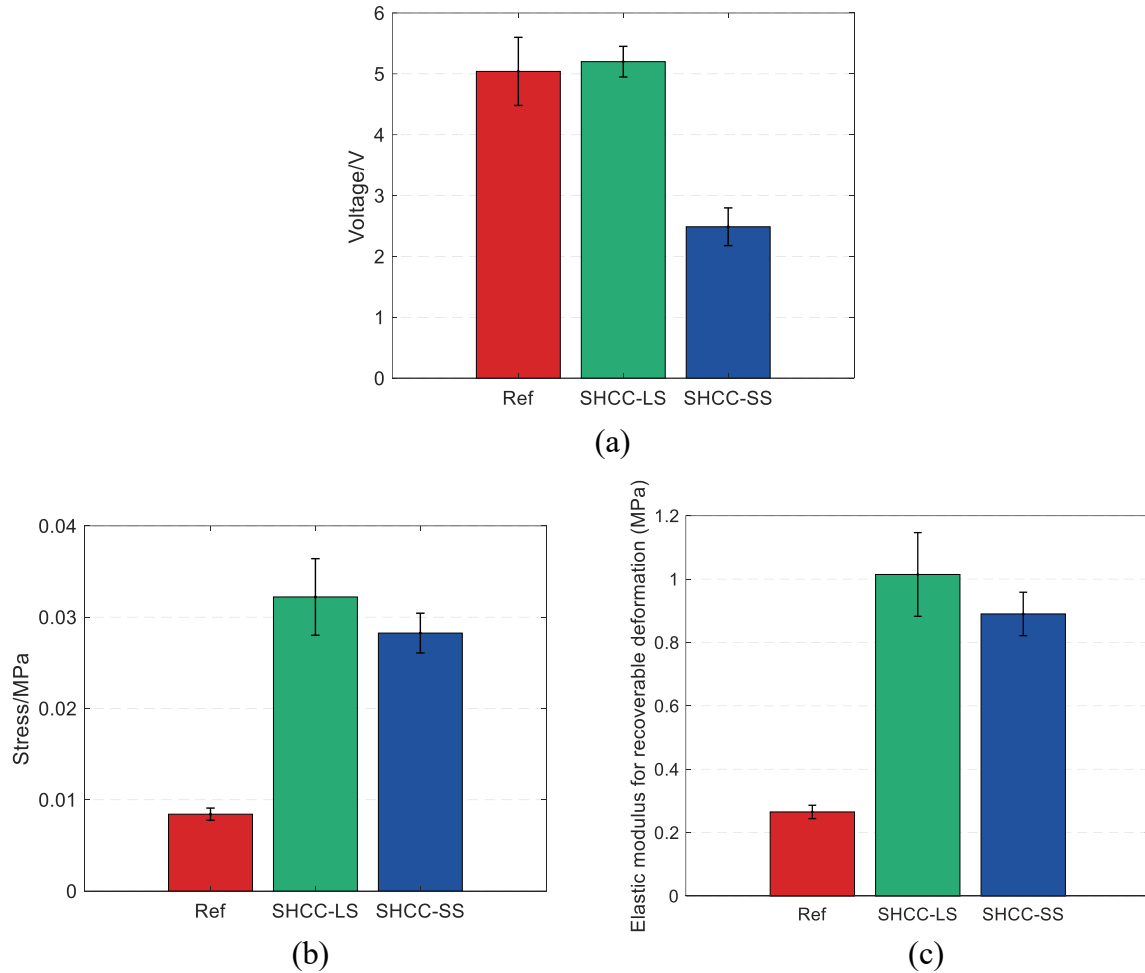


Figure 6-19 (a) Averaging output voltage per cycle, (b) peak-to-peak stress per cycle, (c) recoverable deformation elasticity per cycle during cyclic loading.

Table 6-5 Comparison of energy harvesting results of ACCE energy harvesters with the three mixtures.

Mixture	Voltage (V)	Dynamic peak stress (MPa)	Elastic modulus for recoverable deformation (MPa)
SS	5.04±0.56	0.0084±0.0007	0.2652±0.0211
SHCC-LS	5.20±0.25	0.0322±0.0042	1.01469±0.1321
SHCC-SS	2.49±0.31	0.0283±0.0022	0.8901±0.0685

In general, when the PVDF is fully bonded to the cementitious material in the hinge-joint region, strain should be transferred without loss. However, due to the limited bonding strength of the adhesive layer, only a portion of the force can be effectively transmitted, often resulting in partial debonding. Following such debonding, strain transfer predominantly occurs through friction between their surfaces. Consequently, in hinge-joint regions with higher fiber bridging

capacity, the frictional force is greater, leading to an increased strain transmission to the PVDF. In the study, ACCCs using SHCC-LS exhibit higher stiffness under cyclic loading. The enhanced fiber bridging capacity in the hinge-joint region increases the frictional force. This greater friction enables more effective strain transfer to the PVDF. As a result, the voltage output reaches 5.20 ± 0.25 V, surpassing that of ACCCs fabricated with SHCC-SS. Although the SS-based ACCCs exhibit weaker fiber bridging and lower frictional force transmission, they develop larger crack openings at the hinge joints. These wider cracks contribute to a more tortuous surface morphology and greater recoverable strain during cyclic loading, which in turn enhances the energy harvesting performance. Consequently, the voltage output remains relatively high at 5.04 ± 0.56 V, only slightly lower than that observed in SHCC-LS specimens. The underlying mechanisms have been discussed in detail in [Chapters 3 and 5](#). As shown in [Figure 6-16](#), ACCCs with SS demonstrate larger lateral strain and rotation angles than those with SHCC-LS, reflecting a greater capacity for recoverable strain. In contrast, ACCCs utilizing SHCC-SS exhibit the smallest lateral strain and rotation angles. This indicates the lowest recoverable strain. Consequently, they produce the lowest voltage output during cyclic loading. Although SHCC-SS-based ACCCs exhibit higher fiber bridging forces and greater frictional transmission compared to those incorporating the SS mixture, their limited recoverable strain reduces the overall effectiveness in voltage generation. In contrast, as illustrated in [Figure 6-16](#), ACCCs incorporating SHCC-LS show greater lateral strain and larger rotation angles compared to their SHCC-SS counterparts. Although SHCC-LS exhibits the smallest maximum crack width among the three mixtures ([Figures 6-14 and 6-15](#)), it forms the largest number of cracks. Furthermore, the fiber bridging capacity in each crack of SHCC-LS supports a higher strain level than that of SHCC-SS (see [Figure 6-8](#)). These factors collectively enable the joints in the ACCCs with SHCC-LS to achieve a greater recoverable strain.

6.6 CONCLUSIONS

In this study, elliptical-shaped ACCCs were developed using two types of strain-hardening cementitious composites (SHCCs)—one exhibiting shortened softening behavior and the other prolonged softening—via additive manufacturing-assisted casting. The ACCC specimens were evaluated for their mechanical behavior under uniaxial compression, including compressive stress-strain curve, Poisson's ratio variation, deformation pattern, local joint analysis. Subsequent cyclic loading tests were conducted to assess their energy harvesting capabilities. The results were compared against a reference mixture composed of a strain-softening fiber-reinforced cementitious composite. The key findings of this research are summarized as follows:

- Compared to the reference (SS), ACCCs made with SHCC mixtures accommodate greater joint rotation by developing multiple cracks with strain hardening. This postpones the onset of primary cracks and further reduces the opening of the primary crack. In the later stages, the significant section rotation of ACCCs results in the formation of a primary crack in the joints. Utilizing SHCC with extended softening helps maintain effective fiber bridging within the primary crack and enhance rotational stiffness in the pseudo-hinge joints. As a result, this SHCC mixture enhances load-bearing capacity and recoverable deformation elasticity within the high auxetic

- behavior range of ACCCs.
- Compared to the reference (SS), ACCCs made from SHCC exhibit superior load-bearing capacity during high auxetic behavior range and stable auxetic behavior under uniaxial compression. Following self-contact, ACCCs made from SHCC mitigate the reduction in the magnitude of the negative Poisson's ratio due to their crack-resistance capacity and sustain a negative Poisson's ratio up to a considerably high compressive strain. Their strong fiber-bridging and crack resistance capabilities enhance the structure's ductility and toughness, preventing splitting failure and preserving structural integrity. As a result, they show higher specific energy absorption than the reference (SS).
 - ACCCs incorporating SHCC-LS demonstrate superior performance under cyclic loading. This is due to their higher stiffness and enhanced fiber bridging capacity in the hinge-joint region. The increased fiber bridging capacity leads to greater frictional resistance and enables more efficient strain transfer to the PVDF. As a result, the voltage output is higher than that of ACCCs made with SHCC-SS. Although SHCC-SS-based ACCCs exhibit relatively strong fiber bridging and frictional transmission, their limited recoverable strain reduces their energy harvesting efficiency. In contrast, SHCC-LS forms the greatest number of cracks in the joint region. Combined with strong fiber bridging, this contributes to greater recoverable strain. Consequently, SHCC-LS-based ACCCs achieve more effective voltage generation.

The use of an SHCC mixture with extended softening behavior enables stable auxetic behavior for energy harvesting applications, attributed to its enhanced fiber bridging capacity and superior crack resistance. This makes it applicable for various ACCC geometries and further geometric optimization, thereby expanding the potential engineering applications of auxetic cementitious energy harvesters across a range of loading conditions and service scenarios. A detailed discussion of this will be provided in Chapter 7.

REFERENCES

- [1] S. He, Y. Chen, M. Liang, E.-H. Yang, E. Schlangen, Distribution of porosity surrounding a microfiber in cement paste, *Cement and Concrete Composites*, 142 (2023) 105188. <https://doi.org/10.1016/j.cemconcomp.2023.105188>.
- [2] A.M. Tawfek, Z. Ge, H. Yuan, N. Zhang, H. Zhang, Y. Ling, Y. Guan, B. Šavija, Influence of fiber orientation on the mechanical responses of engineering cementitious composite (ECC) under various loading conditions, *Journal of Building Engineering*, 63 (2023) 105518. <https://doi.org/10.1016/j.jobbe.2022.105518>.
- [3] Y. Gan, M. Liang, E. Schlangen, K. van Breugel, B. Šavija, Two scale models for fracture behaviors of cementitious materials subjected to static and cyclic loadings, *Construction and Building Materials*, 426 (2024) 136107. <https://doi.org/10.1016/j.conbuildmat.2024.136107>.
- [4] J. Sun, J. Xie, Y. Zhou, Y. Zhou, A 3D three-phase meso-scale model for simulation of chloride diffusion in concrete based on ANSYS, *International Journal of Mechanical Sciences*, 219 (2022) 107127. <https://doi.org/10.1016/j.ijmecsci.2022.107127>.
- [5] C. Li Victor, K.Y. Leung Christopher, Steady-State and Multiple Cracking of Short Random Fiber Composites, *Journal of Engineering Mechanics*, 118 (1992) 2246-2264. [10.1061/\(ASCE\)0733-9399\(1992\)118:11\(2246\)](https://doi.org/10.1061/(ASCE)0733-9399(1992)118:11(2246)).

- [6] D.B. Marshall, B.N. Cox, A J-integral method for calculating steady-state matrix cracking stresses in composites, *Mechanics of Materials*, 7 (1988) 127-133.
[https://doi.org/10.1016/0167-6636\(88\)90011-7](https://doi.org/10.1016/0167-6636(88)90011-7).
- [7] S. Zhang, V.C. Li, G. Ye, Micromechanics-guided development of a slag/fly ash-based strain-hardening geopolymer composite, *Cement and Concrete Composites*, 109 (2020) 103510.
<https://doi.org/10.1016/j.cemconcomp.2020.103510>.
- [8] T. Kanda, V.C. Li, Practical Design Criteria for Saturated Pseudo Strain Hardening Behavior in ECC, *Journal of Advanced Concrete Technology*, 4 (2006) 59-72. 10.3151/jact.4.59.
- [9] B. Nematollahi, J. Sanjayan, F.U.A. Shaikh, Matrix design of strain hardening fiber reinforced engineered geopolymer composite, *Composites Part B: Engineering*, 89 (2016) 253-265.
<https://doi.org/10.1016/j.compositesb.2015.11.039>.
- [10] J. Xie, Y. Xu, Z. Meng, M. Liang, Z. Wan, B. Šavija, Peanut shaped auxetic cementitious cellular composite (ACCC), *Construction and Building Materials*, 419 (2024) 135539.
<https://doi.org/10.1016/j.conbuildmat.2024.135539>.
- [11] J. Xie, Y. Xu, Z. Wan, A. Ghaderiaram, E. Schlangen, B. Šavija, Auxetic cementitious cellular composite (ACCC) PVDF-based energy harvester, *Energy and Buildings*, 298 (2023) 113582.
<https://doi.org/10.1016/j.enbuild.2023.113582>.
- [12] Y. Xu, E. Schlangen, M. Luković, B. Šavija, Tunable mechanical behavior of auxetic cementitious cellular composites (CCCs): Experiments and simulations, *Construction and Building Materials*, 266 (2021) 121388. <https://doi.org/10.1016/j.conbuildmat.2020.121388>.
- [13] C.-C. Hung, Y.-F. Su, Y.-M. Su, Mechanical properties and self-healing evaluation of strain-hardening cementitious composites with high volumes of hybrid pozzolan materials, *Composites Part B: Engineering*, 133 (2018) 15-25.
<https://doi.org/10.1016/j.compositesb.2017.09.005>.
- [14] V.C. Li, Tailoring ECC for Special Attributes: A Review, *International Journal of Concrete Structures and Materials*, 6 (2012) 135-144. 10.1007/s40069-012-0018-8.
- [15] V.C. Li, On Engineered Cementitious Composites (ECC) A Review of the Material and Its Applications, *Journal of Advanced Concrete Technology*, 1 (2003) 215-230. 10.3151/jact.1.215.
- [16] Y.-F. Su, R.R. Kotian, N. Lu, Energy harvesting potential of bendable concrete using polymer based piezoelectric generator, *Composites Part B: Engineering*, 153 (2018) 124-129.
<https://doi.org/10.1016/j.compositesb.2018.07.018>.
- [17] J. Xie, Y. Xu, Z. Wan, A. Ghaderiaram, E. Schlangen, B. Šavija, Modelling of energy harvesting with bendable concrete and surface-mounted PVDF, *Smart Materials and Structures*, 33 (2024) 085008. 10.1088/1361-665X/ad43cb.
- [18] E.-H. Yang, V.C. Li, Tailoring engineered cementitious composites for impact resistance, *Cement and Concrete Research*, 42 (2012) 1066-1071.
<https://doi.org/10.1016/j.cemconres.2012.04.006>.
- [19] S. He, S. Mustafa, Z. Chang, M. Liang, E. Schlangen, M. Luković, Ultra-thin Strain Hardening Cementitious Composite (SHCC) layer in reinforced concrete cover zone for crack width control, *Engineering Structures*, 292 (2023) 116584.
<https://doi.org/10.1016/j.engstruct.2023.116584>.
- [20] W. Zhou, Y. Zhang, L. Ma, V.C. Li, Influence of printing parameters on 3D printing engineered cementitious composites (3DP-ECC), *Cement and Concrete Composites*, 130 (2022) 104562.
<https://doi.org/10.1016/j.cemconcomp.2022.104562>.
- [21] K. Tosun-Felekoğlu, B. Felekoğlu, R. Ranade, B.Y. Lee, V.C. Li, The role of flaw size and fiber distribution on tensile ductility of PVA-ECC, *Composites Part B: Engineering*, 56 (2014) 536-545.
<https://doi.org/10.1016/j.compositesb.2013.08.089>.

- [22] K. Rokugo, T. Kanda, H. Yokota, N. Sakata, Applications and recommendations of high performance fiber reinforced cement composites with multiple fine cracking (HPFRCC) in Japan, *Materials and Structures*, 42 (2009) 1197-1208. 10.1617/s11527-009-9541-8.
- [23] H.-H. Huang, K.-S. Chen, Design, analysis, and experimental studies of a novel PVDF-based piezoelectric energy harvester with beating mechanisms, *Sensors and Actuators A: Physical*, 238 (2016) 317-328. <https://doi.org/10.1016/j.sna.2015.11.036>.
- [24] Y. Xu, H. Zhang, E. Schlangen, M. Luković, B. Šavija, Cementitious cellular composites with auxetic behavior, *Cement and Concrete Composites*, 111 (2020) 103624. <https://doi.org/10.1016/j.cemconcomp.2020.103624>.

7

BAYESIAN-DRIVEN MODULATION OF RECOVERABLE STRAIN IN AUXETIC CEMENTITIOUS CELLULAR COMPOSITES FOR OPTIMAL ENERGY HARVESTERS

In Chapter 6, a SHCC mixture with enhanced softening behavior was developed to improve fiber-bridging performance within the joints of ACCCs. This improvement enables the realization of auxetic behavior across various ACCC geometries, making them suitable for energy harvesting applications. Consequently, different geometric configurations of ACCCs can be systematically compared in terms of their energy harvesting potential, allowing for the identification of an optimal design. However, the intrinsic brittleness of cementitious materials may cause structural splitting during geometric adjustments of the ACCC, thereby compromising its auxetic behavior. This presents a major challenge for the efficient and robust design of ACCC-based energy harvesters. To overcome the limitations of time-consuming experimental trials, the numerical models developed in Chapters 4 and 5 can be employed to generate simulation datasets. Nevertheless, model-based computations also require substantial time to produce large datasets. To address this issue and enhance optimization efficiency, a learning-driven framework is proposed herein that integrates the energy harvesting model with Bayesian Optimization (BO) to guide the design of the ACCC energy harvester. The optimal geometry identified through this approach was subsequently fabricated using additive manufacturing-assisted casting and experimentally validated for its energy harvesting capacity.

7.1 INTRODUCTION

In [Chapter 6](#), a SHCC mixture with enhanced softening behavior was developed to improve fiber-bridging capacity within the joints of ACCCs. This enhancement facilitates the manifestation of auxetic behavior across a range of ACCC geometries, thereby expanding their potential for energy harvesting applications. As a result, various geometric configurations of ACCCs can be systematically evaluated and compared with respect to their energy harvesting efficiency, enabling the identification of an optimal structural design. However, in contrast to conventional cementitious cubes, ACCCs possess complex geometries that exhibit high sensitivity to geometric alterations. Modifying their geometry can increase their vulnerability to damage and failure under load. Hence, optimizing their geometry with auxetic behavior and recoverable deformation for multifunctional applications, such as energy harvesting and sensing, poses significant challenges.

Designing the intricate structure of ACCCs has so far been dependent on experimental trial-and-error methods. However, the complexity of preparing ACCC specimens, the extended curing period (typically 28 days), and the uncertainties introduced by the heterogeneity of cementitious materials and manual casting make large-scale experimental trials both time-consuming and costly. Hence, modelling is essential for optimizing the performance of ACCCs. Wan et al. [\[1, 2\]](#) utilized a deep neural network (DNN) and reinforcement learning approach to optimize the vascular structure of self-healing concrete. This optimization was based on finite element models calibrated by experiments, aiming to enhance mechanical properties such as peak load and fracture energy. Ohno et al. [\[3\]](#) proposed a novel framework for the simulation and reinforcement learning-driven design of truss-type architected cement-based materials, enabling the efficient identification of high-performance configurations. Lyngdoh et al. [\[4\]](#) integrated FEM with machine learning to predict Poisson's ratios in cementitious cellular composites. Their focus was on evaluating a negative Poisson's ratio by strategically positioning elliptical voids, without considering plasticity or post-crack behavior. Nevertheless, ML often involves solving many numerical models to create datasets for training a surrogate model, which is used for further optimization. This process incurs substantial computational costs due to the long computing times of numerical models.

Recently, bayesian optimization (BO) has emerged as an interactive optimization method that effectively navigates large design spaces, which are challenging for traditional approaches. It guides a limited number of numerical models toward highly probable optimal results while generating surrogate models that describe the properties of interest based on the design variables [\[5, 6\]](#). Moreover, BO enables optimization to start directly without requiring a training phase and achieves global optimization with fewer sampling points. Vangelatos et al. [\[7\]](#) employed a novel Bayesian approach, "evolutionary Monte Carlo sampling," to optimize the strain energy density of a polymeric material-based architected microlattice by strategically arranging defects to delay catastrophic failure. Kuszczak et al. [\[8\]](#) developed a computational framework that uses BO to identify optimal lattice configurations with varied strut thicknesses in polymeric materials. This approach enhances uniaxial elastic stiffness and increases plastic or buckling strength. However, no research has used BO in any ACMs, including ACCCs, to date. This is because ACCC models face challenges in parametric modelling for dataset creation and optimization. These challenges stem from the plasticity and cracking of the

cementitious matrix, as well as the complex contact boundary conditions associated with intricate geometries.

To achieve high-performance design of ACCC energy harvester, this study developed a parametric energy harvesting model, integrating the CDP and second elasticity models, to optimize ACCCs for recoverable hinge-like strain capacity across various geometric configurations. An interactive BO framework linked with the FEM was established, using the average strain of cementitious material bonded to the piezoelectric film as the objective function. BO constraints excluded cases exhibiting splitting or non-auxetic behavior under compression. The optimized shape was fabricated using additive manufacturing-assisted casting and experimentally tested for output voltage. Geometric and mechanical evolution during BO iterations were further investigated, offering insights for high-performance design. This learning-driven approach enhances auxetic cementitious energy harvesters, demonstrating significant potential as a versatile power source for sustainable and smart cities.

7.2 MATERIALS AND METHODS

7.2.1. Materials and specimen preparation

As in [Chapter 3](#), the fabrication of ACCCs followed the "indirect printing" process [9], as shown in [Figure 7-1](#). First, a unit cell with specific dimensions was designed and produced using fused deposition modeling with a 3D printer (Ultimaker S5). ABS was selected as the printing material. The printed ABS structures were then placed inside a cardboard box. Next, a two-component silicone rubber, Poly-Sil PS 8510, was mixed in a 1:1 mass ratio and poured into the box. The silicone rubber was left to cure at room temperature for at least one hour until it hardened. Once solidified, the silicone rubber was removed from the box to be used as a mold for casting the cementitious materials. Herein, 8510 silicone rubber, with a Shore hardness of 10 A, provides adequate stiffness for use as a mold while maintaining the flexibility needed for easy demolding.

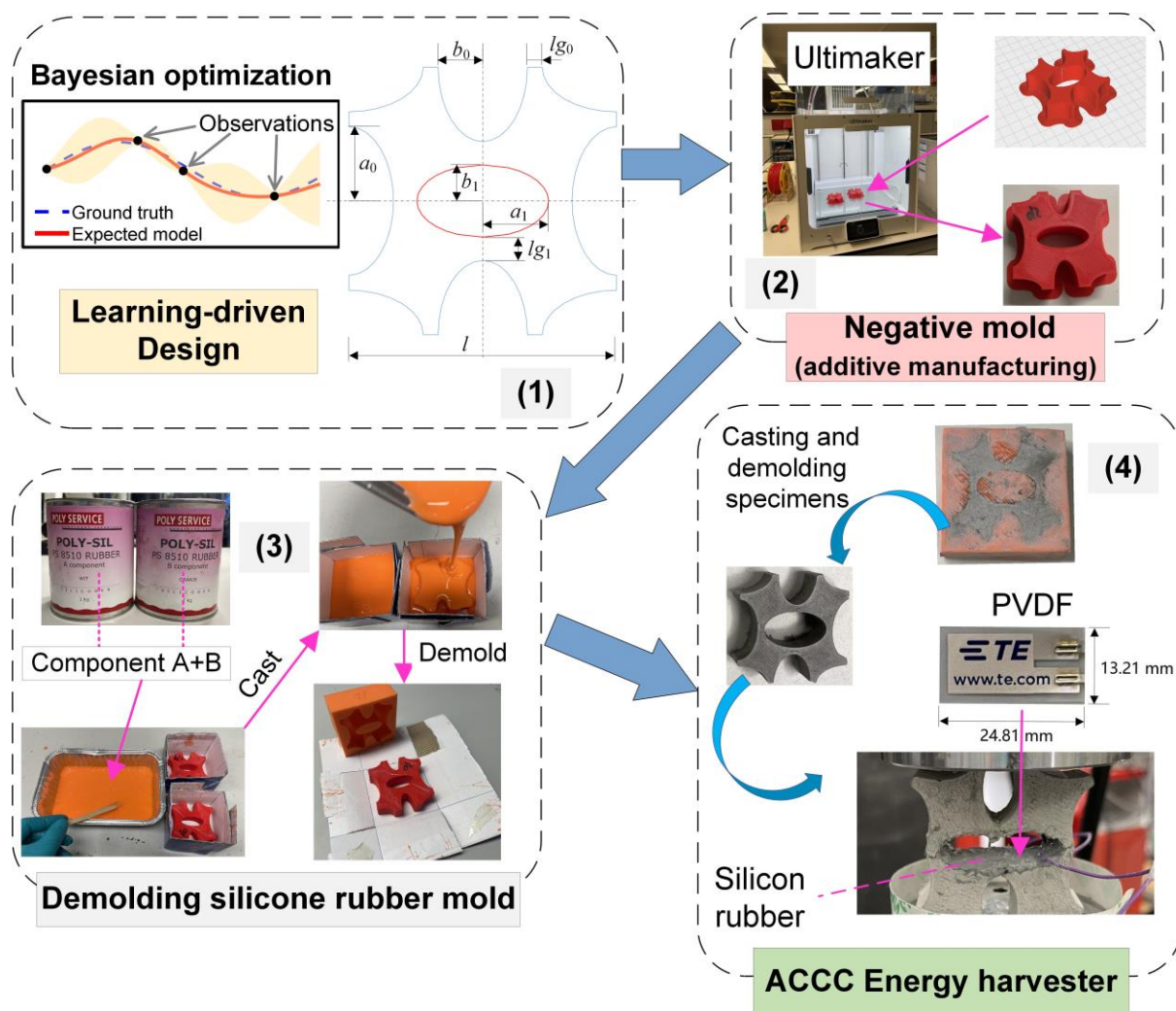


Figure 7-1 Specimen preparation

Table 7-1 Mixture proportions of ACCCs.

C	FA	S/(C + FA)	W/(C + FA)	SP/(C + FA)	VMA/(C + FA)	PVA Fiber (by volume)
1.0	1.2	0.37	0.46	0.0016	0.0003	2%

Table 7-2 Material properties of PVA fibers.

Fiber type	Diameter (μm)	Length (mm)	Tensile strength (MPa)	Young's modulus (Gpa)	Density (g/cm^3)	Ultimate strain
PVA(RECS15)	40	8	1.6	41	1.3	6.0%

The SHCC mixture with extended softening (SHCC-LS) developed in Chapter 6 was used as the base material for the ACCCs, with the mixture proportions detailed in Table 7-1. Fiber specifications are provided in Table 7-2. The mixing and curing procedures of specimens were consistent with those described in Chapter 6. The PVDF was bonded around the ligament region of the central elliptical hole in the specimen using silicone rubber (Poly-Sil PS8540) and allowed to cure for at least 12 hours until fully hardened. This is because 8540 silicone

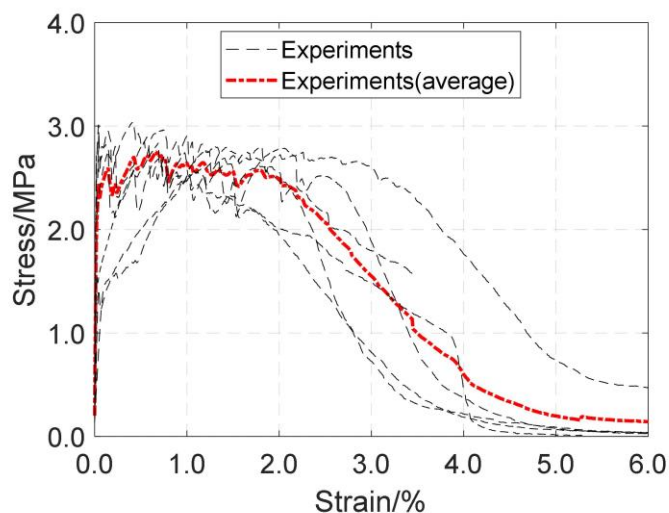
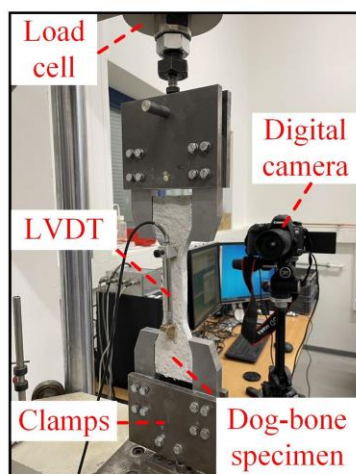
rubber, with a Shore hardness of 40 A, provides good bond strength. The LDT0-028 K PVDF film measures 24.81 mm × 13.21 mm with a total thickness of 0.2 mm, which includes a protective layer designed to prevent surface oxidation of the silver ink electrode area [10-12]. To reduce strain transfer loss from the bonded ligament area to the PVDF during precompression, the PVDF film was bonded to the ligament region after precompression. The bonding was performed when the silicone rubber (Poly-Sil PS8540) had lost its fluidity and exhibited strong adhesive properties, approximately one hour after mixing its components A and B.

7.2.2. Experiments

(1) Material properties test

In Chapter 6, uniaxial tensile tests on dog bone specimens were performed according to Japan Society of Civil Engineers guidelines [13] to assess the tensile behavior of the cementitious matrix after 28 days of curing, as shown in Figure 7-2a. Uniaxial compression tests were also conducted to determine the compressive behavior of the cementitious matrix. Figure 7-2b show the test setup, performed on a UNITRONIC machine with displacement control at a 0.01 mm/s displacement rate. Displacement was measured by LVDTs attached on each side of the cubic specimens with a side length of 20 mm. At least three specimens were tested to ensure reliable results. Figure 7-2 presents the test results for uniaxial tension and uniaxial compression of the cementitious matrix. The average tensile and compressive test results shown in Figure 7-2 will later be used as the material constitutive parameters in the CDP model.

a



b

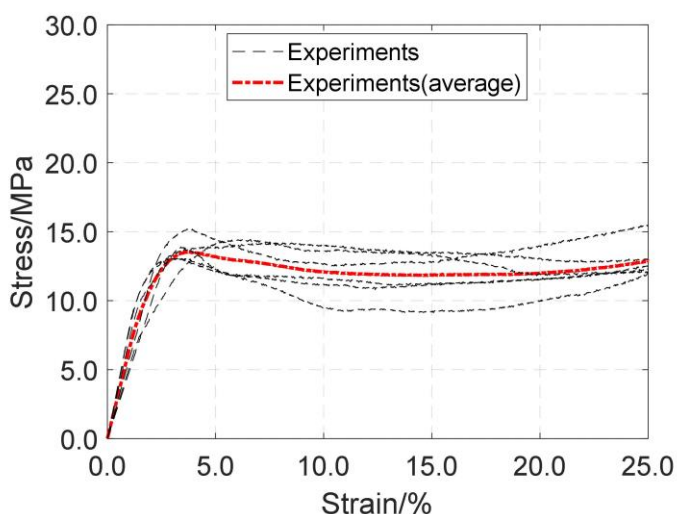
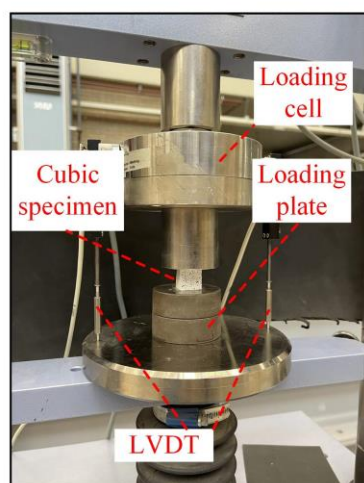


Figure 7-2 Mechanical testing of material properties, (a) uniaxial tension, (b) uniaxial compression.

(2) Uniaxial compression test for ACCCs

Uniaxial compression tests on ACCCs specimens were conducted using the UNITRONIC machine with displacement control at 0.01 mm/s. As shown in Figure 7-3, the displacement of each specimen was measured with two LVDTs placed on its two sides. As illustrated in Figure 7-3a, the P1a-shaped ACCCs were used as a reference for energy harvesting. Its compressive stress-strain curve was derived by calculating stress as compressive force divided by the initial projected cross-sectional area (63 mm × 20 mm) and strain as displacement over initial length (63 mm), which is shown in Figure 7-3b. Plastic films were added to minimize friction with loading plates, aiding section rotation to facilitate auxetic behavior.

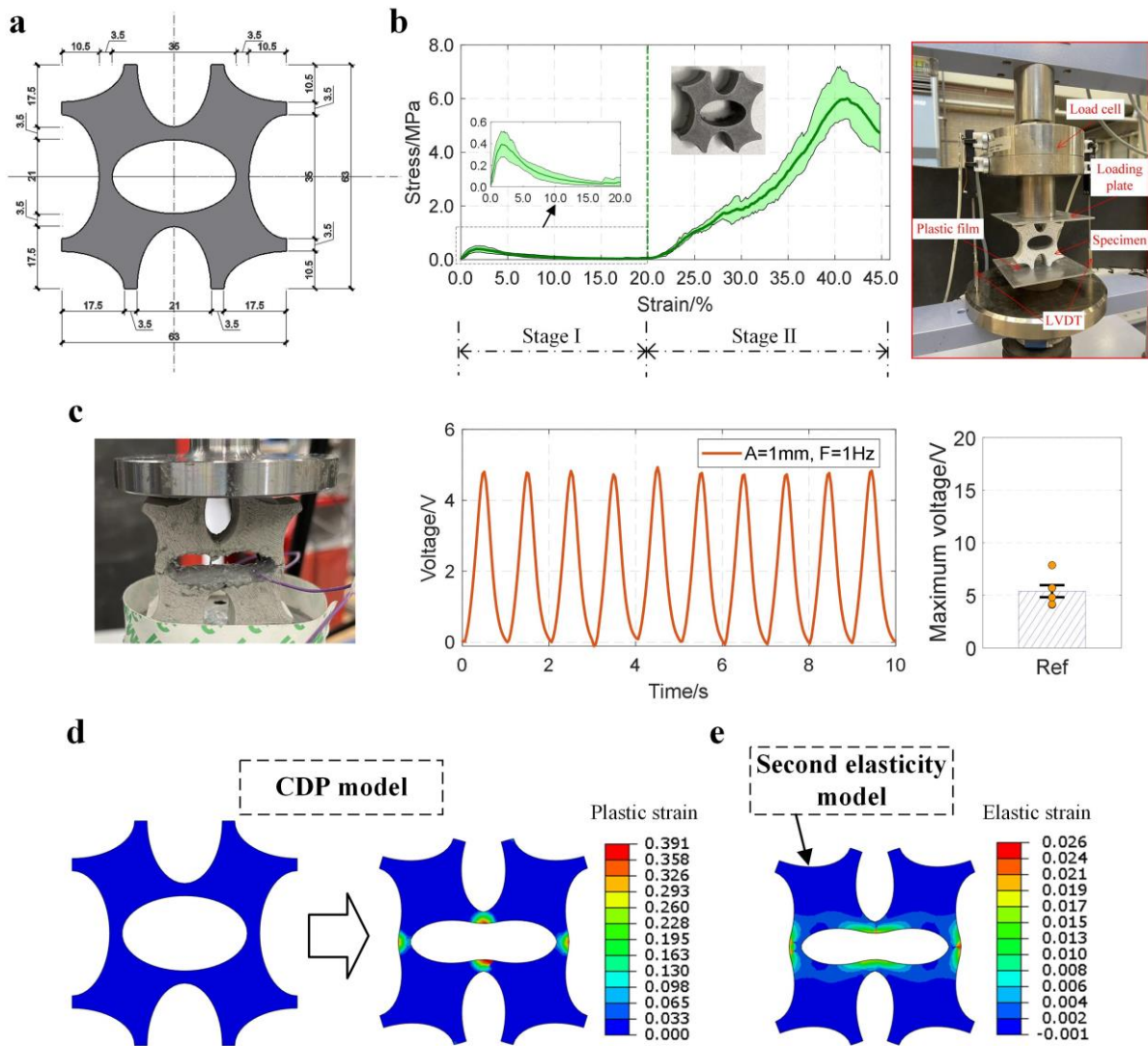


Figure 7-3 ACCCs in P1a shape (reference), (a) dimensions, (b) results of uniaxial compression, (c) output voltage during energy harvesting test, (d) plastic deformation in CDP model, (e) elastic strain distribution in second elasticity model.

(3) Energy harvesting test

Figure 7-4 shows the energy harvesting test setup and loading plan for ACCCs energy harvester. Cyclic testing of the energy harvester was conducted using an MTS fatigue machine with a 10 kN capacity. The harvester's DC output voltage was measured with a Keysight 34461 A digital multimeter. Given LDT0 PVDF's high internal impedance (nearly 11.2 M Ω by using a pure capacitance estimation [12]), the multimeter's input impedance was set to over 10 G Ω for accurate open-circuit voltage measurement. Two wires connected the PVDF to the multimeter, and a plastic film reduced friction between the loading plate and the specimen. To counteract slight horizontal movement from uneven deformation and asymmetrical cracks in the cementitious materials during cyclic tests, tape was applied to the bottom loading plate. Considering the loading plan shown in Figure 7-4c, the P1a-shaped specimen is first compressed by displacement loading. The compression starts at zero and increases to U (5.0 mm), bringing the specimen to a height of 58 mm. Afterwards, cyclic loading under

displacement control is applied with a sinusoidal wave with a constant amplitude A (1 mm) and a frequency f (1 Hz). In Figure 7-3c, the P1a-shaped specimen produces a sinusoidal peak-to-peak voltage of around $5.4 \pm 0.6V$ during each cycle of cyclic loading. To ensure reliability, a minimum of three replicates were tested.

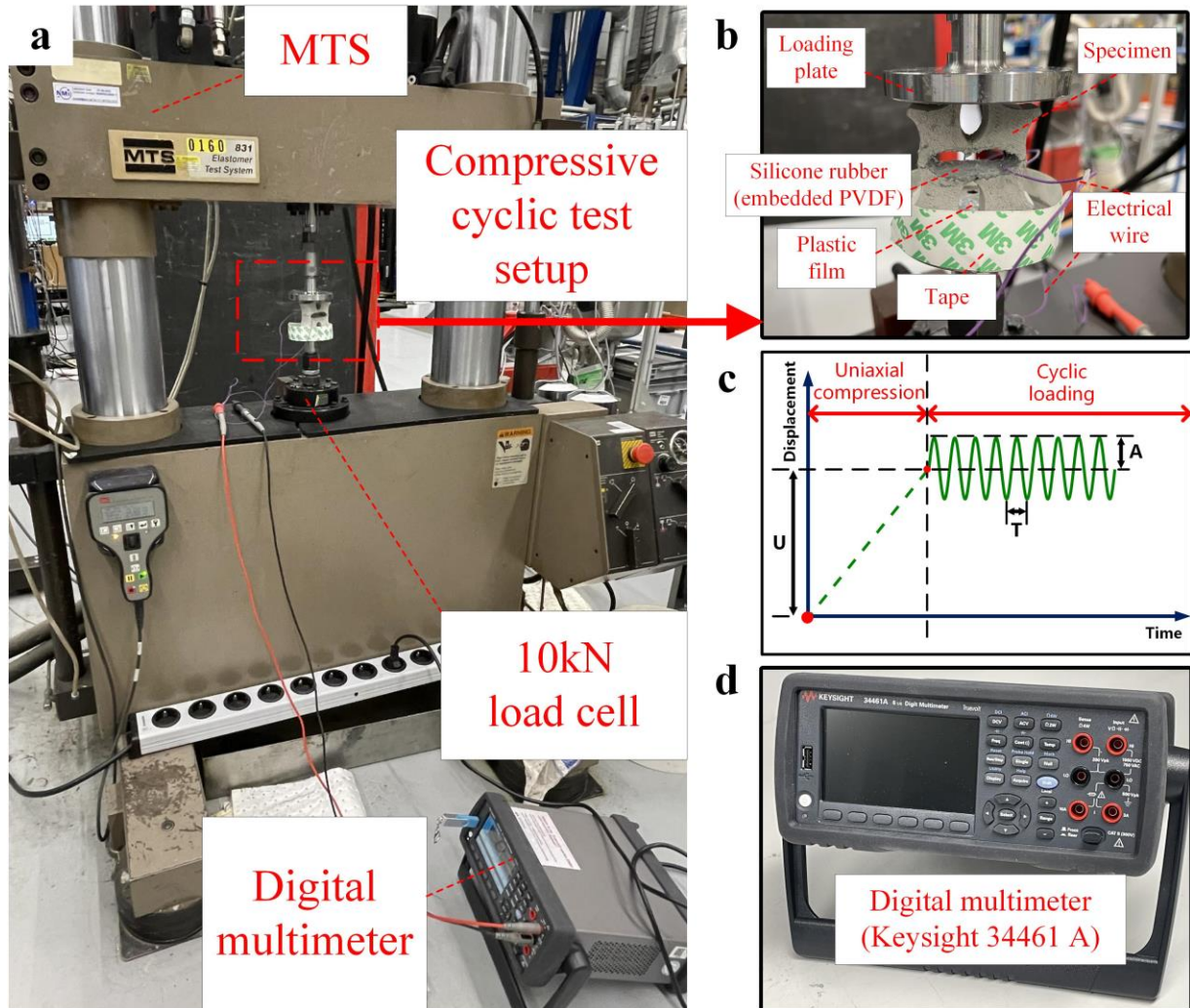


Figure 7-4 Energy harvesting test setup

7.3 ENERGY HARVESTING MODELLING

The energy harvesting model developed in Chapter 5 was further extended in this chapter. Figure 7-5 presents a flowchart of the energy harvesting model for the ACCC energy harvester in this Chapter. The mechanical model of ACCCs comprises two phases: preloading and cyclic loading, as shown in Figure 7-5a. In the pre-compression phase, the CDP model quantifies ACCCs' mechanical behavior [14]. The CDP model parameters are obtained from the tensile and compressive test results of the SHCC mixture with extended softening, which are presented in Section 7.2.2. However, due to its limitations, the CDP model encounters difficulties in simulating the second-elasticity behavior of the ACCCs during cyclic loading, and thus a

second-elasticity model is employed instead. As shown in Figure 7-5b, For transition between models, the ACCCs' deformed shape at a specified loading displacement (calculated by the CDP model) is set as the initial geometry for the second-elasticity model, which is reconstructed through an improved node-order tracking algorithm in this chapter. Next, strain transfer between PVDF and ACCCs is incorporated. The mechanical response of the PVDF film is then extracted to calculate output voltage using the PVDF piezoelectric model.

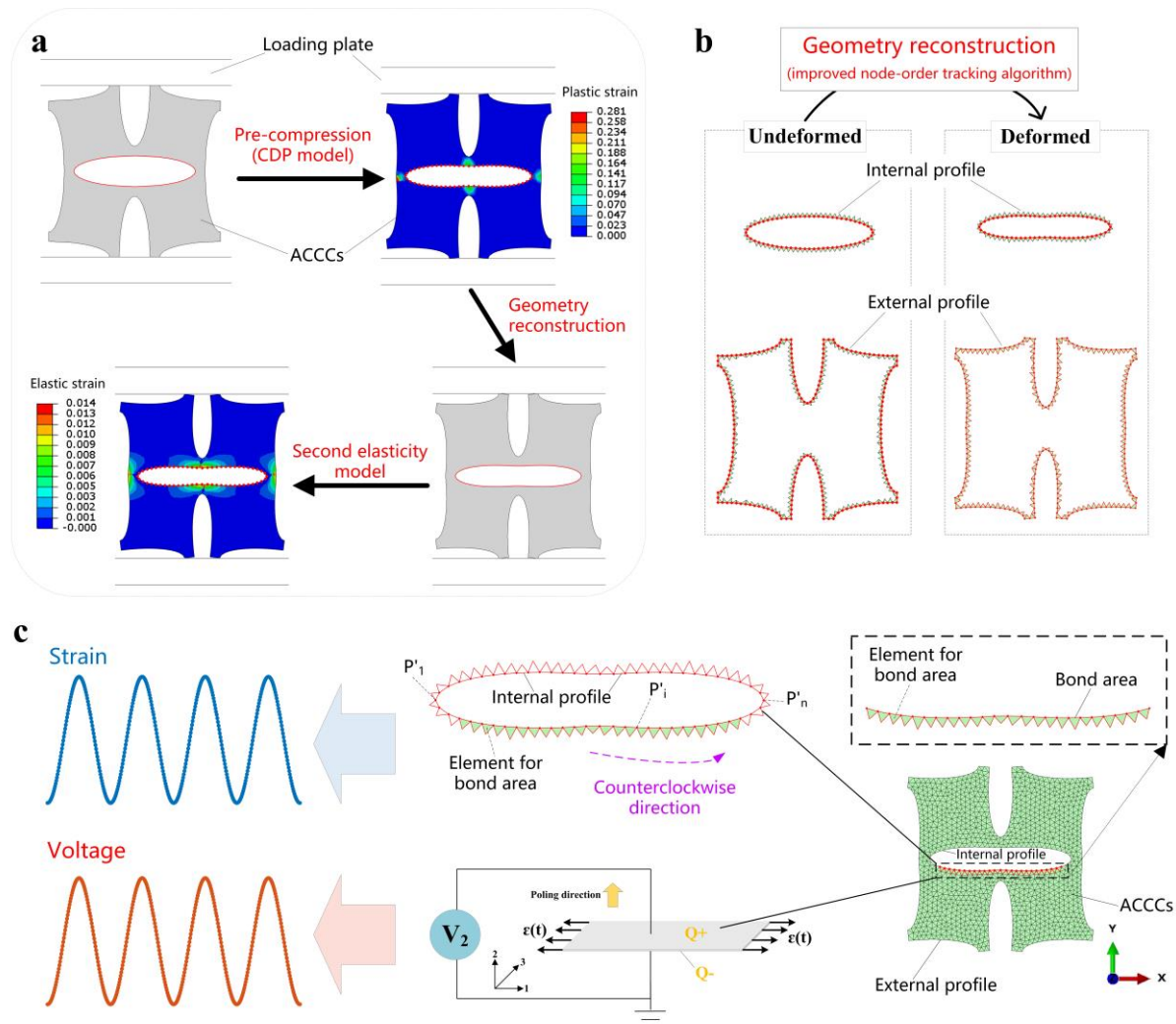


Figure 7-5 Energy harvesting model for ACCCs

7.3.1. Mechanical model

The elastic-plastic behavior of cementitious composites reinforced with PVA fibers can be simulated using the CDP model [15-17]. Chapter 5 has detailed the methodology of applying the CDP model to simulate the mechanical properties of ACCCs. Similarly, the simulation of the CDP model for ACCCs under quasi-compression was performed using the ABAQUS/Explicit module. The ACCC specimen was meshed with CPS3, a 3-node linear plane stress triangular element without hourglass effects. The CDP model parameters for ACCCs are given in Table 7-3. Herein, ρ is the density, E_0 is its initial Young's modulus, and

ν is its Poisson's ratio. $\sigma_{b0} / \sigma_{c0}$ represents the ratio of the initial yield stress in equi-biaxial compression to that in uniaxial compression. K_c represents the ratio of the second stress invariants on the tensile and compressive meridians. ψ refers to the dilation angle. ϵ_{ec} is the flow potential eccentricity. The mechanical behavior of the cementitious matrix is characterized by the experimental results of uniaxial tension and compression in Figure 7-2, which can be incorporated into the CDP model as detailed in Tables 7-3 and 7-4. Three ACCC shapes from the intuitive solution have been designed and fabricated. Detailed information can be found in Figure 7-6, Figure 7-7 and Table 7-6. Herein, P1a is the ACCC shape used in Chapter 3. As shown in Figure 7-8, three ACCC shapes from the intuitive solution were tested under uniaxial compression, and the results were consistent with those of the CDP model. The discrepancy in the first peak stress for P1b between the experimental and model results is due to the larger size of the middle joint compared to the side joint. When plastic strain develops in the middle joint, the much smaller side joint experiences stress concentration and some crushing under the contact pressure from the loading plate. This leads to increased friction in that region, requiring a greater vertical force to overcome the friction and allow the section to rotate.

Table 7-3 CDP model parameters for ACCCs

ρ (kg/m ³)	E_0 (MPa)	ν	$\sigma_{b0} / \sigma_{c0}$	K_c	ψ	ϵ_{ec}	Viscosity Parameter
1870	4576	0.2	1.16	0.667	35	0.1	0.001

Table 7-4 Tensile behavior parameters

Yield stress (MPa)	Displacement (mm)
2.599	0
2.768	0.505
2.583	0.896
2.504	1.406
2.315	1.705
1.106	2.736
0.491	3.263
0.188	4.217
0.138	4.796

Table 7-5 Compressive behavior parameters

Yield stress (MPa)	Inelastic strain
10.5	0
13.022	0.027
13.544	0.035
13.027	0.052
12.078	0.097
11.880	0.121
11.928	0.171
12.294	0.203
12.868	0.229
13.833	0.259

Table 7-6 Design parameters of the three ACCCs shapes in the intuitive solution.

Specimen	l (mm)	a_0 (mm)	b_0 (mm)	a_1 (mm)	b_1 (mm)	g_0 (mm)	g_1 (mm)	Hole area (mm ²)	Specimen area (mm ²)	Relative density
P1a	63	17.5	10.5	17.5	10.5	3.5	3.5	2309.1	1659.9	41.8%
P1b	63	17.5	10.5	15.5	8.5	3.5	5.5	2145.7	1823.3	45.9%
P1c	63	22.3	5.7	22.3	5.7	3.5	3.5	1597.3	2371.7	59.8%

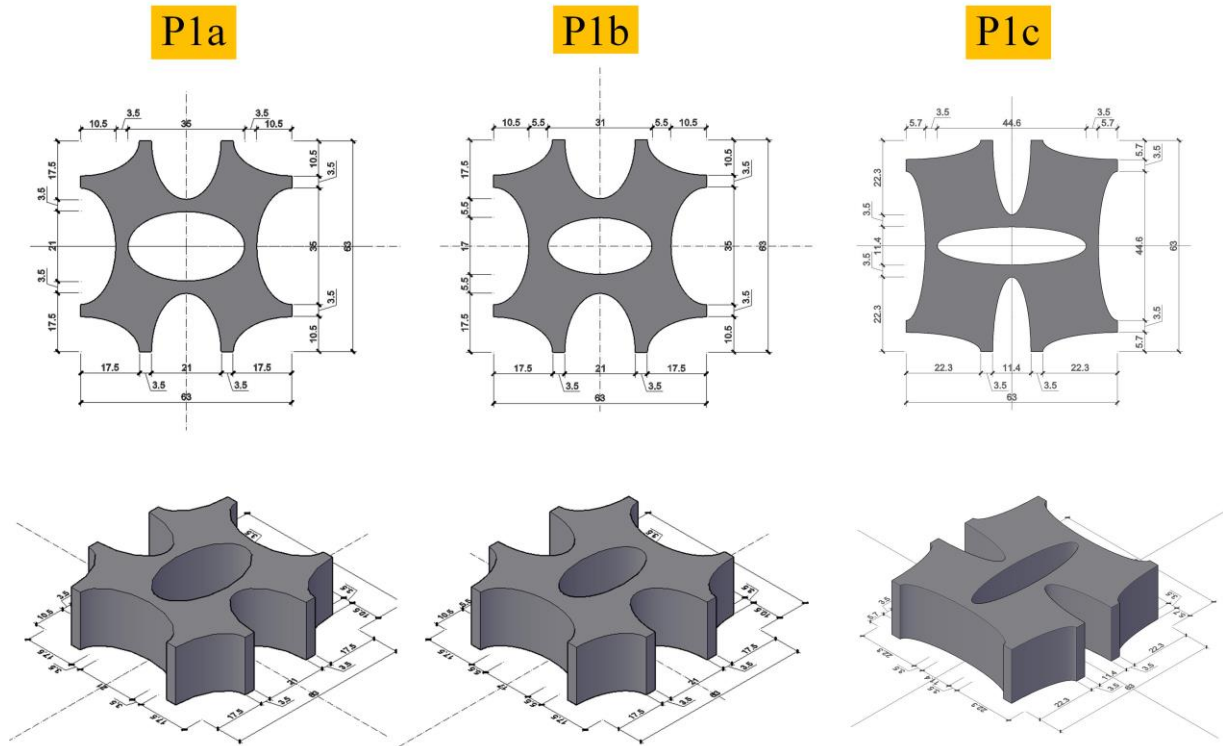


Figure 7-6 Dimensions of three ACCCs shapes in the intuitive solution from both a front view and an isometric view.

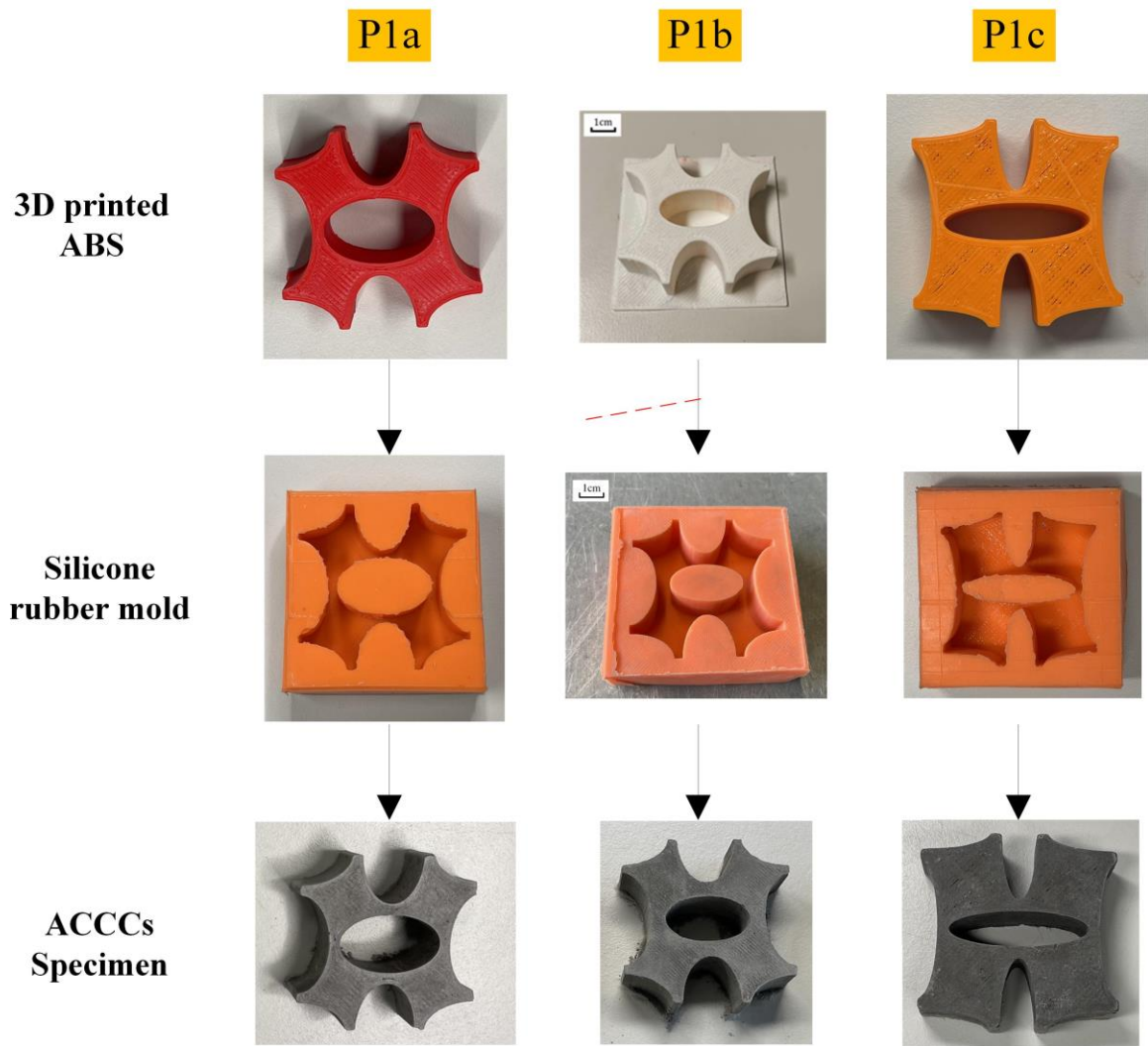


Figure 7-7 Procedures for creating three ACCCs shapes in the intuitive solution

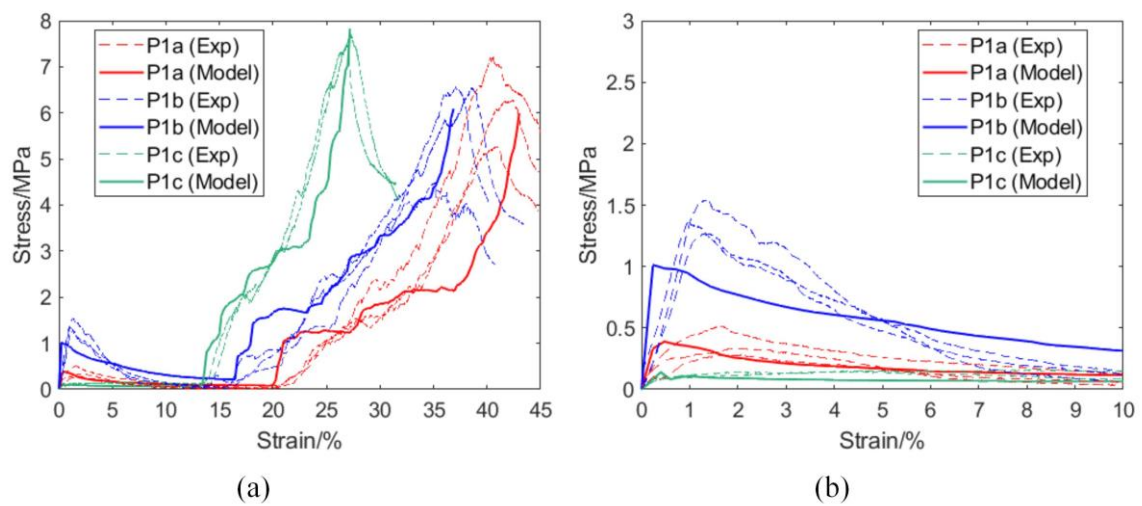


Figure 7-8 Modelling calibration: compressive stress-strain curve

ACCCs display significant recovery after compressive unloading in cyclic tests, attempting to return to their original shape despite minor plastic deformation [9, 15-17]. This uncommon behavior in cementitious materials, termed “compressive deformation resilience” or “recoverable deformation elasticity,” describes the structure’s elastic recovery after compressive stress is released. This compressive deformation resilience can be simulated by a second-elasticity model with an equivalent structural elastic modulus of the whole unit cell during the cyclic loading stage [16]. To achieve this, the deformed ACCCs shape at a specified loading displacement, namely the end of the preloading stage, is used as the initial geometry in the second-elasticity model. The node-order-track algorithm [16] was employed using Python scripting within ABAQUS to achieve topological reconstruction of geometric shapes of ACCCs at a designated moment during the loading process. Specifically, this algorithm reconstructs the shape using topological data including the recorded node order and the current node coordinates. These coordinates are calculated by adding displacements to the original coordinates. However, due to the extensive dataset of shapes generated by ML, the algorithm is not suitable for certain special cases. To address these limitations, an improved node-order-track algorithm has been developed, aimed at accommodating these special scenarios and providing a comprehensive reconstruction method for ACCC shapes in Figure 7-5b. The detailed steps of this improved algorithm are illustrated in Figure 7-9. As shown in Figure 7-9, In in Figure 7-9a, the node-order-track algorithm was used for topological reconstruction of geometric shapes by selecting the next candidate as the nearest point to the previous one. In this study, the algorithm was further improved to address special cases from the extended ML dataset. In Figure 7-9b, the node-order-track algorithm fails to reconstruct the ends of the ACCC internal profile due to Cases I and II. In Case I, blue points are previously reconstructed, with O as the current point. The orange point is the next candidate, but its distance d_1 from O is greater than d_2 , the distance from O to the nearest blue point. To address this, the improved algorithm excludes previously constructed blue points, allowing the orange point to be prioritized as the next nearest. In Case II, the nearest point from O along the reconstruction direction should ideally be the orange point. However, the purple point, located behind the reconstructed blue points, has a shorter distance d_4 than d_3 , the distance between O and the orange point. The cosine of the angle between v_1 (direction vector from O to the nearest blue point) and v_2 (from O to the orange point) is greater than that between v_1 and v_3 (from the purple to the orange point). Using a detection region with radius R centered at O and evaluating these cosine angle values enables the algorithm to prioritize the orange point as the next nearest point. In Figure 7-9c, the external profile of ACCCs was reconstructed using the improved algorithm, incorporating Cases I and II as in Figure 7-9b. In some special regions within Case III in Figure 7-9c, evaluating the cosine angle values may mistakenly identify the purple point as the next candidate instead of the orange point when using a large detection region. Therefore, the detection region should be reduced by lowering R . The model further considers varying R within the loop by applying multiple factors to the mesh size for each shape. This approach allows for selecting the correct next candidate in the direction, thereby addressing these issues without requiring segmented region considerations.

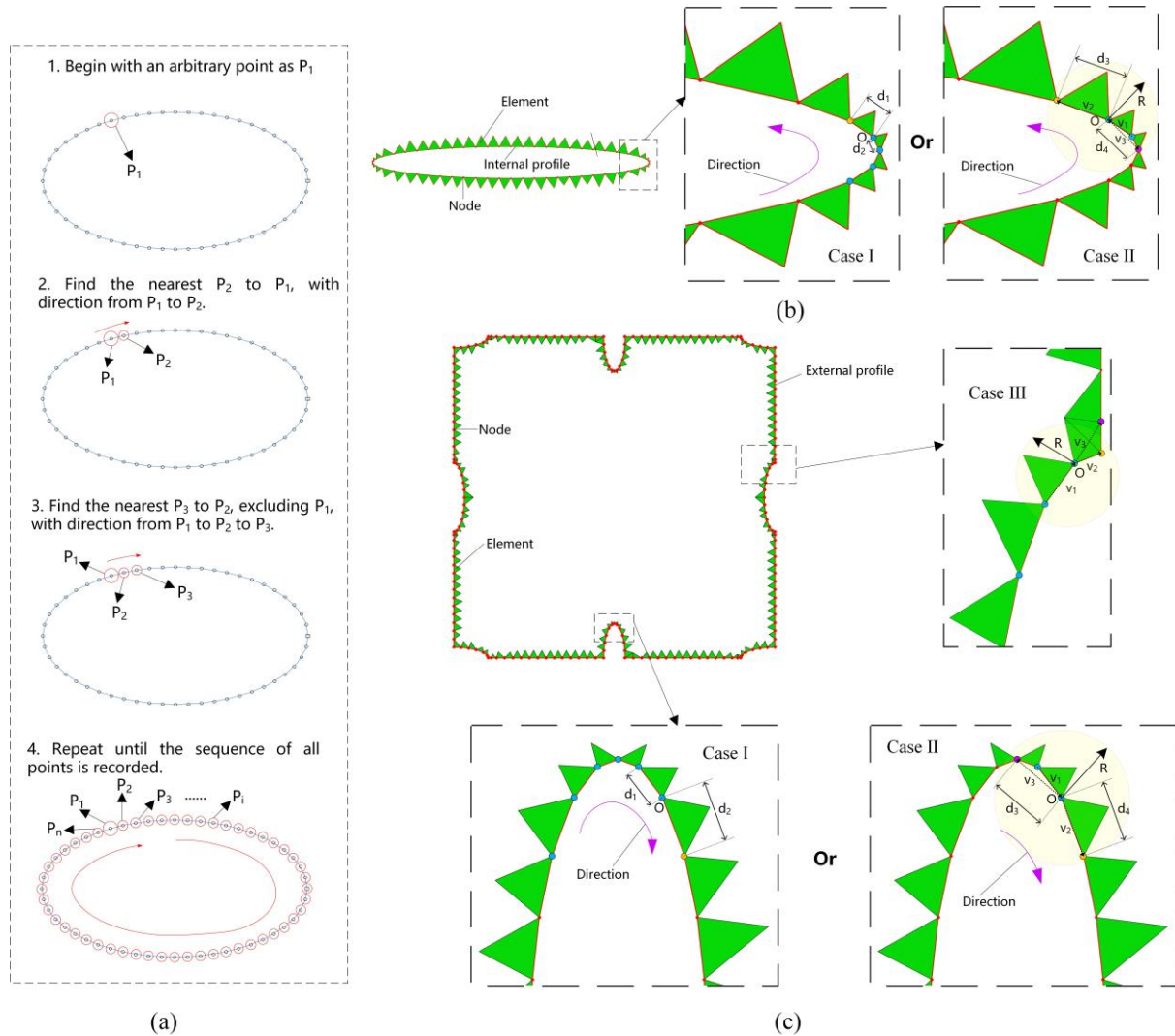


Figure 7-9 (a) Shape topology reconstruction via node-order tracking algorithm, (b) internal profile reconstruction of ACCCs with improved node-order tracking algorithm, (c) external profile reconstruction of ACCCs with improved node-order tracking algorithm.

Afterwards, a sinusoidal displacement consistent with the cyclic test loading scheme is applied to the top plate, while the bottom plate remains fixed in the second elasticity model. Interaction between the specimen and loading plates is maintained as defined in the compression model. Figure 7-3d shows the plastic strain distribution of the reference calculated using the CDP model, after a pre-compression of 5 mm. Subsequently, the deformed specimen in the second-elasticity model is presented with an elastic strain distribution at the peak of cyclic loading in Figure 7-3e.

7.3.2. Energy harvesting model

The mechanical responses of the PVDF film are then incorporated into the piezoelectric model to determine the output voltage. Generally, the interaction between the mechanical and electrical fields in a piezoelectric material is described using the following constitutive equation, with the symbols defined earlier in Chapter 5.

$$\begin{aligned} S_{ij} &= s_{ijkl}^E \cdot T_{kl} + d_{kij} \cdot E_k \\ D_j &= d_{jkl} \cdot T_{kl} + e_{jk}^T \cdot E_k \end{aligned} \quad (44)$$

In the PVDF inset in [Figure 7-3c](#), the local coordinate system designates the length, width, and thickness of the PVDF film as directions 1, 3, and 2, respectively. The piezoelectric strain coefficient d_{31} links the electric charge generated in the thickness direction to stress applied along the length (mode 31), while d_{33} links it to stress applied along the thickness (mode 33). The detailed formula for the piezoelectric model of a PVDF film was provided in our previous study [16]. For the PVDF film, the output voltage V_p can be represented as the sum of two voltage components, associated with charge generation in modes 31 and 33, respectively. $V_{p,1}$ is the cumulative voltage generated due to d_{31} . $V_{p,2}$ is the cumulative voltage produced by d_{33} .

$$V_p = V_{p,1} + V_{p,2} \quad (45)$$

$$V_{p,1} = \frac{l_p w_p d_{31}}{C_p} \frac{E_p}{n(1-\nu_p^2)} \sum_{i=1}^n (\varepsilon_1^i + \nu_p \varepsilon_2^i) = \frac{l_p w_p d_{31}}{C_p} \frac{E_p}{(1-\nu_p^2)} (\bar{\varepsilon}_1 + \nu_p \bar{\varepsilon}_2) \quad (46)$$

$$V_{p,2} = \frac{l_p w_p d_{33}}{C_p} \frac{E_p}{n(1-\nu_p^2)} \sum_{i=1}^n (\nu_p \varepsilon_1^i + \varepsilon_2^i) = \frac{l_p w_p d_{33}}{C_p} \frac{E_p}{(1-\nu_p^2)} (\nu_p \bar{\varepsilon}_1 + \bar{\varepsilon}_2) \quad (47)$$

where l_i and w_i are the length and width of each rectangular segment, respectively. Meanwhile, l_p , w_p represent the length, width of the PVDF film, respectively. C_p represents the capacitance of the PVDF film, while E_p denotes its elastic modulus, and ν_p refers to its Poisson's ratio. The piezoelectric film is divided into n equal-sized rectangular segments along both its length and width (i.e., $l_p = nl_i$ and $w_p = nw_i$). i refers to the i -th segment. ε_1^i represents the strain in direction 1 for the i -th segment. ε_2^i represents the strain in direction 2 for the i -th segment. $\bar{\varepsilon}_1$ represents the equivalent strain in direction 1 for the PVDF film, which is calculated as the average strain of all segments. Similarly, $\bar{\varepsilon}_2$ represents the equivalent strain in direction 2 for the PVDF film, also determined by averaging the strain of all segments.

As shown in our previous study [16], $V_{p,1}$ is significantly greater than $V_{p,2}$ because the PVDF film primarily experiences flexible strain in the scenario of ACCCs-PVDF energy harvester. For $V_{p,1}$, the contribution from $\bar{\varepsilon}_2$ decreases significantly because of Poisson's ratio ν_p . Hence, $V_{p,1}$ is mainly influenced by $\bar{\varepsilon}_1$. As a result, the maximum output voltage is primarily governed by the maximum value of $\bar{\varepsilon}_1$. The $\bar{\varepsilon}_1$ of the PVDF film is mainly transferred through the adhesive layer (i.e., silicon rubber) from the average strain $\bar{\varepsilon}_{\text{int}}$ of the cementitious material bonded to the PVDF film. Therefore, in subsequent Bayesian Optimization, $\bar{\varepsilon}_{\text{int}}$ will be treated as the objective function to simplify the representation of the output voltage.

7.4 BAYESIAN OPTIMIZATION (BO)

7.4.1. Theory

Bayesian optimization is a widely used method for optimizing expensive-to-evaluate black-box functions. It employs a probabilistic surrogate model, often a Gaussian Process (GP), to generate a posterior distribution. This enables a sample-efficient approach to identify optimal trade-offs between objectives. Finite element models used to simulate the elastic-plastic behavior of cementitious materials are typically computationally intensive. BO leverages patterns in limited data through interactive iterations with FEM to identify promising optimal design variables. This significantly reduces the computational cost associated with training a large number of models. Additionally, BO's exploration mechanism helps avoid being trapped in local optima. Assuming the objective function defined in Section 3 follows a multivariate Gaussian distribution, it can be fitted by using a Gaussian Process (GP). For the i -th sample point \mathbf{x}_i , the GP is implemented primarily by fitting the kernel of the covariance matrix as follows:

$$\mathbf{K} = \begin{bmatrix} k(\mathbf{x}_1, \mathbf{x}_1) & \cdots & k(\mathbf{x}_1, \mathbf{x}_n) \\ \vdots & \ddots & \vdots \\ k(\mathbf{x}_n, \mathbf{x}_1) & \cdots & k(\mathbf{x}_n, \mathbf{x}_n) \end{bmatrix} + \beta^{-1} \mathbf{I} \quad (48)$$

where n denotes the number of sample points incorporated into the GP model. $\beta^{-1} = \sigma_{noise}^2$ is the standard deviation of the noise, assumed to follow a standard normal distribution. \mathbf{I} is the identity matrix. k represents the covariance kernel, which is calculated using the squared exponential function in Eq. (6).

$$k(\mathbf{x}, \mathbf{x}') = \sigma_f^2 \exp\left(-\frac{1}{2s^2} \|\mathbf{x} - \mathbf{x}'\|^2\right) \quad (49)$$

where σ_f^2 is a scaling factor, and s represents the length scale that determines the degree of correlation between function values.

Let $\mathbf{t} = (\mathbf{X}, \mathbf{Y})$ represent the multivariate Gaussian distribution of n observed sample points. Herein, \mathbf{X} refers to a stack of \mathbf{x} values from n observations. \mathbf{Y} represents the results from n observations. The performance of the next sample point $\hat{\mathbf{x}}$, can be predicted as \hat{t} using Bayesian rules for a multivariate Gaussian distribution.

$$p(\hat{t} | \mathbf{t}) = \mathbf{N}(\hat{t} | \hat{m}, \hat{\sigma}^2) \quad (50)$$

with posterior mean:

$$\hat{m} = k(\hat{\mathbf{x}}, \mathbf{X}) \left[K(\mathbf{x}, \mathbf{x}) + \beta^{-1} \mathbf{I} \right]^{-1} \mathbf{t} \quad (51)$$

and posterior variance:

$$\hat{\sigma}^2 = k(\hat{\mathbf{x}}, \hat{\mathbf{x}}) - K(\hat{\mathbf{x}}, \mathbf{X}) \left[K(\mathbf{X}, \mathbf{X}) + \beta^{-1} \mathbf{I} \right]^{-1} K(\mathbf{X}, \hat{\mathbf{x}}) + \beta^{-1} \quad (52)$$

$$K(\hat{\mathbf{x}}, \mathbf{X}) = \left[k(\mathbf{x}_{n+1}, \mathbf{X}_1) \quad k(\mathbf{x}_{n+1}, \mathbf{X}_2) \quad \cdots \quad k(\mathbf{x}_{n+1}, \mathbf{X}_n) \right] \quad (53)$$

$$K(\mathbf{X}, \hat{\mathbf{x}}) = K(\hat{\mathbf{x}}, \mathbf{X})^T \quad (54)$$

where $Y_{1:n}$ refers to the results from n observations.

Based on the gaussian process (GP), the performance (i.e., objective value) for any potential sample point can be predicted. Next, the acquisition function (i.e., Expected Improvement [18])

is calculated to estimate the improvement potential of each possible sample point, as shown below:

$$EI(\mathbf{x}) = E[\max(Y - Y_{best}, 0)] \quad (55)$$

$$EI(\hat{\mathbf{x}}) = (Y_{best} - \mu(\hat{\mathbf{x}}))\Phi(Z) + \sigma(\hat{\mathbf{x}}) \cdot \phi(Z) \quad (56)$$

$$Z = \frac{\mu(\hat{\mathbf{x}}) - Y_{best}}{\sigma(\hat{\mathbf{x}})} \quad (57)$$

where $\Phi(Z)$, $\phi(Z)$ are the standard normal distribution function and density function, respectively, while Y_{best} is the current optimal objective value in the sample space. The first term in Eq. (56) captures the difference between each potential sample point and the best-known point, promoting exploitation. The second term in Eq. (56) assigns greater weight to sample points with higher uncertainty, ensuring no “blank” areas in the sample space and promoting exploration. By combining these terms, the acquisition function EI tends to produce higher values at sample points with lower posterior means and greater uncertainty, achieving a balance between exploitation and exploration.

7.4.2. Bayesian Optimization setup

(1) Random generation of initial data set

Figure 7-10 shows the geometric parameterization of elliptical-shaped ACCCs for a sample point (i.e., $\mathbf{x}_i = (l_i, a_{0i}, b_{0i}, a_{1i}, b_{1i})$). The central hole is considered to potentially differ from the surrounding holes in the unit cell. The initial step involves assuming that the central hole has the same size as the surrounding holes in the unit cell (see Figure 7-10). This special case is followed by adjustments to the dimensions of the central hole. Considering the limited space for casting cementitious materials that include fibers, the minimum specified value for the ligament $l_{g_{min}}$ is set at 3.5 mm.

The side length of the unit cell of ACCCs l_i can range from l_{min} mm (20 mm) to l_{max} (80 mm).

$$l_i \in [l_{min}, l_{max}] \quad (58)$$

where i indicates the i -th candidate.

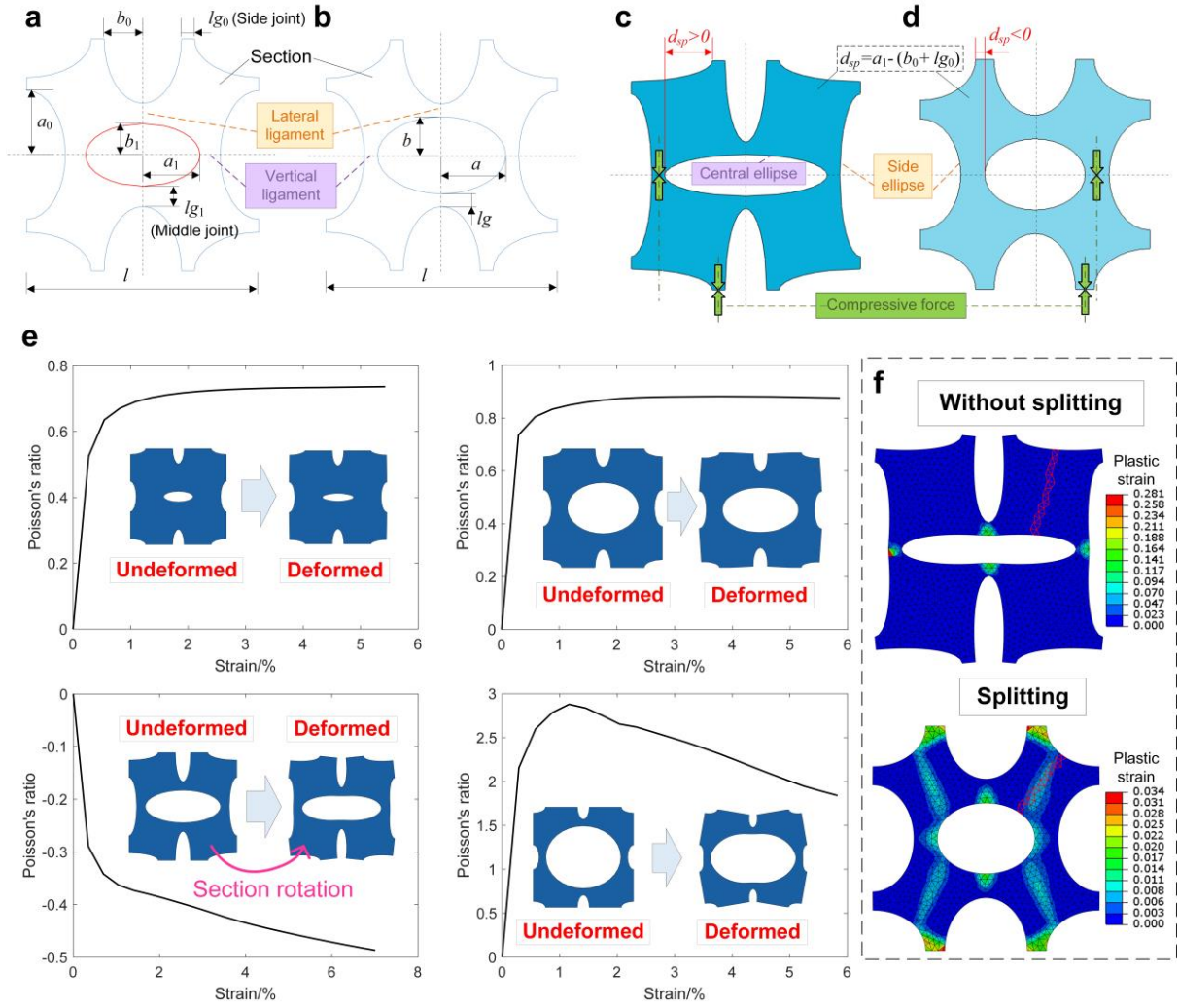


Figure 7-10 (a) Parameterization of elliptical-shaped ACCCs, (b) ACCCs shape with identical ligaments, (c) ACCCs shape with larger d_{sp} , (d) ACCCs shape with smaller d_{sp} , (e) randomly generated samples with different Poisson's ratios, (f) splitting case identified by plastic strain in detection region.

Considering the restricted space for creating the silicon rubber mold, the minimum values of the half major axis a_{\min} and half minor axis b_{\min} are set at 4.5 mm and 3.5 mm, respectively. Once the value of l_i is determined, the ligament $l_{g_{oi}}$ of surrounding holes can be chosen from the following range:

$$l_{g_{oi}} \in [l_{g_{\min}}, (l_i / 2.0 - a_{\min} - b_{\min})] \quad (59)$$

Subsequently, the half major axis a_o of surrounding holes can be constrained within the following range:

$$a_{oi} \in [(l_i / 2.0 - l_{g_{oi}}) / 2.0 + 0.5, l_i / 2.0 - l_{g_{oi}} - b_{\min}] \quad (60)$$

Then, the half minor axis b_o of surrounding holes can be obtained as

$$b_{oi} = l_i / 2.0 - l_{g_{oi}} - a_{oi} \quad (61)$$

The auxetic behavior of ACCCs is achieved through the rotation of ligaments after cracking. As a result, the ligaments $l_{g_{oi}}$ surrounding the central hole are maintained at a uniform size, ensuring symmetric deformation. On this basis, the following equation can be derived:

$$a_{oi} + b_{oi} = a_i + b_{oi} \quad (62)$$

Following that, the half major axis a_1 of the central hole can be adjusted within the range below.

$$a_{1i} \in [b_{\min} + 1, l_i / 2.0 - b_{0i} - lg_{\min}] \quad (63)$$

However, the half minor axis b_{1i} of the central hole needs to satisfy the following equation

$$b_{1i} \geq b_{\min} \quad (64)$$

Based on Eq. (61), Eq. (65) can be obtained as

$$a_{1i} \geq b_{\min} + a_{0i} - b_{0i} \geq b_{\min} + 1.0 \quad (65)$$

Therefore, the half major axis a_1 lies within the range indicated below:

$$a_{1i} \in [b_{\min} + a_{0i} - b_{0i}, l_i / 2.0 - b_{0i} - lg_{\min}] \quad (66)$$

Based on Eq. (62), the half minor axis b_1 of the central hole can be determined as

$$b_{1i} = b_{0i} + a_{1i} - a_{0i} \quad (67)$$

The geometric parameter d_{sp} in Eq. (68), representing the degree of structural chirality, was introduced to characterize the splitting behavior of ACCCs. As illustrated in Figure 7-10c, a higher d_{sp} increases the lateral distance between the side joints and middle joints. This adjustment reduces the compressive force (highlighted by the green arrow in Figure 7-10c) required to create the moment necessary for ligament plastic deformation and subsequent section rotation, thereby promoting the development of a negative Poisson's ratio effect. Conversely, the ACCCs shape depicted in Figure 7-10d is less conducive to auxetic behavior and is prone to splitting due to the increased compressive force exerted on the joints.

$$d_{sp} = a_1 - (b_0 + lg_0) \quad (68)$$

Hence, the input geometric parameters of l , a_0 , b_0 , a_1 , and b_1 (dependent variables) are considered as a five-dimensional decision variable tensor for optimization, resulting in an objective value of $\bar{\mathcal{E}}_{\text{int}}$. In addition to the intra-point constraints above applied to these input dependence geometric parameters, further output constraints (black box constraints) were imposed on the objective value of each individual candidate by multiplying it by zero in two specific cases that needed to be removed.

Removed case (i): The optimization focuses on ACCCs with auxetic behavior under compression. As shown in Figure 7-10e, only limited ACCCs shapes demonstrate auxetic behavior through section rotation under compression, based on four randomly generated examples from the model. To ensure this, a constraint was applied to the objective function, requiring the Poisson's ratio to remain negative during compression. For each candidate, its Poisson's ratio at every incremental step in the model results was monitored. If any Poisson's ratio was found to be non-negative, the objective value was set to zero by multiplying it by 0. Let C_k represent the k -th candidate in the optimization process. For each candidate C_k , let $v_{k,i}$ denote the Poisson's ratio at the i -th incremental step in the model results. The objective value $\bar{\mathcal{E}}_{\text{int},k}$ for candidate C_k is adjusted as follows:

$$\bar{\mathcal{E}}_{\text{int},k} = \begin{cases} \bar{\mathcal{E}}_{\text{int},k}, & \text{if } v_{k,i} < 0 \forall i \\ 0, & \text{if } v_{k,i} \geq 0 \exists i \end{cases} \quad (69)$$

Removed case (ii): When the model reaches the ultimate case to achieve auxetic behavior by rotation with some minor plastic deformation in the central region of the section. However, experimental observations revealed that the specimens failed by splitting before auxetic behavior could manifest. Two representative cases in the Removed case (ii), labeled RCii-1 and RCii-2 with detail information in Table 7-7, are used to illustrate this situation. As

demonstrated in Figure 7-11 and Figure 7-12, both RCii-1 and RCii-2 display auxetic behavior through rotation, despite experiencing minor plastic deformation in the central region of the section. However, during the experiments, the specimen fractured and split. Cracks formed near the plastic region of the model, which prevented it from displaying auxetic behavior. This outcome is attributed to the ultimate state being highly sensitive to boundary conditions. Additionally, uncertainties arise from manual casting and the heterogeneity of the cementitious materials.

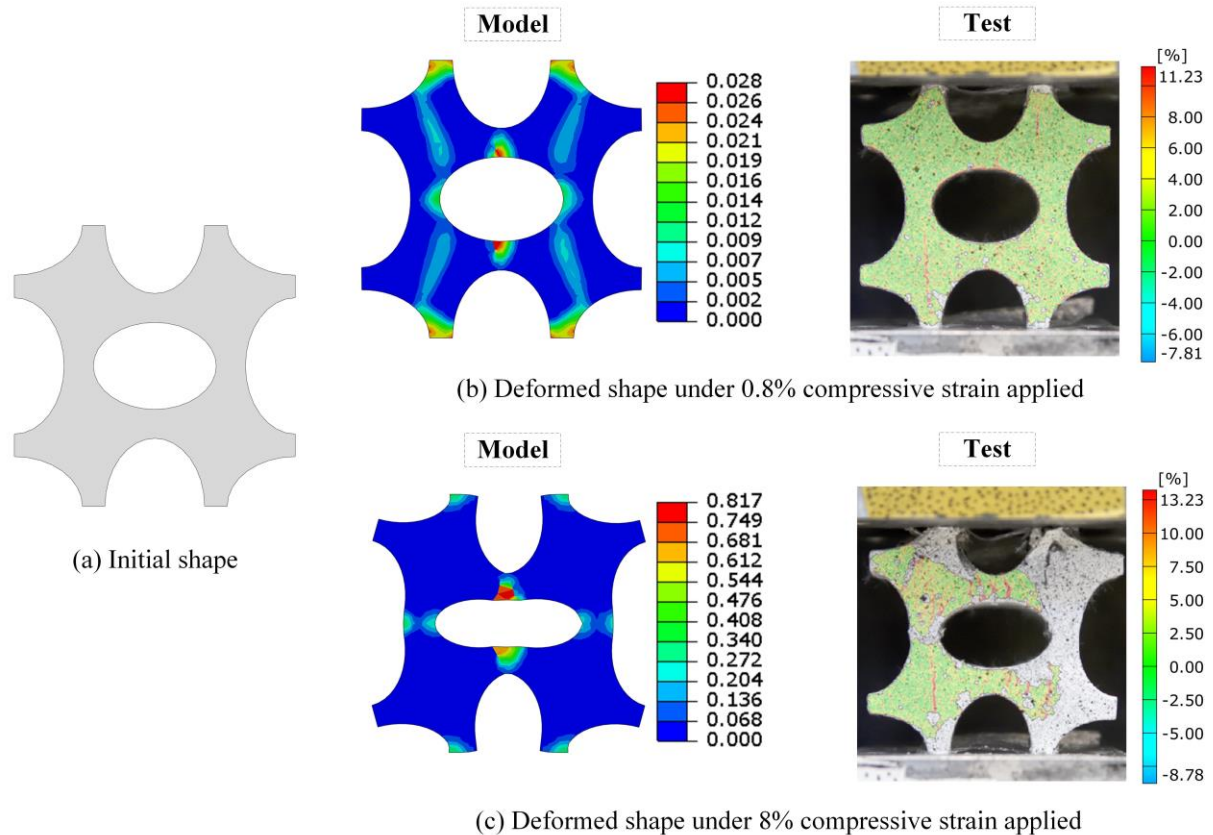


Figure 7-11 RCii-1: (a) Initial shape, (b) deformed shape under 0.8% compressive strain applied, (c) deformed shape under 8% compressive strain applied.

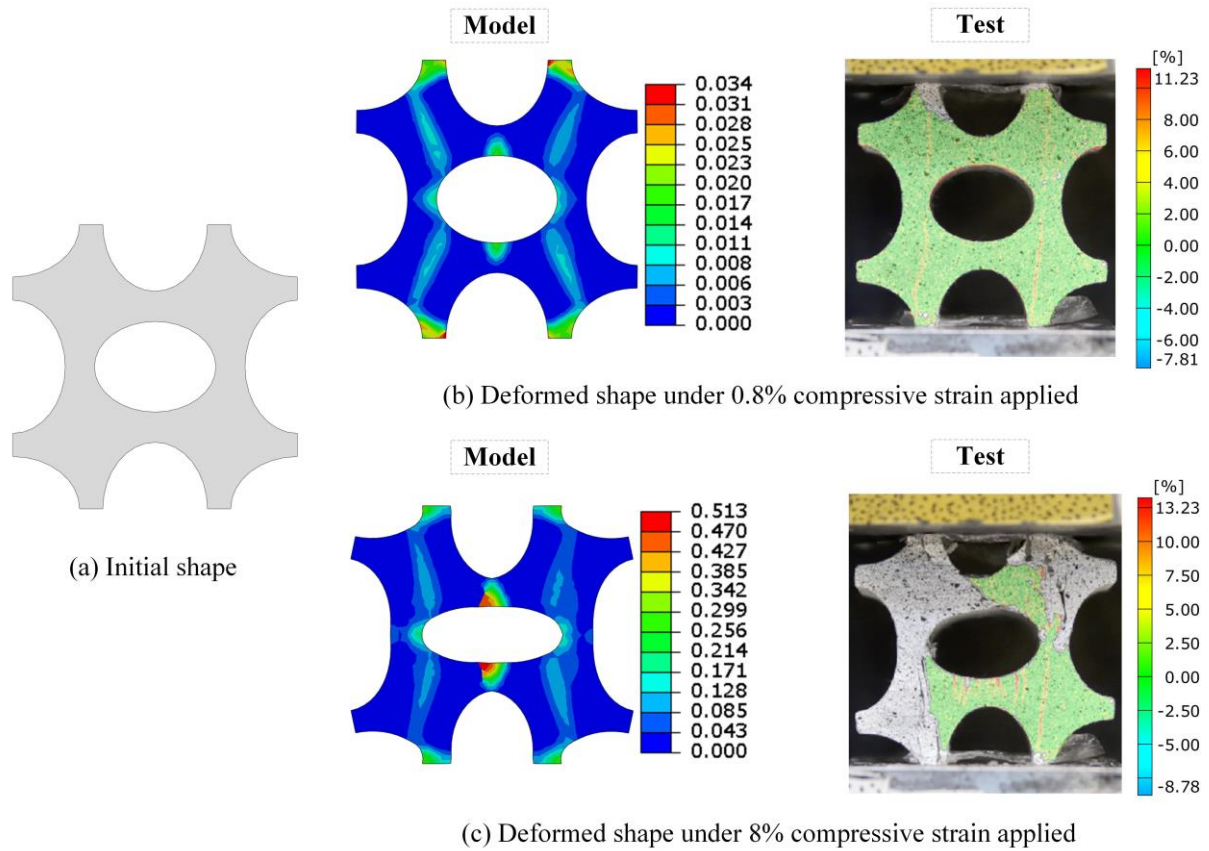


Figure 7-12 RCii-2: (a) Initial shape, (b) deformed shape under 0.8% compressive strain applied, (c) deformed shape under 8% compressive strain applied.

Table 7-7 Specimen details for RCii-1, RCii-2

Case	l	a_0	b_0	a_1	b_1	ε_{in}
RCii-1	66.15	32.08	23.46	28.95	20.48	0.0165
RCii-2	65.86	30.87	24.24	28.14	21.00	0.0191

Therefore, in the case of specimen splitting, the objective value is also set to zero by multiplying it by 0. Specimen splitting in the model is identified if the plastic strain in the central region of the section exceeds ε_p^{th} , as shown in Figure 7-10f. For each candidate C_k , let $\varepsilon_{p,k,i}$ denote the plastic strain in the central region of the section at the i -th incremental step in the model results. The condition for adjusting the objective value $\bar{\varepsilon}_{int,k}$ to zero if the plastic strain $\varepsilon_{p,k,i}$ exceeds the threshold ε_p^{th} , which can be expressed as:

$$\bar{\varepsilon}_{int,k} = \begin{cases} \bar{\varepsilon}_{int,k}, & \text{if } \varepsilon_{p,k,i} < \varepsilon_p^{th} \quad \forall i \\ 0, & \text{if } \varepsilon_{p,k,i} \geq \varepsilon_p^{th} \quad \exists i \end{cases} \quad (70)$$

where ε_p^{th} is set to 0.003 in this study.

50 parameterizations were randomly generated, and those with non-zero objective values were selected. Figure 7-13 shows the distribution of these objective values, where only 5 out of the

50 parameterizations had non-zero objective values. This already indicates the inefficiency of using randomly generated data for optimization. This inefficiency arises from the quasi-brittle nature of the cementitious materials, as modifying the geometry of ACCCs can increase their susceptibility to damage and splitting failure under load. Additionally, the intricate shapes of ACCCs are highly sensitive to geometric changes aimed at enhancing recoverable hinge-like strain capacity while maintaining auxetic behavior. Furthermore, ACCCs initially form small cracks under compression because of the strong fiber-bridging capacity of SHCC materials, requiring a more refined specification of geometric parameters. This, in turn, expands the design space and leads to an exponential increase in computational cost. In Figure 7-6 and Figure 7-7, three ACCC shapes designed as intuitive solutions (including the reference P1a) are compared to the randomly generated shapes based on their objective values.

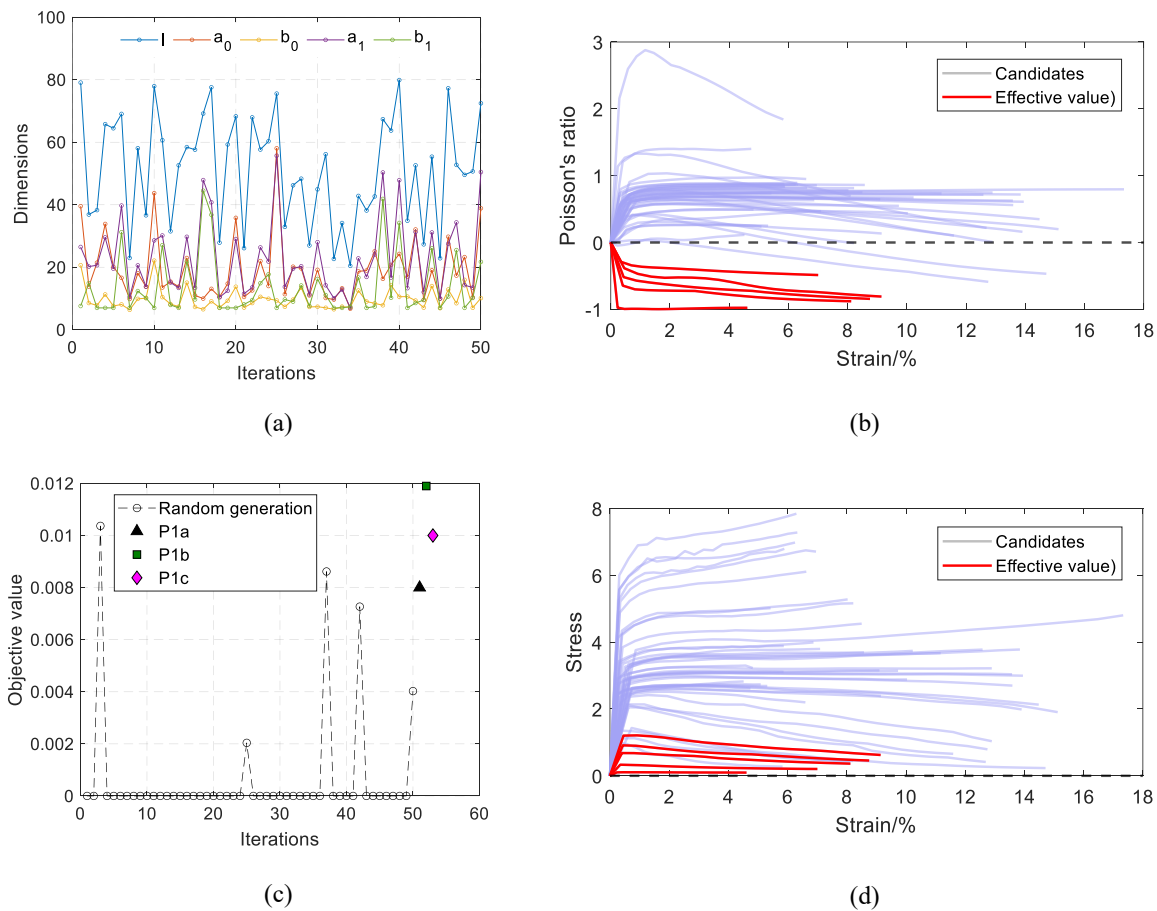


Figure 7-13 Results of random generation, (a) dimensions, (b) Poisson's ratio, (c) objective values, (d) stress-strain curves.

(2) BO-FEM setup

For the dataset generated through random generation, the objective values were manually penalized instead of being directly derived from the model results. This approach may cause challenges in identifying non-zero acquisition function values in BO, thereby hindering the acquisition function from effectively guiding the exploration of the design space. Therefore,

the 5 non-zero values were combined with the three previously used parameterizations to form the initial dataset for subsequent optimization. The optimizations were performed sequentially, with a batch size of one, to maximize the performance of BO [19]. Although BO is inherently a sequential algorithm, it can be adapted to execute multiple optimizations simultaneously, updating the surrogate model only after all evaluations are completed [20]. While this parallel approach can save considerable time, it typically results in less effective optimization outcomes within a fixed number of trials. Expected Improvement (EI) [18] was employed as the acquisition function in BO to estimate the potential improvement over the current best observation at each sample point. It balances exploration of design space regions with high uncertainty (exploring new areas) and exploitation of regions with potentially high objective function values (refining known promising areas) to guide the selection of the next point for evaluation. Since solution quality was the primary focus of this study, BO was conducted in a purely sequential manner. Similar to the input constraints used in random generation, geometric parameter constraints were applied to each candidate generated during BO iterations, expressed as inequalities in Eqs. (71)-(80).

$$20 \leq l_i \leq 80 \quad (71)$$

$$l_i - 2a_{0i} - 2b_{0i} \geq 7 \quad (72)$$

$$l_i - 2a_{0i} - 2b_{0i} \leq 64 \quad (73)$$

$$a_{0i} - b_{0i} \geq 1 \quad (74)$$

$$b_{0i} \geq 3.5 \quad (75)$$

$$-a_{0i} + b_{0i} + a_{1i} \geq 3.5 \quad (76)$$

$$l_i - 2b_{0i} - 2a_{1i} \geq 7 \quad (77)$$

$$a_{1i} - b_{1i} \geq 1 \quad (78)$$

$$a_{0i} + b_{1i} - (a_{1i} + b_{0i}) \geq -0.5 \quad (79)$$

$$a_{1i} + b_{0i} - (a_{0i} + b_{1i}) \geq -0.5 \quad (80)$$

In addition to the constraints applied to the input geometric parameters, further constraints were imposed on the objective value by multiplying it by zero in the two specific cases: Removed case (i), (ii). The multiplier applied to the objective value was determined through trial and errors, allowing the Bayesian Optimization (BO) process to avoid these points without hindering the exploration of candidate points by the acquisition function. This approach also helps enhance the optimization speed.

As indicated in Section 7.3.2, the average strain $\bar{\varepsilon}_{\text{int}}$ of the cementitious material bonded to the PVDF film is treated as our objective function to simplify the representation of the output voltage. To calculate $\bar{\varepsilon}_{\text{int}}$, 80% of the bottom region of the internal profile in each ACCCs shape was designated as the bonding area through node editing algorithm (see Figure 7-14).

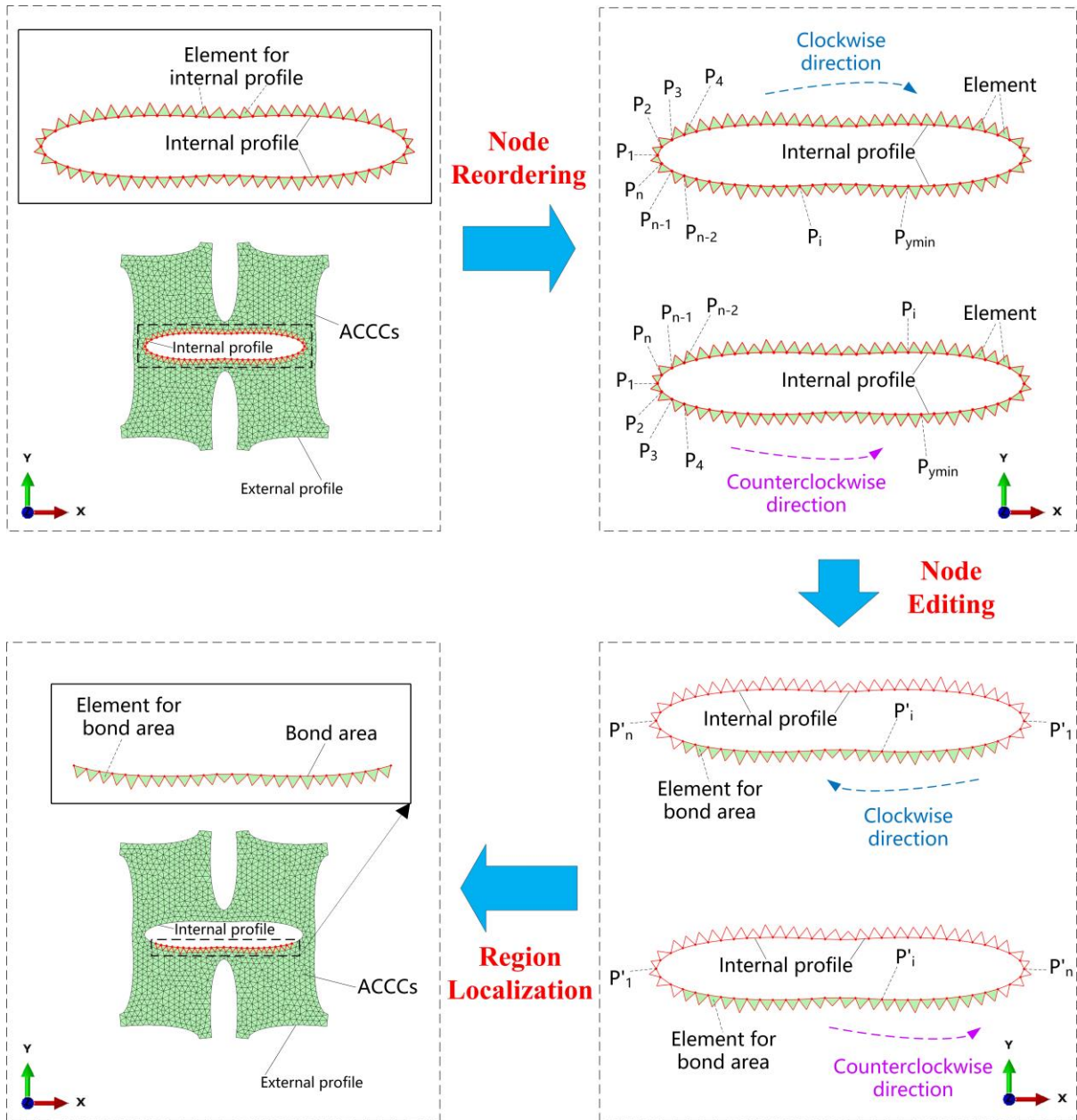


Figure 7-14 Programming for $\bar{\epsilon}_{int}$ calculation in parametric modeling of ACCC Shapes

The internal profile was determined based on shape topology reconstruction of ACCCs using an improved node-order tracking algorithm, as described in Figure 7-9. In Figure 7-14, the point P_1 with the minimum x-coordinate was identified and set as the first node. The remaining nodes were then reordered in either a clockwise or counterclockwise direction. The bottom region of the internal profile was selected as the bonding area for the PVDF film. This bottom region was determined by verifying whether the point P_{ymin} , which has the minimum y-coordinate, is included when traversing in either a clockwise or counterclockwise direction. The nodes in this region were also reordered according to a clockwise or counterclockwise direction. To calculate ϵ_{in} , 80% of the bottom region of the internal profile was designated as the bonding area through node editing (i.e., trimming nodes at both ends). This adjustment accounts for the fact that the two ends of the internal profile primarily experience compression and are geometric transition zones, where bonding piezoelectric films is avoided to prevent

placement on these two ends.

Figure 7-15 shows a schematic diagram for FEM-Bayesian Optimization (BO) setup. In the interactive process between the FEM model and BO, a new parameterization with the highest probability for improving the objective value is (i) selected by BO, (ii) its geometry is generated, (iii) its response is predicted using FE analysis, and (iv) Gaussian probabilistic models of the quantity of interest ($\bar{\varepsilon}_{\text{int}}$) are updated after each evaluation considering the constraints. This iterative process continues until no further improvement in the objective value is observed, or the variation becomes negligible. During the optimization process, the current best objective value, geometric parameters, and mechanical performance (including Poisson's ratio and the stress-strain curve) are recorded. For each generated shape, the applied displacement in the CDP model was only considered up to the smaller value between b_0 and b_1 . Therefore, the contact between the top and bottom ends of the central elliptical hole (i.e., self-contact within this hole) is not considered, nor is the contact at the side joints in the section due to rotation. This is because ACCCs tend to split when these contacts occur, as their negative Poisson's ratio decreases under compression. Experiments revealed that when the compressive displacement approaches half the size of the compressible hole, the ligament accumulates significant plastic deformation and damage, leading to a further reduction in recoverable deformation. For smaller ligaments, this poses a higher risk of failure. Therefore, the deformation shape after a compressive displacement equal to one-quarter of the hole size (i.e., half of the smaller value between b_0 and b_1 .) was uniformly selected as the initial geometry for each candidate in the secondary elastic model. In the second elastic model, the applied displacement amplitude for each shape is set to 10% of the smaller value between b_0 and b_1 .

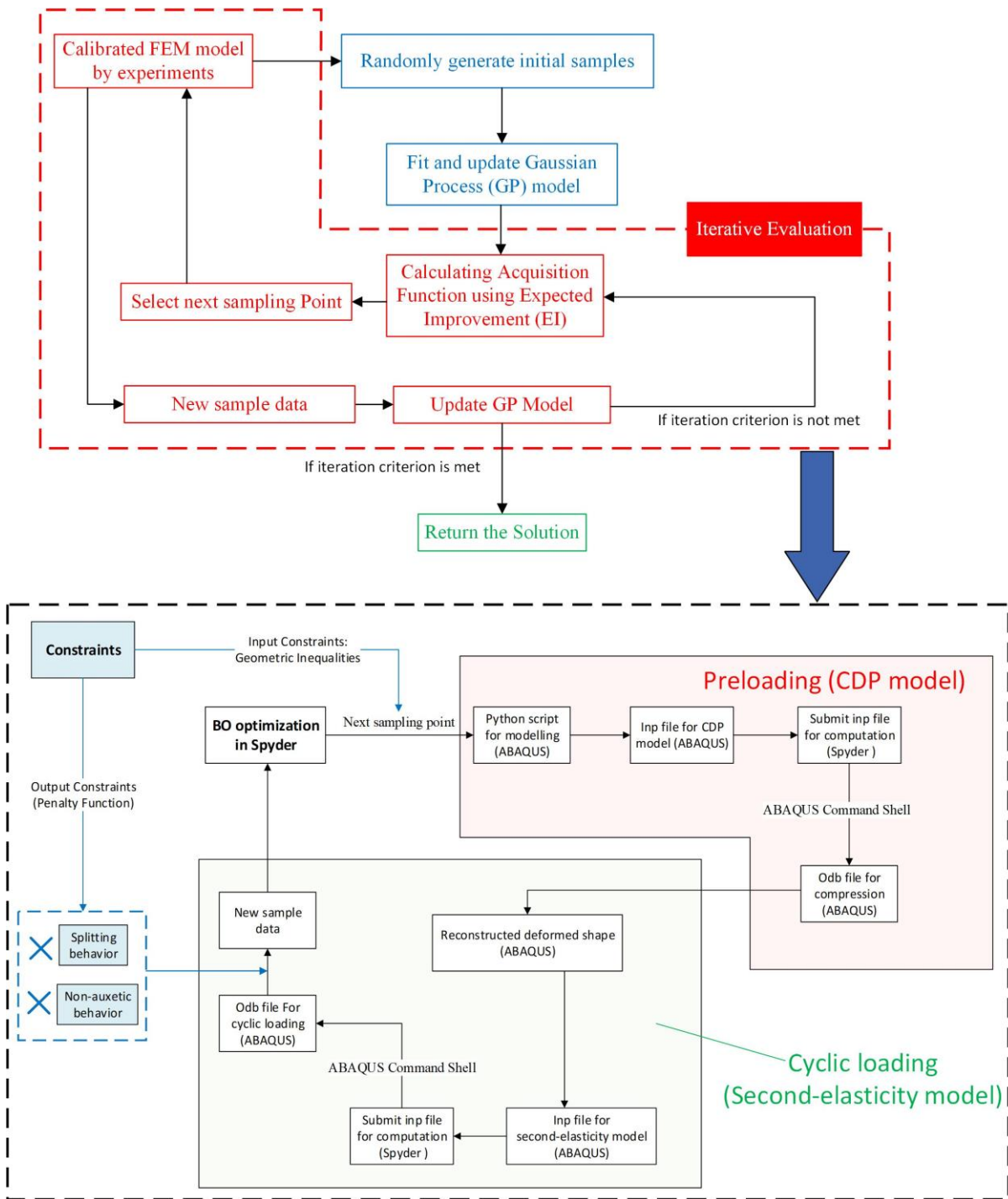


Figure 7-15 Schematic diagram for BO-FEM setup

7.5 RESULTS AND DISCUSSION

7.5.1 Optimization results

As shown in Figure 7-16, the reference shape (Ref in Figure 7-16a), P1a, exhibits a low $\bar{\varepsilon}_{\text{int}}$ of 0.008. For the randomly generated shapes, the best configuration only reached a $\bar{\varepsilon}_{\text{int}}$ of 0.01 (Best random shape in Figure 7-16a), which is higher than the reference. In contrast, during the Bayesian Optimization process, the best objective value $\bar{\varepsilon}_{\text{int}}$ exhibited a general trend of improvement over iterations. In the first 80 iterations, the best objective value increases rapidly, after which it slowly improves and eventually converges. The best shape optimized through BO at iteration 180 achieves a $\bar{\varepsilon}_{\text{int}}$ of 0.0155 (BO optimum in Figure 7-16a), nearly twice the objective value of the reference shape. Notably, the best value obtained at iteration 180 offers only a marginal improvement over the second-best value achieved at iteration 164 (second-best BO optimum in Figure 7-16a). As shown in Figure 7-16b, there were only six candidates where the objective value dropped to zero, indicating violations of the criteria for non-splitting and auxetic behavior. This further highlights the efficiency of BO compared to random generation methods in optimization. It is worth noting that not every iteration led to improvement, as BO balances exploiting high-performing regions with exploring new possibilities. This is reflected in the progression of the objective value throughout the BO process, as shown in Figure 7-16b. The process achieved rapid optimization during the first 100 iterations, marked by significant fluctuations due to exploration. After 100 iterations, fluctuations diminished as the focus shifted to refinement. By 200 iterations, the best objective value remained unchanged through 500 iterations, indicating the optimization had nearly reached a global optimum. To maintain computational efficiency, the analysis utilized the results from the first 200 iterations.

Figure 7-17 illustrates the geometric evolution of the BO process across iterations. The dimensions of the five design variables (Figure 7-17a) and their relative values (Figure 7-17b) exhibit relatively rapid fluctuations during approximately the first 50 iterations. These are followed by smaller fluctuations as the values gradually stabilize near their optimal levels. In Figure 7-17a, it is evident that $a_0 > a_1$, $b_0 > b_1$, a pattern also reflected in their relative values in Figure 7-17b. In Figure 7-17b, a_0/l and a_1/l decrease over nearly the initial 50 iterations, while b_0/l and b_1/l increase. This progression indicates that the elliptical hole shape gradually transitions toward a circular form, with an increase in the lateral distance (b_0) between the two side joints in contact with the loading plate. As b_0 increases, a higher compressive load is required to achieve the same moment necessary for the ligaments to undergo plastic deformation and result in section rotation, assuming the constitutive materials have identical tensile strength. At the same time, the increased frictional force at the loading joints induces greater tensile force in the ligaments, as dictated by force equilibrium. This, in turn, leads to the formation of larger cracks in the ligaments, ultimately contributing to a higher objective value.

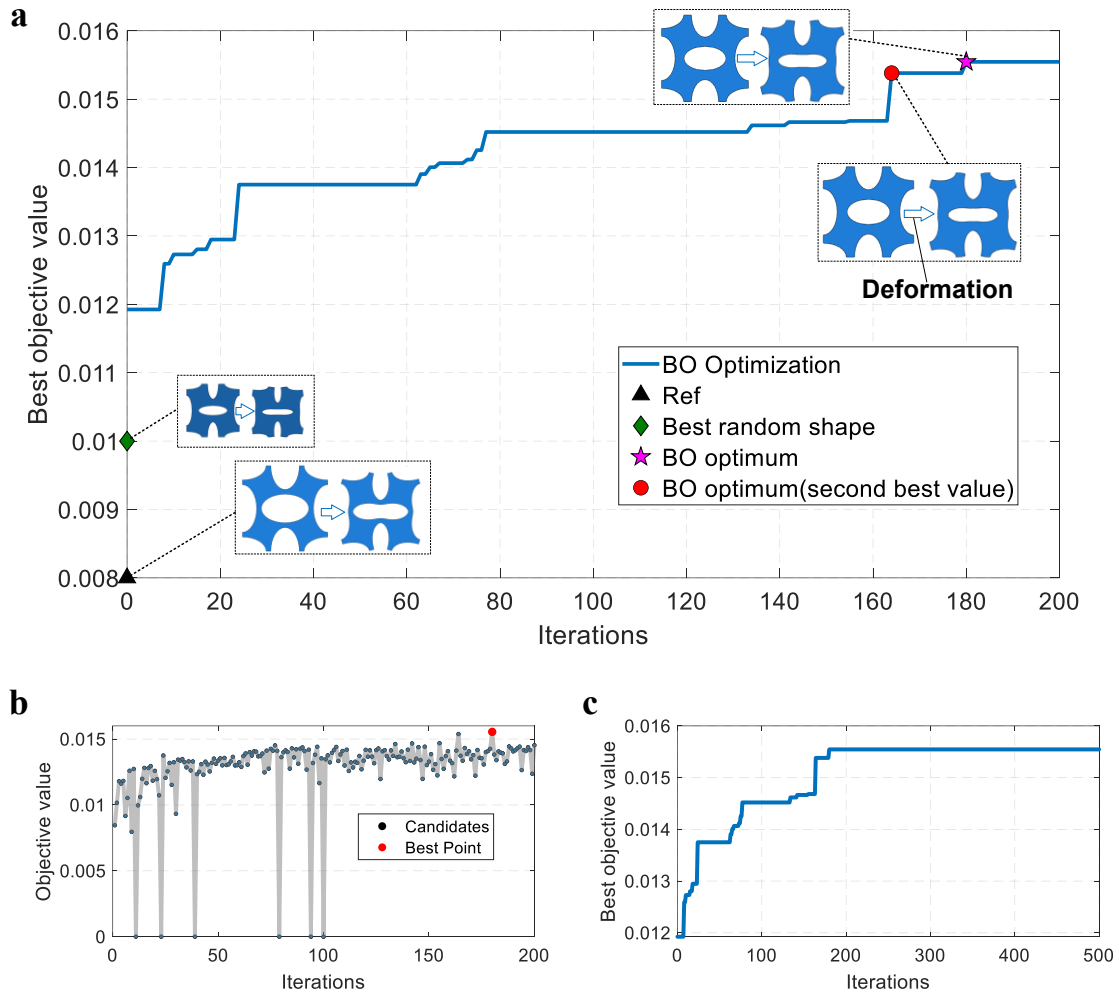


Figure 7-16 Convergence of BO algorithm: (a) best objective value (with insets showing the initial shape and its corresponding deformed shape under cyclic loading), (b) progression of the objective value, (c) best objective value until 500 iterations.

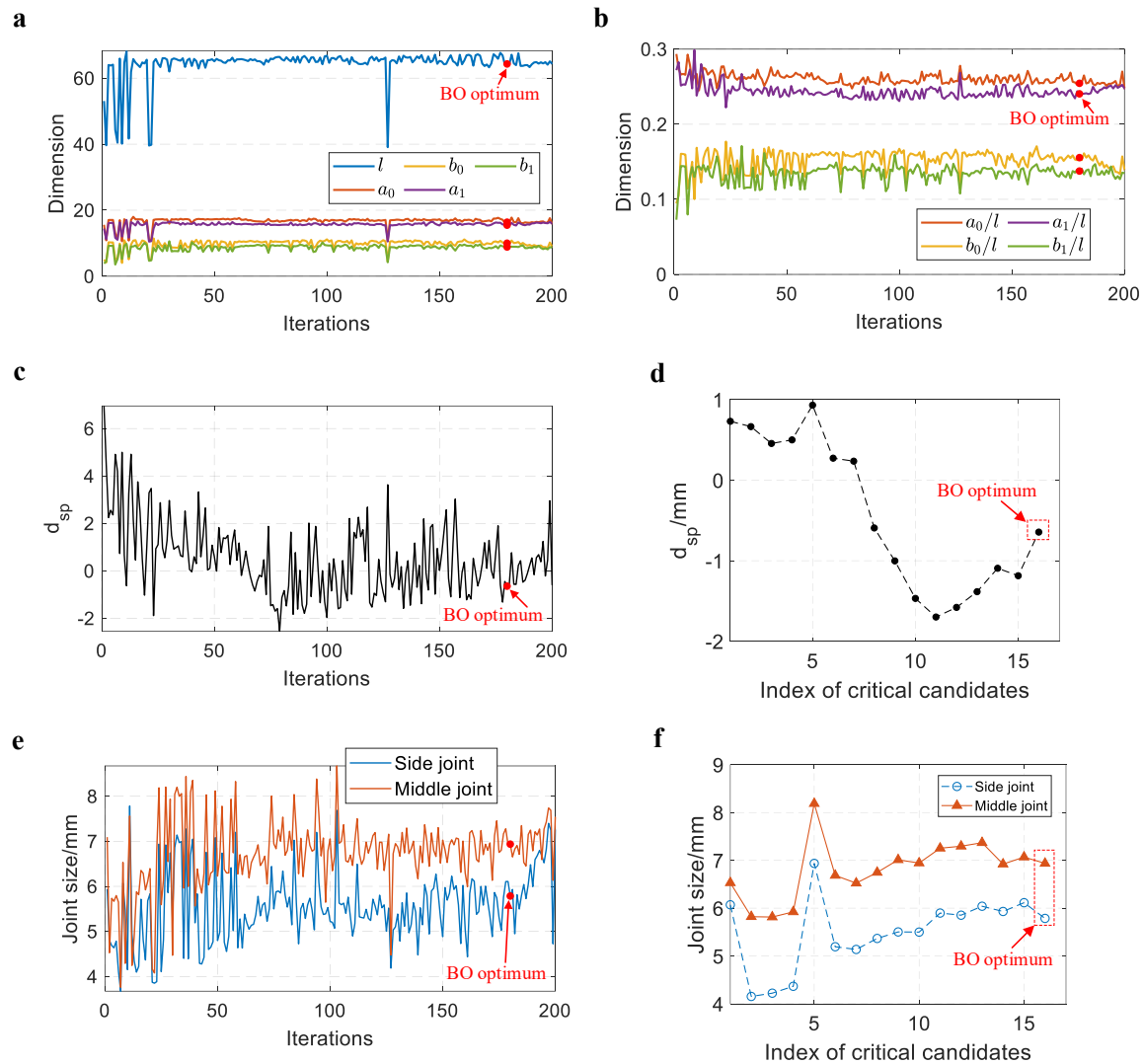


Figure 7-17 Geometric evolution of BO during iterations, (a) dimension, (b) relative dimension, (c) critical parameter for splitting (d_{sp}), (d) d_{sp} of critical points, (e) joint size, (f) joint size of critical candidates.

Similarly, as d_{sp} (defined in Eq. (25)) decreases, the structural chirality diminishes. This reduction requires the ligaments to withstand higher externally applied compressive stress to achieve section rotation, leading to the development of larger cracks in the ligaments. The parameter d_{sp} decreases over iterations in Figure 7-17c, although with some fluctuations, but finally tend to be fluctuate around zero where the optimum point is located. When d_{sp} is negative, that means vertical ligaments are subjected to more compressive force, which may result in local compressive failure locally and further develops to splitting failure. The critical candidates representing the current best objective values in Figure 7-16a are selected for analysis and reordered based on their sequence in the optimization process. These points indicate improvements over the previous best objective values during the BO iterations. In Figure 7-17d, these critical candidates exhibit a downward trend, becoming more negative, which leads to larger cracks in the ligaments. However, this progression eventually results in a condition closer to splitting failure, causing the objective value to drop to zero due to the constraints imposed by BO. Therefore, BO seeks to avoid this situation and focuses on

identifying points that fluctuate around a zero value for d_{sp} to find the optimal solution. In Figure 7-17e, both the side joint and middle joint increase with significant fluctuations during nearly the first 100 iterations before stabilizing with diminished variations. The critical candidates in Figure 7-17f exhibit a similar trend, despite some fluctuations due to the exploration in BO. This indicates that a larger joint size leads to a wider crack opening in the ligaments, thereby improving the objective value of $\bar{\varepsilon}_{int}$. This occurs because larger joints produce greater crack openings at the same rotation angle and increase compressive force due to higher bending resistance, which, in turn, raises frictional force at the loading joints and induces greater tensile force in the ligaments.

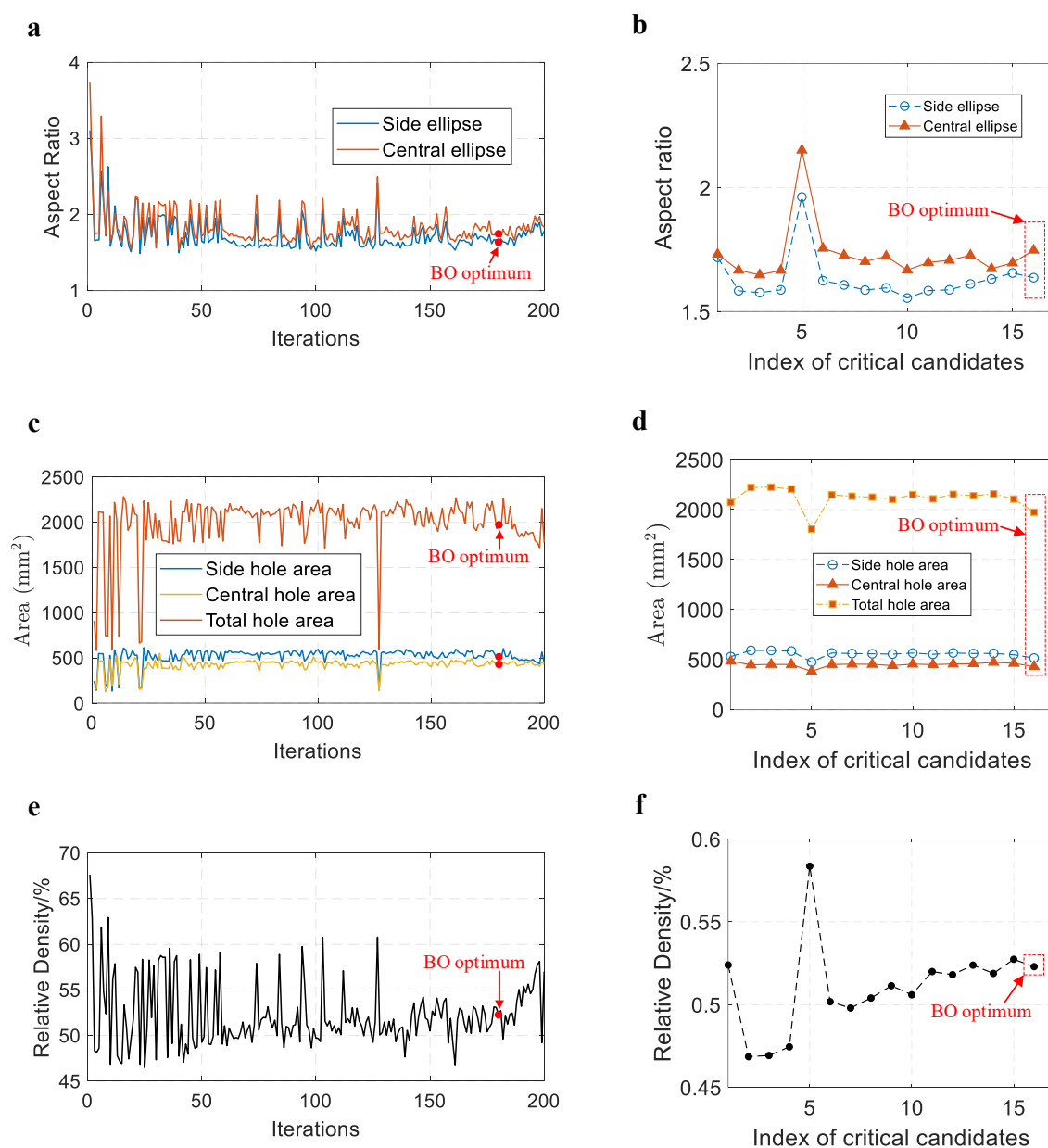


Figure 7-18 Geometric features evolution during BO iterations, (a) aspect ratio, (b) aspect ratio of critical candidates, (c) hole area, (d) hole area of critical candidates, (e) relative density, (f) relative density of critical candidates.

Figure 7-18 displays the evolution of geometric features during BO iterations. As shown in Fig. 12a, the aspect ratios of both the side ellipse and central ellipse (denoted in Figure 7-10) keep decreasing in the initial 50 iterations with significant fluctuations and stabilize after 50 iterations with decreasing fluctuations. This trend also indicates that the elliptical hole shape gradually transitions into a circular form, causing more pronounced cracking in the ligaments, as explained in Figure 7-17a, Figure 7-17b. In Figure 7-18b, the aspect ratio of the critical candidates remains relatively consistent, despite some fluctuations. In Figure 7-18c, the hole areas show significant fluctuations in the early iterations, followed by a slight decrease. In Figure 7-18d, the hole size of the critical candidates decreases slightly as the iterations progress. Correspondingly, the relative density gradually increases with iterations in Figure 7-18e, despite some fluctuations. In Figure 7-18f, the relative density of the critical candidates continues to increase, with some minor fluctuations. The reduction in hole area indicates an increase in material volume (i.e., higher relative density), resulting in larger joint sizes and more pronounced cracking. This benefits the objective function if non-splitting and auxetic behavior are maintained.

Figure 7-19 illustrates the mechanical performance evolution during BO iterations. Figure 7-19a displays the stress-strain curves of all candidates, with critical candidates mainly clustering in the upper-middle region and exhibiting relatively higher peak stress. This clustering occurs because lower curves with reduced peak stress are associated with smaller joint sizes, higher hole aspect ratios, lower relative densities, and larger d_{sp} , which limit the formation of large crack regions to improve the objective function. As the curves shift upward with increasing peak stress, larger cracks develop at the ligaments. However, excessive ligament size eventually leads to splitting behavior, which BO mitigates using penalty constraints. Figure 7-19d shows the stress-strain curves of the critical candidates, with color intensity indicating iteration progress. As iterations advance, the curves move upward (from lighter to darker colors) with increasing peak stress, reflecting larger joint sizes, reduced hole aspect ratios, higher relative densities, and lower d_{sp} (indicated in Figure 7-10). These changes facilitate greater crack formation in the ligaments, improving the objective function. However, the optimized curve is not the one with the highest peak stress (solid line in Figure 7-13d), suggesting that additional factors influence the objective function. Furthermore, Figure 7-13b shows the CDP model of the optimized candidate (BO optimum in Figure 7-16a), which demonstrates a larger plastic strain and a more extensive plastic zone in its deformed shape under compression compared to the reference (Figure 7-3d). Figure 7-19c illustrates the variation in Poisson's ratio during compression for all candidates, with the critical candidates mainly clustering in the middle region. Figure 7-19e shows the Poisson's ratio variation for these critical candidates, with color intensity indicating iteration progress. As iterations advance, the curves shift upward (from lighter to darker colors), reflecting a lower absolute value of negative Poisson's ratio, which suggests larger joint sizes, reduced hole aspect ratios, higher relative densities, and lower d_{sp} . These changes also facilitate greater crack formation in the ligaments and thus improve the objective function. However, the optimized curve does not correspond to the one with the lowest absolute value of negative Poisson's ratio (solid line in Figure 7-19e), indicating the influence of additional factors on the objective function. Furthermore, the maximum absolute value of negative Poisson's ratio (NPR) (denoted as Maximum NPR in Figure 7-19f) shows a slight decrease with some fluctuation due to the balance between exploration and exploitation during BO iterations. Notably, the Maximum NPR for the critical candidates in Figure 7-19h also displays a downward trend, despite some fluctuations due to the balance. In Figure 7-19g,

the optimal design exhibits greater elastic strain and a more extensive tensile zone near the ligaments at the peak point of $\bar{\varepsilon}_{\text{int}}$ during cyclic loading in the second elasticity model, compared to the reference (Figure 7-3e). The highest elastic strain is concentrated at the middle joints, with tensile strain indicated in the strain direction. In Figure 7-19i, $\bar{\varepsilon}_{\text{int}}$ exhibits a sinusoidal curve during cyclic loading, with a peak value of 0.0155.

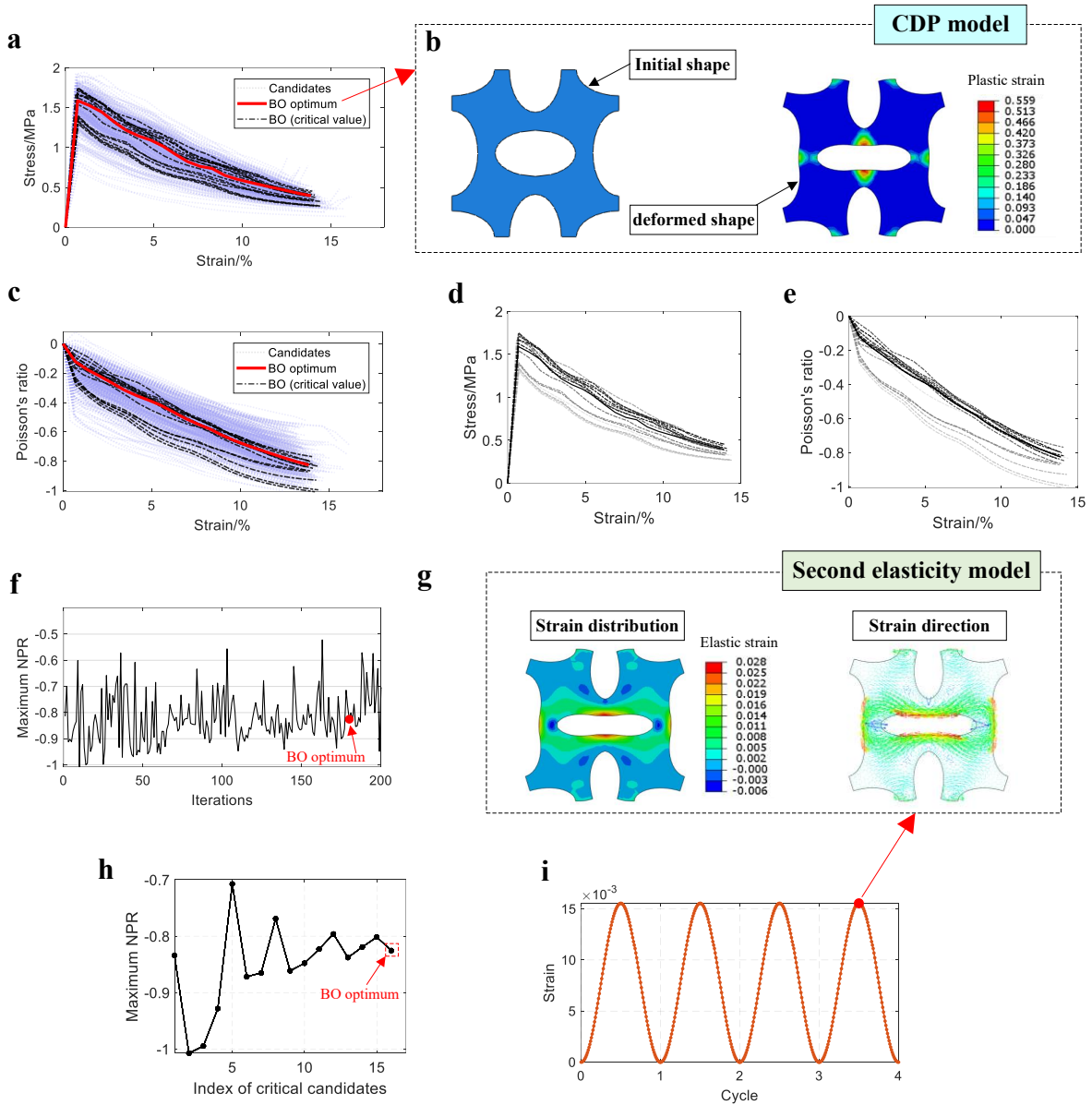


Figure 7-19 Mechanical performance evolution of BO during iterations, (a) stress-strain curves, (b) CDP model of ACCCs shape (BO optimum), (c) variations in Poisson's ratio, (d) stress-strain curves of critical candidates, (e) Poisson's ratio variations of critical candidates, (f) maximum Negative Poisson's ratio (NPR), (g) second elasticity model of ACCCs shape (BO optimum), (h) maximum Negative Poisson's ratio (NPR) of critical candidates, (i) $\bar{\varepsilon}_{\text{int}}$ of ACCCs shape (BO optimum) from its second elasticity model.

7.5.2 Experimental validation

Considering the PVDF size and the solder pin length, the second-best shape from Bayesian optimization (denoted as "BO Optimum (Second Best Value)" in Figure 7-16) was chosen for experimental validation, as shown in Figure 7-20. This shape has a $\bar{\varepsilon}_{\text{int}}$ of 0.0154, very close to the 0.0155 of the best shape (BO optimum in Figure 7-16). Figure 7-20 depicts the manufacturing process and the energy harvesting experimental setup for the optimized shape, aligning with the configurations shown in Figure 7-1 and Figure 7-4. Figure 7-20b displays the CDP model of the optimized shape, which demonstrates similar plastic strain and plastic zone characteristics in its deformed state under compression, comparable to those of the best shape ("BO Optimum" in Figure 7-16). Figure 7-20c also shows similar elastic strain distribution and strain direction for its deformed shape at the peak point of $\bar{\varepsilon}_{\text{int}}$ during cyclic loading in the second elasticity model. The highest tensile elastic strain, concentrated at the middle joints, follows a sinusoidal pattern during cyclic loading, with a peak value of 0.0154. During the energy harvesting test, the second-best shape is initially compressed through displacement loading, starting from zero and increasing to U (8.0 mm), resulting in a deformed specimen height of approximately 59 mm. Considering the thickness of the silicon rubber layer, further compression could cause contact between the upper and lower ends of the holes. Subsequently, cyclic loading is applied under displacement control, utilizing a sinusoidal wave with a constant amplitude A (1 mm) and a frequency f (1 Hz). The energy harvesting test results of ACCCs for the second-best shape based on three replicate specimens are presented in Figure 7-20e. This depicts a sinusoidal output voltage with a peak-to-peak value of $14.8 \pm 0.8\text{V}$ per cycle of cyclic loading, showcasing nearly 2.7 times higher than the reference one. Figure 7-20d presents the dynamic stress-strain curve of the second-best shape obtained from three replicate specimens during the energy harvesting test.

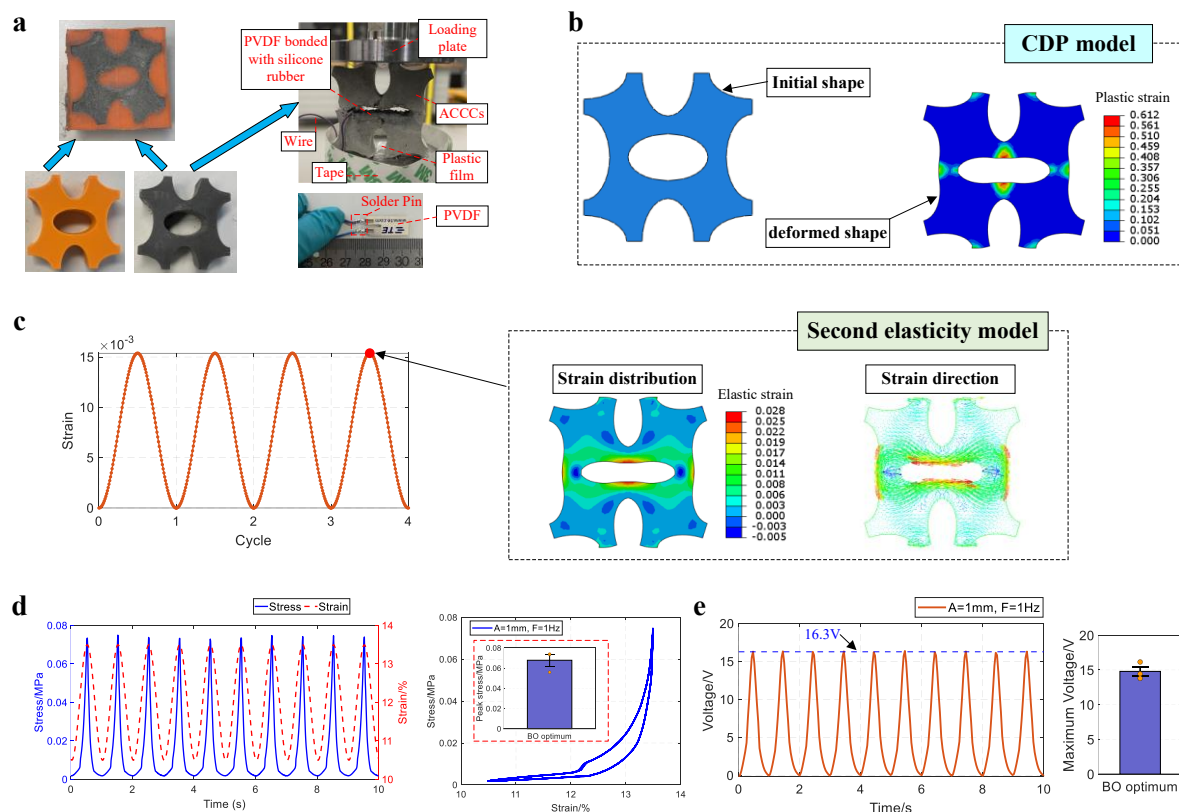


Figure 7-20 Experimental validation, (a) sample preparation and energy harvesting test setup of optimized ACCCs shape, (b) CDP model of optimized ACCCs shape, (c) ε_{int} of optimized ACCCs shape and its second elasticity model, (d) stress-strain curve during energy harvesting test, (e) output voltage of energy harvesting test.

A detailed comparison between the optimal ACCC shape and the reference design is presented below. Figure 7-21 shows the performance of the optimal ACCCs shape under a precompression displacement of 6 mm, corresponding to a similar compressive strain level (compression displacement divided by the shape's length) as the reference design. The optimal design generates a peak-to-peak output voltage of 8.6 ± 0.5 V, approximately 1.6 times higher than that of the reference under equivalent strain levels. Additionally, the objective value ($\bar{\varepsilon}_{\text{int}}$) for the optimal ACCC design (second best) is nearly double that of the reference. This discrepancy arises from reduced strain transfer loss in experiments, as the larger crack in the optimal design leads to debonding of the silicone rubber above the crack region from the cementitious area. At higher precompression levels, the optimal design achieves a peak-to-peak output voltage of 14.8 ± 0.8 V, nearly 2.7 times greater than the reference design, along with improved peak stress. In contrast, starting at a compression of 5 mm (7.94% strain), the reference design shows a decline in both output voltage and peak stress as the compression increases to 6 mm, 7 mm, and 8 mm, corresponding to compressive strains of 9.52%, 11.11%, and 12.70%, respectively, as shown in Figure 7-22 and Table 7-8. The errors in the reference design performance could stem from the heterogeneity of the cementitious materials, the misalignment of the crack relative to the ligament's center, and the irregular variation of the crack along the thickness direction. Furthermore, discrepancies might result from errors in the

manual bonding of the piezoelectric film and the degree of silicone rubber debonding near the main crack.

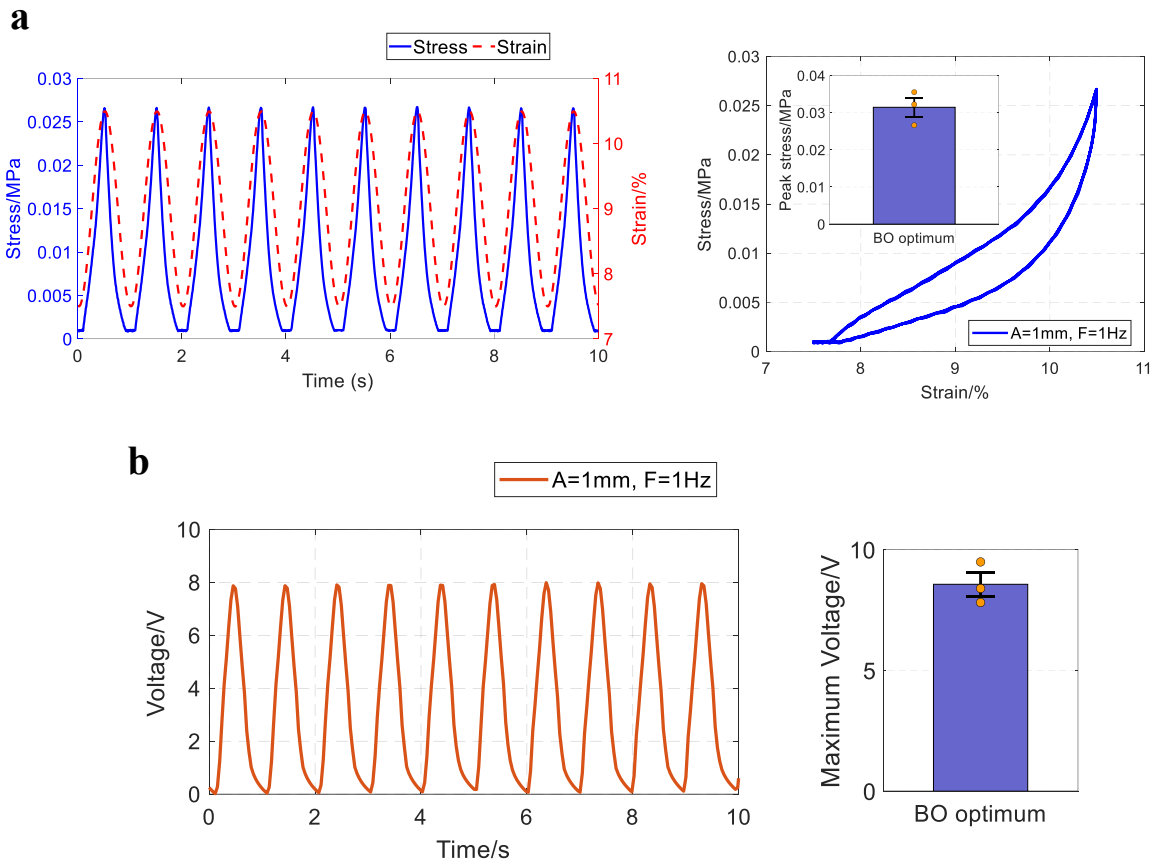


Figure 7-21 Peak-to-peak output voltage and peak stress of BO-optimized shape (second-best) under reduced compression displacement.

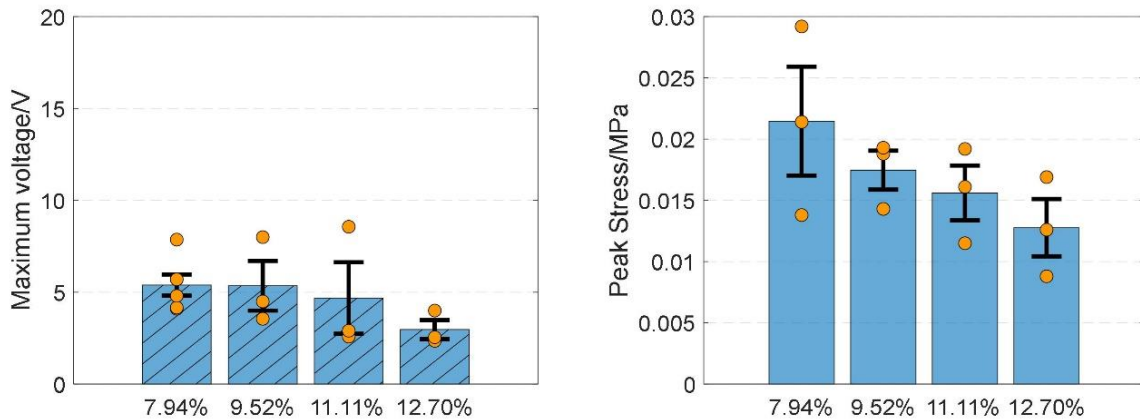


Figure 7-22 Peak-to-peak output voltage and peak stress of the P1a shape under increased compression displacement.

Table 7-8 Peak-to-peak output voltage and peak stress of the refence under increasing compression displacement

Compressive strain	7.94%	9.52%	11.11%	12.70%
Peak stress (MPa)	0.021±0.004	0.017±0.002	0.016±0.002	0.013±0.002
Voltage (V)	5.4±0.6	5.3±1.4	4.7±1.9	3.0±0.5

7.6 CONCLUSIONS

An interactive BO framework was established with the energy harvesting model, using the average strain of cementitious material bonded to the piezoelectric film as the objective function towards optimal flexible energy harvester. BO constraints excluded cases of splitting or non-auxetic behavior under compression. The main conclusions can be summarized as follows:

- A parametric energy harvesting model has been developed for ACCC energy harvester optimization. It incorporates the CDP model and the second elasticity model to analyze the recoverable hinge-like strain capacity of ACCCs with diverse shapes. Herein, an improved node-order tracking algorithm has been introduced, enabling the precise reconstruction of deformed ellipse-shaped ACCC post-compression by accurately reflecting their modified geometric profiles.
- Compared to random generation methods, the BO approach achieves superior optimization efficiency by balancing exploration and exploitation to enhance the recoverable hinge-like strain capacity in ACCC energy harvesters. Additionally, the learning-driven framework proactively and effectively identifies and eliminates cases with splitting or non-auxetic behavior, further enhancing optimization results.
- As BO iterations advance to improve the recoverable hinge-like strain capacity in ACCCs, the joint size increases, the aspect ratio decreases, and the relative densities rise, although some fluctuations occur due to the exploration phase of BO. These changes, within a specific range, lead to greater crack formation in the ligaments while maintaining non-splitting and auxetic behavior, ultimately enhancing the objective function for higher recoverable hinge-like strain capacity.
- As BO iterations progress to improve the recoverable hinge-like strain capacity in ACCCs, the value of d_{sp} decreases, leading to a reduction in chirality and an increase in ligament cracks, eventually fluctuating around 0. To prevent splitting under compression in the ACCCs shape design, it is recommended to maintain d_{sp} above 0.
- As BO iterations advance to enhance the recoverable hinge-like strain capacity in ACCCs, the stress-strain curves shift upward with higher peak stress, while the absolute value of the negative Poisson's ratio decreases. These changes, within a specific range, promote increased crack formation in the ligaments while preserving non-splitting and auxetic behavior, thereby improving recoverable hinge-like strain capacity.
- The optimized results were validated through energy harvesting experiments, demonstrating a peak-to-peak value of approximately 15 volts per cycle of cyclic loading, showcasing nearly 2.7 times higher than the reference.

An interactive BO framework was developed with the FEM model to modulate the recoverable strain capacity towards optimal ACCC energy harvester. This framework can be further extended for the inverse design of ACCC energy harvester in various engineering

scenarios, tailored to specific properties such as specimen sizes, load capacities, and dimensions of the bonded piezoelectric material. The piezoelectric film is bonded to the cementitious matrix using silicone rubber, which serves as an adhesive layer to facilitate strain transfer. However, some strain loss occurs due to larger cracks in the ligaments and partial debonding between the PVDF and silicone rubber. To improve strain transfer from the ligaments to the PVDF, a stronger adhesive material with higher bond strength could be considered in the future study. This chapter's exploration of the optimal design for ACCCs with a single unit cell offers valuable insights for designing multi-cell ACCCs. In practical engineering applications, auxetic cementitious composites typically consist of multiple repeating unit cells. Each unit cell is capable of generating electrical energy. The combined energy harvested from these multiple cells will be examined in a preliminary study presented in the following chapter.

REFERENCES

- [1] Z. Wan, Z. Chang, Y. Xu, B. Šavija, Optimization of vascular structure of self-healing concrete using deep neural network (DNN), *Construction and Building Materials*, 364 (2023) 129955. <https://doi.org/10.1016/j.conbuildmat.2022.129955>.
- [2] Z. Wan, Y. Xu, Z. Chang, M. Liang, B. Šavija, Automatic enhancement of vascular configuration for self-healing concrete through reinforcement learning approach, *Construction and Building Materials*, 411 (2024) 134592. <https://doi.org/10.1016/j.conbuildmat.2023.134592>.
- [3] M. Ohno, M. Pierre, K. Imagawa, T. Ishida, Simulation and learning-driven design for architected cement-based materials, *Journal of Building Engineering*, 65 (2023) 105768. <https://doi.org/10.1016/j.jobe.2022.105768>.
- [4] G.A. Lyngdoh, N.-K. Kelter, S. Doner, N.M.A. Krishnan, S. Das, Elucidating the auxetic behavior of cementitious cellular composites using finite element analysis and interpretable machine learning, *Materials & Design*, 213 (2022) 110341. <https://doi.org/10.1016/j.matdes.2021.110341>.
- [5] M.E. Scyphers, J.E.C. Missik, H. Kujawa, J.A. Paulson, G. Bohrer, Bayesian Optimization for Anything (BOA): An open-source framework for accessible, user-friendly Bayesian optimization, *Environmental Modelling & Software*, 182 (2024) 106191. <https://doi.org/10.1016/j.envsoft.2024.106191>.
- [6] M. Liang, Z. Li, S. He, Z. Chang, Y. Gan, E. Schlangen, B. Šavija, Stress evolution in restrained GGBFS concrete due to autogenous deformation: bayesian optimization of aging creep, *Construction and Building Materials*, 324 (2022) 126690. <https://doi.org/10.1016/j.conbuildmat.2022.126690>.
- [7] Z. Vangelatos, H.M. Sheikh, P.S. Marcus, C.P. Grigoropoulos, V.Z. Lopez, G. Flamourakis, M. Farsari, Strength through defects: A novel Bayesian approach for the optimization of architected materials, *Science Advances*, 7 eabk2218. [10.1126/sciadv.abk2218](https://doi.org/10.1126/sciadv.abk2218).
- [8] I. Kuszczak, F.I. Azam, M.A. Bessa, P.J. Tan, F. Bosi, Bayesian optimisation of hexagonal honeycomb metamaterial, *Extreme Mechanics Letters*, 64 (2023) 102078. <https://doi.org/10.1016/j.eml.2023.102078>.
- [9] Y. Xu, H. Zhang, E. Schlangen, M. Luković, B. Šavija, Cementitious cellular composites with auxetic behavior, *Cement and Concrete Composites*, 111 (2020) 103624. <https://doi.org/10.1016/j.cemconcomp.2020.103624>.

- [10] Y.-F. Su, R.R. Kotian, N. Lu, Energy harvesting potential of bendable concrete using polymer based piezoelectric generator, *Composites Part B: Engineering*, 153 (2018) 124-129. <https://doi.org/10.1016/j.compositesb.2018.07.018>.
- [11] J.W. Sohn, J. Jeon, S.B. Choi, An Investigation on Dynamic Signals of MFC and PVDF Sensors: Experimental Work, *ADVANCES IN MECHANICAL ENGINEERING*, (2013) <https://doi.org/10.1155/2013/420345>.
- [12] H.-H. Huang, K.-S. Chen, Design, analysis, and experimental studies of a novel PVDF-based piezoelectric energy harvester with beating mechanisms, *Sensors and Actuators A: Physical*, 238 (2016) 317-328. <https://doi.org/10.1016/j.sna.2015.11.036>.
- [13] K. Rokugo, T. Kanda, H. Yokota, N. Sakata, Applications and recommendations of high performance fiber reinforced cement composites with multiple fine cracking (HPFRCC) in Japan, *Materials and Structures*, 42 (2009) 1197-1208. 10.1617/s11527-009-9541-8.
- [14] J. Xie, Y. Xu, Z. Wan, A. Ghaderiaram, E. Schlangen, B. Šavija, Modelling of energy harvesting with bendable concrete and surface-mounted PVDF, *Smart Materials and Structures*, 33 (2024) 085008. 10.1088/1361-665X/ad43cb.
- [15] J. Xie, Y. Xu, Z. Meng, M. Liang, Z. Wan, B. Šavija, Peanut shaped auxetic cementitious cellular composite (ACCC), *Construction and Building Materials*, 419 (2024) 135539. <https://doi.org/10.1016/j.conbuildmat.2024.135539>.
- [16] J. Xie, Y. Xu, Z. Wan, A. Ghaderiaram, E. Schlangen, B. Šavija, Auxetic cementitious cellular composite (ACCC) PVDF-based energy harvester, *Energy and Buildings*, 298 (2023) 113582. <https://doi.org/10.1016/j.enbuild.2023.113582>.
- [17] Y. Xu, E. Schlangen, M. Luković, B. Šavija, Tunable mechanical behavior of auxetic cementitious cellular composites (CCCs): Experiments and simulations, *Construction and Building Materials*, 266 (2021) 121388. <https://doi.org/10.1016/j.conbuildmat.2020.121388>.
- [18] D.R. Jones, M. Schonlau, W.J. Welch, Efficient Global Optimization of Expensive Black-Box Functions, *Journal of Global Optimization*, 13 (1998) 455-492. 10.1023/A:1008306431147.
- [19] S. Daulton, M. Balandat, E.J.A.i.N.I.P.S. Bakshy, Parallel bayesian optimization of multiple noisy objectives with expected hypervolume improvement, 34 (2021) 2187-2200. <https://doi.org/10.48550/arXiv.2105.08195>.
- [20] S. Daulton, M. Balandat, E.J.A.i.N.I.P.S. Bakshy, Differentiable expected hypervolume improvement for parallel multi-objective Bayesian optimization, 33 (2020) 9851-9864. <https://doi.org/10.48550/arXiv.2006.05078>.

8

MULTI-CELL AUXETIC CEMENTITIOUS CELLULAR COMPOSITE (ACCC) PVDF-BASED ENERGY HARVESTER

Up to Chapter 7, the experiments, simulations, and machine learning–based optimization were conducted on a single-cell ACCC energy harvester. This optimized unit cell can then be assembled into a multi-cell ACCC configuration to cumulatively harvest energy for practical engineering applications. Initially, pre-compression tests were carried out to ensure that the structure exhibited auxetic behavior without splitting, along with recoverable elastic deformation within the auxetic range. Based on these results, piezoelectric films were bonded to the hinge-like joints of each unit cell. Subsequently, energy harvesting tests were conducted to measure voltage output under varying loading frequencies and amplitudes with resistive loads.

8.1 INTRODUCTION

In [Chapter 7](#), machine learning-based optimization was performed on a single-cell ACCC energy harvester. This was adopted due to the increased complexity associated with multi-cell ACCC systems. As a result, the initial investigation focused on a single unit cell to establish a baseline for energy harvesting performance. Previous studies have shown that, within the auxetic deformation range, the force–displacement response of a single unit cell closely resembles that of a multi-cell configuration with the same geometric pattern. However, when accounting for the inherent heterogeneity of the cementitious matrix, multi-cell ACCCs are more susceptible to uneven deformation across unit cells. This non-uniform deformation can locally impair auxetic behavior and introduce intercellular interactions, which become particularly pronounced after crack initiation (see [Figure 8-1a](#)). In contrast, testing a single unit cell allows for a clearer representation of its intrinsic mechanical performance within the auxetic range, without the influence of intercell coupling effects. Furthermore, previous studies [\[1-3\]](#) on the compressive performance of multi-cell ACCCs have shown that cracks often initiate in a localized unit cell and then propagate outward, while adjacent cells may remain intact. This leads to stress concentration in the cracked region, eventually causing cracks to penetrate through multiple holes, forcing surrounding cells to unload and resulting in the loss of auxetic behavior (see [Figure 8-1b](#) and [Figure 8-1c](#)). These outcomes may be attributed to various factors, including the cementitious mixture used, ACCC geometry, matrix heterogeneity, boundary conditions between specimens and loading plates, and manual casting quality. Therefore, prior to conducting energy harvesting experiments, it is essential to ensure that the multi-cell ACCC energy harvester used in this chapter is capable of consistently exhibiting stable auxetic behavior and recoverable deformation under cyclic loading.

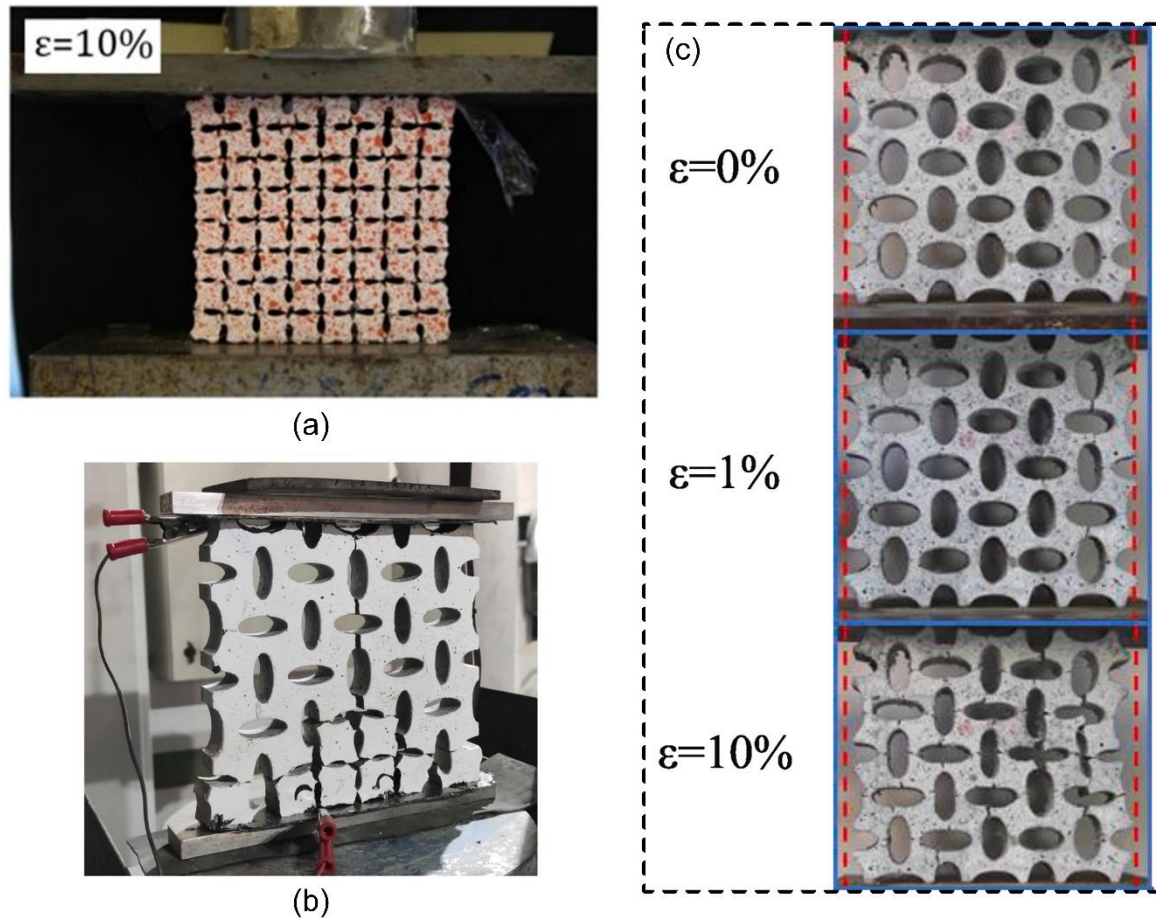


Figure 8-1 Deformation of multi-cell ACCC under compression testing reported in the literature [1-3].

In this chapter, the single-cell ACCC energy harvester optimized in Chapter 7 is extended to a multi-cell ACCC configuration to enable cumulative energy harvesting for practical engineering applications. Pre-compression tests were first conducted to confirm that the multi-cell ACCC demonstrated auxetic behavior without splitting and exhibited recoverable elastic deformation within the auxetic range. Following this, piezoelectric films were bonded to the hinge-like joints of each unit cell. Four PVDF films were bonded and electrically connected in parallel to capture the combined voltage output during the energy harvesting tests. The effects of different loading frequencies and amplitudes on the output voltage was also investigated.

8.2 MATERIALS AND METHODS

8.2.1. Materials and specimen preparation

Figure 8-1 illustrates the fabrication process of multi-cell ACCCs configured in a 2×2 array. The overall geometry and dimensions of the specimen, composed of four repeated unit cells, are presented in Figure 8-1a and Table 8-1. Although the unit cell design is based on the optimized ACCC configuration from Chapter 7, the side and central joints of each cell were adjusted to be identical, ensuring repeatability for multi-cell assembly. The multi-cell ACCCs were fabricated using an indirect 3D printing method [4], as shown in Figure 8-1. Initially, the

four-cell ACCC configuration was printed using FDM with an Ultimaker S5 printer, employing ABS as the printing material. The printed ABS shape was placed inside a cardboard container, into which a two-part silicone rubber (Poly-Sil PS 8620) was subsequently poured. The silicone rubber was prepared by mixing its components at a 1:1 mass ratio and allowed to cure at ambient temperature for at least two hours until full solidification. The solidified silicone rubber serves as a mold for casting the cementitious material. With a Shore A hardness of 20, the 8620 silicone rubber exhibits sufficient stiffness for mold stability, while maintaining enough flexibility to allow easy demolding of complex geometries.

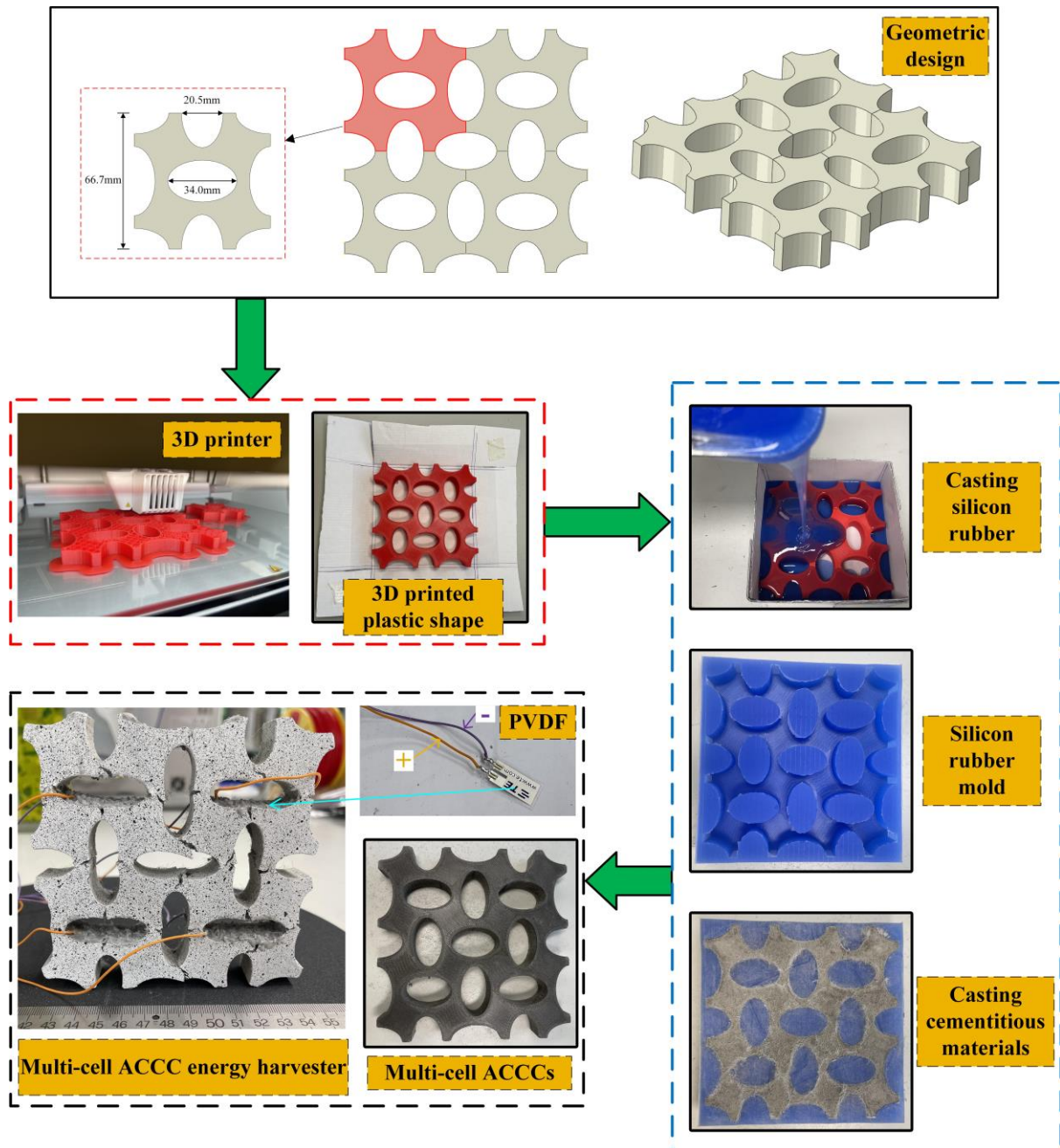


Figure 8-2 Specimen preparation

Table 8-1 Geometric parameters of one unit cell (unit: mm)

l	a_0	b_0	a_1	b_1	lg_0	lg_1
66.70	17.00	10.25	17.00	10.25	6.1	6.1

The SHCC mixture with extended softening (SHCC-LS) developed in Chapter 6 was still used as the base material for the ACCCs. The mixing and curing procedures of specimens were consistent with those described in Chapter 6. In the previous chapters, the PVDF film was bonded to the bottom ligament region surrounding the central elliptical hole of a single unit cell. For the extension to a 2×2 multi-cell configuration comprising four cells, the PVDF film for each unit cell was likewise bonded to the bottom ligament region surrounding the central elliptical hole, using the same silicone rubber (Poly-Sil PS8540) described in Chapter 7. The adhesive was allowed to cure for a minimum of 12 hours to ensure complete hardening. Poly-Sil PS8540, with a Shore A hardness of 40, was selected for its favorable adhesive properties. The LDT0-028K PVDF film, measuring 24.81 mm × 13.21 mm with a total thickness of 0.2 mm, includes a protective layer to prevent oxidation of the silver ink electrode surface [5-7]. To reduce strain transfer loss from the bonded ligament area to the PVDF during precompression, the PVDF film was bonded to the ligament region after precompression. The bonding was performed when the silicone rubber (Poly-Sil PS8540) had lost its fluidity and exhibited strong adhesive properties, approximately one hour after mixing its components A and B. A total of four PVDF films were bonded to the corresponding regions of four unit cells. All PVDF films were aligned in the same orientation to ensure consistent electrode polarity on the front (or back) side of the multi-cell ACCC specimens.

8.2.2. Experiments

The pre-compression test was conducted using the same setup as the uniaxial compression tests described in previous chapters, utilizing an Instron 8872 testing machine under displacement control at a rate of 0.01 mm/s. To reduce friction between the specimen and the loading plates during compression, plastic films were placed on both ends, allowing easier section rotation and promoting auxetic deformation. The compressive stress–strain curve was obtained by calculating stress as the compressive force divided by the specimen’s initial projected cross-sectional area, and strain as the displacement normalized by the initial specimen length. Following the pre-compression test, PVDF films were bonded to the specimen in preparation for the subsequent cyclic tests. The cyclic loading experiments were performed using the same test configuration, applying sinusoidal displacement control. Figure 8-2 presents the setup for the multi-cell ACCC energy harvesting test under cyclic loading conditions. A plastic film was still placed between the loading plate and the specimen to reduce friction. To counteract slight horizontal movement from uneven deformation and asymmetrical cracks in the cementitious materials during cyclic tests, tape was applied to the edges of the bottom loading plate. Using the similar loading plan shown in Chapter 7, the multi-cell ACCC energy harvester was first compressed by displacement loading. The compression process started at zero and progressed to a peak displacement of 10.0 mm. Subsequently, cyclic loading was applied using displacement control with a sinusoidal waveform characterized by a constant amplitude A and frequency f . To ensure reliability, the test was conducted with a minimum of three replicate specimens. For a convenient and consistent comparison, the peak-to-peak voltage was selected

as the metric to evaluate the energy harvesting performance of the multi-cell ACCC energy harvester.

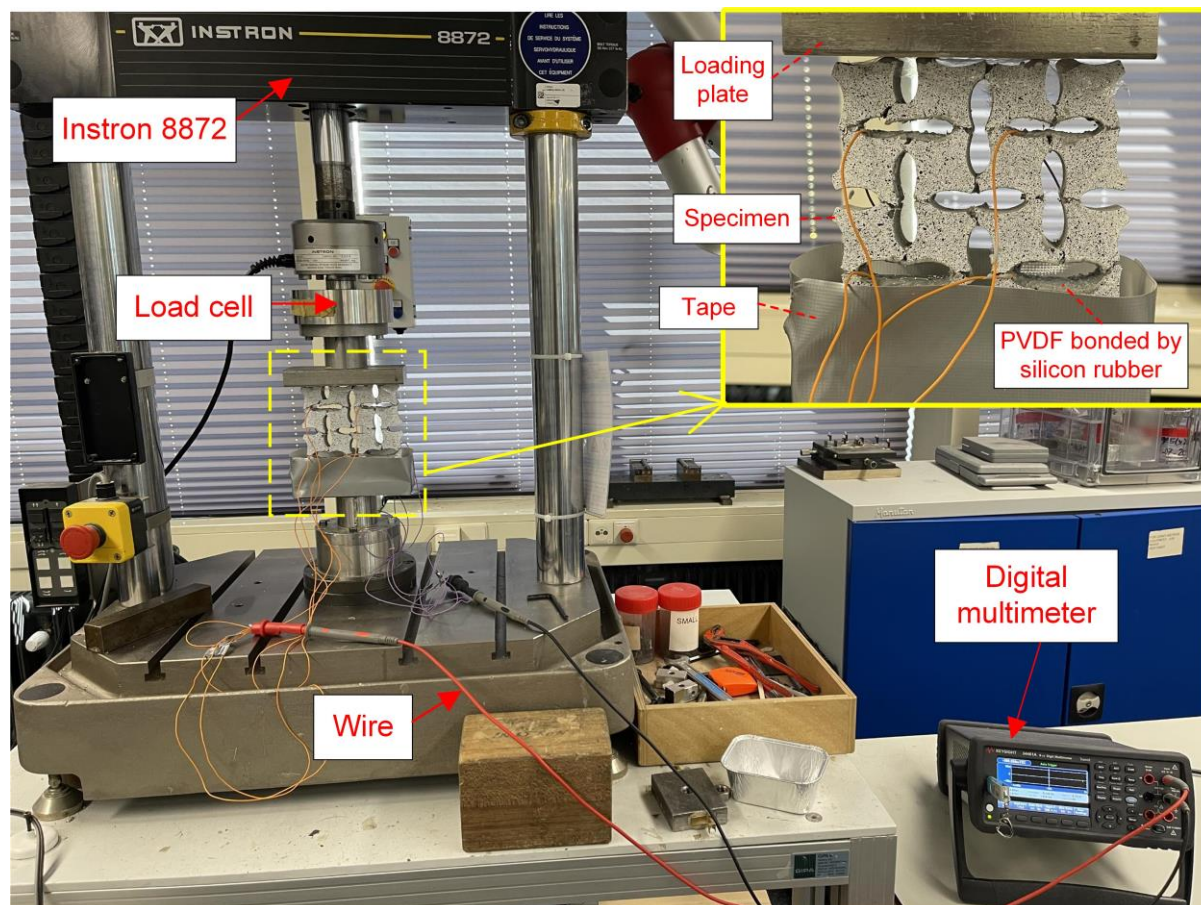


Figure 8-3 Energy harvesting setup of multi-cell ACCC energy harvester.

The DC output voltage of the energy harvester was measured using a Keysight 34461A digital multimeter (DMM). The LDT0 PVDF film exhibits a high internal impedance, estimated to be about $11.2 \text{ M}\Omega$ based on pure capacitance estimation at 25 Hz [7]. At lower frequencies, the impedance increases significantly, reaching approximately $280 \text{ M}\Omega$ at 1 Hz and $140 \text{ M}\Omega$ at 2 Hz based on pure capacitance estimation. These frequency conditions were employed both in the previous chapters and in the present chapter. To ensure accurate open-circuit voltage measurements, a DMM with an input impedance exceeding $10 \text{ G}\Omega$ —significantly higher than that of the PVDF—was employed in the previous chapters. The multimeter employed in this study provides two input impedance options for measuring voltage: $10 \text{ M}\Omega$ and $>10 \text{ G}\Omega$. When set to $10 \text{ M}\Omega$, the measurement no longer represents an ideal open-circuit condition, as the input impedance is lower than the internal impedance of the PVDF film at the low frequencies used in this study (i.e., 1 Hz or 2 Hz). Under this condition, multiple PVDF films can be connected in parallel to enhance the overall current. As a result, this leads to a higher overall power output. Thus, the voltage measured across the $10 \text{ M}\Omega$ input impedance of the multimeter was used as an indicator to evaluate the energy harvesting performance of the multi-cell ACCCs.

The effects of loading amplitude and loading frequency were also investigated for multi-cell energy harvester. To prevent increased uneven cracking at the joints between cells and potential local splitting, lower loading amplitudes of 0.5 mm and 1.0 mm were applied. This approach helps minimize residual plastic deformation and ensures that energy harvesting remains largely within the quasi-elastic range during cyclic loading. Under open-circuit conditions, current flow is nearly absent, and charge flow is minimal. However, when a 10 M Ω input impedance—lower than the internal impedance of the PVDF—is applied, there is a more significant current (i.e., an increased charge flow rate). This current rises with increasing loading frequency. Hence, relatively high loading frequencies of 1 Hz and 2 Hz were selected. Higher frequencies were avoided, as they could potentially damage the fiber-bridging capacity at the joints of ACCC specimens.

Further details for rational for the multimeter setting of the energy harvesting system can be found in Figure 8-4. Two types of electric circuit modes for PVDF are commonly used: the current mode [8, 9] and the charge mode [9-14], both of which have been shown to be effective individually [12, 13]. A piezoelectric film can be considered as a charge generator in parallel with a resistance and a capacitance, as illustrated in Figure 8-4a. In the figure, the dashed red box represents the piezoelectric film, where R_0 and C_0 denote its intrinsic resistance and capacitance, respectively. The dashed blue box corresponds to the digital oscilloscope used for recording the output voltage, where the intrinsic capacitance and resistance known as the input impedance of the measuring device. Given that the PVDF film has an extremely high intrinsic resistivity—over 100 M Ω /cm [15]—the resistance R_0 of the film is not considered. Consequently, the equivalent circuit in Figure 8-4a can be simplified to the configuration shown in Figure 8-4b, where the PVDF film is still represented in the charge mode by a parallel-connected capacitor. The current generated by the PVDF film is denoted as i_s ; however, part of this current is diverted through the capacitor C_0 . If the current through the capacitor is i_c , then the effective output current from the PVDF film is i_p , which can be expressed as $i_p = i_s - i_c$.

For measurement devices such as oscilloscopes, the input impedance typically consists of a parallel connection of a resistance ($R_{d0} = 1 \text{ M}\Omega$) and a capacitance ($C_{d0} = 16 \text{ pF}$) [12]. At low frequencies (e.g., 1–2 Hz, as considered in this study), the impedance of capacitance ($X_c = 1/j\omega C_{d0}$) becomes very large and can be regarded as open-circuited relative to the parallel resistance R_{d0} . Hence, the effective input impedance of the measuring device is dominated by the resistance R_{d0} . In this chapter, when the DMM is employed for voltage measurements, its input impedance is characterized by a purely resistive load R_{d0} under DC voltage testing conditions. Accordingly, the measurement circuit can be further simplified from the configuration in Figure 8-4b to that shown in Figure 8-4c. Accordingly, the instantaneous output power delivered to the electrical load can be expressed as $P(t) = I(t)U(t)$ or $U^2(t)/R$, where $I(t) = i_p$ represents the current flowing through the electrical load, and $U(t)$ denotes the measured voltage across it.

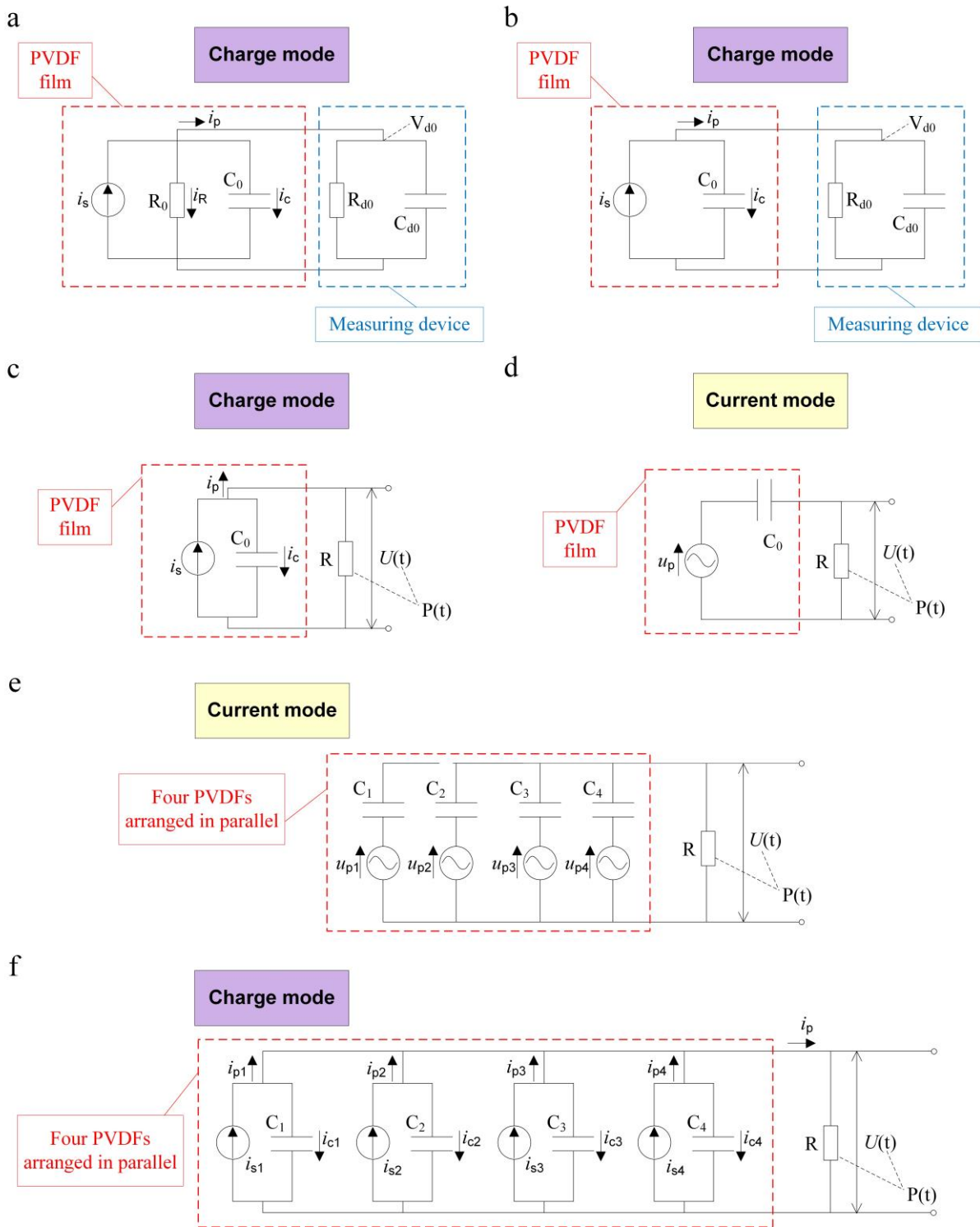


Figure 8-4 Equivalent circuit of PVDFs, (a) charge mode for a single PVDF considering intrinsic resistance and capacitance, (b) charge mode for a single PVDF considering intrinsic capacitance, (c) charge mode for a single PVDF measured with DMM, (d) current mode for a single PVDF, (e) current mode for four PVDFs arranged in parallel, (f) charge mode for four PVDFs arranged in parallel measured with DMM.

As illustrated in Figure 8-4d, the PVDF film can also be represented by a voltage source in series with a capacitance [9], enclosed within the red dashed line. The voltage source u_p corresponds to the piezoelectric generator itself and is directly proportional to the applied stress or strain. The piezofilm capacitance C_0 can be considered as the equivalent source impedance

[8]. Together with the discharge resistance R , this impedance forms a voltage divider. According to the principle of voltage division based on impedance, the high internal impedance of the LDT0 PVDF film [7] necessitated the use of the DMM with an input impedance greater than $10\text{ G}\Omega$ in the previous chapters to ensure accurate open-circuit voltage measurements. Each PVDF can be regarded as an individual voltage source, and when four voltage sources are connected in parallel, the total voltage remains equal to that of a single source, as shown in Figure 8-4e. Under open-circuit conditions with an input impedance R_{d0} greater than $10\text{ G}\Omega$, the resulting current is extremely small and can be neglected; consequently, according to $P(t)=I(t)U(t)$ or $U^2(t)/R$, the output power is minimal.

As reported in literature [7, 12, 13, 16, 17], connecting multiple PVDF elements in parallel can cumulatively enhance the generated current while simultaneously reducing the total resistance of the PVDF-based energy system. Based on the charge mode illustrated in Figure 8-4c, the equivalent circuit of four parallel-connected PVDF elements is shown in Figure 8-4f. When the input impedance of the DMM is set to $10\text{ M}\Omega$, a significant current is observed. Although the output voltage across the load decreases under these conditions, the corresponding power increases, as described by $P(t)=I(t)U(t)$ or $U^2(t)/R$. Furthermore, adding additional piezoelectric elements in parallel enables further accumulation of current, thereby enhancing the output power. Since the digital multimeter offers only two input impedance settings— $10\text{ M}\Omega$ and over $10\text{ G}\Omega$ —future work should systematically investigate the dependence of output power on load resistance to identify the maximum deliverable power to an external electrical load.

8.3 RESULTS AND DISCUSSION

8.3.1 Mechanical behavior during pre-compression

Figure 8-5 presents the stress-strain response of multi-cell ACCCs under pre-compression loading. The dashed lines represent the results from individual experiments, while the solid red line indicates the averaged curve. The mechanical behavior shows an initial elastic stage, followed by plastic deformation, reaching peak stress, and then a gradual stress decrease as the structure undergoes auxetic behavior. The image on the right, highlighted by the blue box, shows the crack pattern of the multi-cell ACCCs at 7% strain. The crack distribution closely resembles that observed in a single unit cell. Cracks are primarily concentrated in the joint regions, with minor cracks forming around them. The main cracks function as hinge-like joints, facilitating localized rotation of the structure. This mechanism is essential for enabling auxetic deformation and exhibits a similar behavior to that observed in the unit cell of ACCCs.

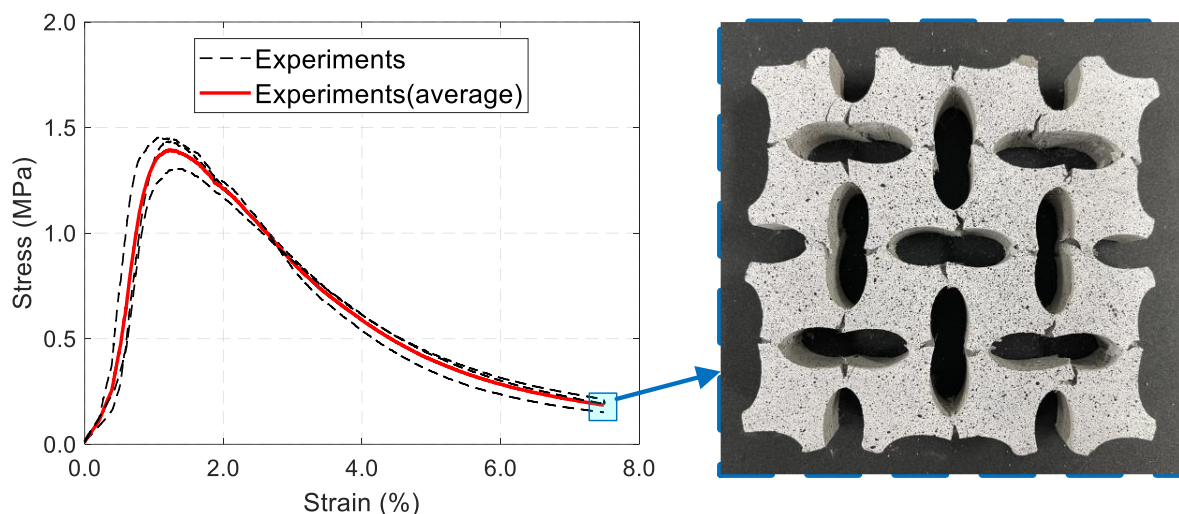


Figure 8-5 Stress-strain curve of multi-cell ACCC during pre-compression

The multi-cell ACCC specimens, constructed using the SHCC mixture with extended softening as developed in [Chapter 6](#), exhibited recoverable elastic deformation behavior under cyclic loading. Cracking was primarily observed within the joint regions; however, due to the heterogeneity of cementitious materials, crack propagation did not consistently align precisely with the joint centers. The multi-cell ACCC, optimized based on the results presented in [Chapter 7](#), utilizes extensive ligament cracking to achieve enhanced recoverable strain while maintaining auxetic behavior and preventing splitting. This optimized configuration approaches the performance limits under the given constraints, resulting in pronounced cracking at the joint centers. As a result, the joint regions are sensitive to the boundary conditions at the interface between the specimen and the loading plates. In this study, smooth loading plates—consistent with those used in the previous chapters—were employed to facilitate the expression of auxetic behavior and to suppress premature joint splitting. In contrast, rough-surfaced loading plates may induce localized splitting within the joints, as increased friction at the specimen–plate interface generates elevated tensile forces acting on the joints.

8.3.2 Energy harvesting results

[Figure 8-6](#) presents the energy harvesting performance of the multi-cell ACCC energy harvester under different loading frequencies and amplitudes, with an input impedance of 10 M Ω . The corresponding averaged results over ten loading cycles are summarized in [Table 8-2](#). During each cycle, the output voltage increases with compressive displacement, reaching a maximum at peak displacement. Conversely, as the loading plate moves away from the ACCCs, the output voltage decreases to zero. Overall, the voltage output exhibits a nearly sinusoidal waveform, albeit with minor fluctuations. Notably, no flat segments were observed in the voltage curve, which are typically caused by cyclic loading-induced detachment due to residual plastic deformation in the specimen. The slight voltage fluctuations are caused by non-synchronized deformations in different cells; when PVDF films bonded over unevenly propagating cracks generate out-of-phase sinusoidal voltages, their superposition leads to partial cancellation and reduces the overall voltage. Additionally, due to the manual bonding process, slight variations

in bonding quality may exist across different unit cells, potentially influencing the results to some extent.

Figure 8-6 and Table 8-2 illustrate the effects of loading frequency and amplitude on the output voltage of the multi-cell ACCC energy harvester. As the loading frequency increases, the output voltage correspondingly rises. This is attributed to the greater dynamic strain experienced by each PVDF film, which generates higher voltages in accordance with piezoelectric equations. Additionally, higher loading frequencies increase the charge flow rate. Similarly, increasing the loading amplitude results in a higher output voltage. The effect of loading amplitude on output voltage is more significant than that of loading frequency, likely because greater loading amplitudes induce larger flexural deformations, thereby supplying more mechanical energy for conversion into electrical energy. These trends are consistent with those observed in the single-unit ACCC energy harvester discussed in Chapter 3, although the loading frequency effect appears stronger in the multi-cell system, potentially resulting from cumulative interactions among multiple piezoelectric cells. The peak output voltage recorded was approximately 4.4 V at 2 Hz loading frequency and 1 mm loading amplitude when input impedance equals 10 M Ω .

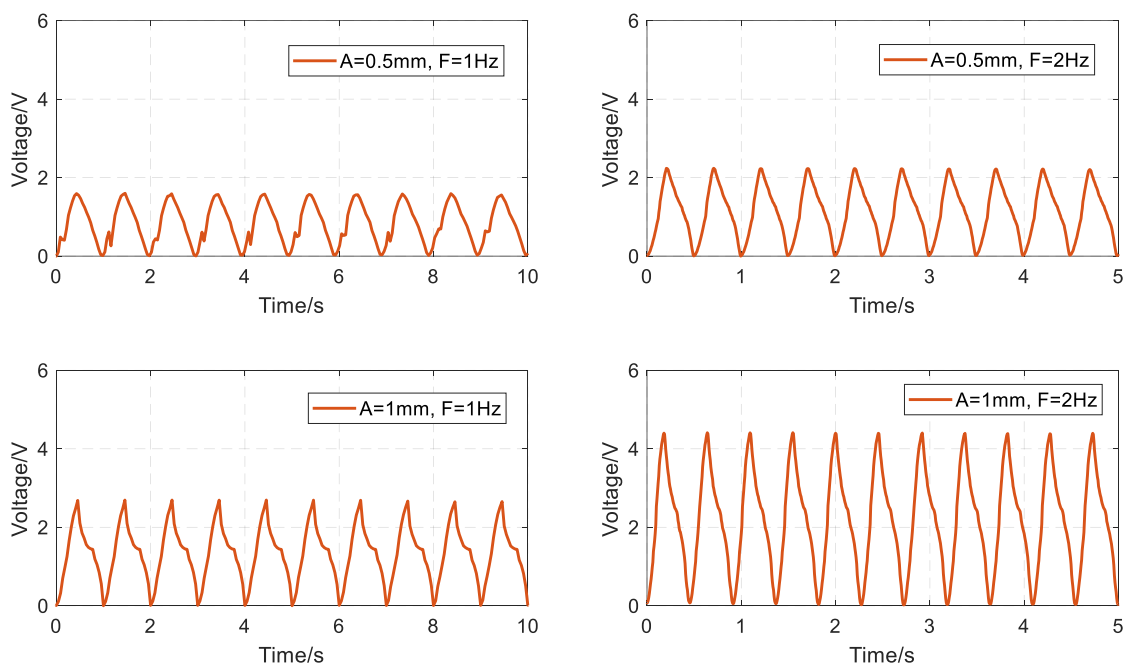


Figure 8-6 Energy harvesting test results of multi-cell ACCC energy harvester (input impedance = 10 M Ω)

Table 8-2 Output voltage under different amplitudes and frequencies (input impedance = 10 M Ω)

	F=1Hz	F=2Hz
A=0.5mm	1.58 V	2.22 V
A=1.0mm	2.68 V	4.41 V

Figure 8-7 and Table 8-3 depict the dynamic stress–strain behavior observed during energy harvesting tests conducted under different loading frequencies and amplitudes over a 10-second period. In each loading cycle, the stress increases progressively with compressive strain, reaching a maximum at the peak strain. As the loading plate retracts from the ACCC specimens, the stress gradually decreases back to zero. The stress–strain curves closely follow a sinusoidal trend, consistent with the applied sinusoidal compressive loading. The multi-cell ACCC energy harvester exhibits quasi-elastic characteristics, with minimal to no residual plastic deformation observed across the cycles.

Figure 8-7 and Table 8-3 further illustrate the influence of loading frequency and loading amplitude on the dynamic stress–strain response of the multi-cell ACCC energy harvester. At a loading amplitude of 0.5 mm, the maximum compressive stresses were 0.0307 MPa at 1.0 Hz and 0.0268 MPa at 2.0 Hz. When the loading amplitude was increased to 1.0 mm, the peak stresses rose to 0.0478 MPa and 0.0425 MPa for the same respective frequencies. These results indicate that, at a constant amplitude, peak stress tends to decrease with increasing loading frequency. This behavior is likely due to the intensified dynamic forces acting on the joints at higher frequencies, which can reduce fiber-bridging efficiency through partial debonding at the fiber–matrix interface. In contrast, increasing the loading amplitude from 0.5 mm to 1.0 mm leads to higher peak stresses, likely resulting from greater flexural deformation that activates more fibers in the bridging mechanism. This enhanced fiber engagement improves resistance to cyclic deformation, thereby increasing the elastic modulus of the multi-cell ACCC harvester, although some degree of fiber–matrix debonding may still occur at higher loading amplitudes.

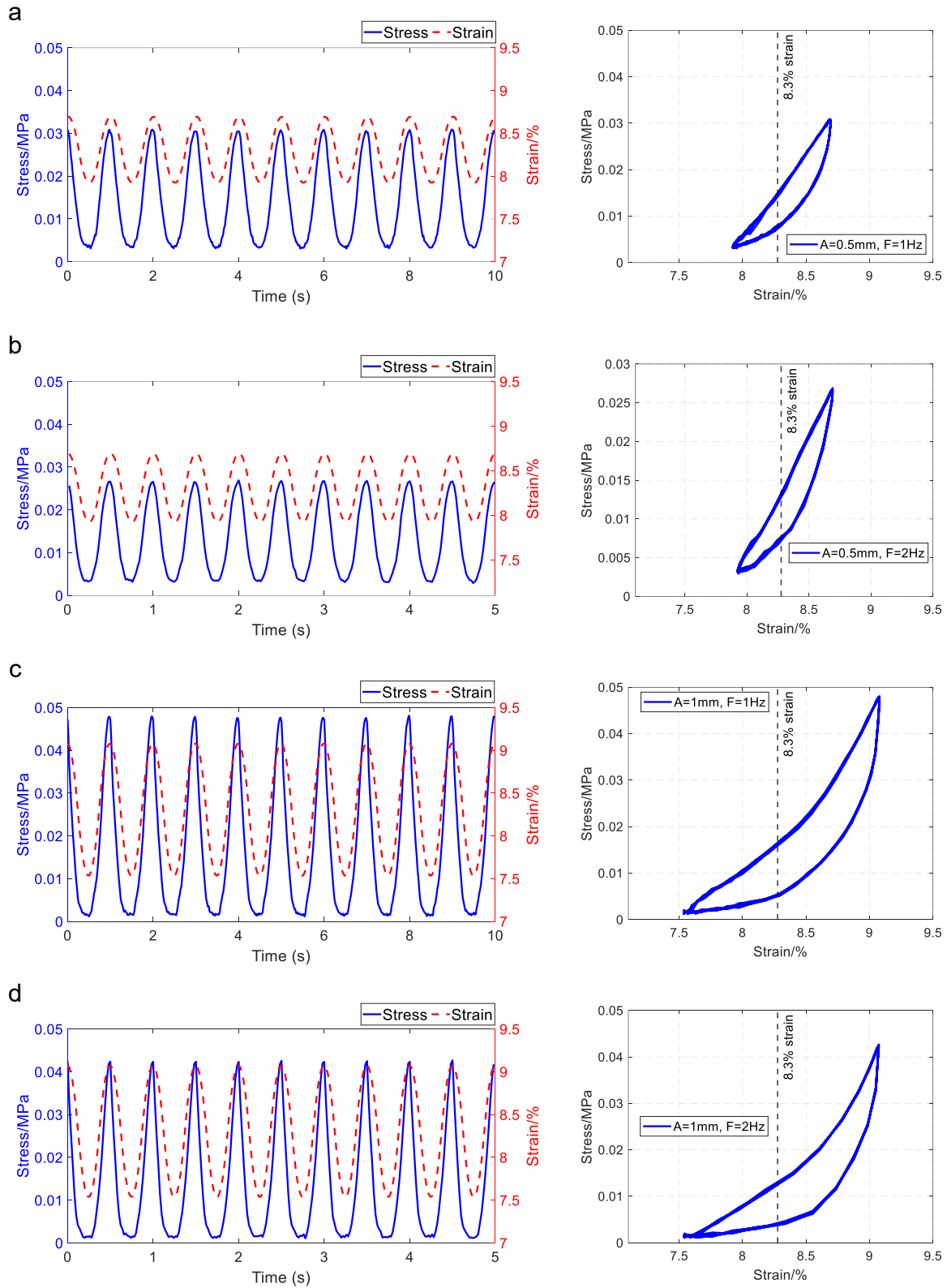


Figure 8-7 Dynamic stress-strain curves of multi-cell ACCC during energy harvesting tests

Table 8-3 Output voltage under different amplitudes and frequencies (input impedance = 10 M Ω)

	F=1Hz	F=2Hz
A=0.5mm	0.0307 MPa	0.0268 MPa
A=1.0mm	0.0478 MPa	0.0425 MPa

In the energy harvesting results discussed above, the peak voltage within a single sinusoidal cycle is approximately 2.2 V, representing half of the peak-to-peak voltage. The root mean square (RMS) voltage over one cycle is calculated to be 1.56 V. Based on the input impedance, the corresponding power output for two sinusoidal cycles per second is determined to be 0.484 μ W. To standardize this, considering the total material volume of the multi-cell ACCC energy harvester (i.e., $1.8082 \times 10^{-4} \text{m}^3$), the volumetric energy harvesting density is calculated to be 2.7 mW/m^3 . In this chapter, the multi-cell ACCC energy harvester is equipped with only four piezoelectric elements; however, the complete 2×2 multi-cell ACCC harvester configuration has the potential to accommodate up to 24 piezoelectric elements. If a 2×2 cell configuration with 24 fully bonded PVDF films is considered, the volumetric energy-harvesting density increases to 16.1 mW/m^3 . It should be noted that the power generated by this multi-cell ACCC energy harvester corresponds to the average power over two sinusoidal cycles per second. By accumulating energy over multiple cycles for an extended period, the harvested energy can become substantial and be stored in capacitors or batteries, enabling on-demand power supply. In particular, assuming continuous accumulation based on the multi-cell configuration over a one-day period, a total energy output of approximately 386.4 mWh/m^3 can be achieved. In addition, multiple piezoelectric elements can be stacked at a single joint to further enhance energy harvesting efficiency. According to literature [17], the cumulative voltage generated by multiple stacked piezoelectric elements under bending deformation can achieve energy conversion efficiencies comparable to those of brittle PZT materials.

The energy harvester can be used to continuously power low-power environmental sensing devices (10–100 μ W), such as temperature, humidity, pressure, light, and noise sensors. It can also continuously supply energy to structural health monitoring sensors, such as accelerometers, which typically consume around 3 μ W. In addition, the harvested energy can power electronic systems with intermittent operation — those that remain mostly in sleep mode and wake briefly for measurement or data transmission — such as wireless beacons or Bluetooth Low Energy (BLE) communication modules (10–200 μ W). Since the energy harvester can continuously generate electricity, the excess energy can be stored in a battery or capacitor to later power higher-power devices, such as cameras, radar units, or Wi-Fi modules used in infrastructure monitoring. Moreover, many environmental and structural health monitoring sensors are deployed in remote or inaccessible locations where battery replacement is difficult, unsafe, or impractical—for instance, on the underside of bridges, where access for maintenance is extremely limited. Because civil structures are typically subjected to a wide range of cyclic dynamic loads from railways, vehicles, pedestrians, waves, rain, and wind, the energy harvester can also function as a structural component, simultaneously enduring these mechanical loads while converting their kinetic energy into electrical energy. It is also worth noting that the energy harvester can also function as a self-sensing stress or strain sensor, as the generated voltage closely follows the variations in stress or strain.

Nevertheless, due to the inherent heterogeneity of the cementitious matrix, multi-cell ACCCs are more prone to uneven deformation among individual unit cells. When PVDF films are bonded over cracks that propagate unevenly, they tend to generate out-of-phase sinusoidal

voltage signals. The superposition of these asynchronous outputs can lead to partial cancellation, thereby reducing the overall voltage output. To address this issue, rectifier circuits can be designed for each PVDF film to convert their individual voltages into a unified polarity. This enables effective accumulation of the output voltage without cancellation, thereby improving the total harvested voltage.

Figure 8-8 presents the open-circuit output voltage of the multi-cell ACCC energy harvester measured with an input impedance over $10\text{ G}\Omega$ during cyclic loading. When the digital multimeter's (DMM) input impedance remains over $10\text{ G}\Omega$, which is significantly higher than the internal impedance of the PVDF, the circuit approaches open-circuit conditions, resulting in negligible current flow. Under these conditions, the open-circuit voltage reaches approximately 13.2 V , comparable to the magnitude of the output from a single PVDF film in a single unit cell, as reported in Chapter 7. The open-circuit voltage corresponds to a state without current or charge flow, producing an almost perfect sinusoidal waveform similar to that of a sensor. In the case of four PVDF films connected in parallel, the output voltage of each film cannot be summed. Moreover, non-uniform deformation among the unit cells bonded to each PVDF film causes variations in voltage outputs across individual piezoelectric elements, leading to an overall internal voltage drop. To more accurately represent the current output and power performance, the input impedance of the DMM was set to $10\text{ M}\Omega$, closely matching the internal impedance of the LDT0 PVDF. Under these measurement conditions, the voltages of the individual PVDF films can be effectively summed. This summation becomes especially significant when multiple PVDF films are connected in parallel. In practical applications, the energy harvester is connected to an electrical load with significantly lower impedance, which consumes electrical energy and consequently reduces the output voltage compared to the open-circuit scenario. This explains why voltage measurements recorded with a $10\text{ M}\Omega$ input impedance are lower than those obtained under open-circuit conditions with an input impedance over $10\text{ G}\Omega$.

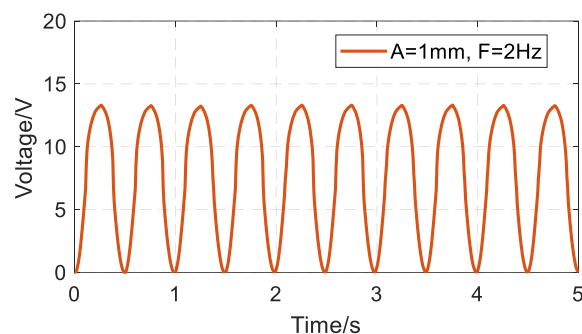


Figure 8-8 Open-circuit output voltage of the multi-cell ACCC energy harvester (measured with input impedance over $10\text{ G}\Omega$)

8.4 CONCLUSIONS

This chapter extends the single-cell ACCC energy harvester optimized in Chapter 7 to a multi-cell configuration for practical energy harvesting applications. Pre-compression tests

confirmed that the multi-cell ACCC exhibited auxetic behavior without splitting and maintained recoverable elastic deformation. Piezoelectric films were then bonded to the hinge-like joints of each unit cell, with four PVDF films connected in parallel to measure combined voltage output. The influence of loading frequency and amplitude on the output voltage was also examined. The key findings of this study are summarized below:

- The multi-cell ACCC specimens made with the extended-softening SHCC mix from Chapter 6 showed recoverable elastic deformation under cyclic loading. The energy harvester displayed quasi-elastic behavior with little to no residual plastic deformation. Cracks mainly formed at the joints, though material heterogeneity caused some deviation from the joint centers.
- The multi-cell ACCC energy harvester exhibits a stable, near-sinusoidal voltage output under cyclic loading, with peak voltage increasing with both loading frequency and amplitude. Minor voltage fluctuations arise from asynchronous crack deformations and slight bonding inconsistencies. Overall, loading amplitude has a stronger effect on output than frequency, with a peak-to-peak voltage of nearly 4.4 V at 2 Hz and 1 mm displacement when input impedance equals 10 M Ω . These results align with single-unit trends but show enhanced frequency sensitivity due to multi-cell interactions.
- The multi-cell ACCC energy harvester exhibits stable, sinusoidal, and quasi-elastic stress–strain behavior under cyclic loading. Peak stress increases with loading amplitude due to increased fiber-bridging engagement. However, peak stress slightly decreases with higher loading frequency, likely because dynamic debonding reduces fiber-bridging efficiency.

REFERENCES

- [1] Y. Xu, E. Schlangen, M. Luković, B. Šavija, Tunable mechanical behavior of auxetic cementitious cellular composites (CCCs): Experiments and simulations, *Construction and Building Materials*, 266 (2021) 121388. <https://doi.org/10.1016/j.conbuildmat.2020.121388>.
- [2] D. Valverde-Burneo, N. García-Troncoso, I. Segura, M. García-Laborda, Multifunctional cementitious composite: Conductive and auxetic behavior, *Case Studies in Construction Materials*, 20 (2024) e03358. <https://doi.org/10.1016/j.cscm.2024.e03358>.
- [3] M. Chen, S. Fang, G. Wang, Y. Xuan, D. Gao, M. Zhang, Compressive and flexural behavior of engineered cementitious composites based auxetic structures: An experimental and numerical study, *Journal of Building Engineering*, 86 (2024) 108999. <https://doi.org/10.1016/j.jobe.2024.108999>.
- [4] Y. Xu, H. Zhang, E. Schlangen, M. Luković, B. Šavija, Cementitious cellular composites with auxetic behavior, *Cement and Concrete Composites*, 111 (2020) 103624. <https://doi.org/10.1016/j.cemconcomp.2020.103624>.
- [5] Y.-F. Su, R.R. Kotian, N. Lu, Energy harvesting potential of bendable concrete using polymer based piezoelectric generator, *Composites Part B: Engineering*, 153 (2018) 124-129. <https://doi.org/10.1016/j.compositesb.2018.07.018>.
- [6] J.W. Sohn, J. Jeon, S.B. Choi, An Investigation on Dynamic Signals of MFC and PVDF Sensors: Experimental Work, *ADVANCES IN MECHANICAL ENGINEERING*, (2013) <https://doi.org/10.1155/2013/420345>.

- [7] H.-H. Huang, K.-S. Chen, Design, analysis, and experimental studies of a novel PVDF-based piezoelectric energy harvester with beating mechanisms, *Sensors and Actuators A: Physical*, 238 (2016) 317-328. <https://doi.org/10.1016/j.sna.2015.11.036>.
- [8] Y. Meng, W. Yi, Application of a PVDF-based stress gauge in determining dynamic stress-strain curves of concrete under impact testing, *Smart Materials and Structures*, 20 (2011) 065004. 10.1088/0964-1726/20/6/065004.
- [9] S. Qin, Z. Yu, X. Zhang, S. Yang, W. Peng, F. Zhao, Calibration of polyvinylidene fluoride (PVDF) stress gauges under high-impact dynamic compression by machine learning, *Journal of Applied Physics*, 131 (2022) 024502. 10.1063/5.0066090.
- [10] H. Hamashima, K. Hokamoto, M. Yamashita, Y. Sato, T. Furukawa, Newly Developed Unsteady Wave Sensing System for Polycarbonate, *Materials Science Forum*, 673 (2011) 185-190. 10.4028/www.scientific.net/MSF.673.185.
- [11] X. Huang, Q. Li, X.a. Wei, X. Yang, D. Luo, H. Zeng, H. Wang, Indoor Test System for Liquid CO₂ Phase Change Shock Wave Pressure with PVDF Sensors, in: *Sensors*, Vol. 20, 2020.
- [12] C. Gao, N. Sakata, T. Iwamoto, Y. Tanaka, T. Kusaka, Impact force measurement by in-plane piezoelectricity of polyvinylidene fluoride films, *International Journal of Mechanical Sciences*, 283 (2024) 109653. <https://doi.org/10.1016/j.ijmecsci.2024.109653>.
- [13] C. Gao, N. Sakata, T. Iwamoto, Y. Tanaka, T. Kusaka, Highly-precise force wave captured by PVDF during instrumented taylor test, *International Journal of Mechanical Sciences*, 303 (2025) 110681. <https://doi.org/10.1016/j.ijmecsci.2025.110681>.
- [14] Y. Tanaka, E. Tamoto, Y. Fujimoto, Development of contact-type sensor using piezoelectric film for guided wave measurement, *International Journal of Applied Electromagnetics and Mechanics*, 33 (2010) 1237-1244. 10.3233/JAE-2010-1244.
- [15] W. Tjhen, T. Tamagawa, C.P. Ye, C.C. Hsueh, P. Schiller, D.L. Polla, Properties of piezoelectric thin films for micromechanical devices and systems, in: [1991] *Proceedings. IEEE Micro Electro Mechanical Systems*, 1991, pp. 114-119.
- [16] F.Ç. Bolat, A. Sugeç, A. Özdemir, Design, numerical analysis and experiments of different types auxetic beams for vibration based energy harvester, *Mechanical Systems and Signal Processing*, 210 (2024) 111170. <https://doi.org/10.1016/j.ymssp.2024.111170>.
- [17] I. Jung, Y.-H. Shin, S. Kim, J.-y. Choi, C.-Y. Kang, Flexible piezoelectric polymer-based energy harvesting system for roadway applications, *Applied Energy*, 197 (2017) 222-229. <https://doi.org/10.1016/j.apenergy.2017.04.020>.

9

CONCLUSIONS AND RECOMMENDATIONS

In this chapter, a brief summary of the thesis is provided. Based on the results obtained, general conclusions are drawn. Finally, recommendations for future research are presented.

9.1 RETROSPECTION

Auxetic cementitious composites (ACCCs), composed of fiber-reinforced cementitious materials, exhibit enhanced deformability and structural resilience stemming from their auxetic behavior. Their reversible deformation under cyclic loading and sustained quasi-elastic response highlight their potential for efficient energy harvesting applications. Current investigations into ACCCs only focused on their mechanical properties, with limited emphasis on their potential for energy harvesting applications. Given the abundance and low cost of cementitious materials, ACCCs present a promising pathway for sustainable energy harvesting systems. This study systematically investigates their feasibility for such applications.

After a general introduction (**Chapter 1**) and literature review of energy harvesting on auxetic cementitious composites (**Chapter 2**) given in the first part, the feasibility of utilizing ACCCs for strain-based energy harvesting was experimentally examined in the second part of this study (**Chapter 3**). A novel piezoelectric energy harvester (PEH) design consisting of ACCCs and surface-mounted PVDF (Polyvinylidene Fluoride) was proposed to convert strain-based energy to useable electrical energy. The ACCC-PVDF energy harvesting system was first compressed to a certain displacement and then subjected to cyclic loading to consistently generate voltage for energy harvesting (**Chapter 3**). The third part of the study employs numerical modeling to quantitatively investigate the piezoelectric mechanisms within the ACCC energy harvester. In **Chapter 4**, a general theoretical model was developed to assess the energy harvesting performance of fiber-reinforced cementitious materials with surface-mounted PVDF. Building upon this computational framework, a specialized model was created to simulate the energy harvesting process of the ACCC harvester, capturing both mechanical deformation and electrical response (**Chapter 5**). This model adapts the general approach to account for the unique deformation characteristics of ACCCs and the corresponding piezoelectric behavior of the PVDF film. Validation against experimental results from **Chapter 3** showed good agreement between simulation and experimental data.

The fourth part of this thesis (**Chapters 6 to 8**) centers on the optimization of the ACCC energy harvester. In **Chapter 6**, a strain-hardening cementitious composite (SHCC) with enhanced softening behavior was developed to improve fiber-bridging performance at the joints of ACCCs. This advancement enables stable auxetic behavior across various ACCC geometries, facilitating the identification of an optimal design. However, the inherent brittleness of cementitious materials presents a significant challenge, as geometric modifications may cause structural splitting and compromise the desired auxetic behavior. To address the issue, **Chapter 7** introduces a machine learning-driven framework that integrates the energy harvesting model (developed in **Chapters 4 and 5**) with Bayesian Optimization (BO), effectively guiding the design process toward high-performance geometries. The optimal configuration identified through this framework was fabricated and experimentally validated for its energy harvesting capability. Building on this, **Chapter 8** extends the machine learning-driven unit cell design by assembling the optimized single-cell ACCC unit into a multi-cell configuration, enabling scalable and practical energy harvesting in real-world engineering applications.

9.2. CONCLUSIONS

Based on the findings presented in each chapter, several general conclusions can be drawn.

- A piezoelectric energy harvester integrating ACCCs with surface-mounted PVDF was developed to convert strain energy into usable electrical energy. The harvester was pre-compressed within the auxetic behavior range and subjected to cyclic loading. It exhibited pseudo-elastic stress-strain behavior and generated a sinusoidal open-circuit output voltage under dynamic cyclic loading. Experimental results indicate that the open-circuit voltage increases with both loading amplitude and loading frequency, while the peak stress decreases as these parameters increase. Moreover, loading amplitude has a significantly greater influence than loading frequency. These findings demonstrate the strong potential of the developed harvester for powering self-sustained electronics in infrastructure applications.
- The proposed energy harvesting model effectively captures the influence of loading amplitude and frequency on the output voltage of the ACCC-PVDF system. Higher frequencies enhance interfacial friction and strain transfer, while larger amplitudes increase PVDF flexural deformation and friction—both leading to higher voltage output. The model reveals that energy generation primarily occurs through d_{31} and d_{33} modes, with tangential (d_{31} -directional) stress dominating. By incorporating ACCC mechanical behavior, PVDF-ACCC interaction, and a detailed piezoelectric model, the simulation aligns well with experimental results and offers valuable guidance for designing cementitious composites with integrated flexible piezoelectric materials.
- Compared to ACCCs made with a strain softening base material, ACCCs made with SHCC mixtures exhibit enhanced joint rotation through multiple cracking and strain hardening, delaying primary crack formation and reducing crack openings. Specially, the use of SHCC with long softening tail (SHCC-LS) further maintains effective fiber bridging in primary cracks, improving rotational stiffness and resulting in greater load-bearing capacity and elastic recoverable deformation within the high auxetic behavior range. Additionally, ACCCs incorporating SHCC-LS exhibit superior performance under cyclic loading, owing to their higher stiffness and enhanced fiber bridging capacity in the hinge-joint region. ACCCs with SHCC-LS develops the greatest number of microcracks in the joint area, and when combined with strong fiber bridging, this results in increased frictional resistance and greater recoverable strain. These characteristics facilitate more efficient strain transfer to the surface-mounted PVDF, leading to significantly higher voltage output compared to ACCCs made from a base material with strain softening.
- A machine learning-driven framework that integrates an energy harvesting model with Bayesian Optimization (BO) was developed to optimize the hinge-like recoverable strain in ACCCs. The optimization maximizes piezoelectric output voltage while preventing splitting failure and non-auxetic behavior under compression. Herein, the energy harvesting model integrates the concrete damage plasticity (CDP) model for pre-compression and the second elasticity model for cyclic loading to calculate recoverable strain in generalized ACCC shapes. It accounts for their deformed geometries for energy harvesting, which are reconstructed using an improved node-order tracking algorithm. The learning-driven approach proved far more efficient than random

generation in identifying optimal ACCC configurations. The optimized shape was tested experimentally and exhibited an open-circuit peak-to-peak voltage output of approximately 15.0 V per cycle, about 2.7 times higher than the reference design. The geometric and mechanical evolution during optimization provides valuable insights for designing high-performance ACCC energy harvesters for smart infrastructure applications.

- The multi-cell ACCCs fabricated with the extended-softening SHCC mixture exhibit recoverable elastic deformation and quasi-elastic behavior, with minimal residual plasticity under cyclic loading. As intended, cracks predominantly develop at the joints, despite some material heterogeneity. The multi-cell energy harvester generates stable, nearly sinusoidal voltage outputs, which increase with both loading frequency and loading amplitude, with loading amplitude exerting a more pronounced influence. At a loading frequency of 2.0 Hz and a loading amplitude of 1.0 mm, the energy harvester produces a peak-to-peak voltage of approximately 4.4 V when measured with a 10 M Ω input impedance. Specifically, assuming continuous accumulation based on the multi-cell configuration over a one-day period, a total energy output of nearly 386.4 mWh/m³ can be achieved. The energy harvester is capable of continuously supplying micro-watt-level power to environmental sensors, such as temperature and light sensors, while simultaneously serving as a load-bearing structural material with self-sensing functionality. The stress-strain response remains stable and quasi-elastic, with peak stress increasing as loading amplitude rises, attributed to enhanced fiber bridging engagement. However, peak stress slightly decreases at higher frequencies, likely due to dynamic debonding that reduces fiber bridging effectiveness.

9.3 RECOMMENDATIONS

This study presents the development of a strain-based ACCC energy harvester, which harnesses the recoverable deformation within the auxetic behavior range of ACCC energy harvesting. Through a comprehensive approach involving experiments, simulations, and machine learning, the research aims to enhance the recoverable deformation capability of ACCC structures, thereby improving the energy output of the harvester. The recoverable deformation serves as the fundamental mechanism, as the amount of energy harvested is determined by the mechanical energy generated through this deformation and the method of energy conversion. By integrating experimental and simulation methods, the study optimizes the mechanical energy produced by recoverable deformation from the perspectives of material selection, structural geometry, and mechanical mechanisms. These findings provide valuable insights for future research on other ACCC-based energy harvesting approaches, such as vibration-based ACCC energy harvesters, piezoelectric ACCC energy harvesters, and triboelectric ACCC energy harvesters. Future studies could also focus on enhancing the mechanical performance of the hinge joint in ACCC energy harvesters by mitigating stress concentrations in the hinge joint region.

9.3.1. Other types of ACCC energy harvester

- (1) Vibration-based ACCC energy harvester

Although the strain-based ACCC energy harvester is capable of undergoing large recoverable deformation and delivering substantial mechanical strain energy, its energy conversion efficiency remains relatively low. This limitation is largely due to the high elastic modulus of the PVDF film, which reduces the strain effectively transferred from the cement-based hinge joint to the piezoelectric layer through the adhesive interface. To increase the strain transmitted to the piezoelectric film, the adhesive layer would need to withstand greater stress. However, in this study, the adhesive layer exhibits a limited bonding strength. Once this limit is exceeded, partial debonding occurs, and the interface transitions to friction-dominated behavior, significantly reducing energy transfer efficiency. Consequently, an extended period of energy accumulation is necessary to generate sufficient power for electrical loads (i.e., the devices or components that consume electricity).

Furthermore, while PVDF has the potential to produce significant electrical output under high-frequency and large-strain excitation, the current operational conditions impose certain constraints. To preserve the structural integrity of the cementitious matrix, the loading frequency is kept low. In addition, the strain amplitude is limited to maintain recoverable deformation. These factors together limit the voltage output of PVDF film. To address this challenge, a vibration-based ACCC energy harvester is proposed by integrating piezoelectric films with tip masses at the hinge-like joint region. The rotational deformation around the hinge joint can induce a significant inertial force of the tip mass, thereby increasing both the vibration amplitude and frequency of the piezoelectric element and enhancing its energy harvesting performance. This mechanism effectively converts low environmental loading frequencies into higher-frequency vibrations of the piezoelectric element. In particular, when the energy harvester is installed on a speed hump, it can produce substantial power output through the strong vibrations induced by the impact forces of passing vehicles.

Further development of the energy harvesting circuit can be considered, including the use of a rectifier to convert alternating current (AC) into directional current, filtering through parallel capacitors to obtain a stable direct current (DC), and storing the collected energy in capacitors or batteries. On this basis, power management strategies—such as impedance matching—can also be introduced to optimize the circuit and maximize power output.

(2) Piezoelectric ACCC energy harvester incorporating PZT powders

Recent advancements have explored the integration of PZT powders into cement-based materials to enable energy harvesting through piezoelectric effects. Inspired by this, a novel piezoelectric energy harvester utilizing auxetic cementitious composites (ACCC) can be engineered by embedding PZT powders within the matrix. The unique deformation characteristics of ACCCs—particularly their resilience to recover under cyclic loading—present high potential for converting mechanical strain into electrical energy. However, incorporating PZT powders may alter the material's microstructure, potentially diminishing the auxetic behavior of ACCCs and compromising overall mechanical integrity. To address this, a tailored design approach is needed to optimize both energy harvesting and mechanical performance.

(3) Triboelectric ACCC energy harvester

In recent studies, carbon-based conductive fillers have been incorporated into cementitious composites to facilitate energy harvesting via triboelectric mechanisms [3-7]. Building on this approach, a triboelectric ACCC energy harvester can be developed by embedding such conductive fillers and coupling them with materials like polytetrafluoroethylene (PTFE) films. The ACCC's high and recoverable deformation capacity under cyclic loading offers favorable conditions for efficient energy conversion. However, the inclusion of carbon fibers may negatively impact the composite's mechanical performance, potentially compromising its auxetic behavior. Therefore, careful optimization of the mixture design is required to balance both auxetic and conductive properties. Additionally, the piezoresistive characteristics introduced by these fillers may be utilized to enable self-sensing functionality in the ACCC system.

9.3.2. Enhanced hinge-joint of ACCC energy harvester

While enlarging joint sizes can increase crack openings at joints and improve voltage generation, it also poses challenges. In elliptical ACCCs with enlarged joints, the pre-compression process often results in stress concentration at the joint regions. Since most of the compressive force is initially transmitted to these areas, localized damage tends to occur at the joints in contact with the loading plates. When rough boundary conditions are applied, this stress concentration can result in splitting behavior, ultimately compromising the auxetic effect. To address this issue, a modified geometry is proposed by replacing the large central crack formed in the joint of the deformed elliptical ACCC with a smooth arc segment, resulting in a peanut-shaped ACCC. This initiates compression from the already-deformed geometry of the elliptical ACCC, which may reduce sensitivity to boundary conditions and mitigates the risk of splitting. As a result, it offers improved mechanical stability and broader applicability for engineering applications. Furthermore, the arc of the peanut-shaped hole design can be refined and optimized using a Bézier curve. Leveraging the interactive active learning framework that integrates Bayesian algorithms with finite element modeling, as introduced in Chapter 7, allows for a systematic optimization of both mechanical and energy harvesting properties.

REFERENCES

- [1] Y. Xu, H. Zhang, E. Schlangen, M. Luković, B. Šavija, Cementitious cellular composites with auxetic behavior, *Cement and Concrete Composites*, 111 (2020) 103624. <https://doi.org/10.1016/j.cemconcomp.2020.103624>.
- [2] Y. Xu, E. Schlangen, M. Luković, B. Šavija, Tunable mechanical behavior of auxetic cementitious cellular composites (CCCs): Experiments and simulations, *Construction and Building Materials*, 266 (2021) 121388. <https://doi.org/10.1016/j.conbuildmat.2020.121388>.
- [3] S. Kuntharin, V. Harnchana, J. Sintusiri, P. Thongbai, A. Klamchuen, K. Sinthiptharakoon, V. Amornkitbamrung, P. Chindaprasirt, Smart triboelectric floor based on calcium silicate-carbon composite for energy harvesting and motion sensing applications, *Sensors and Actuators A: Physical*, 358 (2023) 114423. <https://doi.org/10.1016/j.sna.2023.114423>.
- [4] Y. Ra, I. You, M. Kim, S. Jang, S. Cho, D. Kam, S.-J. Lee, D. Choi, Toward smart net zero energy structures: Development of cement-based structural energy material for contact electrification

driven energy harvesting and storage, *Nano Energy*, 89 (2021) 106389.

<https://doi.org/10.1016/j.nanoen.2021.106389>.

[5] D. Valverde-Burneo, N. García-Troncoso, I. Segura, M. García-Laborda, Multifunctional cementitious composite: Conductive and auxetic behavior, *Case Studies in Construction Materials*, 20 (2024) e03358. <https://doi.org/10.1016/j.cscm.2024.e03358>.

[6] W. Dong, S. Gao, S. Peng, L. Shi, S.P. Shah, W. Li, Graphene reinforced cement-based triboelectric nanogenerator for efficient energy harvesting in civil infrastructure, *Nano Energy*, 131 (2024) 110380. <https://doi.org/10.1016/j.nanoen.2024.110380>.

[7] W. Dong, C. Zhao, S. Peng, C. Wu, T. Kim, K. Wang, W. Li, Recycled carbon fibre/cement-based triboelectric nanogenerators toward energy-efficient and smart civil infrastructure, *Composites Part B: Engineering*, 303 (2025) 112603.

<https://doi.org/10.1016/j.compositesb.2025.112603>.

APPENDIX A

Supplementary information to Chapter 5

A.1 Parametric modeling of PVDF film based on deformed ACCCs

The reconstructed ACCC specimen for second-elasticity has been re-meshed, which induced the internal profile with a different topology information compared with the initial one. Thus, the node-order-track algorithm was used again for recoding the new topology information of the internal profile (including node coordinates and node order), as illustrated in [Figure A1a](#). Then, the internal profile was used to build one edge of the whole PVDF film. This edge was translated by a distance of the PVDF film thickness to obtain another edge of the PVDF film (see [Figure A1d](#)). [Figure A1d](#) also shows that how one segment of the PVDF film was constructed. First, the local coordinates x'_m of one edge of the segment with two points were calculated as

$$x'_m = \beta_m^i x_i \quad (\text{A1})$$

where superscript ' indicates variables in the local coordinate system. x_i is the coordinates in the global coordinate system. β_m^i is the Jacobian matrix for coordinates conversion, which can be written as

$$\beta_m^i = \frac{\partial x^i}{\partial x'^m} = \begin{bmatrix} \cos \theta & \sin \theta \\ -\sin \theta & \cos \theta \end{bmatrix} \quad (\text{A2})$$

Thus, [Eq. \(A1\)](#) can be rewritten as

$$\begin{bmatrix} x'_1 \\ x'_2 \end{bmatrix} = \begin{bmatrix} \cos \theta & \sin \theta \\ -\sin \theta & \cos \theta \end{bmatrix} \begin{bmatrix} x_1 \\ x_2 \end{bmatrix} \quad (\text{A3})$$

Then, another edge of the segment with two points (coordinates x'_3, x'_4) can be easily obtained by translating a distance of the thickness h_p in the local coordinate system.

$$\begin{bmatrix} x'_3 \\ x'_4 \end{bmatrix} = \begin{bmatrix} x'_1 \\ x'_2 \end{bmatrix} + \begin{bmatrix} 0 \\ h_p \end{bmatrix} \quad (\text{A4})$$

Finally, the global coordinates of another edge with two points are calculated as

$$x_i = \beta_i^m x'_m = [\beta_i^m]^{-1} x'_m \quad (\text{A5})$$

Meanwhile, the inverse matrix of β_m^i can be calculated as

$$[\beta_m^i]^{-1} = \begin{bmatrix} \cos \theta & -\sin \theta \\ \sin \theta & \cos \theta \end{bmatrix} \quad (\text{A6})$$

Hence, the global coordinates x'_5, x'_6 of another edge with two points are obtained by

$$\begin{bmatrix} x'_5 \\ x'_6 \end{bmatrix} = \begin{bmatrix} \cos \theta & \sin \theta \\ -\sin \theta & \cos \theta \end{bmatrix} \begin{bmatrix} x'_3 \\ x'_4 \end{bmatrix} \quad (\text{A7})$$

Using the same procedure, each segment was treated in a similar manner and then connected to a film loop (as shown in [Figure A1d](#)), which covered the entire internal profile. In fact, only

a portion of the film loop is used to model the PVDF film, taking into account the actual sizes of the PVDF film and the bonding area between the PVDF film and the ACCCs, as illustrated in Figure A1b.

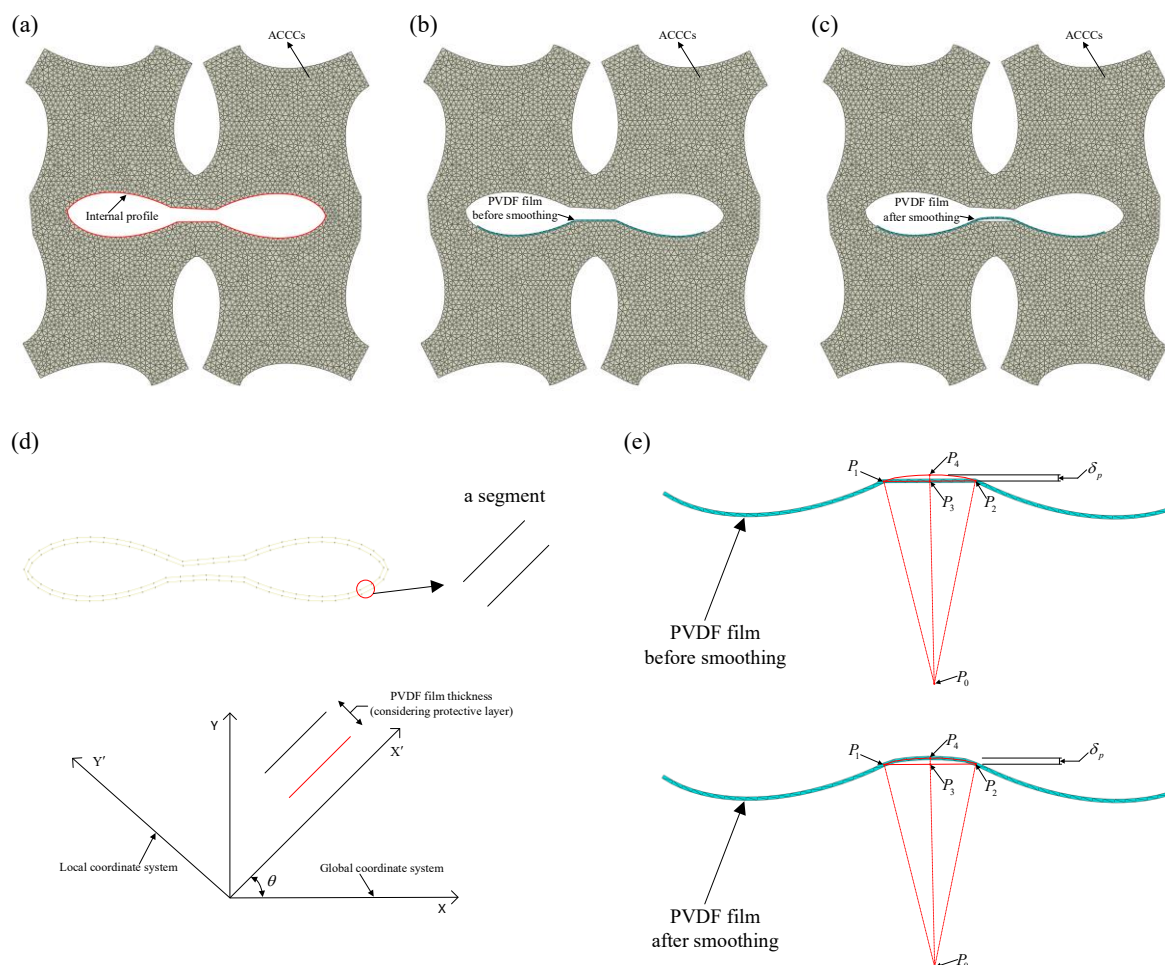


Figure A1. Parametric modeling for PVDF film, (a) internal profile of the specimen, (b) PVDF film construction before smoothing, (c) PVDF film construction after smoothing, (d) coordinates conversion between different coordinate system, (e) geometry information used for PVDF film smoothing.

In experiments, the internal profile of the ACCCs cracks in the middle part [1, 2]. In CDP model, correspondingly, elements in the crack area have a large deformation due to large plastic strain. According to experimental observations, the middle part of PVDF film presents a circular arc above the crack area. Hence, the flatten middle part of the PVDF film needs to be modified to a transition arc by smoothing, as shown in Figure A1c, e. Find two end points P_1, P_2 in the middle flat part, and their midpoint P_3 . Then, P_4 is determined by the distance of δ_p , which is determined by experiments. The coordinates of P_0 can be calculated as the center of the circle through three points of P_1, P_2, P_4 . Finally, the arc connecting P_1, P_2 can be constructed to serve as the central axis of the PVDF film along the thickness direction. The parametric construction of the PVDF film enables it to be accurately fitted to the bonding area of the ACCCs, while also facilitating easy tailoring for parametric analysis and optimization design based on factors such as the practical bonding area, as well as the dimensions of the PVDF film

and ACCCs.

A.2 Limitations for displacement penalty method

As shown in Figure A2a, the greater relative movement differences of the surface elements in their normal direction significantly precludes the sliding of the PVDF film along the curved specimen surface. Figure A2b gives an explanation for this phenomenon via theoretical mechanism. Take one element as an example, when this element moves from the original position (dash box) with the normal direction of n_1 to the current position (solid box) with the normal direction of n_2 . The θ_2 indicates the degree of surface curvature, which represents the angle change of the normal directions after movement. l_1, l_2 are geometric dimensions of the element. d_s is the sliding distance, which can be calculated by Eq. (A8) based on formula derivation. Figure A2c reveals the variation of d_s versus θ_2 when θ_1 takes a value of 1° for sliding forward. This gives a clear indication that the d_s decreases significantly with the increase of θ_2 , which elucidates the significant limitation for sliding distance when displacement penalty method is adopted.

$$d_s = l_1(1 - \cos \theta_1) + \frac{l_1 \sin \theta_1}{\tan \theta_2} \quad (\text{A8})$$

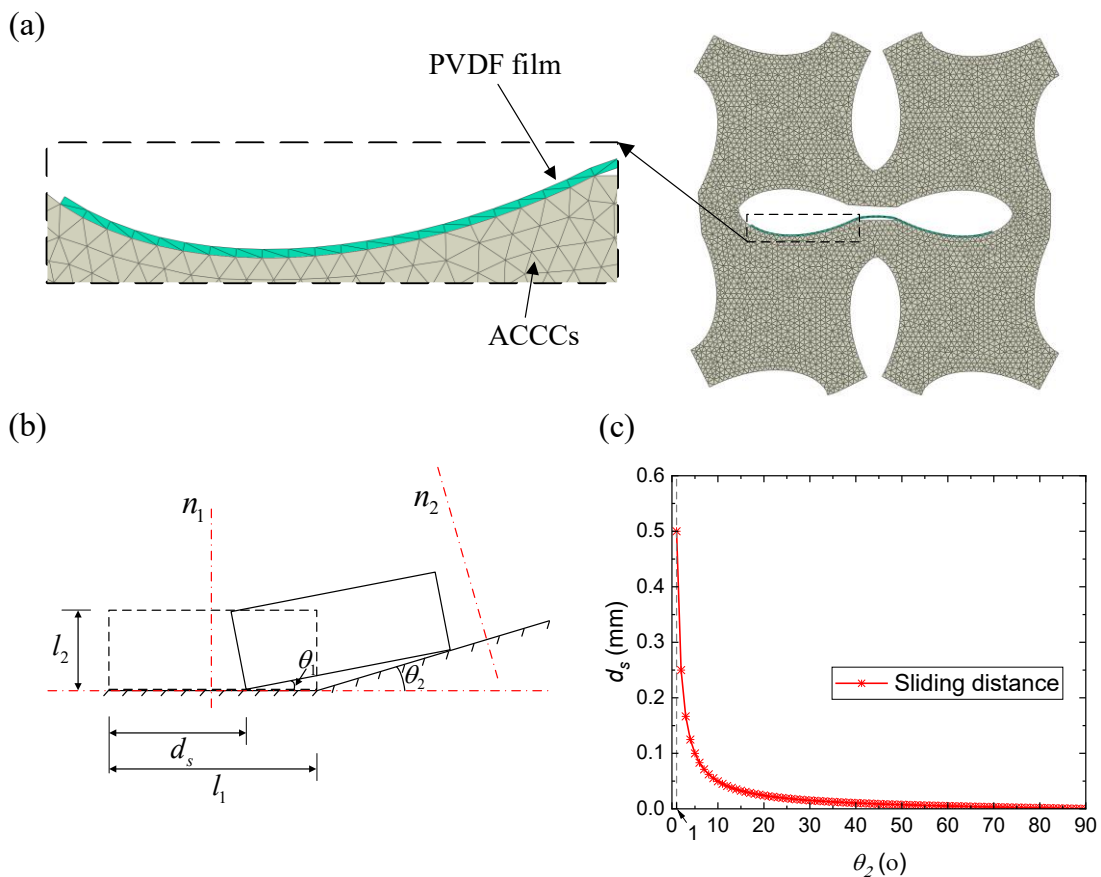


Figure A2. Limitations for normal inseparability based on displacement penalty method, (a) curved surface

between ACCCs and PVDF film, (b) theoretical mechanism of displacement penalty method, (c) the variation of d_s versus θ_2 when PVDF film slides forward at the θ_1 of 1.0° .

A.3 Conversions of displacement and strain between coordinate systems

The displacement conversion (see Figure A3a) between coordinate systems can be formulated as

$$u'_m = \beta_{m,i}^i u_i \quad (\text{A9})$$

where superscript ' indicates variables in the local coordinate system. u_i is the displacement vector in the global coordinate system. u'_m is the displacement vector in the local coordinate system.

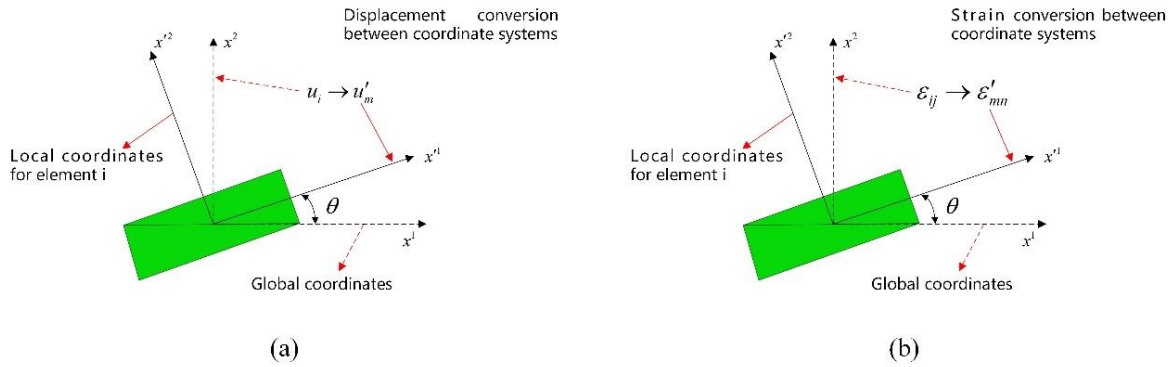


Figure A3. Component conversion between coordinate systems, (a) displacement, (b) strain

Further, Eq. (A9) can be rewritten as

$$\begin{bmatrix} u'_1 \\ u'_2 \end{bmatrix} = \begin{bmatrix} \cos \theta & \sin \theta \\ -\sin \theta & \cos \theta \end{bmatrix} \begin{bmatrix} u_1 \\ u_2 \end{bmatrix} \quad (\text{A10})$$

As schematically displayed in Figure A3b, the strain of each rectangular segment in the global coordinate system can be converted into its equivalent strain in the local coordinate system by Eq. (A11).

$$\begin{aligned} \varepsilon'_{mn} &= \frac{1}{2} \left(\frac{\partial u'_m}{\partial x'^n} + \frac{\partial u'_n}{\partial x'^m} \right) \\ &= \frac{1}{2} \left(\beta_{m,i}^i \frac{\partial u_i}{\partial x^j} \frac{\partial x^j}{\partial x'^n} + \beta_{n,j}^j \frac{\partial u_j}{\partial x^i} \frac{\partial x^i}{\partial x'^m} \right) \\ &= \frac{1}{2} \left(\beta_{m,i}^i \frac{\partial u_i}{\partial x^j} \beta_{n,j}^j + \beta_{n,j}^j \frac{\partial u_j}{\partial x^i} \beta_{m,i}^i \right) \\ &= \frac{1}{2} \left(\frac{\partial u_i}{\partial x^j} + \frac{\partial u_j}{\partial x^i} \right) \beta_{m,i}^i \beta_{n,j}^j \\ &= \beta_{m,i}^i \beta_{n,j}^j \varepsilon_{ij} \end{aligned} \quad (\text{A11})$$

Compared with $\beta_{m,i}^i$, $\beta_{n,j}^j$ can be expressed as

$$\beta_{n,j}^j = \frac{\partial x^j}{\partial x'^n} = \begin{bmatrix} \cos \theta & -\sin \theta \\ \sin \theta & \cos \theta \end{bmatrix} \quad (\text{A12})$$

As indicated in Eq. (A12), the inverse matrix of $\beta_{m,i}^i$ is equal to $\beta_{n,j}^j$.

$$\beta_n^j = [\beta_m^i]^{-1} \quad (\text{A13})$$

Hence, the matrix form of Eq. (A11) can be expressed as

$$\begin{aligned} [\varepsilon'_{mn}] &= [\beta_m^i][\varepsilon_{ij}][\beta_n^j] \\ &= [\beta_m^i][\varepsilon_{ij}][\beta_m^i]^{-1} \end{aligned} \quad (\text{A14})$$

Therefore, Eq. (A14) can be rewritten as

$$\begin{aligned} \begin{bmatrix} \varepsilon'_{11} & \varepsilon'_{12} \\ \varepsilon'_{21} & \varepsilon'_{22} \end{bmatrix} &= \begin{bmatrix} \cos \theta & \sin \theta \\ -\sin \theta & \cos \theta \end{bmatrix} \begin{bmatrix} \varepsilon_{11} & \varepsilon_{12} \\ \varepsilon_{21} & \varepsilon_{22} \end{bmatrix} \begin{bmatrix} \cos \theta & -\sin \theta \\ \sin \theta & \cos \theta \end{bmatrix} \\ &= \begin{bmatrix} \varepsilon_{11} \cos^2 \theta + \varepsilon_{22} \sin^2 \theta & \cos \theta \sin \theta (\varepsilon_{11} - \varepsilon_{22}) \\ \cos \theta \sin \theta (\varepsilon_{11} - \varepsilon_{22}) & \varepsilon_{11} \sin^2 \theta + \varepsilon_{22} \cos^2 \theta \end{bmatrix} \end{aligned} \quad (\text{A15})$$

REFERENCES

- [1] Y. Xu, E. Schlangen, M. Luković, B. Šavija, Tunable mechanical behavior of auxetic cementitious cellular composites (CCCs): Experiments and simulations, *Construction and Building Materials*, 266 (2021) 121388. <https://doi.org/10.1016/j.conbuildmat.2020.121388>.
- [2] Y. Xu, H. Zhang, E. Schlangen, M. Luković, B. Šavija, Cementitious cellular composites with auxetic behavior, *Cement and Concrete Composites*, 111 (2020) 103624. <https://doi.org/10.1016/j.cemconcomp.2020.103624>.

ACKNOWLEDGEMENTS

It has been a long journey since the beginning of my PhD, and I am now finally approaching its end. It feels like reaching the final stretch of a long-distance marathon, where, after a path filled with adventure, setbacks, luck, pain, resilience, perseverance, joy, challenges, emotional ups and downs, moments of despair, breakthroughs, collaboration, and determination, I can finally see the finish banner ahead. Looking back, I indeed enjoy every step of this journey—even during the times when my research encountered unexpected and uncontrollable bottlenecks, whether arising from the work itself or from the surrounding environment. Despite the challenges, this experience has shaped me in ways I deeply value. I would also like to express my sincere appreciation to my friends and colleagues for their support and companionship throughout this journey, which has been both rewarding and memorable.

First, I sincerely acknowledge the China Scholarship Council (CSC) for its financial support, which made this research possible. This funding enabled the successful completion of the work conducted at Microlab, within the Department of Materials, Mechanics and Management & Design (3MD), Faculty of Civil Engineering and Geosciences, Delft University of Technology.

I would like to express my sincere gratitude to my promotor and daily supervisor, Dr. Branko Šavija, for his continuous guidance and support. He encouraged us to freely explore scientific questions driven by our own interests and motivation, while consistently ensuring that our work remained aligned with the overall objectives and logical framework of the research project. He often shared recent literature in related research field, which greatly inspired my work and provided valuable technical insights and methodological guidance. His broad expertise in experimental research, modelling, and machine learning has been instrumental in guiding me to investigate the underlying mechanisms of our research both qualitatively and quantitatively. In addition, our brief conversations during lunch or coffee breaks offered refreshing pauses in the rhythm of research life. These informal discussions not only helped clear my mind and spark new research ideas, but also deepened my understanding of PhD life and the broader path of an academic career.

I also would like to thank the other promotor, Prof. Erik Schlangen. Whenever I encountered questions or challenges in my research, I could simply walk into his office and discuss them openly with him. His careful review of my work provided invaluable and detailed comments, particularly on experimental experience and technical skills, and offered significant inspiration for subsequent research directions, such as the upscaling of auxetic cementitious energy harvesters for practical applications. Moreover, his optimistic and humorous attitude made scientific research feel relaxed and genuinely engaging. I was also inspired by his strong self-discipline and enthusiasm for an active lifestyle—he is known to swim regularly at seven o'clock in the morning. Motivated by this, I also tried morning running, though not very frequently.

Nevertheless, it helped me better balance my research life and strengthened my perseverance when facing challenging research problems.

Besides my promoters, I would like to express my sincere appreciation to the chairperson and all members of my PhD defence committee: Prof. Klaas van Breugel, Prof. dr. G. Ye, Prof. L. J. Sluys, Dr. G. Lavidas, Prof. Y. Farnam, and Prof. Y. Xu. I am grateful for the time they devoted to reviewing my manuscript and for their insightful and constructive comments, which significantly contributed to improving this thesis.

I would like to sincerely thank Prof. Y. Xu for his significant contributions to my PhD thesis. He provided invaluable support in the research on auxetic cementitious materials, including mixture design, fabrication processes, testing methods, innovative ideas, and modeling approaches. He also offered valuable technical assistance with energy harvesting tests of using auxetic cementitious materials. Also, I would like to express my sincere gratitude to Dr. Wen Zhou, Zhaozheng Meng, and Rowin Bol for their assistance with the preparation of auxetic cementitious materials and technical support in 3D printing, and to Shan He, Anne Linde van Overmeir, Yitao Huang, and Shizhe Zhang for their support in the preparation of strain-hardening cementitious composites (SHCC), which further enhanced the mechanical performance stability of the ACCC-based energy harvester developed in this study. I am particularly grateful to Ali Ghaderiaram for his extensive support in electrical engineering, including practical guidance on electrical machine operation, in-depth discussions on piezoelectric theory, and valuable expertise in energy harvesting. I also sincerely thank my colleagues for their valuable assistance with experimental work, including testing on relevant equipment, laboratory safety procedures, sample preparation, experimental methods, and practical guidance on experimental workflows, especially Chen Liu, Eyuphan Kucukkalfa, Patrick Holthuizen, Guilherme da Silva Munhoz, Gabriel Mohallem Ferreira, Rui Wu, Yu Chen, Xuhui Liang, Yu Zhang, Yu Zeng, Boyu Chen, Yun Chen, Laura Gómez Jaramillo, Zhanchong Shi, Pei He, Weikang Feng, and Hongli Su. Furthermore, I gratefully acknowledge Zhi Wan, Minfei Liang, Iuri Rocha, Yubao Zhou, and Hao Cheng for their valuable discussions, technical support, and insightful contributions to the modelling and machine learning aspects of this research.

In the MicroLab, I would like to sincerely thank Maiko van Leeuwen for always bringing a positive atmosphere to the laboratory with his great sense of humor. As a technician, he was consistently willing to help and provided extensive support with Instron-related work, including experimental training, material procurement and management, and guidance on experimental procedures. Beyond his technical contributions, as a friend he also helped keep our group united by organizing various events and gatherings, such as BBQ, PSOR drinks, and food nights. I would also like to express my sincere thanks to Arjan Thijssen and John van den Berg for their professional assistance in laboratory work, their valuable suggestions, and their patience in answering my many questions regarding my experiments.

Regarding my work in other laboratories, I would first like to thank Ton Blom in the MacroLab for his assistance with the fabrication of numerous specimens, including casting, cutting, curing, and basic material preparation. I am also deeply grateful to Kees van Beek for his help in assembling a compression testing machine with a wide load capacity range and a tensile testing machine with a flexible, easy-to-change setup. His excellent experimental design, guidance on the associated software, and the enthusiasm he brings to his work were truly inspiring. When the Instron system was unavailable for an extended period, I sought alternative testing opportunities in other laboratories. I sincerely thank Dave Ruijtenbeek, Alexander Uithol, Chantal de Zeeuw, Wenjie Tu, and Zhiyuan Xu from the Aerospace Structures and Materials Laboratory for their

support with cyclic energy absorption experiments using the MTS machine. I also greatly appreciate Marco Poot for his long-term support with fatigue cyclic testing in the Pavement Engineering Laboratory. In addition, during my extensive mechanical testing in the MacroLab, I would like to thank Giorgos Stamoulis, Fred Schilperoort, Michèle van Aggelen, Paul Vermeulen, and Sergio Sánchez Gómez for their assistance with experimental scheduling, training, and the use of various testing equipment.

I would like to express my sincere gratitude to my wonderful and supportive officemates—Guilherme da Silva Munhoz, Shi Xu, Zhi Wan, and Xuhui Liang. Throughout my PhD journey, they have helped me navigate many challenges in both my research and daily life, offering constant support, encouragement, and companionship. Our discussions, shared experiences, and especially the enjoyable office dinners made my PhD life not only manageable but also truly memorable.

I would also like to thank Luiz Miranda de Lima Junior, Zhaochong Cai, Hu Shi, Wei Yuan, Ismail Yetim, Erbing Hua, and Binbin Zhang. We ran together and participated in numerous running events, sharing both the joy and fun of running. This running spirit not only motivated us and strengthened our passion for work and life, but also helped us maintain a healthy and strong body.

I would also like to thank Jacqueline Berghenengouwen, Jaap Meijer, Iris Batterham, and Sandra Schuchmann for their invaluable support of my PhD research and daily life. They brought us together and organized summer and winter events filled with games, activities, sports, delicious food and drinks, and wonderful team interactions, which helped us connect and truly get to know one another within the 3MD department. These moments remain cherished memories and a source of joy in my PhD life. I am also deeply grateful for their continuous support from the very beginning of my PhD until its completion, including assistance with various university administrative procedures, expense reimbursements, office supplies, meeting arrangements, and countless consultations on practical matters.

I would also like to thank my master's students, Jan Hojnik and Sarah Sultana, for their excellent work on the multifunctional investigation of cementitious composites. The time we spent exploring research together was truly memorable, and I learned a great deal throughout this process. I am also grateful for the valuable experimental experience and skills gained while supervising the bachelor students' tests, particularly those conducted by Paul Hofman and Ruth Dekker.

In addition, I would like to express my special appreciation to my colleagues and friends: Dr. Mladena Luković, Dr. Mohammad Fortouhi, Prof. Henk Jonkers, Dr. Oğuzhan Çopuroğlu, Dr. Dessi Koleva, Dr. Rita Esposito, Dr. Zhuojun Nan, Zhiwei Qian, Hua Dong, Zhenming Li, Zhiyuan Xu, Ze Chang, Lu Cheng, Hongzhi Zhang, Til Gärtner, Mayank Gupta, Reza Mohammad, Max Veeger, Burcu Aytakin Turkoglu, Ameya Kamat, Marija Nedeljković, Farnaz Aghabeyk, Irving Alfredo Flores Beltran, Fanxiang Xu, Langzi Chang, Xinrui Zhang, Jiandong Lu, Zhenxu Qian, Dawei Gu, Rauf Hassan, Fengqiao Zhang, Pengwei Guo, Shihao Fu, Xue Yao, Yi Zheng, Laura Gómez Jaramillo, Kangtai Yan, and Sofia Papoulidou. I sincerely thank you all for your help, valuable suggestions and discussions, as well as for the friendship, coffee breaks, parties, and all the wonderful moments we shared together. Because of all of you, I have gained some of the most beautiful and precious memories of my time at TU Delft. In addition, the buildings, architecture, and landscapes in the Netherlands are full of color and character. Together with the diverse and inclusive environment I experienced here, they have been a truly meaningful part of my PhD journey. Meeting people from different countries, cultures, ethnic backgrounds, and perspectives

has broadened my horizons and enriched both my academic path and my life beyond research, while also bringing vibrancy to my PhD life and inspiring moments of creativity and fresh insight in my work.

I would like to express my deepest gratitude to my parents for their unwavering understanding and support. Their constant care, help, encouragement, and love have been the safe harbor of my life and the guiding light on my path of growth—like a lighthouse, quietly illuminating my way forward.

Centuries ago, during the Age of Great Navigation, Captain James Cook sailed across unknown seas aboard two ships, *Resolution* and *Discovery*. These vessels of exploration embody curiosity, courage, and resilience—qualities that have inspired me to remain steadfast on my own boundless journey of scientific discovery. In the end, I wish to thank the stubborn person—*myself*—for the persistence, endurance, and unwavering passion that carried me through the PhD journey. “*You didn’t come this far only to come this far*”—so keep going. Or, as expressed in Chinese, “百尺竿头, 更进一步”. Carry this passion forward and continue the voyage ahead. As a line from the novel “*Run with the Wind*” asks, “*Do you like running?*” Each runner moves toward a different destination, driven by pain, setbacks, emotion, and passion, while constantly questioning their inner selves. Though anxiety often accompanies an uncertain future, we choose to focus on the present and embrace each step of the journey.

Jinbao Xie (谢津宝)

Delft, January 2026

LIST OF PUBLICATIONS

Journal Publications

- [1] **J. Xie**, Y. Xu, Z. Wan, A. Ghaderiaram, E. Schlangen, B. Šavija, Auxetic cementitious cellular composite (ACCC) PVDF-based energy harvester, *Energy and Buildings*, 298 (2023) 113582.
- [2] **J. Xie**, Y. Xu, Z. Wan, A. Ghaderiaram, E. Schlangen, B. Šavija, Modelling of energy harvesting with bendable concrete and surface-mounted PVDF, *Smart Materials and Structures*, 33 (2024) 085008.
- [3] **J. Xie**, S. He, Y. Xu, Z. Meng, W. Zhou, E. Schlangen, B. Šavija, Enhanced elastomer-like auxetic cementitious materials through strain-hardening cementitious composites (SHCC) with extended softening properties, *Cement and Concrete Composites*, 161 (2025) 106069.
- [4] **J. Xie**, Y. Xu, Z. Meng, M. Liang, Y. Zhou, B. Šavija, Impact behavior of auxetic cementitious cellular composites (ACCCs) architected through additive manufacturing (AM) assisted casting: Experiment and modelling, *Construction and Building Materials*, 471 (2025) 140692.
- [5] **J. Xie**, Y. Xu, Z. Meng, M. Liang, Z. Wan, B. Šavija, Peanut shaped auxetic cementitious cellular composite (ACCC), *Construction and Building Materials*, 419 (2024) 135539.
- [6] **J. Xie**, Y. Xu, Z. Meng, M. Liang, W. Zhou, Y. Zhou, Chen Liu, E. Schlangen, B. Šavija (2025), Bayesian-Driven Modulation of Recoverable Strain in Auxetic Cementitious Cellular Composites for Optimal Energy Harvesters (major revision).
- [7] **J. Xie**, Y. Xu, Y. Zhou, Z. Meng, W. Zhou, C. Liu, M. Fotouhi, B. Šavija (2025). Compliant auxetic cementitious composites for piezoresistive sensing. (under review)
- [8] **J. Xie**, Y. Xu, S. He, Z. Meng, Z. Shi, B. Šavija (2026). Reinforcing piezoelectric energy harvesting and self-sensing in compliant auxetic cementitious materials through strain-hardening cementitious composites with extended softening. (in preparation)
- [9] C. Liu, **J. Xie**, Z. Li, G. Ye, An experimental and numerical study on the cracking of alkali-activated slag pastes induced by water immersion, *Cement and Concrete Research*, 193 (2025) 107877.
- [10] W. Zhou, Y. Xu, Z. Meng, **J. Xie**, Y. Zhou, E. Schlangen, B. Šavija, Filament stitching: An architected printing strategy to mitigate anisotropy in 3D-Printed engineered cementitious composites (ECC), *Cement and Concrete Composites*, 160 (2025) 106044.
- [11] W. Zhou, R.J.M. Bol, Y. Zhou, Z. Meng, Y. Xu, **J. Xie**, B. Šavija, Reinforcing mechanism of lattice-reinforced cementitious composites: insights into flexural performance and material interactions, *Materials & Design*, 256 (2025) 114332.
- [12] Z. Meng, Y. Xu, W. Zhou, **J. Xie**, B. Šavija, Foamed cementitious composites with 3D-printed auxetic lattice reinforcement: enhancing static and cyclic performance, *Composites Part B: Engineering*, 303 (2025) 112614.
- [13] M. Liang, K. Feng, **J. Xie**, Y. Wei, S. Contera, E. Schlangen, B. Šavija, Conditional generative AI for high-fidelity synthesis of hydrating cementitious microstructures, *Materials & Design*, 256 (2025) 114251.

- [14] Z. Meng, Y. Xu, **J. Xie**, W. Zhou, R.J.M. Bol, Q.-f. Liu, B. Šavija, Unraveling the reinforcing mechanisms for cementitious composites with 3D printed multidirectional auxetic lattices using X-ray computed tomography, *Materials & Design*, 246 (2024) 113331.
- [15] M. Liang, **J. Xie**, S. He, Y. Chen, E. Schlangen, B. Šavija, Autogenous deformation-induced stress evolution in cementitious materials considering viscoelastic properties: A review of experiments and models, *Developments in the Built Environment*, 17 (2024) 100356.
- [16] Z. Wan, Y. Xu, S. He, Y. Chen, **J. Xie**, B. Šavija, Direct ink writing of vascularized self-healing cementitious composites, *Cement and Concrete Composites*, 144 (2023) 105295.

Conference Contributions

- [1] **J. Xie**, S. He, Y. Xu, Z. Meng, B. Šavija (2024). Elliptical shaped auxetic cementitious cellular composites (ACCCs) incorporating SHCC: mechanical insights. 12th International Conference of Concrete Creep, Delft, the Netherlands.
- [2] **J. Xie**, Y. Xu, B. Šavija (2024). Renewable Energy Harvester: Integrating Auxetic Cementitious Cellular Composite (ACCC) and PVDF. Net-Zero Future Conference: 1st International Conference on Net-Zero Built Environment for Innovations in Materials, Structures, and Management Practices, Oslo, Norway.
- [3] **J. Xie**, Y. Xu, Z. Meng, B. Šavija (2025). Peanut shaped auxetic cementitious cellular composites (ACCCs). 5th RILEM International Conference on Numerical Modelling Strategies for Sustainable Concrete Structures (SSCS2025), Rotterdam, the Netherlands.
- [4] **J. Xie**, B. Šavija (2025). Low-velocity impact behavior of auxetic cementitious cellular composites (ACCCs). 1st RILEM Youth Symposium (RYS2025, online).

CURRICULUM VITAE

Jinbao Xie

xiejinbao2019@gmail.com

January 28th 1995 Born in Sichuan, China



12/2021 – Present	Doctor of Philosophy Faculty of Civil Engineering and Geosciences Delft University of Technology Delft, the Netherlands
08/2020-10/2021	Research Assistant College of Civil Engineering Tongji University Shanghai, China
09/2017-06/2020	Master of Engineering College of Civil Engineering Tongji University Shanghai, China “Shanghai Outstanding Graduate Award”
09/2013-06/2017	Bachelor of Science School of Civil Engineering Central South University Changsha, China

This PhD dissertation develops an energy harvester that harnesses the recoverable deformation of auxetic cementitious composites, integrating experiments, numerical modeling, and machine learning to enhance energy harvesting performance.



Delft, The Netherlands
March 2026

